Modelization and discretization of two-phase flows in porous media with discrete fracture networks

Mayya Groza

UNIVERSITE DE NICE-SOPHIA ANTIPOLIS - UFR Sciences
Ecole Doctorale en Sciences Fondamentales et Appliquées EDSFA

T H E S E

pour obtenir le titre de
Docteur en Sciences
de l'UNIVERSITE de Nice-Sophia Antipolis

Discipline : Mathématiques

présentée et soutenue par

Mayya GROZA

Modélisation et discretisation des écoulements diphasiques en milieux poreux avec réseaux de fractures discrètes

Thèse dirigée par Roland MASSON
soutenue le 10 novembre 2016

Jury :

M. BRENNER Konstantin	Examinateur
M. CANCES Clément	Rapporteur
M. FORMAGGIA Luca	Rapporteur
M. JEANNIN Laurent	Examinateur
M. MASSON Roland	Directeur de thèse
M. VOHRALIK Martin	Examinateur
M. THEBAULT Jean-Frédéric	Invité

Modélisation et discrétisation des écoulements diphasiques en milieux poreux avec réseaux de fractures discrètes

Résumé: les travaux de cette thèse portent sur la modélisation et la discrétisation des écoulements diphasiques dans les milieux poreux fracturés. On se place dans le cadre des modèles dits dimensionnels hybrides couplant l'écoulement dans la matrice 3D à l'écoulement dans un réseau de fractures modélisées comme des surfaces 2D. La discrétisation s'appuie sur le cadre abstrait des schémas gradients. Les objectifs sont motivés par l'application cible de la thèse qui concerne les procèdès de récupération assistée de gaz par fracturation hydraulique dans les réservoirs de très faibles perméabilités.

Le Chapitre 1 se concentre sur la définition du modèle monophasique dimensionnel hybride pour des réseaux complexes de fractures planes, et sur sa discrétisation par les schémas Vertex Approximate Gradient (VAG) et Volume Finis Hybride (HFV). Nous étendons le modèle réduit dit à pression continu au cas de réseaux complexes de fractures planes comportant des intersections, des fractures débouchantes et des fractures non débouchantes et analysons la convergence des schémas dans le cadre général des schémas gradients. Les résultats de densité de sous espaces de fonctions lisses dans les espaces de pression et de flux présentés dans ce Chapitre sont essentiels afin d'établir la convergence des schèmas numériques étudiés.

Au Chapitre 2, nous étendons le modèle dimensionnel hybride et les schémas VAG et HFV décrits au Chapitre 1 au cas des écoulements diphasiques immiscibles. On utilise pour cela une formulation implicite en pressions des phases qui est adaptée aux pressions capillaires discontinues au sens où elle capte le saut des saturations aux interfaces entre différents types de roches, en particulier à l'interface matrice fracture. Elle suppose en revanche que les pressions capillaires sont strictement croissantes et ne peut donc pas traiter le cas d'une pression capillaire nulle dans la fracture. Les schémas nodaux tels que le schéma VAG ont l'avantage, par rapport aux schémas Control Volume Finite Element (CVFE) d'éviter le mélange des milieux matrice et fracture dans les volumes de contrôle, tout en conservant un coût du même ordre que les méthodes nodales sur des maillages non structurés. On démontre la convergence du schèma VAG sous l'hypothèse que les perméabilités relatives sont minorées par une constante strictement positive. Les tests numériques présentés étudient le choix des volumes de contrôle aux interfaces matrice fracture et comparent les schémas VAG et HFV.

Au Chapitre 3, nous proposons une nouvelle formulation des écoulements diphasique qui repose sur une paramétrisation des graphes monotones des pressions capillaires pour les rocktypes présents à l'interface. Cette nouvelle approche prend en compte des pressions capillaires non strictement croissantes et nous permet de capturer le saut des saturations aux interfaces entre différents types de roches et d'utiliser un nombre minimal d'inconnues par degré de libertè à savoir deux inconnues dans le cas de notre modèle diphasique immiscible. Diffèrents cas tests incluant la simulation de la récupération de gaz dans des réservoirs peu perméables par fracturation hydraulique sont présentés.

Mots-clés: écoulements diphasiques en milieu poreux, milieux fracturés, réseaux de fractures discrètes, schéma volume fini, schémas gradients, analyse numérique, pressions capillaires discontinues

Modelization and discretization of two-phase flows in porous media with discrete fracture networks

Abstract: this thesis presents the work on modelling and discretisation of two-phase flows in the fractured porous media. These models couple the flow in the fractures represented as the surfaces of codimension one with the flow in the surrounding matrix. The discretisation is made in the framework of Gradient schemes which accounts for a large family of conforming and nonconforming discretizations. The test cases are motivated by the target application of the thesis concerning the gas recovery under the hydraulic fracturing process in low-permeability reservoirs.

In Chapter 1 we introduce the hybrid dimensional single-phase flow model for the complex network of plane fractures. We assume the case with continuous pressure at the interfaces between the fractures and the matrix domain. The convergence analysis is carried out in the framework of Gradient schemes which accounts for a large family of conforming and nonconforming discretizations. The Vertex Approximate Gradient (VAG) scheme and the Hybrid Finite Volume (HFV) scheme are applied to this model and are shown to verify the Gradient scheme framework. The key result provides the density of smooth functions subspaces in both the variational space and in the flux space of the model. These density results are shown to hold for a general 3D network of possibly intersecting, immersed or non immersed planar fractures.

In Chapter 2 we extend the hybrid dimensional model, VAG and HFV schemes described in the Chapter 1 to the case of immiscible two-phase flows. In this context we use the phase pressures formulation which allows to capture the saturation jump condition at the interface between different rocktypes without introducing any additional unknowns at these interfaces. On the other hand, it is limited to strictly increasing capillary pressure curves and lacks robustness compared to pressure saturation formulations. Compared with Control Volume Finite Element (CVFE) approaches, the nodal schemes as VAG have the advantage to avoid the mixing of the fracture and matrix rocktypes at the interfaces between the matrix and the fractures, while keeping the low cost of a nodal discretization on unstructured meshes. The convergence of the scheme is proved under the assumption that the relative permeabilities are bounded from below by a strictly positive constant. This assumption is needed in the convergence proof in order to take into account discontinuous capillary pressures in particular at the matrix fracture interfaces. The efficiency of our approach compared with CVFE discretizations is shown on two numerical examples of fracture networks in 2D and 3D.

In Chapter 3 we propose an elegant mathematical framework for two-phase flow in heterogeneous porous media resulting in a family of formulations, which apply to general monotone capillary pressure/saturation relations and handle the saturation jumps at rocktype interfaces. It also allows us to maintain the minimal number of primary unknowns per degree of freedom and deal with arbitrary capillary pressures including multi-valued saturation curves. This framework has been tested on a family of tight gas recovery test cases and compared with the classical pressure-saturation formulation using the Vertex Approximate Gradient scheme for gas liquid hybrid dimensional Darcy flows in the frac-

tured porous media.

Keywords: two-phase flows in porous media, fractured media, discrete fractures network, finite volume scheme, gradient schemes, numerical analysis, discontinuous capillary pressures

Remerciements

"La reconnaissance est la mémoire du coeur."
Hans Christian Andersen

Avant tout je souhaite remercier et exprimer toute ma reconnaissance à mon directeur de thèse Roland Masson pour ses précieux conseils, ses orientations utiles, ses enseignements, son soutien, son enthousiasme permanent et surtout ses qualités humaines exceptionnelles qui m'ont permis de passer trois années passionnantes en ayant toujours envie d'apprendre. Je suis profondément reconnaissante de ce que vous avez fait pour moi. Je veux vous dire aussi merci de m'avoir fait confiance, m'avoir guidée, encouragée, conseillée, pendant ces trois années tout en me laissant une grande liberté.

Plusieurs travaux présentés ici sont le fruit de collaborations, et mes sincères remerciements vont à Konstantin Brenner pour sa disponibilité amicale et les fructueuses discussions que j'ai eues avec lui. Travailler avec lui a été, est et sera toujours un plaisir.

Je tiens à remercier l'ensemble des membres du jury. Merci à Clément Cancès et Luca Formaggia d'avoir accepté d'être les rapporteurs de ma thèse. Vos relectures attentives ont contribué à améliorer à ce manuscrit. Je suis très reconnaissante à Laurent Jeannin, Martin Vohralik et Jean-Frédéric Thebault d'avoir accepté de participer à mon jury.

J'ai aussi eu la chance, tout au long de cette thèse, de pouvoir assister à des conférences un peu partout dans le monde, à Berlin, Padoue, Paris, Catania et Marseille. Cela n'aurait pas été possible sans les financements de ENGIE et je tiens à remercier Laurent Jeanine qui m'a suivie pendant mes trois années de recherches.

Je veux aussi témoigner toute ma reconnaissance à l'Université d'Etat de Novossibirsk (ma chère Alma Mater) où "ils ne m'ont pas rendue plus intelligente mais m'ont appris à penser".

J'exprime ma reconnaissance à Didier Auroux qui a facilité mes démarches administratives auprès de l'université de Nice. J'adresse également mes remerciements à tous les membres du laboratoire J.A. Dieudonne pour cette bonne ambiance durant ces trois années et surtout pour les pauses café...Je vais garder dans mon coeur les meilleurs souvenirs de ma vie en France. J'adresse mes plus chers remerciements à la ville de Nice pour son accueil très chaleureux, pour les personnes très ouvertes et aimables que j'ai rencontrées ici et pour cette amitié entre la Côte d'Azur et la Russie. Je me suis vraiment sentie ici comme chez moi.

"Quand j'étais plus jeune, ce qui veut dire plus vulnérable, mon père me donna un conseil que je ne cesse de retourner dans mon esprit : Quand tu auras envie de critiquer quelqu'un, songe que tout le monde n'a pas joui des mêmes avantages que toi."

F. Scott Fitzgerald

Finalement, je voulais remercier mes parents et mes soeurs de m'avoir permis de devenir la personne que je suis aujourd'hui, de m'avoir supportée et appuyée durant toutes ces années, de m'avoir appris qu'on est vraiment fort quand on a une famille comme la notre. Un grand merci va à ma petite fille Varvara pour avoir été tres sage pendant mon travail sur cette thèse.

Enfin, je garde ces derniers mots pour toi Vladimir, pour ta présence à mes côtés, pour ton soutien, pour tes conseils et ta douceur. Tu es ma motivation et ma force. Merci de m'avoir appris que l'on continuait d'avancer même après avoir pensé qu'il nous était impossible de le faire.

À toute ma grande famille.

Contents

Introduction

Contexte de l'étude et état de l'art

Les roches fracturées sont omniprésentes dans les milieux géologiques, on estime par exemple que la moitié des réservoirs pétroliers sont fracturés. La Figure 1 présente quelques exemples de tels milieux avec des échelles différentes de fractures. L'écoulement dans ces milieux est dominé par la connectivité et la conductivité du réseau de fractures en interaction avec le milieu matrice environnant. Leur modélisation numérique est donc cruciale pour une meilleure gestion des ressources du sous sol. Elle représente un défi du fait de la complexité et du caractère multiéchelle du réseau et du fait des très forts contrastes d'échelles et de propriétés pétrophysiques et hydrodynamiques entre la matrice et les fractures.

Il existe deux types de modèles pour représenter ces écoulements. Le premier concerne les réseaux de fractures suffisamment connectés et uniformes pour que les fractures puissent être homogénéïsées et représentées par un milieu poreux 3D équivalent couplé au milieu poreux 3D matriciel environnant. Le modèle d'écoulement couple alors les écoulements 3D de type Darcy dans chacun des milieux matrice et fracture couplés par des termes sources d'échange entre le milieu matrice et le milieu fracture (voir les travaux pionniers de Warren et Root [61] et de Kazemi [47] et la Figure 2 qui illustre schématiquement ce modèle).

Le deuxième type de modèles, dits à dimension réduite ou dimensionnels hybrides sur lequel se concentre la thèse, représente les réseaux de fractures explicitement comme des surfaces de codimension 1 immergées dans la matrice (voir Figure 3). L'écoulement couple alors un écoulement de Darcy 3D dans le milieu matriciel avec un écoulement 2D dans le réseau de fractures, le couplage étant obtenu par les conditions de transmission à l'interface matrice fracture. Dans le cadre de cette thèse on s'intéresse aux modèles de fractures perméables permettant d'imposer la continuité de la pression comme condition de transmission à l'interface matrice fracture. Ce type de modèle a été introduit dans [3] pour des écoulements monophasiques. Ce choix se justifie par la motivation principale de la thèse qui est l'application de ces modèles à la simulation de la récupération assistée de gaz dans des réservoirs de très faible perméabilité par des méthodes de fracturation hydraulique. Le cas dit à pressions discontinues des modèles prenant en compte les fractures pouvant agir soit comme des drains soit comme des barrières est traité dans [39], [49], [6], dans le cas d'écoulement monophasiques, par des conditions de transmission de type Robin à l'interface matrice fracture autorisant les sauts de pression.

Figure 1: Exemples de milieux poreux fracturés avec différentes échelles de fractures: métrique (au dessus à gauche), hectométrique (au dessus à droite), kilométrique (en dessous). Figures de J. R. de Dreuzy, Geosciences Rennes et équipe-projet Inria Sage.

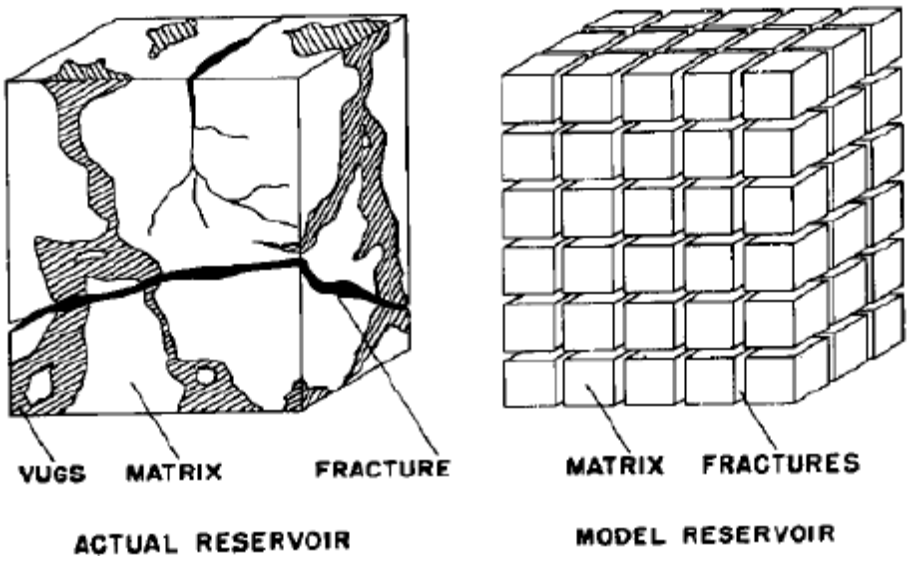

Figure 2: Illustration schématique par Warren et Root du modèle double milieu.

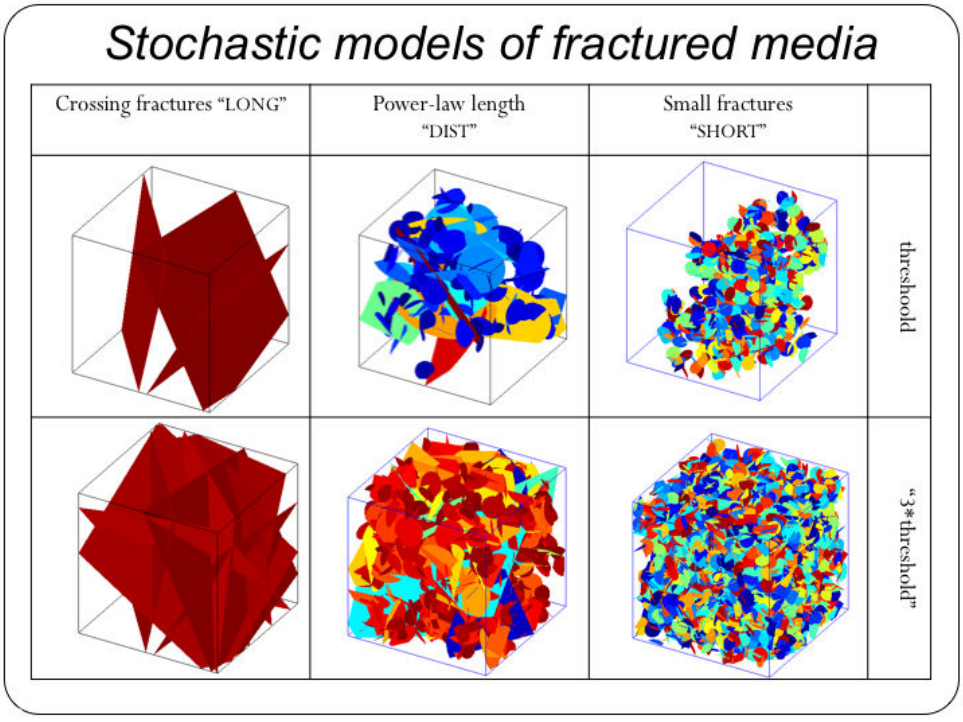

Figure 3: Représentation de milieux poreux fracturés par des réseaux de fractures discrètes avec différentes échelles de longueurs. Figure de J. R. de Dreuzy, Geosciences Rennes et équipe-projet Inria Sage.

Afin d'introduire le principe de réduction de dimension du modèle présenté dans [3], considérons un domaine Ω et une fracture plane traversante d'épaisseur $d_f << diam(\Omega)$ dont le modèle volumique et le modèle à dimension réduite (ou dimensionnel hybride) sont schématisés Figure 4.

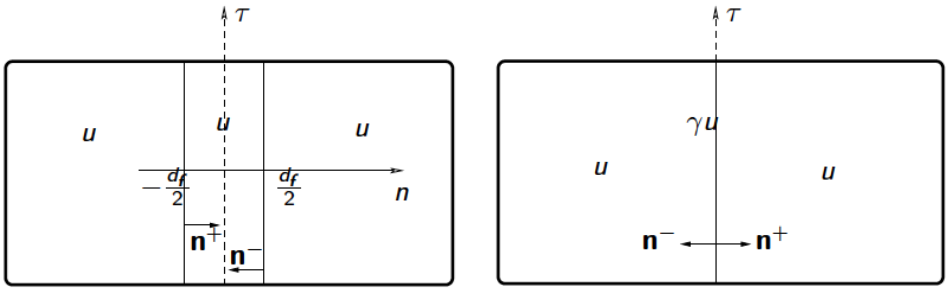

Figure 4: Modèle de fracture volumique (à gauche) et modèle à dimension réduite ou dimensionnel hybride (à droite).

Pour le modèle volumique on note u la pression et $\mathbf{q}$ le flux de Darcy définis sur Ω et

$$\begin{pmatrix} \Lambda_f & 0 \\ 0 & \lambda_{f,n} \end{pmatrix}$$

le tenseur de perméabilité dans la fracture supposé aligné avec les directions longitudinale τ et normale n de la fracture. Le flux de Darcy dans la fracture s'écrit dans ce système de coordonnées

$$\mathbf{q} = -\Lambda_{f,\tau}\nabla_\tau u - \lambda_{f,n}(\partial_n u)\mathbf{n},$$

où $\nabla_\tau = \nabla - (\nabla \cdot \mathbf{n})\mathbf{n}$ est le gradient tangentiel. Pour définir le modèle réduit on intégre la pression et le flux dans l'épaisseur de la fracture, ce qui conduit à définir la pression moyenne u_f le long de la fracture

$$u_f(\tau) = \frac{1}{d_f}\int_{-\frac{d_f}{2}}^{\frac{d_f}{2}} u(\tau, n)\ dn,$$

et le flux longitudinal intégré dans l'épaisseur de la fracture

$$\mathbf{q}_f(\tau) = \int_{-\frac{d_f}{2}}^{\frac{d_f}{2}} -\Lambda_f \nabla_\tau u\ dn = -d_f \Lambda_f \nabla_\tau u_f(\tau).$$

On intégre ensuite l'équation de conservation $\mathrm{div}(\mathbf{q}) = h$ dans l'épaisseur de la fracture de façon à obtenir l'équation de conservation le long de la fracture suivante:

$$\int_{-\frac{d_f}{2}}^{\frac{d_f}{2}} \Big(\mathrm{div}(\mathbf{q}) - h\Big)\ dn = \mathrm{div}_\tau(\mathbf{q}_f) - \mathbf{q}(\tau, \frac{d_f}{2}) \cdot \mathbf{n}^- - \mathbf{q}(\tau, -\frac{d_f}{2}) \cdot \mathbf{n}^+ - d_f h_f = 0,$$

en notant h_f le terme source moyenné dans l'épaisseur de la fracture et div_τ la divergence tangentielle. La condition de transmission dans le cas d'une fracture perméable néglige le saut de pression entre la matrice et le centre de la fracture en supposant la pression moyenne u_f dans la fracture égale aux deux pressions de part et d'autre de la fracture coté matrice. En notant γ l'opérateur de trace sur la fracture on suppose donc que la pression (toujours notée u par abus de notations) du modèle réduit est globalement dans H^1 et que $u_f = \gamma u$ comme illustré sur la Figure 4. Le modèle de Darcy dimensionnel hybride s'écrit alors:

$$\begin{cases} \mathrm{div}(\mathbf{q}_m) = h_m, \\ \mathrm{div}_\tau(\mathbf{q}_f) - [\![\mathbf{q}_m \cdot \mathbf{n}]\!] = d_f h_f \\ \mathbf{q}_f = -d_f \Lambda_f \nabla_\tau \gamma u \\ \mathbf{q}_m = -\Lambda_m \nabla_\tau u \end{cases}$$

où $[\![\mathbf{q}_m \cdot \mathbf{n}]\!]$ est le saut de la trace normale du flux matriciel $\mathbf{q}_m$ et Λ_m le tenseur de perméabilité dans la matrice. A noter que l'hypothèse de pression continue à l'interface matrice fracture pour le modèle réduit est justifiée dès lors que

$$\frac{\lambda_{f,n}}{d_f} >> \frac{\Lambda_m}{\mathrm{diam}(\Omega)},$$

c'est à dire d'autant plus que la fracture est de faible épaisseur et de forte perméabilité.

La principale difficulté pour l'extension des modèles de Darcy dimensionnels hybrides au cas diphasique repose sur la prise en compte des sauts de saturations aux interfaces matrice fracture liés à la discontinuité des pressions capillaires entre le milieu matrice et le milieu fracture. Le point de départ naturel sera donc les travaux [29], [20], [21] sur la formulation mathématique des écoulements diphasiques traitant les interfaces entre différents types de roches avec pressions capillaires discontinues. Le modèle proposé dans [35] nous servira de point de départ. Il utilise les pressions des deux phases comme variables primaires et exprime les saturations comme fonctions de la pression capillaire de façon à capter les sauts des saturations aux interfaces entre différents types de roches. On peut aussi mentionner les modèles formulés en pression globale proposés dans [11] dans le cas simple milieu et dans [45] dans le cas de modèles dimensionnels hybrides à pressions discontinues.

La discrétisation des modèles de Darcy dimensionnels hybrides avec pressions continues ou discontinues aux interfaces matrice fracture a fait l'objet de nombreux travaux. Les auteurs proposent dans [46], [6] un schéma volume finis centré avec approximation deux point des flux (Two Point Flux Approximation ou TPFA) qui suppose une condition d'orthogonalité du maillage et l'isotropie des perméabilités. Les schémas volume finis centrés ont été étendus au cas de maillages généraux et de perméabilités anisotropes dans [60], [57], [2] pour les modèles à pressions discontinues. Néanmoins ces schémas peuvent manquer de robustesse dans le cas de mailles déformées et de fortes anisotropies du fait de leur coercivité dépendante du maillage et de l'anisotropie. Ils sont aussi très coûteux dans le cas de maillages tétraèdriques par comparaison à des discrétisations nodales.

Dans [3], une méthode d'Eléments Finis Mixtes (EFM) a été introduite pour les modèles monophasiques à pression continue. Pour les modèles monophasiques à pressions discontinues, les EFM sont introduits dans [49] et les méthodes Mimetiques dans [7] et dans [38]. L'extension au cas diphasique est traité dans [43] dans le cadre d'un schéma ImPES (Implicite en Pression et Explicite en Saturation) en utilisant une méthode d'Eléments Finis Mixtes Hybrides (EFMH) pour l'équation de pression et d'une méthode de Galerkin Discontinue pour l'équation de saturation. Ces méthodes sont adaptées aux maillages généraux et aux perméabilités anisotropes mais nécessitent un grand nombre de degrés de liberté de l'ordre du nombre de faces du maillage. Les méthodes de type Control Volume Finite Element (CVFE) proposées dans [54], [53] dans le cas diphasique ont l'avantage de n'utiliser que des inconnues nodales ce qui conduit à un faible nombre de degré de liberté dans le cas de maillages tétraèdriques. Néanmoins, ces méthodes ont l'inconvénient dans le cas diphasique de mélanger les différents types de roches aux noeuds situés à l'interface entre différents types de roches. Il est alors nécessaire de raffiner fortement le maillage à l'interface matrice fracture pour éviter d'élargir artificiellement les drains que constituent les fractures.

L'analyse de la convergence des schémas numériques pour ce type de modèles est restreinte dans le cas monophasique au cas d'une unique fracture débouchante dans [3] et [49] ou non débouchante dans [6]. Le cas de réseaux complexes de fractures s'intersectant, débouchantes ou non débouchantes n'a pas à notre connaissance été étudié avant ces travaux de thèse. Cette analyse nécessite notamment d'établir la densité de sous espaces de fonctions lisses à la fois pour l'espace des pressions et pour l'espace des flux.

Dans le cas diphasique, aucun travaux avant cette thèse n'a porté à notre connaissance sur l'analyse de convergence des schémas pour les modèles dimensionnels hybrides. Dans le cas sans fractures, les premiers résultats de convergence par compacité vers une solution faible d'un écoulement diphasique ont été obtenus dans [51] et [33] dans le cas d'un schéma volume finis centré avec approximation TPFA des flux sur maillages orthogonaux. Dans [33] la convergence du schéma est obtenue dans le cadre de la formulation de référence dans l'ingénierie pétrolière basée sur les deux inconnues primaires pression et saturation et sur le décentrage par phase des mobilités. Ce résultat très technique repose sur des fonctions tests non linéaires et est restreint aux schémas TPFA sur maillages orthogonaux. Dans [51] la convergence est établie toujours pour les schémas TPFA sur maillages orthogonaux dans le cas plus simple d'une formulation en pression globale introduite dans [22] (voir aussi [8]) en supposant une pression capillaire homogène. Dans le cadre de cette formulation en pression globale pour une pression capillaire homogène, l'extension à des schémas volume finis sur maillages généraux est étudiée dans [10] dans le cas des schémas Volume Finis Hybride (HFV), dans [16] dans le cas du schéma Vertex Approximate Gradient (VAG) et dans [37] dans le cadre général des schémas gradients introduit dans [31].

Dans le cadre de cette thèse, il nous faut prendre en compte une difficulté essentielle liée à la discontinuité des pressions capillaires notamment à l'interface matrice fracture. Ce problème est traité dans [11] en utilisant un schéma TPFA sur maillages orthogonaux adapté aux discontinuités de la pression capillaire à l'aide d'inconnues d'interface. Une

extension au cas de maillages polyèdriques généraux est proposée dans [35] dans le cadre général des schémas gradients en utilisant une formulation en pressions des phases. Cette formulation a l'avantage d'utiliser uniquement deux inconnues primaires par degré de liberté, à savoir les pressions des deux phases. Contrairement aux résultats obtenus dans [11] pour un schéma TPFA, la preuve de convergence nécessite une hypothèse restrictive sur le plan physique de non dégénerescence des perméabilités relatives.

Les objectifs de la thèse sont motivés par l'application cible de la thèse qui concerne les procédés de récupération assistée de gaz par fracturation hydraulique dans les réservoirs de très faibles perméabilités. Les fractures seront supposées déjà formées et l'objectif est de simuler les écoulements gaz liquide dans le milieu poreux fracturé modélisé par un modèle de Darcy dimensionnel hybride. On souhaite prendre en compte des réseaux de fractures de complexité moyenne, pouvant néanmoins comporter quelques intersections entre les fractures issues de la fracturation hydraulique et des fractures naturelles. Un point essentiel en terme de modélisation géométrique et physique est le très fort constraste de perméabilités et de capillarités entre la matrice et les fractures. De ce fait, l'eau injectée dans les fractures pénètre sur une très faible épaisseur dans la direction normale aux fractures, quelques dizaines de centimètres à comparer à l'extension décamétrique des fractures. Cette eau est retenue dans la matrice par effet capillaire ce qui contribue à diminuer la mobilité du gaz lors de la phase de production, il est donc essentiel de la modéliser avec précision. Afin de représenter cette géométrie et de capter l'échelle de pénétration de l'eau au voisinage des fractures, le maillage comportera typiquement des prismes pour le raffinement anisotrope au voisinage des fractures, et des tétraèdres pour le raccord avec la frontière du réservoir (voir Figures 5 et 6). La discrétisation spaciale devra donc être adaptée aux milieux anisotropes et aux maillages polyèdriques qui offrent une grande souplesse en terme de représentation géométrique. En terme de modélisation, l'accent sera mis sur la prise en compte précise des conditions de transmission à l'interface matrice fracture et du fort constraste de capillarités entre la matrice et les fractures. On souhaite en particulier pouvoir traiter des capillarités nulles dans les fractures et des pressions d'entrée non nulles dans la matrice.

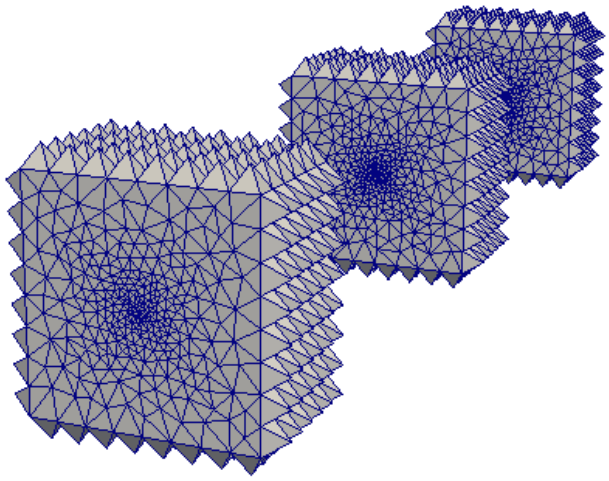

Figure 5: Maillage prismatique autour de chaque fracture et couche de pyramide pour le raccord avec le maillage tétraèdrique du réservoir. L'épaisseur des prismes a été aggrandie pour une meilleure visibilité.

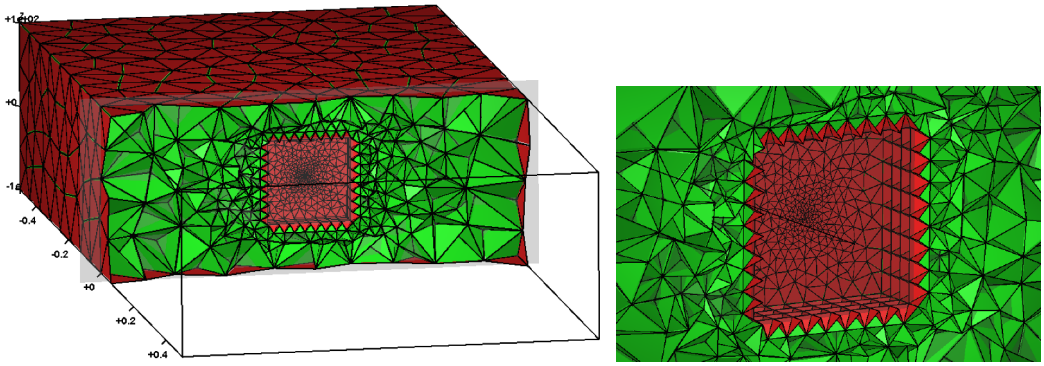

Figure 6: Maillage tétraèdrique du réservoir raccordé avec les couches de prismes au voisinage des fractures à l'aide d'une couche de pyramides. L'épaisseur des prismes a été aggrandie pour une meilleure visibilité.

Plan de la thèse

La thèse comporte trois Chapitres ainsi qu'un Appendice. Le premier Chapitre se concentre sur la définition du modèle monophasique dimensionnel hybride pour des réseaux complexes de fractures planes, sa discrétisation par les schémas VAG et HFV et sur l'analyse de la convergence des schémas dans le cadre général des schémas gradients. Le second Chapitre porte sur le modèle diphasique en formulation pressions des phases adaptée aux pressions capillaires discontinues et permettant de capter les sauts de saturations aux interfaces entre différents types de roches notamment à l'interface matrice

fracture. Les schémas VAG et HFV sont étendus à ce modèle dans le cadre d'une formulation fully implicite et la convergence par compacité vers une solution faible est analysée sous l'hypothèse de non dégénesrence des perméabilités relatives. Le troisième Chapitre étend la formulation précédente du modèle diphasique de façon à pouvoir traiter notamment des pressions capillaires nulles dans les fractures tout en captant les sauts de saturations aux interfaces matrice fracture. Pour cela, un cadre général est introduit qui repose sur la paramétrisation des graphes des pressions capillaires et maintient le nombre minimal d'inconnues primaires par degré de liberté. Dans chacun des trois Chapitres, des tests numériques principalement 3D illustrent la performance des méthodes numériques introduites et les comparent. L'Appendice démontre quelques résultats techniques utilisés dans les preuves de convergence des Chapitres 1 et 2, notamment les résultats de densités de sous espaces de fonctions lisses pour les espaces de pression et de flux du modèle.

Chapitre 1: modèles monophasiques

Ce Chapitre présente le modèle d'écoulement monophasique dit dimensionnel hybride couplant l'écoulement dans la matrice et celui dans le réseau de fractures représentées comme des surfaces de codimension 1. On considère le cas de fractures perméables dont le modèle à dimension réduite a été introduit dans [3]. Le premier objectif du Chapitre 1 est d'étendre ce modèle au cas de réseaux complexes de fractures planes comportant des intersections, des fractures débouchantes et des fractures non débouchantes. Le cadre fonctionnel est détaillé et on établit notamment des résultats de densité de sous espaces de fonctions lisses dans les espaces de pression et de flux dont les preuves sont dans l'Appendice. Ces résultats sont essentiels afin d'établir la convergence des schémas numériques étudiés dans ce Chapitre. Le deuxième objectif du Chapitre 1 est d'étendre les discrétisations Vertex Approximate Gradient (VAG) et Volume Finis Hybride (HFV) introduits dans [31] et [30] pour les problèmes de diffusion en milieu hétérogène anisotrope. Le troisième objectif est d'étudier théoriquement et numériquement la convergence des schémas VAG et HFV. On utilise pour leur analyse numérique, le cadre général abstrait des schémas gradients introduit dans [31], [28], [26] pour analyser la convergence de méthodes numériques pour des problèmes de diffusion linéaires et non linéaires. Ce cadre inclut de nombreuses discrétisations conformes ou non conformes telles que les Eléments Finis, les Eléments Finis Mixtes et Mixtes Hybrides, certains schémas volumes finis symétriques comme les schémas MultiPoint Flux Approximation (MPFA), le schéma VAG, le schéma HFV et les méthodes de différences finis mimétiques (MFD) faisant partie de la classe plus générale des méthodes mixtes hybrides (HMM) [27].

Le plan du Chapitre 1 est le suivant: dans la Section 1.2 on introduit le cadre géométrique pour les réseaux complexes de fractures planes, le cadre fonctionnel ainsi que les formulations forte et variationnelle du modèle de Darcy monophasique dimensionnel hybride. La Section 1.3 étend le cadre abstrait des schémas gradient à notre modèle en définissant les opérateurs et en énonçant les hypothèses de coercivité, de consistence, de conformité à la limite et de compacité qu'ils sont supposés satisfaire. Ensuite

la discrétisation du modèle par le schéma gradient est définie et sa convergence établie sous les hypothèses précédentes. La Section 1.4 étend les schémas VAG et HFV à notre modèle et on montre que ces deux schémas satisfont le cadre des schémas gradient. La Section 1.5 compare numériquement les deux schémas VAG et HFV sur des solutions analytiques 3D en milieu homogène ou hétérogène, isotrope ou anisotrope, et pour différentes familles de maillages cartésiens, hexaèdriques ou tétraèdriques.

Chapitre 2: modèles diphasiques

Dans ce Chapitre nous étendons le modèle dimensionnel hybride décrit au Chapitre précédent au cas des écoulements diphasiques immiscibles. On utilise pour cela une formulation implicite en pressions des phases qui est adaptée aux pressions capillaires discontinues au sens où elle capte le saut des saturations aux interfaces entre différents types de roche, en particulier à l'interface matrice fracture. Elle suppose en revanche que les pressions capillaires sont strictement croissantes et ne peut donc pas traiter le cas d'une pression capillaire nulle dans la fracture qui sera considéré au Chapitre 3. Les schémas VAG et HFV du Chapitre 1 sont étendus au cas d'un écoulement diphasique en utilisant les flux du Chapitre 1 combinés à un décentrage par phase des mobilités. Une difficulté essentielle pour les schémas nodaux tels que le schéma VAG réside dans le choix des volumes de contrôle aux noeuds situés à l'interface matrice fracture. Ces volumes de contrôle ne doivent pas mélanger les types de roches matrice et fracture afin d'éviter d'élargir artificiellement les fractures ce qui conduirait à ralentir la propagation du front dans les fractures. On propose une stratégie simple et efficace pour résoudre ce problème qui est comparée numériquement à l'approche classique pour les schémas de type Control Volume Finite Element (CVFE) sur des cas tests avec fort contraste de perméabilités entre la matrice et les fractures. Les tests numériques incluent également, comme au Chapitre 1, la comparaison des schémas VAG et HFV sur un cas test traceur et un cas test diphasique 3D. L'analyse de convergence par compacité du schéma vers une solution faible est détaillée, pour fixer les idées, dans le cas du schéma VAG en formulation variationnelle et sans décentrage des mobilités. Cette analyse s'étendrait sans difficultés supplémentaires au cadre général des schémas gradient du Chapitre 1. Elle suppose, tout comme dans [35], la non dégénerescence des perméabilités relatives. Il s'agit à notre connaissance de la première preuve de convergence pour ce type de modèle.

Le plan du Chapitre est le suivant. La Section 2.2 introduit le modèle en formulation variationnelle et sa discrétisation par le schéma VAG fait l'objet de la Section 2.3. La convergence du schéma vers une solution faible est étudiée dans la Section 2.4. La Section 2.5 présente la discrétisation VAG et HFV du modèle en formulation flux avec décentrage par phase qui est celle utilisée dans les tests numériques du fait de sa plus grande robustesse pour les régimes à convection dominante. Des tests numériques étudiant le choix des volumes de contrôle aux interfaces matrice fracture et comparant les schémas VAG et HFV sont présentés dans la Section 2.6.

Chapitre 3: nouvelle formulation des modèles diphasiques

L'objectif du Chapitre 3 est d'étendre la formulation en pressions des phases du Chapitre précédent de façon à prendre en compte des pressions capillaires non strictement croissantes et en particulier pouvant s'annuler dans les fractures. Cette extension se doit de toujours capturer le saut des saturations aux interfaces entre différents types de roches et d'utiliser le nombre minimal d'inconnues par degré de liberté à savoir deux inconnues dans le cas de notre modèle diphasique immiscible. La méthodologie proposée repose sur une paramétrisation des graphes monotones des pressions capillaires pour les rocktypes présents à l'interface et peut être vue comme un cadre général rigoureux pour les méthodes de type variable switch [53] .

Le plan du Chapitre est le suivant. La Section 3.2 présente le cadre méthodologique de la paramétrisation et en déduit l'extension de la discrétisation VAG du Chapitre précédent au cas général de pressions capillaires avec graphes monotones. La Section 3.3 teste la méthode en la comparant à une formulation en variables pression saturation sur plusieurs cas tests incluant la simulation de la récupération de gaz dans des réservoirs peu perméables par fracturation hydraulique.

Chapter 1

Hybrid Dimensional Single Phase Darcy Flows in Fractured Porous Media

Abstract: this Chapter deals with the discretization of hybrid dimensional Darcy flows in fractured porous media. These models couple the flow in the fractures represented as surfaces of codimension one with the flow in the surrounding matrix. The convergence analysis is carried out in the framework of gradient schemes which accounts for a large family of conforming and nonconforming discretizations. The Vertex Approximate Gradient (VAG) scheme and the Hybrid Finite Volume (HFV) scheme are extended to such models and are shown to verify the gradient scheme framework. Our theoretical results are confirmed by numerical experiments performed on tetrahedral, Cartesian and hexahedral meshes in heterogeneous isotropic and anisotropic porous media.

1.1 Introduction

This Chapter deals with the discretization of Darcy flows in fractured porous media for which the fractures are modeled as interfaces of codimension one. In this framework, the $d-1$ dimensional flow in the fractures is coupled with the d dimensional flow in the matrix leading to the so called hybrid dimensional Darcy flow model. We focus on the particular case where the pressure is continuous at the interfaces between the fractures and the matrix domain. This type of Darcy flow model introduced in [3] corresponds physically to pervious fractures for which the ratio of the transversal permeability of the fracture to the width of the fracture is large compared with the ratio of the permeability of the matrix to the size of the domain. Note that it does not cover the case of fractures acting as barriers for which the pressure is discontinuous at the matrix fracture interfaces (see [39], [49], [6] for discontinuous pressure models). It is also assumed in our model that the pressure is continuous at the fracture intersections. It corresponds to a high ratio assumption between the permeability at the fracture intersections and the width of the fracture compared with the ratio between the tangential permeability of each fracture and its length. We refer to [40] for a more general reduced model taking into account discontinuous pressures at fracture intersections in dimension $d = 2$.

The discretization of the hybrid dimensional Darcy flow model with continuous pressures has been the object of several works. In [46] a cell-centered Finite Volume scheme using a Two Point Flux Approximation (TPFA) is proposed assuming the orthogonality of the mesh and isotropic permeability fields. Cell-centered Finite Volume schemes can be extended to general meshes and anisotropic permeability fields using MultiPoint Flux Approximations (MPFA) following the ideas introduced in [60], [57], and [2] for discontinuous pressure models. In [3], a Mixed Finite Element (MFE) method is proposed, and Control Volume Finite Element Methods (CVFE) using nodal unknowns have been introduced for such models in [54] and [53]. A MFE discretization adapted to non-matching fracture and matrix grids is also studied in [24].

The main goal of this Chapter is to extend the gradient scheme framework to the case of hybrid dimensional Darcy flow models. This framework has been introduced in [31], [28], [26] to analyse the convergence of numerical methods for linear and nonlinear second order diffusion problems. As shown in [28], this framework accounts for various conforming

and non conforming discretizations such as Finite Element methods, Mixed and Mixed Hybrid Finite Element methods, and some Finite Volume schemes like symmetric MPFA, Vertex Approximate Gradient (VAG) schemes [31], and Hybrid Finite Volume (HFV) schemes [30].

The extension of the gradient scheme framework to the hybrid dimensional Darcy flow model is defined by a vector space of degrees of freedom, two discrete gradient reconstruction operators and two discrete function reconstruction operators in the matrix and the fracture domains. The gradient discretization of the hybrid dimensional Darcy flow model is then based on a primal non conforming variational formulation using the previous operators. In the spirit of [31],[28] the well posedness and convergence of the gradient scheme is obtained assuming that the gradient discretization satisfies the so-called coercivity, consistency, and limit conformity assumptions.

Two examples of gradient discretization are given, namely we extend the VAG and HFV schemes defined in [31] and [30] to the hybrid dimensional Darcy flow model. In both cases, it is assumed that the fracture network is conforming to the mesh in the sense that it is defined as a collection of faces of the mesh. The VAG scheme uses nodal and fracture face unknowns in addition to the cell unknowns which can be eliminated without any fill-in. It leads to a sparse discretization on tetrahedral or mainly tetrahedral meshes. It has the advantage, compared with CVFE approaches to avoid the mixing of the control volumes at the fracture matrix interfaces, which is a key feature for its application to multiphase Darcy flows (see [13]). It will be compared to the HFV discretization using face and fracture edge unknowns in addition to the cell unknowns which can be as well eliminated without any fill-in.

The proof that both the VAG and HFV schemes satisfy the coercivity, consistency, and limit conformity assumptions of the gradient scheme framework is based on a key result providing the density of smooth functions subspaces in both the variational space and in the flux space of the model. These density results are shown to hold for a general 3D network of possibly intersecting, immersed or non immersed planar fractures.

The outline of the Chapter is the following, in Section 1.2 we introduce the general 3D network of planar fractures, the function spaces, as well as the primal variational formulation of the hybrid dimensional Darcy flow model. Section 1.3 defines the gradient discretization framework stating the coercivity, consistency, limit conformity, and compactness assumptions. Then, the gradient scheme is introduced for the hybrid dimensional model and its well posedness and convergence is shown to hold under the coercivity, consistency, and limit conformity assumptions. Section 1.4 extends the VAG and HFV schemes to our model and prove that each of them satisfies the gradient scheme assumptions. Section 4 proves the density of smooth functions subspaces in both the variational space and in the flux space which is the key ingredient to show that the VAG and HFV schemes satisfy the gradient scheme assumptions. Section 1.5 provides a numerical comparison of the VAG and HFV schemes on 3D analytical solutions using Cartesian, hexahedral and tetrahedral meshes. Both heterogeneous and anisotropic test cases are considered.

1.2 Hybrid dimensional Darcy Flow Model in Fractured Porous Media

1.2.1 Discrete Fracture Network and functional setting

Let Ω denote a bounded domain of $\mathbb{R}^d$, $d = 2, 3$ assumed to be polyhedral for $d = 3$ and polygonal for $d = 2$. To fix ideas the dimension will be fixed to $d = 3$ when it needs to be specified, for instance in the naming of the geometrical objects or for the space discretization in the next section. The adaptations to the case $d = 2$ are straightforward.

We consider the asymptotic model introduced in [3] where fractures are represented as interfaces of codimension 1. Let I be a finite set and let $\overline{\Gamma} = \bigcup_{i\in I} \overline{\Gamma}_i$ and its interior $\Gamma = \overline{\Gamma} \setminus \partial\overline{\Gamma}$ denote the network of fractures $\Gamma_i \subset \Omega$, $i \in I$, such that each Γ_i is a planar polygonal simply connected open domain included in an oriented plane $\mathcal{P}_i$ of $\mathbb{R}^d$. It is assumed that the angles of Γ_i are strictly smaller than 2π and that $\Gamma_i \cap \overline{\Gamma}_j = \emptyset$ for all $i \neq j$. For all $i \in I$, let us set $\Sigma_i = \partial\Gamma_i$, $\Sigma_{i,j} = \Sigma_i \cap \Sigma_j$, $j \in I \setminus \{i\}$, $\Sigma_{i,0} = \Sigma_i \cap \partial\Omega$, $\Sigma_{i,N} = \Sigma_i \setminus (\bigcup_{j\in I\setminus\{i\}} \Sigma_{i,j} \cup \Sigma_{i,0})$, and $\Sigma = \bigcup_{(i,j)\in I\times I, i\neq j} \Sigma_{i,j}$. It is assumed that $\Sigma_{i,0} = \overline{\Gamma}_i \cap \partial\Omega$. Let us define the following trace operator $\gamma_{\Sigma_i} : H^1(\Gamma_i) \to L^2(\Sigma_i)$. We will denote

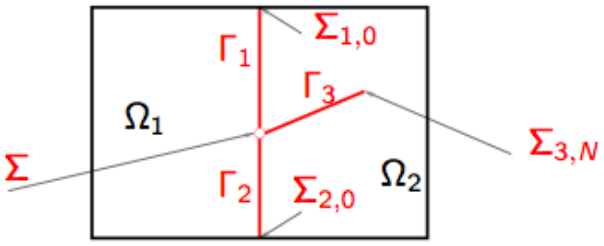

Figure 1.1: Example of a 2D domain with 3 intersecting fractures $\Gamma_1, \Gamma_2, \Gamma_3$ and 2 connected components Ω_1, Ω_2.

by $d\tau(\mathbf{x})$ the $d-1$ dimensional Lebesgue measure on Γ. On the fracture network Γ, we define the function space $L^2(\Gamma) = \{v = (v_i)_{i\in I}, v_i \in L^2(\Gamma_i), i \in I\}$, endowed with the norm $\|v\|_{L^2(\Gamma)} = (\sum_{i\in I} \|v_i\|^2_{L^2(\Gamma_i)})^{\frac{1}{2}}$. Its subspace $H^1(\Gamma)$ is defined as the space of functions $v = (v_i)_{i\in I}$ such that $v_i \in H^1(\Gamma_i)$, $i \in I$ with continuous traces at the fracture intersections i.e. $\gamma_{\Sigma_i} v_i = \gamma_{\Sigma_j} v_j$ on $\Sigma_{i,j}$ for all $i \neq j$ such that $\Sigma_{i,j}$ has a non zero $d-2$ Lebesgue measure. The space $H^1(\Gamma)$ is endowed with the norm $\|v\|_{H^1(\Gamma)} = (\sum_{i\in I} \|v_i\|^2_{H^1(\Gamma_i)})^{\frac{1}{2}}$ and its subspace with vanishing traces on $\Sigma_0 = \bigcup_{i\in I} \Sigma_{i,0}$ is denoted by $H^1_{\Sigma_0}(\Gamma)$.

Let us also consider the trace operator γ_i from $H^1(\Omega)$ to $L^2(\Gamma_i)$ as well as the trace operator γ from $H^1(\Omega)$ to $L^2(\Gamma)$ such that $(\gamma v)_i = \gamma_i(v)$ for all $i \in I$.

On Ω, the gradient operator from $H^1(\Omega)$ to $L^2(\Omega)^d$ is denoted by ∇. On the fracture network Γ, the tangential gradient ∇_τ acting from $H^1(\Gamma)$ to $L^2(\Gamma)^{d-1}$ is defined by

$$\nabla_\tau v = (\nabla_{\tau_i} v_i)_{i\in I},$$

where, for each $i \in I$, the tangential gradient ∇_{τ_i} is defined from $H^1(\Gamma_i)$ to $L^2(\Gamma_i)^{d-1}$ by fixing a reference Cartesian coordinate system of the plane $\mathcal{P}_i$ containing Γ_i. We also denote by div_{τ_i} the divergence operator from $H_{\mathrm{div}}(\Gamma_i)$ to $L^2(\Gamma_i)$.

The function spaces arising in the variational formulation of the hybrid dimensional Darcy flow model are

$$V = \{v \in H^1(\Omega) \text{ such that } \gamma v \in H^1(\Gamma)\},$$

and its subspace

$$V^0 = \{v \in H^1_0(\Omega) \text{ such that } \gamma v \in H^1_{\Sigma_0}(\Gamma)\}.$$

From Poincaré inequality on $H^1_0(\Omega)$ and the continuity of the trace operator γ, we deduce the following inequality.

Proposition 1.2.1 *There exists $C_P > 0$ such that for all $v \in V^0$ one has*

$$\|v\|_{L^2(\Omega)} + \|\gamma v\|_{L^2(\Gamma)} \leq C_P \|\nabla v\|_{L^2(\Omega)^d}.$$

Thus, the space V^0 is endowed with the Hilbertian norm

$$\|v\|_{V^0} = \left(\|\nabla v\|^2_{L^2(\Omega)^d} + \|\nabla_\tau \gamma v\|^2_{L^2(\Gamma)^{d-1}}\right)^{1/2},$$

and the space V with the Hilbertian norm $\|v\|_V = \left(\|v\|^2_{V^0} + \|v\|^2_{L^2(\Omega)} + \|\gamma v\|^2_{L^2(\Gamma)}\right)^{1/2}$.

The following density result is proved in the Appendix.

Proposition 1.2.2 *The spaces $C^\infty(\overline{\Omega})$ and $C^\infty_c(\Omega)$ are dense subspaces of respectively V and V^0.*

Let $\Omega_\mathfrak{a}, \mathfrak{a} \in \mathcal{A}$ denote the connected components of $\Omega \setminus \overline{\Gamma}$, and let us define the space $H_{\mathrm{div}}(\Omega \setminus \overline{\Gamma}) = \{\mathbf{q}_m = (\mathbf{q}_{m,\mathfrak{a}})_{\mathfrak{a}\in\mathcal{A}} \,|\, \mathbf{q}_{m,\mathfrak{a}} \in H_{\mathrm{div}}(\Omega_\mathfrak{a})\}$. For all $i \in I$, we can define the two sides $\pm$ of the fracture Γ_i and the corresponding unit normal vector $\mathbf{n}_i^\pm$ at Γ_i outward to the sides $\pm$. Each side $\pm$ corresponds to the subdomain $\mathfrak{a}_i^\pm \in \mathcal{A}$ with possibly $\mathfrak{a}_i^+ = \mathfrak{a}_i^-$. For all $\mathbf{q}_m \in H_{\mathrm{div}}(\Omega \setminus \overline{\Gamma})$, let $\mathbf{q}_{m,\mathfrak{a}_i^\pm} \cdot \mathbf{n}_i^\pm|_{\Gamma_i}$ denote the two normal traces at the fracture Γ_i and let us define the jump operator $H_{\mathrm{div}}(\Omega \setminus \overline{\Gamma}) \to \mathcal{D}'(\Gamma_i)$ in the sense of distributions by $[\![\mathbf{q}_m \cdot \mathbf{n}_i]\!] = \mathbf{q}_{m,\mathfrak{a}_i^+} \cdot \mathbf{n}_i^+|_{\Gamma_i} + \mathbf{q}_{m,\mathfrak{a}_i^-} \cdot \mathbf{n}_i^-|_{\Gamma_i}$.

For all $i \in I$, we denote by $\mathbf{n}_{\Sigma_i}$ the unit vector normal to Σ_i outward (and tangent) to Γ_i.

Let us define the function space $H(\Omega, \Gamma)$ by

$$H(\Omega,\Gamma) = \left\{ \begin{array}{l} \mathbf{q}_m = (\mathbf{q}_{m,\mathfrak{a}})_{\mathfrak{a}\in\mathcal{A}},\ \mathbf{q}_f = (\mathbf{q}_{f,i})_{i\in I} \,|\, \mathbf{q}_m \in H_{\mathrm{div}}(\Omega \setminus \overline{\Gamma}), \\ \mathbf{q}_{f,i} \in L^2(\Gamma_i)^{d-1},\ \mathrm{div}_{\tau_i}(\mathbf{q}_{f,i}) - [\![\mathbf{q}_m \cdot \mathbf{n}_i]\!] \in L^2(\Gamma_i), i \in I \end{array} \right\}.$$

It is an Hilbert space endowed with the scalar product

$$\langle(\mathbf{p}_m,\mathbf{p}_f),(\mathbf{q}_m,\mathbf{q}_f)\rangle_H=\sum_{\mathfrak{a}\in\mathcal{A}}\int_{\Omega_\mathfrak{a}}(\mathbf{p}_{m,\mathfrak{a}}\cdot\mathbf{q}_{m,\mathfrak{a}}+\mathrm{div}(\mathbf{p}_{m,\mathfrak{a}})\mathrm{div}(\mathbf{q}_{m,\mathfrak{a}}))d\mathbf{x}$$
$$+\sum_{i\in I}\int_{\Gamma_i}(\mathbf{p}_{f,i}\cdot\mathbf{q}_{f,i}+\Big(\mathrm{div}_{\tau_i}(\mathbf{p}_{f,i})-[\![\mathbf{p}_m\cdot\mathbf{n}_i]\!]\Big)\Big(\mathrm{div}_{\tau_i}(\mathbf{q}_{f,i})-[\![\mathbf{q}_m\cdot\mathbf{n}_i]\!]\Big)d\tau(\mathbf{x}).$$

and the norm

$$\|(\mathbf{q}_m,\mathbf{q}_f)\|_H=\langle(\mathbf{q}_m,\mathbf{q}_f),(\mathbf{q}_m,\mathbf{q}_f)\rangle_H^{1/2}.$$

On $H(\Omega,\Gamma)\times\Big(L^2(\Omega)\times L^2(\Gamma)\times L^2(\Omega)^d\times L^2(\Gamma)^{d-1}\Big)$ we define the continuous bilinear form

$$\begin{aligned}a_\Sigma\Big((\mathbf{q}_m,\mathbf{q}_f),(v_m,v_f,\mathbf{g}_m,\mathbf{g}_f)\Big)&=\sum_{\mathfrak{a}\in\mathcal{A}}\int_{\Omega_\mathfrak{a}}(\mathbf{q}_{m,\mathfrak{a}}\cdot\mathbf{g}_m+\mathrm{div}(\mathbf{q}_{m,\mathfrak{a}})v_m)d\mathbf{x}\\&+\sum_{i\in I}\int_{\Gamma_i}(\mathbf{q}_{f,i}\cdot\mathbf{g}_f+(\mathrm{div}_{\tau_i}(\mathbf{q}_{f,i})-[\![\mathbf{q}_m\cdot\mathbf{n}_i]\!])v_f)d\tau(\mathbf{x}).\end{aligned}\tag{1.1}$$

For all $\mathfrak{a}\in\mathcal{A}$ let us denote by $C_b^\infty(\Omega_\mathfrak{a})$ the set of functions $\boldsymbol{\varphi}$ such that for all $\mathbf{x}\in\overline{\Omega}_\mathfrak{a}$, there exists $r>0$ such that for all connected component ω of the domain $\{\mathbf{x}\in\mathbb{R}^d\,|\,|\mathbf{x}|<r\}\cap\Omega_\mathfrak{a}$, one has $\boldsymbol{\varphi}|_\omega\in C^\infty(\overline{\omega})^d$.

For all $(\mathbf{q}_m,\mathbf{q}_f)\in H(\Omega,\Gamma)$ with $\mathbf{q}_{m,\mathfrak{a}}\in C_b^\infty(\Omega_\mathfrak{a})$, $\mathfrak{a}\in\mathcal{A}$, and $\mathbf{q}_{f,i}\in C^\infty(\overline{\Gamma}_i)^{d-1}$, $i\in I$, and for all $v\in V^0$, it is readily checked that

$$\begin{aligned}a_\Sigma\Big((\mathbf{q}_m,\mathbf{q}_f),(v,\gamma v,\nabla v,\nabla_\tau\gamma v\Big)=&\int_{\Sigma\setminus\Sigma_0}\gamma v(\sum_{i\in I}\mathbf{q}_{f,i}\cdot\mathbf{n}_{\Sigma_i})dl(\mathbf{x})\\&+\sum_{i\in I}\int_{\Sigma_{i,N}}\gamma v(\mathbf{q}_{f,i}\cdot\mathbf{n}_{\Sigma_i})dl(\mathbf{x}).\end{aligned}$$

This lead us to the definition of the following closed Hilbert subspace of $H(\Omega,\Gamma)$

$$H_\Sigma(\Omega,\Gamma)=\left\{\begin{array}{l}(\mathbf{q}_m,\mathbf{q}_f)\in H(\Omega,\Gamma)\,|\\\quad a_\Sigma\Big((\mathbf{q}_m,\mathbf{q}_f),(v,\gamma v,\nabla v,\nabla_\tau\gamma v\Big)=0\text{ for all }v\in V^0\end{array}\right\}\tag{1.2}$$

corresponding to impose in a weak sense the conditions

(i) the sum to zero of the output normal fluxes at fracture intersections $\sum_{i\in I}\mathbf{q}_{f,i}\cdot\mathbf{n}_{\Sigma_i}=0$ on $\Sigma\setminus\Sigma_0$, assuming that the volume at the intersection can be neglected,

(ii) a zero normal flux boundary condition at the immersed boundaries of the fractures $\mathbf{q}_{f,i}\cdot\mathbf{n}_{\Sigma_i}=0$ on $\Sigma_{i,N}, i\in I$, assuming that the width at the tip of the fracture is small compared to the lengh of the fracture.

Finally let us define a subspace of smooth functions in $H_\Sigma(\Omega,\Gamma)$ by

$$\mathcal{C}^\infty_{H_\Sigma}(\Omega,\Gamma)=\left\{ \begin{array}{l} (\mathbf{q}_{m,\mathfrak{a}})_{\mathfrak{a}\in\mathcal{A}},(\mathbf{q}_{f,i})_{i\in I}\,|\,\mathbf{q}_{m,\mathfrak{a}}\in C^\infty_b(\Omega_\mathfrak{a}),\mathbf{q}_{f,i}\in C^\infty(\overline{\Gamma}_i)^{d-1}, \\ \displaystyle\sum_{i\in I}\mathbf{q}_{f,i}\cdot\mathbf{n}_{\Sigma_i}=0 \text{ on } \Sigma\setminus\Sigma_0,\ \mathbf{q}_{f,i}\cdot\mathbf{n}_{\Sigma_i}=0 \text{ on } \Sigma_{i,N}, i\in I \end{array} \right\}. \tag{1.3}$$

The proof of the following density result is given in the Appendix.

Proposition 1.2.3 *The space $\mathcal{C}^\infty_{H_\Sigma}(\Omega,\Gamma)$ is a dense subspace of $H_\Sigma(\Omega,\Gamma)$.*

1.2.2 Hybrid dimensional Darcy Flow Model

In the matrix domain $\Omega\setminus\overline{\Gamma}$ (resp. in the fracture network Γ), let us denote by $\Lambda_m\in L^\infty(\Omega)^{d\times d}$ (resp. $\Lambda_f\in L^\infty(\Gamma)^{(d-1)\times(d-1)}$) the permeability tensor such that there exist $\overline{\lambda}_m\geq\underline{\lambda}_m>0$ (resp. $\overline{\lambda}_f\geq\underline{\lambda}_f>0$) with

$$\underline{\lambda}_m|\boldsymbol{\xi}|^2\leq(\Lambda_m(\mathbf{x})\boldsymbol{\xi},\boldsymbol{\xi})\leq\overline{\lambda}_m|\boldsymbol{\xi}|^2 \text{ for all } \boldsymbol{\xi}\in\mathbb{R}^d,\mathbf{x}\in\Omega,$$

(resp. $\underline{\lambda}_f|\boldsymbol{\xi}|^2\leq(\Lambda_f(\mathbf{x})\boldsymbol{\xi},\boldsymbol{\xi})\leq\overline{\lambda}_f|\boldsymbol{\xi}|^2$ for all $\boldsymbol{\xi}\in\mathbb{R}^{d-1},\mathbf{x}\in\Gamma$).

We also denote by $d_f\in L^\infty(\Gamma)$ the width of the fractures assumed to be such that there exist $\overline{d}_f\geq\underline{d}_f>0$ with $\underline{d}_f\leq d_f(\mathbf{x})\leq\overline{d}_f$ for all $\mathbf{x}\in\Gamma$. Let us define the weighted Lebesgue $d-1$ dimensional measure on Γ by $d\tau_f(\mathbf{x})=d_f(\mathbf{x})d\tau(\mathbf{x})$. We consider the source terms $h_m\in L^2(\Omega)$ (resp. $h_f\in L^2(\Gamma)$) in the matrix domain $\Omega\setminus\overline{\Gamma}$ (resp. in the fracture network Γ).

The strong formulation of the hybrid dimensional Darcy flow model amounts to find $u\in V^0$ and $(\mathbf{q}_m,\mathbf{q}_f)\in H_\Sigma(\Omega,\Gamma)$ such that:

$$\left\{ \begin{array}{rl} \mathrm{div}(\mathbf{q}_{m,\mathfrak{a}})=h_m & \text{on } \Omega_\mathfrak{a},\mathfrak{a}\in\mathcal{A}, \\ \mathbf{q}_{m,\mathfrak{a}}=-\Lambda_m\nabla u & \text{on } \Omega_\mathfrak{a},\mathfrak{a}\in\mathcal{A}, \\ \mathrm{div}_{\tau_i}(\mathbf{q}_{f,i})-[\![\mathbf{q}_m\cdot\mathbf{n}_i]\!]=d_fh_f & \text{on } \Gamma_i,i\in I, \\ \mathbf{q}_{f,i}=-d_f\ \Lambda_f\nabla_{\tau_i}\gamma_i u & \text{on } \Gamma_i,i\in I. \end{array} \right. \tag{1.4}$$

The weak formulation of (1.4) amounts to find $u\in V^0$ satisfying the following variational equality for all $v\in V^0$:

$$\left\{ \begin{array}{l} \displaystyle\int_\Omega\Lambda_m(\mathbf{x})\nabla u(\mathbf{x})\cdot\nabla v(\mathbf{x})d\mathbf{x}+\int_\Gamma\Lambda_f(\mathbf{x})\nabla_\tau\gamma u(\mathbf{x})\cdot\nabla_\tau\gamma v(\mathbf{x})d\tau_f(\mathbf{x}) \\ \displaystyle-\int_\Omega h_m(\mathbf{x})v(\mathbf{x})d\mathbf{x}-\int_\Gamma h_f(\mathbf{x})\gamma v(\mathbf{x})d\tau_f(\mathbf{x})=0. \end{array} \right. \tag{1.5}$$

The following proposition is a direct application of the Lax-Milgram theorem and Proposition 1.2.1.

Proposition 1.2.4 *The variational problem* (1.5) *has a unique solution $u\in V^0$ which satisfies the a priori estimate*

$$\|u\|_{V^0}\leq\frac{C_P}{\min(\underline{\lambda}_m,\underline{\lambda}_f\underline{d}_f)}\Big(\|h_m\|_{L^2(\Omega)}+\|d_fh_f\|_{L^2(\Gamma)}\Big).$$

In addition $(\mathbf{q}_m,\mathbf{q}_f)=(-\Lambda_m\nabla u,-d_f\Lambda_f\nabla_\tau\gamma u)$ belongs to $H_\Sigma(\Omega,\Gamma)$.

1.3 Gradient discretization of the hybrid dimensional model

In this section we extend the gradient scheme framework introduced in [31], [28] for elliptic and parabolic problems to our hybrid dimensional Darcy flow model.

1.3.1 Gradient discretization

A gradient discretization $\mathcal{D}$ of (1.5) is defined by a vector space of degrees of freedom $X_{\mathcal{D}}$, its subspace associated with homogeneous Dirichlet boundary conditions $X_{\mathcal{D}}^0$, and the following set of linear operators:

- Two discrete gradient operators on the matrix and fracture domains:
$$\nabla_{\mathcal{D}_m} : X_{\mathcal{D}} \to L^2(\Omega)^d \text{ and } \nabla_{\mathcal{D}_f} : X_{\mathcal{D}} \to L^2(\Gamma)^{d-1}.$$
- Two function reconstruction operators on the matrix and fracture domains:
$$\Pi_{\mathcal{D}_m} : X_{\mathcal{D}} \to L^2(\Omega) \text{ and } \Pi_{\mathcal{D}_f} : X_{\mathcal{D}} \to L^2(\Gamma).$$

The vector space $X_{\mathcal{D}}$ is endowed with the semi-norm

$$\|v_{\mathcal{D}}\|_{\mathcal{D}} = \left(\|\nabla_{\mathcal{D}_m} v_{\mathcal{D}}\|^2_{L^2(\Omega)^d} + \|\nabla_{\mathcal{D}_f} v_{\mathcal{D}}\|^2_{L^2(\Gamma)^{d-1}}\right)^{\frac{1}{2}},$$

which is assumed to define a norm on $X_{\mathcal{D}}^0$.

In the following, the gradient discretization of the hybrid dimensional model with homogeneous Dirichlet boundary conditions will be denoted by the quintuplet

$$\mathcal{D} = \left(X_{\mathcal{D}}^0, \Pi_{\mathcal{D}_m}, \Pi_{\mathcal{D}_f}, \nabla_{\mathcal{D}_m}, \nabla_{\mathcal{D}_f}\right).$$

Next, we define the coercivity, consistency, limit conformity and compactness properties for sequences of gradient discretizations. Note that the compactness property is useful for the convergence analysis of nonlinear models and hence will not be used for the convergence analysis of our model. Nevertheless, for the sake of completeness, it is stated in this section and will be proved to be verified for the VAG and HFV schemes in section 1.4.

Coercivity: Let $C_{\mathcal{D}} > 0$ be defined by

$$C_{\mathcal{D}} = \max_{0 \neq v_{\mathcal{D}} \in X_{\mathcal{D}}^0} \frac{\|\Pi_{\mathcal{D}_m} v_{\mathcal{D}}\|_{L^2(\Omega)} + \|\Pi_{\mathcal{D}_f} v_{\mathcal{D}}\|_{L^2(\Gamma)}}{\|v_{\mathcal{D}}\|_{\mathcal{D}}}. \tag{1.6}$$

Then, a sequence of gradient discretizations $(\mathcal{D}^l)_{l \in \mathbb{N}}$ is said to be coercive if there exist $\overline{C}_P > 0$ such that $C_{\mathcal{D}^l} \leq \overline{C}_P$ for all $l \in \mathbb{N}$.

Consistency: For all $u \in V^0$ and $v_{\mathcal{D}} \in X_{\mathcal{D}}^0$ let us define

$$\begin{aligned} S_{\mathcal{D}}(u, v_{\mathcal{D}}) = &\|\nabla_{\mathcal{D}_m} v_{\mathcal{D}} - \nabla u\|_{L^2(\Omega)^d} + \|\nabla_{\mathcal{D}_f} v_{\mathcal{D}} - \nabla_\tau \gamma u\|_{L^2(\Gamma)^{d-1}} \\ &+ \|\Pi_{\mathcal{D}_m} v_{\mathcal{D}} - u\|_{L^2(\Omega)} + \|\Pi_{\mathcal{D}_f} v_{\mathcal{D}} - \gamma u\|_{L^2(\Gamma)}, \end{aligned} \tag{1.7}$$

and

$$\mathcal{S}_{\mathcal{D}}(u) = \min_{v_{\mathcal{D}} \in X^0_{\mathcal{D}}} S_{\mathcal{D}}(u, v_{\mathcal{D}}). \tag{1.8}$$

Then, a sequence of gradient discretizations $(\mathcal{D}^l)_{l\in\mathbb{N}}$ is said to be consistent if for all $u \in V^0$ one has $\lim_{l\to+\infty} \mathcal{S}_{\mathcal{D}^l}(u) = 0$.

Limit Conformity: For all $(\mathbf{q}_m, \mathbf{q}_f) \in H_\Sigma(\Omega, \Gamma)$ and $v_{\mathcal{D}} \in X^0_{\mathcal{D}}$, let us define

$$W_{\mathcal{D}}(\mathbf{q}_m, \mathbf{q}_f, v_{\mathcal{D}}) = a_\Sigma\Big((\mathbf{q}_m, \mathbf{q}_f), (\Pi_{\mathcal{D}_m} v_{\mathcal{D}}, \Pi_{\mathcal{D}_f} v_{\mathcal{D}}, \nabla_{\mathcal{D}_m} v_{\mathcal{D}}, \nabla_{\mathcal{D}_f} v_{\mathcal{D}})\Big) \tag{1.9}$$

and

$$\mathcal{W}_{\mathcal{D}}(\mathbf{q}_m, \mathbf{q}_f) = \max_{0\neq v_{\mathcal{D}} \in X^0_{\mathcal{D}}} \frac{|W_{\mathcal{D}}(\mathbf{q}_m, \mathbf{q}_f, v_{\mathcal{D}})|}{\|v_{\mathcal{D}}\|_{\mathcal{D}}}. \tag{1.10}$$

Then, a sequence of gradient discretizations $(\mathcal{D}^l)_{l\in\mathbb{N}}$ is said to be limit conforming if for all $(\mathbf{q}_m, \mathbf{q}_f) \in H_\Sigma(\Omega, \Gamma)$ one has $\lim_{l\to+\infty} \mathcal{W}_{\mathcal{D}^l}(\mathbf{q}_m, \mathbf{q}_f) = 0$.

Compactness: A sequence of gradient discretizations $(\mathcal{D}^l)_{l\in\mathbb{N}}$ is said to be compact if for all sequences $(v_{\mathcal{D}^l})_{l\in\mathbb{N}}$ with $v_{\mathcal{D}^l} \in X^0_{\mathcal{D}^l}$ for all $l \in \mathbb{N}$ such that there exists $C > 0$ with $\|v_{\mathcal{D}^l}\|_{\mathcal{D}^l} \leq C$ for all $l \in \mathbb{N}$, then there exist $u_m \in L^2(\Omega)$ and $u_f \in L^2(\Gamma)$ such that one has up to a subsequence

$$\lim_{l\to+\infty} \|\Pi_{\mathcal{D}^l_m} v_{\mathcal{D}^l} - u_m\|_{L^2(\Omega)} = 0 \text{ and } \lim_{l\to+\infty} \|\Pi_{\mathcal{D}^l_f} v_{\mathcal{D}^l} - u_f\|_{L^2(\Gamma)} = 0.$$

The following proposition states a property of limit conforming and coercive sequences of gradient discretizations.

Proposition 1.3.1 Regularity at the limit. *Let $(\mathcal{D}^l)_{l\in\mathbb{N}}$ be a family of discretizations assumed to be limit conforming and coercive. Let $(v_{\mathcal{D}^l})_{l\in\mathbb{N}}$ with $v_{\mathcal{D}^l} \in X^0_{\mathcal{D}^l}$ for all $l \in \mathbb{N}$ be a bounded sequence in the sense that there exists C such that $\|v_{\mathcal{D}^l}\|_{\mathcal{D}^l} \leq C$ for all $l \in \mathbb{N}$. Then, there exist $v \in V^0$ and a subsequence still denoted by $(v_{\mathcal{D}^l})_{l\in\mathbb{N}}$ such that*

$$\begin{cases} \Pi_{\mathcal{D}^l_m} v_{\mathcal{D}^l} \rightharpoonup v \text{ weakly in } L^2(\Omega), \\ \nabla_{\mathcal{D}^l_m} v_{\mathcal{D}^l} \rightharpoonup \nabla v \text{ weakly in } L^2(\Omega)^d, \\ \Pi_{\mathcal{D}^l_f} v_{\mathcal{D}^l} \rightharpoonup \gamma v \text{ weakly in } L^2(\Gamma), \\ \nabla_{\mathcal{D}_f} v_{\mathcal{D}^l} \rightharpoonup \nabla_\tau \gamma v \text{ weakly in } L^2(\Gamma)^{d-1}. \end{cases}$$

Proof: From the boundedness of the sequence $\|v_{\mathcal{D}^l}\|_{\mathcal{D}^l}$, $l \in \mathbb{N}$ and the coercivity assumption, there exist $v_m \in L^2(\Omega)$, $v_f \in L^2(\Gamma)$, $\mathbf{g}_m \in L^2(\Omega)^d$, and $\mathbf{g}_f \in L^2(\Gamma)^{d-1}$ such that $\Pi_{\mathcal{D}^l_m} v_{\mathcal{D}^l}$ weakly converges to v_m in $L^2(\Omega)$, $\Pi_{\mathcal{D}^l_f} v_{\mathcal{D}^l}$ weakly converges to v_f in $L^2(\Gamma)$, $\nabla_{\mathcal{D}^l_m} v_{\mathcal{D}^l}$ weakly converges to $\mathbf{g}_m$ in $L^2(\Omega)^d$, and $\nabla_{\mathcal{D}^l_f} v_{\mathcal{D}^l}$ weakly converges to $\mathbf{g}_f$ in $L^2(\Gamma)^{d-1}$. From the limit conformity it follows that $a_\Sigma\Big((\mathbf{q}_m, \mathbf{q}_f), (v_m, v_f, \mathbf{g}_m, \mathbf{g}_f)\Big) = 0$ for all $(\mathbf{q}_m, \mathbf{q}_f) \in H_\Sigma(\Omega, \Gamma)$. From Lemma 4.0.5, we deduce that $v = v_m \in V^0$, $v_f = \gamma v$, $\mathbf{g}_m = \nabla v$ and $\mathbf{g}_f = \nabla_\tau \gamma v$. □

The following Lemma will be used in the next sections to prove the coercivity, consistency, limit conformity and compactness of sequences of families of gradient discretizations.

Lemma 1.3.1 *Let $(\mathcal{D}^l)_{l\in\mathbb{N}}$ be a sequence of gradient discretizations with $\mathcal{D}^l = (X^0_{\mathcal{D}^l}, \Pi_{\mathcal{D}^l_m}, \Pi_{\mathcal{D}^l_f}, \nabla_{\mathcal{D}^l_m}, \nabla_{\mathcal{D}^l_f})$ and let for all $l \in \mathbb{N}$, $\widetilde{\Pi}_{\mathcal{D}^l_m}, \widetilde{\Pi}_{\mathcal{D}^l_f}$ be a couple of linear mappings from $X^0_{\mathcal{D}^l}$ to $L^2(\Omega)$ and $L^2(\Gamma)$ respectively such that there exists a real sequence $(\xi_{\mathcal{D}^l})_{l\in\mathbb{N}}$ satisfying $\lim_{l\to\infty} \xi_{\mathcal{D}^l} = 0$ and*

$$\|\Pi_{\mathcal{D}^l_m} v_{\mathcal{D}^l} - \widetilde{\Pi}_{\mathcal{D}^l_m} v_{\mathcal{D}^l}\|_{L^2(\Omega)} + \|\Pi_{\mathcal{D}^l_f} v_{\mathcal{D}^l} - \widetilde{\Pi}_{\mathcal{D}^l_f} v_{\mathcal{D}^l}\|_{L^2(\Gamma)} \le \xi_{\mathcal{D}^l} \|v_{\mathcal{D}^l}\|_{\mathcal{D}^l}$$

for all $v_{\mathcal{D}^l} \in X^0_{\mathcal{D}^l}$ and all $l \in \mathbb{N}$. Let us define the following new sequence of gradient discretizations $(\widetilde{\mathcal{D}}^l)_{l\in\mathbb{N}}$ with $\widetilde{\mathcal{D}}^l = (X^0_{\mathcal{D}^l}, \widetilde{\Pi}_{\mathcal{D}^l_m}, \widetilde{\Pi}_{\mathcal{D}^l_f}, \nabla_{\mathcal{D}^l_m}, \nabla_{\mathcal{D}^l_f})$. Then, each property (coercivity or consistency or limit conformity or compactness) for the sequence $(\mathcal{D}^l)_{l\in\mathbb{N}}$ is equivalent to the same property for the sequence $(\widetilde{\mathcal{D}}^l)_{l\in\mathbb{N}}$.

Proof: By symmetry it suffices to show that each property for the sequence $(\mathcal{D}^l)_{l\in\mathbb{N}}$ implies the same property for the sequence $(\widetilde{\mathcal{D}}^l)_{l\in\mathbb{N}}$. Assuming the coercivity of $(\mathcal{D}^l)_{l\in\mathbb{N}}$, the coercivity property of the sequence $(\widetilde{\mathcal{D}}^l)_{l\in\mathbb{N}}$ derives from $\|v_{\mathcal{D}^l}\|_{\mathcal{D}^l} = \|v_{\mathcal{D}^l}\|_{\widetilde{\mathcal{D}}^l}$ for all $v_{\mathcal{D}^l} \in X^0_{\mathcal{D}^l}$ and from the estimate

$$\|\widetilde{\Pi}_{\mathcal{D}^l_m} v_{\mathcal{D}^l}\|_{L^2(\Omega)} + \|\widetilde{\Pi}_{\mathcal{D}^l_f} v_{\mathcal{D}^l}\|_{L^2(\Gamma)} \le \Big(C_{\mathcal{D}^l} + \xi_{\mathcal{D}^l}\Big)\|v_{\mathcal{D}^l}\|_{\mathcal{D}^l}.$$

Let $u \in V^0$, for all $v_{\mathcal{D}^l} \in X^0_{\mathcal{D}^l}$ one has the estimates

$$\|v_{\mathcal{D}^l}\|_{\mathcal{D}^l} \le \|\nabla u\|_{L^2(\Omega)^d} + \|\nabla_\tau \gamma u\|_{L^2(\Gamma)^{d-1}} + S_{\mathcal{D}^l}(u, v_{\mathcal{D}^l}),$$

and

$$S_{\widetilde{\mathcal{D}}^l}(u, v_{\mathcal{D}^l}) \le \xi_{\mathcal{D}^l}\|v_{\mathcal{D}^l}\|_{\mathcal{D}^l} + S_{\mathcal{D}^l}(u, v_{\mathcal{D}^l}).$$

We deduce that

$$S_{\widetilde{\mathcal{D}}^l}(u, v_{\mathcal{D}^l}) \le \xi_{\mathcal{D}^l}(\|\nabla u\|_{L^2(\Omega)^d} + \|\nabla_\tau \gamma u\|_{L^2(\Gamma)^{d-1}}) + (1 + \xi_{\mathcal{D}^l}) S_{\mathcal{D}^l}(u, v_{\mathcal{D}^l})$$

and hence the consistency of the sequence $\widetilde{\mathcal{D}}^l$, $l \in \mathbb{N}$ derives from the consistency of the sequence $(\mathcal{D}^l)_{l\in\mathbb{N}}$.

For all $(\mathbf{q}_m, \mathbf{q}_f) \in H_\Sigma(\Omega, \Gamma)$ and all $v_{\mathcal{D}^l} \in X^0_{\mathcal{D}^l}$, it follows from (1.9) that

$$W_{\widetilde{\mathcal{D}}^l}(\mathbf{q}_m, \mathbf{q}_f, v_{\mathcal{D}^l}) \le W_{\mathcal{D}^l}(\mathbf{q}_m, \mathbf{q}_f, v_{\mathcal{D}^l}) + \xi_{\mathcal{D}^l}\|(\mathbf{q}_m, \mathbf{q}_f)\|_H \|v_{\mathcal{D}^l}\|_{\mathcal{D}^l},$$

from which we deduce that the limit conformity of the sequence $(\widetilde{\mathcal{D}}^l)_{l\in\mathbb{N}}$ derives from the limit conformity of the sequence $(\mathcal{D}^l)_{l\in\mathbb{N}}$.

Finally, using the following estimates

$$\|\widetilde{\Pi}_{\mathcal{D}^l_m} v_{\mathcal{D}^l} - u_m\|_{L^2(\Omega)} \le \|\Pi_{\mathcal{D}^l_m} v_{\mathcal{D}^l} - u_m\|_{L^2(\Omega)} + \xi_{\mathcal{D}^l}\|v_{\mathcal{D}^l}\|_{\mathcal{D}^l},$$

$$\|\widetilde{\Pi}_{\mathcal{D}^l_f} v_{\mathcal{D}^l} - u_f\|_{L^2(\Gamma)} \le \|\Pi_{\mathcal{D}^l_f} v_{\mathcal{D}^l} - u_f\|_{L^2(\Gamma)} + \xi_{\mathcal{D}^l}\|v_{\mathcal{D}^l}\|_{\mathcal{D}^l},$$

it is clear that the compactness of the sequence of gradient discretizations $(\mathcal{D}^l)_{l\in\mathbb{N}}$ implies the compactness of the sequence of gradient discretizations $(\widetilde{\mathcal{D}}^l)_{l\in\mathbb{N}}$. □

1.3.2 Application to the hybrid dimensional model

The gradient discretization of the hybrid dimensional model (1.4) is based on the primal variational formulation (1.5). It is defined by: find $u_{\mathcal{D}} \in X_{\mathcal{D}}^0$ such that for all $v_{\mathcal{D}} \in X_{\mathcal{D}}^0$:

$$\begin{aligned}&\int_\Omega \Lambda_m(\mathbf{x}) \nabla_{\mathcal{D}_m} u_{\mathcal{D}}(\mathbf{x}) \cdot \nabla_{\mathcal{D}_m} v_{\mathcal{D}}(\mathbf{x}) d\mathbf{x} + \int_\Gamma \Lambda_f(\mathbf{x}) \nabla_{\mathcal{D}_f} u_{\mathcal{D}}(\mathbf{x}) \cdot \nabla_{\mathcal{D}_f} v_{\mathcal{D}}(\mathbf{x}) d\tau_f(\mathbf{x}) \\ &\quad - \int_\Omega h_m(\mathbf{x}) \Pi_{\mathcal{D}_m} v_{\mathcal{D}}(\mathbf{x}) d\mathbf{x} - \int_\Gamma h_f(\mathbf{x}) \Pi_{\mathcal{D}_f} v_{\mathcal{D}}(\mathbf{x}) d\tau_f(\mathbf{x}) = 0.\end{aligned} \tag{1.11}$$

Proposition 1.3.2 *Let $\mathcal{D}$ be a gradient discretization of* (1.5)*. Then* (1.11) *has a unique solution $u_{\mathcal{D}} \in X_{\mathcal{D}}^0$ satisfying the a priori estimate*

$$\|u_{\mathcal{D}}\|_{\mathcal{D}} \le \frac{C_{\mathcal{D}}}{\min(\underline{\lambda}_m, \underline{\lambda}_f \underline{d}_f)} \Big(\|h_m\|_{L^2(\Omega)} + \|d_f h_f\|_{L^2(\Gamma)} \Big).$$

Proof: For any solution $u_{\mathcal{D}} \in X_{\mathcal{D}}^0$ of (1.11), setting $v_{\mathcal{D}} = u_{\mathcal{D}}$ in (1.11), and using the Cauchy Schwarz inequality, the definition (1.6) of $C_{\mathcal{D}}$, and the assumption that $\|.\|_{\mathcal{D}}$ defines a norm on $X_{\mathcal{D}}^0$, we obtain the estimates

$$\begin{aligned}\min(\underline{\lambda}_m, \underline{\lambda}_f \underline{d}_f) \|u_{\mathcal{D}}\|_{\mathcal{D}}^2 &\le \int_\Omega h_m(\mathbf{x}) \Pi_{\mathcal{D}_m} u_{\mathcal{D}}(\mathbf{x}) d\mathbf{x} + \int_\Gamma h_f(\mathbf{x}) \Pi_{\mathcal{D}_f} u_{\mathcal{D}}(\mathbf{x}) d\tau_f(\mathbf{x}) \\ &\le C_{\mathcal{D}} \Big(\|h_m\|_{L^2(\Omega)} + \|d_f h_f\|_{L^2(\Gamma)} \Big) \|u_{\mathcal{D}}\|_{\mathcal{D}},\end{aligned}$$

from which we deduce the a priori estimate and hence the uniqueness and existence of a solution. □

Proposition 1.3.3 Error estimates. *Let $u \in V^0$ be the solution of* (1.5) *and let us set $(\mathbf{q}_m, \mathbf{q}_f) = (-\Lambda_m \nabla u, -d_f \Lambda_f \nabla_\tau \gamma u) \in H_\Sigma(\Omega, \Gamma)$. Let $\mathcal{D}$ be a gradient discretization of* (1.5)*, and let $u_{\mathcal{D}} \in X_{\mathcal{D}}^0$ be the solution of* (1.11)*. Then, there exist C_1, C_2 depending only on $\overline{\lambda}_m$, $\underline{\lambda}_m$, $\overline{\lambda}_f$, $\underline{\lambda}_f$, $\overline{d}_f$, $\underline{d}_f$, and C_3, C_4 depending only on $C_{\mathcal{D}}$, $\overline{\lambda}_m$, $\underline{\lambda}_m$, $\overline{\lambda}_f$, $\underline{\lambda}_f$, $\overline{d}_f$, $\underline{d}_f$ such that one has the following error estimates:*

$$\begin{cases} \|\nabla u - \nabla_{\mathcal{D}_m} u_{\mathcal{D}}\|_{L^2(\Omega)^d} + \|\nabla_\tau \gamma u - \nabla_{\mathcal{D}_f} u_{\mathcal{D}}\|_{L^2(\Gamma)^{d-1}} \\ \qquad\qquad \le C_1 \mathcal{S}_{\mathcal{D}}(u) + C_2 \mathcal{W}_{\mathcal{D}}(\mathbf{q}_m, \mathbf{q}_f), \\ \|\Pi_{\mathcal{D}_m} u_{\mathcal{D}} - u\|_{L^2(\Omega)} + \|\Pi_{\mathcal{D}_f} u_{\mathcal{D}} - \gamma u\|_{L^2(\Gamma)} \le C_3 \mathcal{S}_{\mathcal{D}}(u) + C_4 \mathcal{W}_{\mathcal{D}}(\mathbf{q}_m, \mathbf{q}_f). \end{cases}$$

Proof: Using the definition of $\mathcal{W}_{\mathcal{D}}$ and the definitions of the solution $u_{\mathcal{D}}$ of (1.11) and of the solution $u, (\mathbf{q}_m, \mathbf{q}_f)$ of (1.4), we obtain that for all $v_{\mathcal{D}} \in X_{\mathcal{D}}^0$

$$\begin{aligned}\Big| \int_\Omega \Big(\Lambda_m \nabla_{\mathcal{D}_m} v_{\mathcal{D}} \cdot (\nabla u - \nabla_{\mathcal{D}_m} u_{\mathcal{D}}) \Big) d\mathbf{x} + \\ \int_\Gamma \Big(\Lambda_f \nabla_{\mathcal{D}_f} v_{\mathcal{D}} \cdot (\nabla_\tau \gamma u - \nabla_{\mathcal{D}_f} u_{\mathcal{D}}) \Big) d\tau_f(\mathbf{x}) \Big| \le \|v_{\mathcal{D}}\|_{\mathcal{D}} \mathcal{W}_{\mathcal{D}}(\mathbf{q}_m, \mathbf{q}_f).\end{aligned}$$

Let us introduce $w_{\mathcal{D}} \in X^0_{\mathcal{D}}$ defined as

$$w_{\mathcal{D}} = \mathrm{argmin}_{v_{\mathcal{D}} \in X^0_{\mathcal{D}}} S_{\mathcal{D}}(u, v_{\mathcal{D}}),$$

and let us set in the previous estimate $v_{\mathcal{D}} = w_{\mathcal{D}} - u_{\mathcal{D}}$. Applying the Cauchy Schwarz inequality, we obtain the first estimate. In addition, from the definition of $C_{\mathcal{D}}$, we have that

$$\|\Pi_{\mathcal{D}_m} w_{\mathcal{D}} - \Pi_{\mathcal{D}_m} u_{\mathcal{D}}\|_{L^2(\Omega)} + \|\Pi_{\mathcal{D}_f} w_{\mathcal{D}} - \Pi_{\mathcal{D}_f} u_{\mathcal{D}}\|_{L^2(\Gamma)} \leq C_{\mathcal{D}} \|w_{\mathcal{D}} - u_{\mathcal{D}}\|_{\mathcal{D}},$$

which proves the second estimate using the definition of $w_{\mathcal{D}}$. □

1.4 Two examples of Gradient Discretizations

Following [31], we consider generalised polyhedral meshes of Ω which allow for non planar faces. Let us stress that this general definition is used for the VAG scheme introduced in subsection 1.4.1 while the HFV scheme described in subsection 1.4.2 requires in addition that the faces are planar and that the face center $\mathbf{x}_\sigma$ is the center of gravity of the face σ.

Definition 1.4.1 (Polyhedral mesh) *Let $\mathcal{M}$ be the set of cells that are disjoint open polyhedral subsets of Ω such that $\bigcup_{K\in\mathcal{M}} \overline{K} = \overline{\Omega}$. For all $K \in \mathcal{M}$, $\mathbf{x}_K$ denotes the so-called "center" of the cell K under the assumption that K is star-shaped with respect to $\mathbf{x}_K$. We then denote by $\mathcal{F}_K$ the set of interfaces of non zero $d-1$ dimensional measure among the interior faces $\overline{K} \cap \overline{L}$, $L \in \mathcal{M} \setminus \{K\}$, and the boundary interface $\overline{K} \cap \partial\Omega$, which possibly splits in several boundary faces. Let us denote by*

$$\mathcal{F} = \bigcup_{K\in\mathcal{M}} \mathcal{F}_K$$

the set of all faces of the mesh. Remark that the faces are not assumed to be planar, hence the term "generalised polyhedral mesh". For $\sigma \in \mathcal{F}$, let $\mathcal{E}_\sigma$ be the set of interfaces of non zero $d-2$ dimensional measure among the interfaces $\overline{\sigma} \cap \overline{\sigma}'$, $\sigma' \in \mathcal{F} \setminus \{\sigma\}$. Then, we denote by

$$\mathcal{E} = \bigcup_{\sigma\in\mathcal{F}} \mathcal{E}_\sigma$$

the set of all edges of the mesh. Let $\mathcal{V}_\sigma = \bigcup_{e,e'\in\mathcal{E}_\sigma, e\neq e'} \left(e \cap e'\right)$ be the set of vertices of σ. For each $K \in \mathcal{M}$ we define $\mathcal{V}_K = \bigcup_{\sigma\in\mathcal{F}_K} \mathcal{V}_\sigma$, and we also denote by

$$\mathcal{V} = \bigcup_{K\in\mathcal{M}} \mathcal{V}_K$$

the set of all vertices of the mesh. It is then assumed that for each face $\sigma \in \mathcal{F}$, there exists a so-called "center" of the face $\mathbf{x}_\sigma \in \sigma \setminus \bigcup_{e\in\mathcal{E}_\sigma} e$ such that $\mathbf{x}_\sigma = \sum_{\mathbf{s}\in\mathcal{V}_\sigma} \beta_{\sigma,\mathbf{s}}\, \mathbf{x}_\mathbf{s}$, with $\sum_{\mathbf{s}\in\mathcal{V}_\sigma} \beta_{\sigma,\mathbf{s}} = 1$, and $\beta_{\sigma,\mathbf{s}} \geq 0$ for all $\mathbf{s} \in \mathcal{V}_\sigma$; moreover the face σ is assumed to be defined by the union of the triangles $T_{\sigma,e}$ defined by the face center $\mathbf{x}_\sigma$ and each edge $e \in \mathcal{E}_\sigma$.

The mesh is also supposed to be conforming w.r.t. the fracture network Γ in the sense that for each $i \in I$ there exists a subset $\mathcal{F}_{\Gamma_i}$ of $\mathcal{F}$ such that $\overline{\Gamma}_i = \bigcup_{\sigma\in\mathcal{F}_{\Gamma_i}} \overline{\sigma}$. We will denote by $\mathcal{F}_\Gamma$ the set of fracture faces $\bigcup_{i\in I} \mathcal{F}_{\Gamma_i}$, and by $\mathcal{E}_\Gamma$ the set of fracture edges $\bigcup_{\sigma\in\mathcal{F}_\Gamma} \mathcal{E}_\sigma$.

A tetrahedral sub-mesh of $\mathcal{M}$ is defined by

$$\mathcal{T} = \{T_{K,\sigma,e}, e \in \mathcal{E}_\sigma, \sigma \in \mathcal{F}_K, K \in \mathcal{M}\},$$

where $T_{K,\sigma,e}$ is the tetrahedron joining the cell center $\mathbf{x}_K$ to the triangle $T_{\sigma,e}$ (see Figure 1.2 for examples of such tetrahedra).

Let ρ_T denote the insphere diameter of a given tetrahedron T, h_T its diameter, and $h_\mathcal{T} = \max_{T\in\mathcal{T}} h_T$. We will assume in the convergence analysis that the family of tetrahedral submeshes $\mathcal{T}$ is shape regular. Hence let us set

$$\theta_\mathcal{T} = \max_{T\in\mathcal{T}} \frac{h_T}{\rho_T}.$$

1.4.1 Vertex Approximate Gradient Discretization

The VAG discretization has been introduced in [31] for diffusive problems on heterogeneous anisotropic media. Its extension to the hybrid dimensional Darcy model is based on the following vector space of degrees of freedom:

$$X_\mathcal{D} = \{v_K, v_\mathbf{s}, v_\sigma \in \mathbb{R}, K \in \mathcal{M}, \mathbf{s} \in \mathcal{V}, \sigma \in \mathcal{F}_\Gamma\}, \tag{1.12}$$

and its subspace with homogeneous Dirichlet boundary conditions on $\partial\Omega$:

$$X^0_\mathcal{D} = \{v_\mathcal{D} \in X_\mathcal{D} \,|\, v_\mathbf{s} = 0 \text{ for } \mathbf{s} \in \mathcal{V}_{ext}\}. \tag{1.13}$$

where $\mathcal{V}_{ext} = \mathcal{V} \cap \partial\Omega$ denotes the set of boundary vertices, and $\mathcal{V}_{int} = \mathcal{V} \setminus \partial\Omega$ denotes the set of interior vertices.

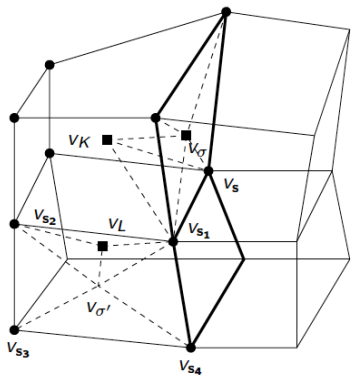

Figure 1.2: Degrees of freedom of the VAG scheme: cell unknowns v_K, v_L, fracture face unknown v_σ, and node unknowns $v_\mathbf{s}, v_{\mathbf{s}_1}, v_{\mathbf{s}_2}, v_{\mathbf{s}_3}, v_{\mathbf{s}_4}$. The fracture faces of $\mathcal{F}_\Gamma$ are in bold. The value of $v_{\sigma'}$ is obtained by interpolation of the node unknowns $v_{\mathbf{s}_1}, v_{\mathbf{s}_2}, v_{\mathbf{s}_3}, v_{\mathbf{s}_4}$ of the face $\sigma' \in \mathcal{F} \setminus \mathcal{F}_\Gamma$ while v_σ is kept as an unknown for $\sigma \in \mathcal{F}_\Gamma$.

A $\mathbb{P}_1$ finite element discretization of V is built using the tetrahedral sub-mesh $\mathcal{T}$ of $\mathcal{M}$ and a second order interpolation at the face centers $\mathbf{x}_\sigma$, $\sigma \in \mathcal{F} \setminus \mathcal{F}_\Gamma$ defined by the operator $I_\sigma : X_\mathcal{D} \to \mathbb{R}$ such that

$$I_\sigma(v_\mathcal{D}) = \sum_{\mathbf{s}\in\mathcal{V}_\sigma} \beta_{\sigma,\mathbf{s}} v_\mathbf{s}.$$

For a given $v_\mathcal{D} \in X_\mathcal{D}$, we define the function $\Pi_\mathcal{T} v_\mathcal{D} \in V$ as the continuous piecewise affine function on each tetrahedron of $\mathcal{T}$ such that $\Pi_\mathcal{T} v_\mathcal{D}(\mathbf{x}_K) = v_K$, $\Pi_\mathcal{T} v_\mathcal{D}(\mathbf{x}_\mathbf{s}) = v_\mathbf{s}$, $\Pi_\mathcal{T} v_\mathcal{D}(\mathbf{x}_\sigma) = v_\sigma$, and $\Pi_\mathcal{T} v_\mathcal{D}(\mathbf{x}_{\sigma'}) = I_{\sigma'}(v_\mathcal{D})$ for all $K \in \mathcal{M}$, $\mathbf{s} \in \mathcal{V}$, $\sigma \in \mathcal{F}_\Gamma$, and $\sigma' \in \mathcal{F} \setminus \mathcal{F}_\Gamma$. The discrete gradient operators are obtained from this finite element discretization of V, setting

$$\nabla_{\mathcal{D}_m} = \nabla \Pi_\mathcal{T} \text{ and } \nabla_{\mathcal{D}_f} = \nabla_\tau \gamma \Pi_\mathcal{T}. \tag{1.14}$$

In addition to this conforming finite element discretization of V, the VAG discretization uses two non conforming piecewise constant reconstructions of functions from $X_\mathcal{D}$ into respectively $L^2(\Omega)$ and $L^2(\Gamma)$ based on a partition of the cells and of the fracture faces. These partitions are respectively denoted, for all $K \in \mathcal{M}$, by

$$\overline{K} \;=\; \overline{\omega}_K \;\cup\; \Big(\bigcup_{\mathbf{s}\in\mathcal{V}_K\cap\mathcal{V}_{int}} \overline{\omega}_{K,\mathbf{s}} \Big) \;\cup\; \Big(\bigcup_{\sigma\in\mathcal{F}_K\cap\mathcal{F}_\Gamma} \overline{\omega}_{K,\sigma} \Big),$$

and, for all $\sigma \in \mathcal{F}_\Gamma$, by

$$\overline{\sigma} \;=\; \overline{\omega}_\sigma \;\cup\; \Big(\bigcup_{\mathbf{s}\in\mathcal{V}_\sigma\cap\mathcal{V}_{int}} \overline{\omega}_{\sigma,\mathbf{s}} \Big).$$

Then, the function reconstruction operators are defined by

$$\Pi_{\mathcal{D}_m} v_\mathcal{D}(\mathbf{x}) = \begin{cases} v_K & \text{for all } \mathbf{x} \in \omega_K,\ K \in \mathcal{M}, \\ v_\mathbf{s} & \text{for all } \mathbf{x} \in \omega_{K,\mathbf{s}},\ \mathbf{s} \in \mathcal{V}_K \cap \mathcal{V}_{int},\ K \in \mathcal{M}, \\ v_\sigma & \text{for all } \mathbf{x} \in \omega_{K,\sigma},\ \sigma \in \mathcal{F}_K \cap \mathcal{F}_\Gamma,\ K \in \mathcal{M}, \end{cases} \tag{1.15}$$

and

$$\Pi_{\mathcal{D}_f} v_\mathcal{D}(\mathbf{x}) = \begin{cases} v_\sigma & \text{for all } \mathbf{x} \in \omega_\sigma,\ \sigma \in \mathcal{F}_\Gamma, \\ v_\mathbf{s} & \text{for all } \mathbf{x} \in \omega_{\sigma,\mathbf{s}},\ \mathbf{s} \in \mathcal{V}_\sigma \cap \mathcal{V}_{int},\ \sigma \in \mathcal{F}_\Gamma. \end{cases} \tag{1.16}$$

It is shown below that the above VAG discretization defines a coercive, consistent, limit conforming and compact gradient discretization whatever the choice of these partitions.

Properties of VAG discretization: we state without proof two results that can be readily adapted from [16] Lemmas 3.4 and 3.7 noticing that the shape regularity of $\mathcal{T}$ implies the shape regularity of the triangular submesh of Γ defined by $\mathcal{T} \cap \Gamma$.

Lemma 1.4.1 *There exists $C > 0$ depending only on $\theta_\mathcal{T}$ such that, for all $v_\mathcal{D} \in X_\mathcal{D}$, one has the estimates*

$$\|\Pi_{\mathcal{D}_m} v_\mathcal{D} - \Pi_\mathcal{T} v_\mathcal{D}\|_{\mathrm{L}^2(\Omega)} \le C h_\mathcal{T} \|\nabla_{\mathcal{D}_m} v_\mathcal{D}\|_{L^2(\Omega)^d},$$
$$\|\Pi_{\mathcal{D}_f} v_\mathcal{D} - \gamma \Pi_\mathcal{T} v_\mathcal{D}\|_{\mathrm{L}^2(\Gamma)} \le C h_\mathcal{T} \|\nabla_{\mathcal{D}_f} v_\mathcal{D}\|_{L^2(\Gamma)^{d-1}}.$$

For any continuous function $\varphi \in C^0(\overline{\Omega})$, let us introduce the operator $P_{\mathcal{D}} : C^0(\overline{\Omega}) \to X_{\mathcal{D}}$ such that

$$(P_{\mathcal{D}}\varphi)_K = \varphi(\mathbf{x}_K), (P_{\mathcal{D}}\varphi)_s = \varphi(\mathbf{x}_s), (P_{\mathcal{D}}\varphi)_\sigma = \varphi(\mathbf{x}_\sigma)$$

for all $K \in \mathcal{M}$, $s \in \mathcal{V}$ and $\sigma \in \mathcal{F}_\Gamma$.

We have the following classical finite element approximation result for the finite element interpolation operator $\Pi_{\mathcal{T}} P_{\mathcal{D}}$.

Proposition 1.4.1 *For all $\varphi \in C^\infty(\overline{\Omega})$, there exists $C_\varphi > 0$ depending only on φ, $\theta_{\mathcal{T}}$ such that one has the error estimates*

$$\|\varphi - \Pi_{\mathcal{T}} P_{\mathcal{D}}\varphi\|_{L^2(\Omega)} + \|\gamma\varphi - \gamma\Pi_{\mathcal{T}} P_{\mathcal{D}}\varphi\|_{L^2(\Gamma)} \leq h_{\mathcal{T}}^2 C_\varphi,$$

and

$$\|\nabla\varphi - \nabla\Pi_{\mathcal{T}} P_{\mathcal{D}}\varphi\|_{L^2(\Omega)^d} + \|\nabla\gamma\varphi - \nabla_\tau\gamma\Pi_{\mathcal{T}} P_{\mathcal{D}}\varphi\|_{L^2(\Gamma)^{d-1}} \leq h_{\mathcal{T}} C_\varphi.$$

Let us now state our main result concerning the VAG discretization.

Proposition 1.4.2 (Main result on VAG) *Let us consider a family of meshes $(\mathcal{M}^l)_{l\in\mathbb{N}}$ as defined above. It is assumed that the family of tetrahedral submeshes $\mathcal{T}^l$ of $\mathcal{M}^l$ is shape regular in the sense that there exists $\theta > 0$ such that $\theta_{\mathcal{T}^l} \leq \theta$ for all $l \in \mathbb{N}$. It is also assumed that $h_{\mathcal{T}^l}$ tends to zero when $l \to +\infty$. Then, the sequence of VAG discretizations $(\mathcal{D}^l)_{l\in\mathbb{N}}$ with $\mathcal{D}^l = (X^0_{\mathcal{D}^l}, \Pi_{\mathcal{D}^l_m}, \Pi_{\mathcal{D}^l_f}, \nabla_{\mathcal{D}^l_m}, \nabla_{\mathcal{D}^l_f})$ defined by (1.13), (1.15), (1.16), (1.14) is coercive, consistent, limit conforming and compact.*

Proof: Let us denote by

$$\mathcal{D}_{FE} = (X^0_{\mathcal{D}}, \Pi_{\mathcal{T}}, \gamma\Pi_{\mathcal{T}}, \nabla_{\mathcal{D}_m}, \nabla_{\mathcal{D}_f}),$$

the conforming $\mathbb{P}_1$ finite element VAG discretization. It results from Lemma 1.2.1 that

$$\|\Pi_{\mathcal{T}} v_{\mathcal{D}}\|_{L^2(\Omega)} + \|\gamma\Pi_{\mathcal{T}} v_{\mathcal{D}}\|_{L^2(\Gamma)} \leq C_P \|\nabla_{\mathcal{D}_m} v_{\mathcal{D}}\|_{L^2(\Omega)^d} \tag{1.17}$$

for all $v_{\mathcal{D}} \in X^0_{\mathcal{D}}$. On the other hand for all $(\mathbf{q}_m, \mathbf{q}_f) \in H_\Sigma(\Omega, \Gamma)$ and all $v_{\mathcal{D}} \in X^0_{\mathcal{D}}$ one has

$$W_{\mathcal{D}_{FE}}(\mathbf{q}_m, \mathbf{q}_f, v_{\mathcal{D}}) = 0. \tag{1.18}$$

We deduce from (1.17) and (1.18) that the sequence of conforming gradient discretizations $(\mathcal{D}^l_{FE})_{l\in\mathbb{N}}$ is coercive and limit conforming. The consistency of $(\mathcal{D}^l_{FE})_{l\in\mathbb{N}}$ results from Proposition 1.4.1 and from the density of $C^\infty_c(\Omega)$ in V^0 given by Proposition 1.2.2. The following estimates

$$\|\Pi_{\mathcal{T}} v_{\mathcal{D}}\|_{H^1(\Omega)} \leq C_1 \|\nabla\Pi_{\mathcal{T}} v_{\mathcal{D}}\|_{L^2(\Omega)^d},$$

and

$$\|\gamma_i\Pi_{\mathcal{T}} v_{\mathcal{D}}\|_{H^1(\Gamma_i)} \leq C_2\Big(\|\nabla\Pi_{\mathcal{T}} v_{\mathcal{D}}\|_{L^2(\Omega)^d} + \|\nabla_\tau\gamma\Pi_{\mathcal{T}} v_{\mathcal{D}}\|_{L^2(\Gamma)^{d-1}}\Big)$$

for constants C_1 and C_2 independent on the mesh and on $v_{\mathcal{D}} \in X^0_{\mathcal{D}}$ are deduced from the Poincaré inequality and the Trace theorem. Then, thanks to the Rellich Compactness Theorem, one obtains the compactness of $(\mathcal{D}^l_{FE})_{l\in\mathbb{N}}$. From Lemma 1.3.1 and Lemma 1.4.1 we deduce that the sequence $(\mathcal{D}^l)_{l\in\mathbb{N}}$ is also coercive, consistent, limit conforming and compact. □

1.4.2 Hybrid Finite Volume Discretization

In this subsection, the HFV scheme introduced in [30] is extended to the hybrid dimensional Darcy flow model. Let us recall that the HFV scheme of [30] has been generalised in [27] as the family of Hybrid Mimetic Mixed methods which encompasses the family of Mimetic Finite Difference schemes [19]. In the following, we focus on the particular case presented in [30] for the sake of simplicity.

Let us recall that, for the HFV scheme, the faces $\sigma \in \mathcal{F}$ are assumed to be planar and $\mathbf{x}_\sigma$ is assumed to be the center of gravity of the face σ. We also denote by $\mathbf{x}_e$ the center of the edge $e \in \mathcal{E}$. Let $\mathcal{F}_{int} \subset \mathcal{F}$ (resp. $\mathcal{E}_{int} \subset \mathcal{E}$) denote the subset of interior faces (resp. interior edges). The vector space of degrees of freedom $X_\mathcal{D}$ is defined by

$$X_\mathcal{D} = \{u_K \in \mathbb{R}, u_\sigma \in \mathbb{R}, u_e \in \mathbb{R} \text{ for all } K \in \mathcal{M}, \sigma \in \mathcal{F}, e \in \mathcal{E}_\Gamma\}, \tag{1.19}$$

and its subspace $X^0_\mathcal{D}$ is defined by

$$X^0_\mathcal{D} = \{u_\mathcal{D} \in X_\mathcal{D} \,|\, u_\sigma = 0, u_e = 0 \text{ for all } \sigma \in \mathcal{F} \setminus \mathcal{F}_{int} \text{ and } e \in \mathcal{E}_\Gamma \setminus \mathcal{E}_{int}\}. \tag{1.20}$$

For any continuous function $\varphi \in C^0(\overline{\Omega})$, let us define its projection $P_\mathcal{D}\varphi$ onto $X_\mathcal{D}$ such that $(P_\mathcal{D}\varphi)_K = \varphi(\mathbf{x}_K)$, $(P_\mathcal{D}\varphi)_\sigma = \varphi(\mathbf{x}_\sigma)$, $(P_\mathcal{D}\varphi)_e = \varphi(\mathbf{x}_e)$ for $K \in \mathcal{M}, \sigma \in \mathcal{F}, e \in \mathcal{E}_\Gamma$.

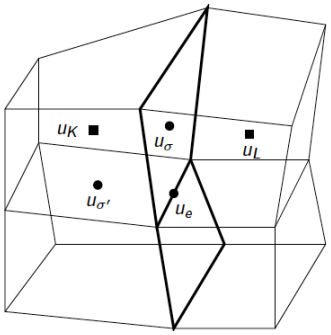

Figure 1.3: Degrees of freedom of the HFV scheme: cell unknowns u_K, u_L, fracture face unknown u_σ, matrix face unknown $u_{\sigma'}$ and fracture edge unknown u_e.

For each cell K and $u_\mathcal{D} \in X_\mathcal{D}$, let us define

$$\nabla_K u_\mathcal{D} = \frac{1}{|K|} \sum_{\sigma \in \mathcal{F}_K} |\sigma|(u_\sigma - u_K)\mathbf{n}_{K,\sigma},$$

where $|K|$ is the volume of the cell K, $|\sigma|$ is the surface of the face σ, and $\mathbf{n}_{K,\sigma}$ is the unit normal vector of the face $\sigma \in \mathcal{F}_K$ outward to the cell K. We recall from [30] that $\nabla_K u_\mathcal{D}$ is exact on affine functions φ in the sense that $\nabla_K P_\mathcal{D}\varphi = \nabla\varphi$. Also note that $\nabla_K u_\mathcal{D}$ does not depend on u_K since $\sum_{\sigma \in \mathcal{F}_K} |\sigma|\mathbf{n}_{K,\sigma} = 0$. Hence a stabilised discrete gradient is defined as follows:

$$\nabla_{K,\sigma} u_\mathcal{D} = \nabla_K u_\mathcal{D} + R_{K,\sigma}(u_\mathcal{D})\mathbf{n}_{K,\sigma},\ \sigma \in \mathcal{F}_K,$$

with

$$R_{K,\sigma}(u_{\mathcal{D}}) = \frac{\sqrt{d}}{d_{K,\sigma}}\Big(u_\sigma - u_K - \nabla_K u_{\mathcal{D}} \cdot (\mathbf{x}_\sigma - \mathbf{x}_K)\Big),$$

setting $d_{K,\sigma} = \mathbf{n}_{K,\sigma} \cdot (\mathbf{x}_\sigma - \mathbf{x}_K)$ which leads to the definition of the matrix discrete gradient

$$\nabla_{\mathcal{D}_m} u_{\mathcal{D}}(\mathbf{x}) = \nabla_{K,\sigma} u_{\mathcal{D}} \text{ on } K_\sigma \text{ for all } K \in \mathcal{M}, \sigma \in \mathcal{F}_K, \tag{1.21}$$

where K_σ is the cone joining the face σ to the cell center $\mathbf{x}_K$. The fracture discrete gradient is defined similarly by

$$\nabla_{\mathcal{D}_f} u_{\mathcal{D}}(\mathbf{x}) = \nabla_{\sigma,e} u_{\mathcal{D}} \text{ on } \sigma_e \text{ for all } \sigma \in \mathcal{F}_\Gamma, e \in \mathcal{E}_\sigma, \tag{1.22}$$

with

$$\nabla_{\sigma,e} u_{\mathcal{D}} = \nabla_\sigma u_{\mathcal{D}} + R_{\sigma,e}(u_{\mathcal{D}}) \mathbf{n}_{\sigma,e},$$

and

$$\nabla_\sigma u_{\mathcal{D}} = \frac{1}{|\sigma|} \sum_{e \in \mathcal{E}_\sigma} |e| (u_e - u_\sigma) \mathbf{n}_{\sigma,e},$$

$$R_{\sigma,e}(u_{\mathcal{D}}) = \frac{\sqrt{d-1}}{d_{\sigma,e}}\Big(u_e - u_\sigma - \nabla_\sigma u_{\mathcal{D}} \cdot (\mathbf{x}_e - \mathbf{x}_\sigma)\Big),$$

where $\mathbf{n}_{\sigma,e}$ is the unit normal vector to the edge e in the tangent plane of the face σ and outward to the face σ, $d_{\sigma,e} = \mathbf{n}_{\sigma,e} \cdot (\mathbf{x}_e - \mathbf{x}_\sigma)$, and σ_e is the triangle of base e and vertex $\mathbf{x}_\sigma$.

The matrix and fracture discrete gradients are both consistent in the sense that for any affine function $\varphi \in C^0(\overline{\Omega})$ one has $\nabla_{\mathcal{D}_m} P_{\mathcal{D}} \varphi = \nabla \varphi$, and for any function $\varphi \in C^0(\overline{\Omega})$ affine on the fracture Γ_i one has $\nabla_{\mathcal{D}_f} P_{\mathcal{D}} \varphi = \nabla_{\tau_i} \varphi$ on Γ_i. We recall also from [30] that for all $u_{\mathcal{D}} \in X_{\mathcal{D}}$ one has

$$\sum_{\sigma \in \mathcal{F}_K} |\sigma| d_{K,\sigma} R_{K,\sigma}(u_{\mathcal{D}}) \mathbf{n}_{K,\sigma} = 0 \text{ and } \sum_{e \in \mathcal{E}_\sigma} |e| d_{\sigma,e} R_{\sigma,e}(u_{\mathcal{D}}) \mathbf{n}_{\sigma,e} = 0. \tag{1.23}$$

The function reconstruction operators are piecewise constant on a partition of the cells and of the fracture faces. These partitions are respectively denoted, for all $K \in \mathcal{M}$, by

$$\overline{K} \;=\; \overline{\omega}_K \;\cup\; \Big(\bigcup_{\sigma \in \mathcal{F}_K \cap \mathcal{F}_{int}} \overline{\omega}_{K,\sigma} \Big),$$

and, for all $\sigma \in \mathcal{F}_\Gamma$, by

$$\overline{\sigma} \;=\; \overline{\omega}_\sigma \;\cup\; \Big(\bigcup_{e \in \mathcal{E}_\sigma \cap \mathcal{E}_{int}} \overline{\omega}_{\sigma,e} \Big).$$

Then, the function reconstruction operators are defined for all $v_{\mathcal{D}} \in X_{\mathcal{D}}$ by

$$\Pi_{\mathcal{D}_m} v_{\mathcal{D}}(\mathbf{x}) = \begin{cases} v_K & \text{for all } \mathbf{x} \in \omega_K,\ K \in \mathcal{M}, \\ v_\sigma & \text{for all } \mathbf{x} \in \omega_{K,\sigma},\ \sigma \in \mathcal{F}_K \cap \mathcal{F}_{int},\ K \in \mathcal{M}, \end{cases} \tag{1.24}$$

and

$$\Pi_{\mathcal{D}_f} v_{\mathcal{D}}(\mathbf{x}) = \begin{cases} v_\sigma & \text{for all } \mathbf{x} \in \omega_\sigma,\ \sigma \in \mathcal{F}_\Gamma, \\ v_e & \text{for all } \mathbf{x} \in \omega_{\sigma,e},\ e \in \mathcal{E}_\sigma \cap \mathcal{E}_{int},\ \sigma \in \mathcal{F}_\Gamma. \end{cases} \tag{1.25}$$

As for the VAG scheme, it is shown below that the above HFV discretization defines a coercive, consistent, limit conforming and compact gradient discretization whatever the choice of these partitions.

Let us define the two piecewise constant mappings $\Pi_{\mathcal{M}}$ (resp. $\Pi_{\mathcal{F}}$) from $X_{\mathcal{D}}$ to $L^2(\Omega)$ (resp. $L^2(\Gamma)$) such that for all $v_{\mathcal{D}} \in X_{\mathcal{D}}$

$$\Pi_{\mathcal{M}} v_{\mathcal{D}}|_K = v_K \text{ for all } K \in \mathcal{M} \text{ (resp } \Pi_{\mathcal{F}} v_{\mathcal{D}}|_\sigma = v_\sigma \text{ for all } \sigma \in \mathcal{F}_\Gamma). \tag{1.26}$$

Following the proof of Lemma 4.1 from [30], one can obtain the following Lemma.

Lemma 1.4.2 *There exists $C > 0$ depending only on $\theta_{\mathcal{T}}$ such that for all $u_{\mathcal{D}} \in X_{\mathcal{D}}$ one has*

$$\|\Pi_{\mathcal{D}_m} u_{\mathcal{D}} - \Pi_{\mathcal{M}} u_{\mathcal{D}}\|_{L^2(\Omega)} + \|\Pi_{\mathcal{D}_f} u_{\mathcal{D}} - \Pi_{\mathcal{F}} u_{\mathcal{D}}\|_{L^2(\Omega)} \le C h_{\mathcal{T}} \|u_{\mathcal{D}}\|_{\mathcal{D}}.$$

Properties of HFV discretizations: Let us first consider the HFV discretization

$$\mathcal{D} = \Big(X_{\mathcal{D}}^0, \Pi_{\mathcal{M}}, \Pi_{\mathcal{F}}, \nabla_{\mathcal{D}_m}, \nabla_{\mathcal{D}_f}\Big),$$

defined by the vector space $X_{\mathcal{D}}^0$ from (1.20), the discrete gradient operators $\nabla_{\mathcal{D}_m}$ from (1.21) and $\nabla_{\mathcal{D}_f}$ from (1.22), and the function reconstruction operators $\Pi_{\mathcal{M}}$, $\Pi_{\mathcal{F}}$ from (1.26). From Lemma 5.3 and Lemma 4.1 of [30] and Lemma 1.51 of [26], one has the following discrete Poincaré estimates

$$\begin{aligned} \|\Pi_{\mathcal{M}} u_{\mathcal{D}}\|_{L^2(\Omega)} &\le C_{\mathcal{D},m} \|\nabla_{\mathcal{D}_m} u_{\mathcal{D}}\|_{L^2(\Omega)^d}, \\ \|\Pi_{\mathcal{F}} u_{\mathcal{D}}\|_{L^2(\Gamma)} &\le C_{\mathcal{D},f} \Big(\|\nabla_{\mathcal{D}_m} u_{\mathcal{D}}\|_{L^2(\Omega)^d} + \|\nabla_{\mathcal{D}_f} u_{\mathcal{D}}\|_{L^2(\Gamma)^{d-1}} \Big), \end{aligned} \tag{1.27}$$

for all $u_{\mathcal{D}} \in X_{\mathcal{D}}^0$ with $C_{\mathcal{D},m}$ and $C_{\mathcal{D},f}$ depending only on $\theta_{\mathcal{T}}$.

It follows from Lemma 4.3 of [30] that for all $\varphi \in C^\infty(\overline{\Omega})$ there exists $C > 0$ depending only on $\theta_{\mathcal{T}}$ and φ such that

$$\|\nabla_{\mathcal{D}_m} P_{\mathcal{D}} \varphi - \nabla \varphi\|_{L^2(\Omega)} + \|\nabla_{\mathcal{D}_f} P_{\mathcal{D}} \varphi - \nabla \varphi\|_{L^2(\Gamma)} \le C h_{\mathcal{T}} \tag{1.28}$$

It is easy to show that for all $\varphi \in C^\infty(\overline{\Omega})$, there exists $C > 0$, depending only on φ and $\theta_{\mathcal{T}}$ such that

$$\|\Pi_{\mathcal{M}} P_{\mathcal{D}} \varphi - \varphi\|_{L^2(\Omega)} + \|\Pi_{\mathcal{F}} P_{\mathcal{D}} \varphi - \varphi\|_{L^2(\Gamma)} \le C h_{\mathcal{T}}. \tag{1.29}$$

Proposition 1.4.3 *Let $(\boldsymbol{\varphi}_m, \boldsymbol{\varphi}_f) \in \mathcal{C}_{H_\Sigma}^\infty(\Omega, \Gamma)$, there exist C depending only on $(\boldsymbol{\varphi}_m, \boldsymbol{\varphi}_f)$ and $\theta_{\mathcal{T}}$ such that for all $u_{\mathcal{D}} \in X_{\mathcal{D}}^0$*

$$W_{\mathcal{D}}(\boldsymbol{\varphi}_m, \boldsymbol{\varphi}_f, u_{\mathcal{D}}) \le C h_{\mathcal{T}} \|u_{\mathcal{D}}\|_{\mathcal{D}}.$$

Proof: Let us define $\boldsymbol{\varphi}_K = \frac{1}{|K|}\int_K \boldsymbol{\varphi}_m d\mathbf{x}$ for all $K \in \mathcal{M}$, and $\boldsymbol{\varphi}_{K,\sigma} = \lim\limits_{\epsilon\to 0^+} \dfrac{1}{|\sigma|}\displaystyle\int_\sigma \boldsymbol{\varphi}_m(\mathbf{x} - \mathbf{n}_{K,\sigma}\epsilon)d\tau(\mathbf{x})$ for all $\sigma \in \mathcal{F}_K$.

Let us define

$$A_1^{\mathcal{D}} = A_{11}^{\mathcal{D}} + A_{12}^{\mathcal{D}} = \int_\Omega \nabla_{\mathcal{D}_m} u_{\mathcal{D}} \cdot \boldsymbol{\varphi}_m dx,$$

with

$$A_{11}^{\mathcal{D}} = \sum_{K\in\mathcal{M}} \sum_{\sigma\in\mathcal{F}_K} |\sigma|(u_\sigma - u_K)\boldsymbol{\varphi}_K \cdot \mathbf{n}_{K,\sigma},$$

and

$$A_{12}^{\mathcal{D}} = \sum_{K\in\mathcal{M}} \sum_{\sigma\in\mathcal{F}_K} R_{K,\sigma}(u_{\mathcal{D}})\mathbf{n}_{K,\sigma} \cdot \int_{K_\sigma} \boldsymbol{\varphi}_m d\mathbf{x}.$$

Using (1.23), one has

$$A_{12}^{\mathcal{D}} = \sum_{K\in\mathcal{M}} \sum_{\sigma\in\mathcal{F}_K} R_{K,\sigma}(u_{\mathcal{D}})\mathbf{n}_{K,\sigma} \cdot \int_{K_\sigma} (\boldsymbol{\varphi}_m - \boldsymbol{\varphi}_K) d\mathbf{x}.$$

We can deduce as in Lemma 4.2 from [30] that there exists C depending only on $\boldsymbol{\varphi}_m$, $\theta_{\mathcal{T}}$ such that

$$|A_{12}^{\mathcal{D}}| \le C h_{\mathcal{T}} \|\nabla_{\mathcal{D}_m} u_{\mathcal{D}}\|_{L^2(\Omega)^d}. \tag{1.30}$$

Let us consider the term $A_2^{\mathcal{D}}$ defined by

$$A_2^{\mathcal{D}} = \sum_{\mathfrak{a}\in\mathcal{A}} \int_{\Omega_\mathfrak{a}} (\Pi_{\mathcal{M}} u_{\mathcal{D}}) \mathrm{div}(\boldsymbol{\varphi}_{m,\mathfrak{a}}) d\mathbf{x} = \sum_{K\in\mathcal{M}} \sum_{\sigma\in\mathcal{F}_K} |\sigma| u_K \boldsymbol{\varphi}_{K,\sigma} \cdot \mathbf{n}_{K,\sigma}.$$

Adding and subtracting $\displaystyle\sum_{K\in\mathcal{M}} \sum_{\sigma\in\mathcal{F}_K} |\sigma| u_\sigma \boldsymbol{\varphi}_{K,\sigma} \cdot \mathbf{n}_{K,\sigma}$ to $A_2^{\mathcal{D}}$ and using that $\displaystyle\sum_{K\in\mathcal{M}_\sigma} |\sigma| \boldsymbol{\varphi}_{K,\sigma} \cdot \mathbf{n}_{K,\sigma} = 0$ for all $\sigma \in \mathcal{F} \setminus \mathcal{F}_\Gamma$, leads to

$$A_2^{\mathcal{D}} = \sum_{K\in\mathcal{M}} \sum_{\sigma\in\mathcal{F}_K} |\sigma|(u_K - u_\sigma)\boldsymbol{\varphi}_{K,\sigma} \cdot \mathbf{n}_{K,\sigma} + \sum_{\sigma\in\mathcal{F}_\Gamma} \sum_{K\in\mathcal{M}_\sigma} |\sigma| u_\sigma \boldsymbol{\varphi}_{K,\sigma} \cdot \mathbf{n}_{K,\sigma}.$$

It results that

$$\begin{aligned} A_{11}^{\mathcal{D}} + A_2^{\mathcal{D}} - \sum_{i\in I} \int_{\Gamma_i} (\Pi_{\mathcal{F}} u_{\mathcal{D}}) [\![\boldsymbol{\varphi}_m \cdot \mathbf{n}_i]\!] d\tau(\mathbf{x}) \\ = \sum_{K\in\mathcal{M}} \sum_{\sigma\in\mathcal{F}_K} |\sigma|(u_K - u_\sigma)(\boldsymbol{\varphi}_{K,\sigma} - \boldsymbol{\varphi}_K) \cdot \mathbf{n}_{K,\sigma} \end{aligned} \tag{1.31}$$

Therefore, applying Cauchy-Schwartz inequality to (1.31), using the regularity of $\boldsymbol{\varphi}_m$, and the estimate (1.30), we deduce that there exists C depending only on $\boldsymbol{\varphi}_m$, $\theta_{\mathcal{T}}$ such that

$$\begin{aligned} \Bigg| \sum_{\mathfrak{a}\in\mathcal{A}} \int_{\Omega_\mathfrak{a}} (\nabla_{\mathcal{D}_m} u_{\mathcal{D}} \cdot \boldsymbol{\varphi}_{m,\mathfrak{a}} + (\Pi_{\mathcal{M}} u_{\mathcal{D}}) \mathrm{div}(\boldsymbol{\varphi}_{m,\mathfrak{a}})) d\mathbf{x} - \\ \sum_{i\in I} \int_{\Gamma_i} (\Pi_{\mathcal{F}} u_{\mathcal{D}}) [\![\boldsymbol{\varphi}_m \cdot \mathbf{n}_i]\!] d\tau(\mathbf{x}) \Bigg| \le C h_{\mathcal{T}} \|\nabla_{\mathcal{D}_m} u_{\mathcal{D}}\|_{L^2(\Omega)^d}. \end{aligned} \tag{1.32}$$

Next, we define for all $\sigma \in \mathcal{F}_\Gamma$ and $e \in \mathcal{E}_\sigma$

$$\boldsymbol{\varphi}_\sigma = \frac{1}{|\sigma|}\int_\sigma \boldsymbol{\varphi}_f d\tau(\mathbf{x}) \text{ and } \boldsymbol{\varphi}_{\sigma,e} = \lim_{\epsilon\to 0^+}\frac{1}{|e|}\int_e \boldsymbol{\varphi}_f(\mathbf{x}-\mathbf{n}_{\sigma,e}\epsilon)dl(\mathbf{x}).$$

Let us set

$$B_1^{\mathcal{D}} = B_{11}^{\mathcal{D}} + B_{12}^{\mathcal{D}} = \sum_{i\in I}\int_{\Gamma_i} \nabla_{\mathcal{D}_f} u_{\mathcal{D}} \cdot \boldsymbol{\varphi}_{f,i} d\tau(\mathbf{x}),$$

with

$$B_{11}^{\mathcal{D}} = \sum_{\sigma\in\mathcal{F}_\Gamma}\sum_{e\in\mathcal{E}_\sigma} |e|(u_e - u_\sigma)\boldsymbol{\varphi}_\sigma \cdot \mathbf{n}_{\sigma,e},$$

and

$$B_{12}^{\mathcal{D}} = \sum_{\sigma\in\mathcal{F}_\Gamma}\sum_{e\in\mathcal{E}_\sigma} R_{\sigma,e}(u_{\mathcal{D}})\mathbf{n}_{\sigma,e} \cdot \int_{\sigma_e} \boldsymbol{\varphi}_f d\tau(\mathbf{x}).$$

Using (1.23), one has

$$B_{12}^{\mathcal{D}} = \sum_{\sigma\in\mathcal{F}_\Gamma}\sum_{e\in\mathcal{E}_\sigma} R_{\sigma,e}(u_{\mathcal{D}})\mathbf{n}_{\sigma,e} \cdot \int_{\sigma_e} (\boldsymbol{\varphi}_f - \boldsymbol{\varphi}_\sigma) d\tau(\mathbf{x}).$$

We can deduce as in [30] that there exists C depending only on $\boldsymbol{\varphi}_f$, $\theta_{\mathcal{T}}$ such that

$$|B_{12}^{\mathcal{D}}| \le C h_{\mathcal{T}} \|\nabla_{\mathcal{D}_f} u_{\mathcal{D}}\|_{L^2(\Gamma)^{d-1}}. \tag{1.33}$$

Let us consider the term $B_2^{\mathcal{D}}$ defined by

$$B_2^{\mathcal{D}} = \sum_{i\in I}\int_{\Gamma_i} (\Pi_{\mathcal{F}} u_{\mathcal{D}})\mathrm{div}(\boldsymbol{\varphi}_{f,i}) d\tau(\mathbf{x}) = \sum_{\sigma\in\mathcal{F}_\Gamma}\sum_{e\in\mathcal{E}_\sigma} |e| u_\sigma \boldsymbol{\varphi}_{\sigma,e} \cdot \mathbf{n}_{\sigma,e}.$$

Adding and subtracting $\sum_{\sigma\in\mathcal{F}_\Gamma}\sum_{e\in\mathcal{E}_\sigma} |e| u_e \boldsymbol{\varphi}_{\sigma,e} \cdot \mathbf{n}_{\sigma,e}$ to $B_2^{\mathcal{D}}$ we obtain that

$$B_2^{\mathcal{D}} = \sum_{\sigma\in\mathcal{F}_\Gamma}\sum_{e\in\mathcal{E}_\sigma} |e|(u_\sigma - u_e)\boldsymbol{\varphi}_{\sigma,e} \cdot \mathbf{n}_{\sigma,e} + \sum_{\sigma\in\mathcal{F}_\Gamma}\sum_{e\in\mathcal{E}_\sigma} |e| u_e \boldsymbol{\varphi}_{\sigma,e} \cdot \mathbf{n}_{\sigma,e}$$

Taking into account the definition of $\boldsymbol{\varphi}_{f,i}$ and the fact that $u_e = 0$ for all $e \in \mathcal{E}_\Gamma \setminus \mathcal{E}_{int}$ we conclude that

$$\sum_{\sigma\in\mathcal{F}_\Gamma}\sum_{e\in\mathcal{E}_\sigma} |e| u_e \boldsymbol{\varphi}_{\sigma,e} \cdot \mathbf{n}_{\sigma,e} = 0.$$

It results that

$$B_{11}^{\mathcal{D}} + B_2^{\mathcal{D}} = \sum_{\sigma\in\mathcal{F}_\Gamma}\sum_{e\in\mathcal{E}_\sigma} |e|(u_\sigma - u_e)(\boldsymbol{\varphi}_{\sigma,e} - \boldsymbol{\varphi}_\sigma) \cdot \mathbf{n}_{\sigma,e},$$

from which we can deduce as in [30] and using (1.33) that there exists C depending only on $\boldsymbol{\varphi}_f$ and $\theta_{\mathcal{T}}$ such that

$$\left|\sum_{i\in I}\int_{\Gamma_i}\Big(\nabla_{\mathcal{D}_f} u_{\mathcal{D}} \cdot \boldsymbol{\varphi}_{f,i} + (\Pi_{\mathcal{F}} u_{\mathcal{D}})\mathrm{div}(\boldsymbol{\varphi}_{f,i})\Big) d\tau(\mathbf{x})\right| \le C h_{\mathcal{T}} \|\nabla_{\mathcal{D}_f} u_{\mathcal{D}}\|_{L^2(\Gamma)^{d-1}}. \tag{1.34}$$

Combining the estimates (1.32) and (1.34) concludes the proof of Proposition 1.4.3. □

Proposition 1.4.4 (Main result on HFV) *Let us consider a family of meshes $(\mathcal{M}^l)_{l\in\mathbb{N}}$ as defined above. It is assumed that the family of tetrahedral submeshes $\mathcal{T}^l$ of $\mathcal{M}^l$ is shape regular in the sense that there exists a positive constant θ such that $\theta_{\mathcal{T}^l} < \theta$ for all $l \in \mathbb{N}$. It is also assumed that $h_{\mathcal{T}^l}$ tends to zero when $l \to +\infty$. Then, the sequence of HFV discretizations $(\mathcal{D}^l)_{l\in\mathbb{N}}$ with $\mathcal{D}^l = (X^0_{\mathcal{D}^l}, \Pi_{\mathcal{D}^l_m}, \Pi_{\mathcal{D}^l_f}, \nabla_{\mathcal{D}^l_m}, \nabla_{\mathcal{D}^l_f})$ defined by* (1.20), (1.24), (1.25), (1.21), (1.22) *is coercive, consistent, limit conforming and compact.*

Proof: The coercivity of the sequence of HFV discretizations

$$\left(X^0_{\mathcal{D}^l}, \Pi_{\mathcal{M}^l}, \Pi_{\mathcal{F}^l}, \nabla_{\mathcal{D}^l_m}, \nabla_{\mathcal{D}^l_f}\right)_{l\in\mathbb{N}},$$

results from (1.27). Its consistency is obtained using (1.28), (1.29) and the density of $C^\infty_c(\Omega)$ in V^0 given by Proposition 1.2.2. Its limit conformity is obtained by Proposition 1.4.3 and the density of $C^\infty_{H_\Sigma}(\Omega,\Gamma)$ in $H_\Sigma(\Omega,\Gamma)$ given by Proposition 1.2.3. Its compactness results from Lemma 5.6 of [30] and Lemma 1.57 of [26]. Then, the coercivity, consistency, limit conformity and compactness of the sequence of HFV discretizations $(\mathcal{D}^l)_{l\in\mathbb{N}}$ results from Lemma 1.3.1 and Lemma 1.4.2. □

Remark 1.4.1 *The proofs of Propositions 1.4.2, 1.4.4 and of Lemma 1.3.1 show that for solutions $u \in V^0$ and $(\mathbf{q}_m, \mathbf{q}_f) \in H_\Sigma(\Omega,\Gamma)$ of* (1.4) *such that $u \in C^2(\overline{K})$, $\mathbf{q}_m \in (C^1(\overline{K}))^d$, $\mathbf{q}_f \in (C^1(\overline{\sigma}))^{d-1}$ for all $K \in \mathcal{M}$ and all $\sigma \in \mathcal{F}_\Gamma$, the VAG and HFV schemes are consistent and limit conforming of order 1, and therefore convergent of order 1.*

1.4.3 Finite Volume Formulation of the VAG and HFV schemes

Both the VAG and HFV schemes can be formulated as finite volume schemes. Moreover, the definition of the fluxes and of the conservation equations for both schemes can be unified using the following data structure which has been used in the practical implementation of the code. Let us define the set of degrees of freedom (d.o.f.)

$$dof_{\mathcal{D}} = \begin{cases} \mathcal{M} \cup \mathcal{V} \cup \mathcal{F}_\Gamma & \text{for VAG,} \\ \mathcal{M} \cup \mathcal{F} \cup \mathcal{E}_\Gamma & \text{for HFV.} \end{cases}$$

The subset of d.o.f. located at the boundary of Ω where Dirichlet boundary conditions are imposed is denoted by dof_{Dir} and is defined by

$$dof_{Dir} = \begin{cases} \mathcal{V}_{ext} & \text{for VAG,} \\ (\mathcal{F} \setminus \mathcal{F}_{int}) \cup (\mathcal{E}_\Gamma \setminus \mathcal{E}_{int}) & \text{for HFV.} \end{cases}$$

For each cell $K \in \mathcal{M}$ let us also define the subset $dof_{\partial K}$ of d.o.f. located at the boundary of K with

$$dof_{\partial K} = \begin{cases} \mathcal{V}_K \cup (\mathcal{F}_K \cap \mathcal{F}_\Gamma) & \text{for VAG,} \\ \mathcal{F}_K & \text{for HFV.} \end{cases}$$

Similarly, we define for each fracture face $\sigma \in \mathcal{F}_\Gamma$ the subset $dof_{\partial\sigma}$ of d.o.f. located at the boundary of σ

$$dof_{\partial\sigma} = \begin{cases} \mathcal{V}_\sigma & \text{for VAG,} \\ \mathcal{E}_\sigma & \text{for HFV.} \end{cases}$$

Finally, the vector space $X_\mathcal{D}$ is identified to $\mathbb{R}^{dof_\mathcal{D}}$ and its subspace $X_\mathcal{D}^0$ to $\mathbb{R}^{dof_\mathcal{D} \backslash dof_{Dir}}$ and we denote by $(e_\nu, \nu \in dof_\mathcal{D})$ the canonical basis of $X_\mathcal{D}$.

Using these unified notations and following [13] Section 4 for the VAG scheme and [30] Remark 2.7 for the HFV scheme, we can define for both schemes the matrix and fracture fluxes which are exhibited in Figure 1.4 inside a cell K with a fracture face σ. The matrix fluxes connect a cell $K \in \mathcal{M}$ to its boundary d.o.f. $\nu \in dof_{\partial K}$ and are defined for all $u_\mathcal{D} \in X_\mathcal{D}$ by

$$F_{K,\nu}(u_\mathcal{D}) = -\int_K \Lambda_m \nabla_{\mathcal{D}_m} u_\mathcal{D} \cdot \nabla_{\mathcal{D}_m} e_\nu d\mathbf{x} = \sum_{\nu' \in dof_{\partial K}} T_{K,\nu}^{\nu'}(u_K - u_{\nu'}),$$

with

$$T_{K,\nu}^{\nu'} = \int_K \Lambda_m \nabla_{\mathcal{D}_m} e_{\nu'} \cdot \nabla_{\mathcal{D}_m} e_\nu d\mathbf{x}.$$

Similarly, the fracture fluxes connect a fracture face $\sigma \in \mathcal{F}_\Gamma$ to its boundary d.o.f. $\nu \in dof_{\partial\sigma}$ and are defined for all $u_\mathcal{D} \in X_\mathcal{D}$ by

$$F_{\sigma,\nu}(u_\mathcal{D}) = -\int_\sigma d_f \Lambda_f \nabla_{\mathcal{D}_f} u_\mathcal{D} \cdot \nabla_{\mathcal{D}_f} e_\nu d\tau(\mathbf{x}) = \sum_{\nu' \in dof_{\partial\sigma}} T_{\sigma,\nu}^{\nu'}(u_K - u_{\nu'}),$$

with

$$T_{\sigma,\nu}^{\nu'} = \int_\sigma d_f \Lambda_f \nabla_{\mathcal{D}_f} e_{\nu'} \cdot \nabla_{\mathcal{D}_f} e_\nu d\tau(\mathbf{x}).$$

These fluxes are such that for all $(u_\mathcal{D}, v_\mathcal{D}) \in X_\mathcal{D} \times X_\mathcal{D}$ one has

$$\begin{aligned} &\int_\Omega \Lambda_m(\mathbf{x}) \nabla_{\mathcal{D}_m} u_\mathcal{D}(\mathbf{x}) \cdot \nabla_{\mathcal{D}_m} v_\mathcal{D}(\mathbf{x}) d\mathbf{x} + \int_\Gamma \Lambda_f(\mathbf{x}) \nabla_{\mathcal{D}_f} u_\mathcal{D}(\mathbf{x}) \cdot \nabla_{\mathcal{D}_f} v_\mathcal{D}(\mathbf{x}) d\tau_f(\mathbf{x}) \\ &= \sum_{K \in \mathcal{M}} \sum_{\nu \in dof_{\partial K}} F_{K,\nu}(u_\mathcal{D})(v_K - v_\nu) + \sum_{\sigma \in \mathcal{F}_\Gamma} \sum_{\nu \in dof_{\partial\sigma}} F_{\sigma,\nu}(u_\mathcal{D})(v_\sigma - v_\nu). \end{aligned}$$

It follows that the variational formulation (1.11) is equivalent to the following finite

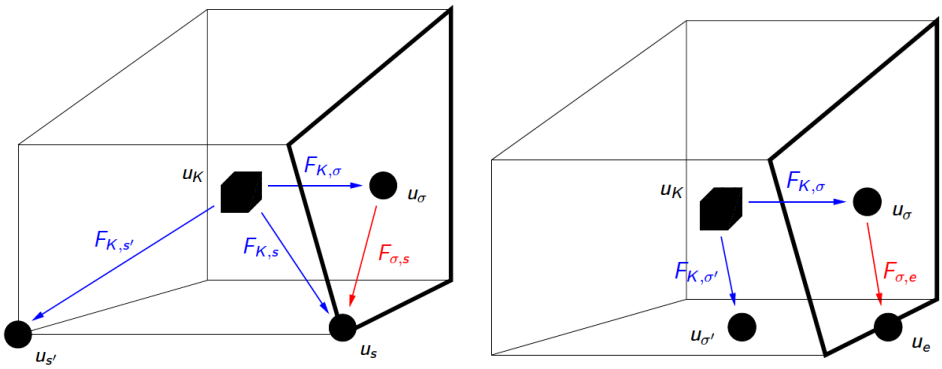

Figure 1.4: Matrix (in blue) and fracture (in red) fluxes inside a cell K with a fracture face σ (in bold) for the VAG (left) and HFV (right) schemes. The matrix fluxes $F_{K,\nu}$ connect the cell K to the d.o.f. $\nu \in dof_{\partial K}$ located at the boundary of K. The fracture fluxes $F_{\sigma,\nu}$ connect the face σ to the d.o.f. $\nu \in dof_{\partial\sigma}$ located at the boundary of σ.

volume formulation: Find $u_\mathcal{D} \in X_\mathcal{D}$ such that

$$\begin{cases} \displaystyle\sum_{\nu\in dof_{\partial K}} F_{K,\nu}(u_\mathcal{D}) = \int_{\omega_K} h_m(\mathbf{x})d\mathbf{x}, \text{ for all } K \in \mathcal{M}, \\ \displaystyle\sum_{\nu\in dof_{\partial\sigma}} F_{\sigma,\nu}(u_\mathcal{D}) + \sum_{K\in\mathcal{M}_\sigma} -F_{K,\sigma}(u_\mathcal{D}) \\ \displaystyle= \sum_{K\in\mathcal{M}_\sigma} \int_{\omega_{K,\sigma}} h_m(\mathbf{x})d\mathbf{x} + \int_{\omega_\sigma} h_f(\mathbf{x})d\tau_f(\mathbf{x}), \text{ for all } \sigma \in \mathcal{F}_\Gamma, \\ \displaystyle\sum_{K\in\mathcal{M}_\nu} -F_{K,\nu}(u_\mathcal{D}) + \sum_{\sigma\in\mathcal{F}_{\Gamma,\nu}} -F_{\sigma,\nu}(u_\mathcal{D}) = \sum_{K\in\mathcal{M}_\nu} \int_{\omega_{K,\nu}} h_m(\mathbf{x})d\mathbf{x} \\ \displaystyle+ \sum_{\sigma\in\mathcal{F}_{\Gamma,\nu}} \int_{\omega_{\sigma,\nu}} h_f(\mathbf{x})d\tau_f(\mathbf{x}), \text{ for all } \nu \in dof_\mathcal{D} \setminus (\mathcal{M} \cup \mathcal{F}_\Gamma \cup dof_{Dir}), \\ \\ u_\nu = 0, \text{ for all } \nu \in dof_{Dir}, \end{cases} \tag{1.35}$$

with $\mathcal{M}_\nu = \{K \in \mathcal{M} \,|\, \nu \in dof_{\partial K}\}$ and $\mathcal{F}_{\Gamma,\nu} = \{\sigma \in \mathcal{F}_\Gamma \,|\, \nu \in dof_{\partial\sigma}\}$. Following [13], when applying the VAG or HFV discretization to two phase Darcy flow models or to the coupling of the Darcy flow equation with a tracer equation, the choice of the cells and fracture faces partitioning defining the control volumes is done in order to avoid the mixture of heterogeneous properties inside each control volume. In particular, at the matrix fracture interfaces, one simply need to set $\omega_{K,\nu} = \emptyset$ for all ν such that $\mathbf{x}_\nu \in \Gamma$. Note also that, in practice for such models, one does not need to build the partitions but only to choose the volume distribution ratios $\alpha_{K,\nu} = \frac{\int_{\omega_{K,\nu}} d\mathbf{x}}{|K|}$, $\nu \in dof_{\partial K} \setminus dof_{Dir}$, and $\alpha_{\sigma,\nu} = \frac{\int_{\omega_{\sigma,\nu}} d\tau_f(\mathbf{x})}{|\sigma|}$, $\nu \in dof_{\partial\sigma} \setminus dof_{Dir}$.

1.5 Numerical experiments

Let Ω denote a bounded domain in $\mathbb{R}^d$, $d = 3$, and let us consider four non immersed planar fractures splitting the domain Ω into four subdomains $\Omega_{\mathfrak{a}}$, $\mathfrak{a} = 1, \cdots, 4$. Dirichlet boundary conditions are imposed on both the boundary of the domain $\partial\Omega$ and on the boundary of the fracture network $\partial\Gamma = \partial\Omega \cap \Gamma = \Sigma_0$. The permeability of the fractures is defined by $\Lambda_f(\mathbf{x}) = 100\ Id$ and their width by $d_f(\mathbf{x}) = 0.01$. In the matrix, the permeability tensor $\Lambda_m(\mathbf{x})$ is fixed to $\Lambda_{m,\mathfrak{a}}$ on each subdomain $\Omega_{\mathfrak{a}}$, $\mathfrak{a} = 1, \cdots, 4$ with two choices of the subdomain permeabilities. The first choice considers isotropic heterogeneous permeabilities setting $\Lambda_{m,\mathfrak{a}} = \lambda_{\mathfrak{a}}\ Id$ with $\lambda_1 = 1$, $\lambda_2 = 0.1$, $\lambda_3 = 0.01$, $\lambda_4 = 10$. The second choice corresponds to the anisotropic heterogeneous permeabilities defined by

$$\Lambda_{m,1} = \begin{pmatrix} a_1 & b_1 & 0 \\ b_1 & c_1 & 0 \\ 0 & 0 & \lambda \end{pmatrix}, \Lambda_{m,2} = \begin{pmatrix} a_2 & 0 & b_2 \\ 0 & \lambda & 0 \\ b_2 & 0 & c_2 \end{pmatrix}, \Lambda_{m,3} = \begin{pmatrix} a_3 & b_3 & 0 \\ b_3 & c_3 & 0 \\ 0 & 0 & \lambda \end{pmatrix}, \Lambda_{m,4} = \begin{pmatrix} \lambda & 0 & 0 \\ 0 & a_4 & b_4 \\ 0 & b_4 & c_4 \end{pmatrix},$$

with $a_{\mathfrak{a}} = \cos^2\beta_{\mathfrak{a}} + \omega \sin^2\beta_{\mathfrak{a}}$, $b_{\mathfrak{a}} = (1-\omega)\cos\beta_{\mathfrak{a}} \sin\beta_{\mathfrak{a}}$, $c_{\mathfrak{a}} = \omega\cos^2\beta_{\mathfrak{a}} + \sin^2\beta_{\mathfrak{a}}$, $\lambda = 0.01$, $\beta_1 = \frac{\pi}{6}$, $\beta_2 = -\frac{\pi}{6}$, $\beta_3 = 0$, $\beta_4 = \frac{\pi}{6}$ and $\omega = 0.01$.

Next, let us describe the two families of test cases that will be presented in this section.

Test cases: For the first test case $\Omega = (0,1)^3$, the fracture network is defined by the union of the two rectangles $\{(x,y,z) \in \Omega \,|\, x = 0.5\}$ and $\{(x,y,z) \in \Omega \,|\, y = 0.5\}$, and the four subdomains correspond to $\Omega_1 = \{(x,y,z) \in \Omega \,|\, x < 0.5, y < 0.5\}$, $\Omega_2 = \{(x,y,z) \in \Omega \,|\, x > 0.5, y < 0.5\}$, $\Omega_3 = \{(x,y,z) \in \Omega \,|\, x > 0.5, y > 0.5\}$ and $\Omega_4 = \{(x,y,z) \in \Omega \,|\, x < 0.5, y > 0.5\}$ (see the left picture of Figure 1.5). Let us define the functions $t_1(\mathbf{x}) = y - x + z$, $t_2(\mathbf{x}) = x + y + z - 1$, $t_3(\mathbf{x}) = x - y + z$ and $t_4(\mathbf{x}) = 1 - x - y + z$. One can check that the function $u(\mathbf{x}) = e^{\cos(t_{\mathfrak{a}}(\mathbf{x}))}$, $\mathbf{x} \in \Omega_{\mathfrak{a}}$, $\mathfrak{a} = 1, \cdots, 4$, belongs to V, and that the fluxes $(\mathbf{q}_m, \mathbf{q}_f) = (-\Lambda_m \nabla u, -d_f \Lambda_f \nabla_\tau \gamma u)$ belongs to $H_\Sigma(\Omega, \Gamma)$ since it satisfies $\sum_{i \in I} \mathbf{q}_{f,i} \cdot \mathbf{n}_{\Sigma_i} = 0$ on $\Sigma \setminus \Sigma_0$.

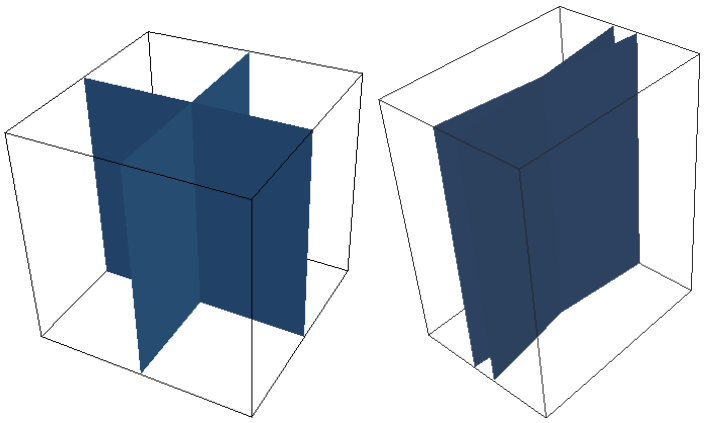

Figure 1.5: (Left): domain $\Omega = (0,1)^3$ and fracture network for the first test case. (Right): domain $\Omega = (-1.5, 1.5) \times (-2, 2) \times (0, 5)$ and fracture network for the second test case.

For the numerical solutions using both the VAG and HFV schemes, three different families of meshes are considered. The first family is defined by uniform Cartesian grid of size $n \times n \times n$ with $n = 4, 8, 16, 32, 64, 128$ (see Table 1.1). The second family of meshes is obtained from the previous one by a perturbation of its nodes excluding the nodes on the boundary of Ω and on the boundary of each fracture Γ_i, $i \in I$. The perturbation is chosen randomly inside the ball of radius $\frac{1}{4n}$ and of center the Cartesian mesh node. The perturbation of a fracture node is done in the fracture plane. Note that it leads to hexahedral cells with non planar faces and hence the HFV scheme is no longer consistent on this family of meshes. Finally we consider a family of uniformly refined tetrahedral meshes generated by TetGen[59] (see Table 1.2). Tables 1.1 and 1.2 provide respectively for the Cartesian or randomly perturbated Cartesian meshes, and for the tetrahedral meshes, as well as for both schemes, the number of degrees of freedom (d.o.f.), the number of d.o.f. after elimination of the cell and Dirichlet unknowns (Reduced d.o.f.), and the number of nonzero element in the linear system after elimination without any fill-in of the cell and Dirichlet unknowns (Nonzero elts).

Vertex Approximate Gradient Discretization				*Hybrid Finite Volume Discretization*			
Nb	**d.o.f.**	**Reduced d.o.f**	**Nonzero elts**	**Nb**	**d.o.f.**	**Reduced d.o.f.**	**Nonzero elts**
1	221	59	839	1	380	188	1 644
2	1 369	471	9 403	2	2 520	1 560	15 336
3	9 521	3 887	90 947	3	18 224	12 464	129 600
4	70 753	31 839	802 003	4	138 336	99 168	1 060 464
5	544 961	258 239	6 738 419	5	1 077 440	790 208	8 570 064
6	4 276 609	2 081 151	55 247 923	6	8 503 680	6 307 200	68 888 976

Table 1.1: For the first test case, the VAG and HFV schemes and the six Cartesian and randomly perturbated Cartesian meshes: mesh number, number of d.o.f., number of d.o.f. after elimination of the cell and Dirichlet unknowns, number of nonzero elements in the matrix after elimination.

Vertex Approximate Gradient Discretization				*Hybrid Finite Volume Discretization*			
Nb	**d.o.f.**	**Reduced d.o.f.**	**Nonzero elts**	**Nb**	**d.o.f.**	**Reduced d.o.f.**	**Nonzero elts**
1	1 888	294	2 660	1	4 569	2 661	17 677
2	13 593	1 924	23 148	2	34 150	21 409	146 147
3	121 818	16 780	233 978	3	311 261	201 748	1 395 908
4	263 391	36 214	519 694	4	675 298	440 798	3 058 868
5	509 038	69 762	1 021 940	5	1308 518	858 252	5 967 626
6	939 007	128 324	1 904 390	6	2 417 392	1 589 624	11 064 478
7	1 386 833	189 300	2 830 880	7	3 573 654	2 354 004	16 396 536
8	1 874 186	255 370	3 840 778	8	4 832 987	3 187 229	22 210 505
9	2 383 038	324 682	4 901 360	9	6 147 875	4 058 104	28 290 370
10	4 813 285	654 670	9 979 004	10	12 432 788	8 223 946	57 382 094

Table 1.2: For the first test case, the VAG and HFV schemes and the ten tetrahedral meshes: mesh number, number of d.o.f., number of d.o.f. after elimination of the cell and Dirichlet unknowns, number of nonzero elements in the matrix after elimination.

The second test case considers the domain $\Omega = (-1.5, 1.5) \times (-2, 2) \times (0, 5)$ and the fracture network defined by the union of two rectangles $\{(x, y, z) \in \Omega \,|\, y = mx\}$ and $\{(x, y, z) \in \Omega \,|\, y = -mx\}$ with $m = 8$ (see the right picture of Figure 1.5). The domain Ω is splitted into the following four subdomains: $\Omega_1 = \{(x, y, z) \in \Omega \,|\, mx < y, mx < -y\}$, $\Omega_2 = \{(x, y, z) \in \Omega \,|\, mx > y, mx < -y\}$, $\Omega_3 = \{(x, y, z) \in \Omega \,|\, mx > y, mx > -y\}$ and $\Omega_4 = \{(x, y, z) \in \Omega \,|\, mx < y, mx > -y\}$. In this test we set $t_1(\mathbf{x}) = 2y + z$, $t_2(\mathbf{x}) = 2mx + z$, $t_3(\mathbf{x}) = -2y + z$ and $t_4(\mathbf{x}) = -2mx + z$. It can be verified that the function $u(\mathbf{x}) = e^{\cos(t_{\mathfrak{a}}(\mathbf{x}))}$, $\mathbf{x} \in \Omega_{\mathfrak{a}}$, $\mathfrak{a} = 1, \cdots, 4$, belongs to V, and that the fluxes $(\mathbf{q}_m, \mathbf{q}_f) = (-\Lambda_m \nabla u, -d_f \Lambda_f \nabla_\tau \gamma u)$ belong to $H_\Sigma(\Omega, \Gamma)$. For the numerical solutions using the VAG and HFV schemes, a family of ten tetrahedral uniformly refined meshes is generated by TetGen [59]. Table 1.3 gives for both schemes, the number of degrees of freedom (d.o.f.), the number of d.o.f. after elimination of the cell and Dirichlet unknowns (Reduced d.o.f.), and the number of nonzero element in the linear system after elimination without any fill-in of the cell and Dirichlet unknowns (Nonzero elts).

Vertex Approximate Gradient Discretization				*Hybrid Finite Volume Discretization*			
Nb	**d.o.f.**	**Reduced d.o.f.**	**Nonzero elts**	**Nb**	**d.o.f.**	**Reduced d.o.f.**	**Nonzero elts**
1	12 930	2 081	24 687	1	32 218	20 369	140 055
2	62 177	9 280	123 096	2	157 522	101 864	705 466
3	132 712	19 321	265 709	3	337 883	219 755	1 524 503
4	251 969	36 103	510 459	4	644 056	421 122	2 926 982
5	463 906	65 850	949 882	5	1 188 904	780 117	5 429 401
6	1 002 529	140 712	2 070 638	6	2 576 269	1 696 321	11 820 151
7	1 366 875	190 979	2 832 163	7	3 516 282	2 318 255	16 161 367
8	1 934 904	269 381	4 022 379	8	4 982 226	3 289 061	22 940 167
9	2 342 305	325 513	4 877 093	9	6 034 003	3 985 462	27 803 112
10	4 542 801	627 526	9 501 798	10	11 719 544	7 754 712	54 132 280

Table 1.3: For the second test case, the VAG and HFV schemes and the ten tetrahedral meshes: mesh number, number of d.o.f., number of d.o.f. after elimination of the cell and Dirichlet unknowns, number of nonzero elements in the matrix after elimination.

Numerical Results: All test cases are performed using the $\Pi_{\mathcal{D}_m}$ and $\Pi_{\mathcal{D}_f}$ function reconstruction operators obtained by setting $\omega_K = K$ for all $K \in \mathcal{M}$, and $\omega_\sigma = \sigma$ for all $\sigma \in \mathcal{F}_\Gamma$. To assess the error estimates of Proposition 1.3.3, we have computed the following relative errors

$$\mathrm{Err}_u = \frac{\|u - \Pi_{\mathcal{D}_m} u_{\mathcal{D}}\|_{L^2(\Omega)}}{\|u\|_{L^2(\Omega)}} + \frac{\|\gamma u - \Pi_{\mathcal{D}_f} u_{\mathcal{D}}\|_{L^2(\Gamma)}}{\|\gamma u\|_{L^2(\Gamma)}},$$

for the function reconstructions in the matrix and in the fractures, and

$$\mathrm{Err}_g = \frac{\|\nabla u - \nabla_{\mathcal{D}_m} u_{\mathcal{D}}\|_{L^2(\Omega)^d}}{\|\nabla u\|_{L^2(\Omega)^d}} + \frac{\|\nabla \gamma u - \nabla_{\mathcal{D}_f} u_{\mathcal{D}}\|_{L^2(\Gamma)^{d-1}}}{\|\nabla \gamma u\|_{L^2(\Gamma)^{d-1}}}$$

for the gradient reconstructions in the matrix and in the fractures. These errors are reported for both schemes in Figure 1.6 for the first test case, and in Figure 1.7 for the second test case as function of the number of d.o.f. after elimination of the cell and Dirichlet unknowns. The convergence rate between two successive meshes k and $k + 1$ is

also provided and computed as follows:

$$\mathrm{CR}_u^{k+1} = d\,\frac{\ln\left(\frac{\|\mathrm{Err}_u{}^k\|}{\|\mathrm{Err}_u{}^{k+1}\|}\right)}{\ln\left(\frac{\#(Nb_{cells}^{k+1})}{\#(Nb_{cells}^{k})}\right)},\quad \mathrm{CR}_g^{k+1} = d\,\frac{\ln\left(\frac{\|\mathrm{Err}_g{}^k\|}{\|\mathrm{Err}_{g_{grad}}^{k+1}\|}\right)}{\ln\left(\frac{\#(Nb_{cells}^{k+1})}{\#(Nb_{cells}^{k})}\right)}.$$

It is reported for both schemes in tables 1.4 and 1.5 for the first test case, and in table 1.6 for the second test case. A second order convergence rate is observed on Cartesian meshes for both the function and gradient reconstructions, which is a typical super convergence behavior on such meshes. On randomly perturbated Cartesian meshes, the VAG scheme exhibits a second order convergence rate for the function reconstructions and a first order convergence rate for the gradient reconstructions. Since on randomly perturbated Cartesian meshes the faces are no longer planar, the HFV scheme no longer converges as expected, at least for the gradient reconstructions. On tetrahedral meshes a second order of convergence is also obtained for the function reconstructions and a first order of convergence is noticed for the gradient reconstructions for both test cases. This observed second order of convergence for the function reconstructions is as usual better than the first order estimate given by Remark 1.4.1, while the observed first order of convergence for the gradient reconstructions confirms the estimate given by Remark 1.4.1. It is also clear on both test cases that the HFV scheme is much less robust w.r.t. anisotropy than the VAG scheme, especially on tetrahedral meshes.

In all test cases, the linear system obtained after elimination of the cell and Dirichlet unknowns is solved using the GMRes iterative solver with the stopping criteria 10^{-10} and a maximum Krylov subspace dimension fixed to 1000 (not attained in our tests). The GMRes solver is preconditioned by ILUT [55], [56] using the thresholding parameter 10^{-4} chosen small enough in such a way that all the linear systems can be solved for both schemes and for all meshes. In tables 1.4, 1.5 and 1.6, we report the number of GMRes iterations It, the fill-in factor F of the ILUT factorization defined as the ratio between the number of nonzero elements of the ILUT factorization by the number of nonzero elements of the matrix. We also report the CPU time taking into account the elimination of the cell and Dirichlet unknowns, the ILUT factorization, the GMRes iterations, and the computation of the cell values. It can be noticed that, on topologically Cartesian meshes, the CPU time is roughly speaking 4 times larger for the HFV scheme than for the VAG scheme. This large difference is not due to the number of nonzero elements in the matrices which is only slightly larger for the HFV scheme than for the VAG scheme. As can be checked in table 1.4, this difference is due to a larger number of GMRes iterations and to a higher fill-in factor of the ILUT factorization for the HFV scheme than for the VAG scheme. On tetrahedral meshes, the CPU time for the computation of the HFV solution is larger of a factor from 10 to 20 than the CPU time obtained with the VAG scheme. This is due to a larger number of GMRes iterations, a larger fill-in factor for ILUT combined with a 5 times larger number of nonzero elements in the matrix.

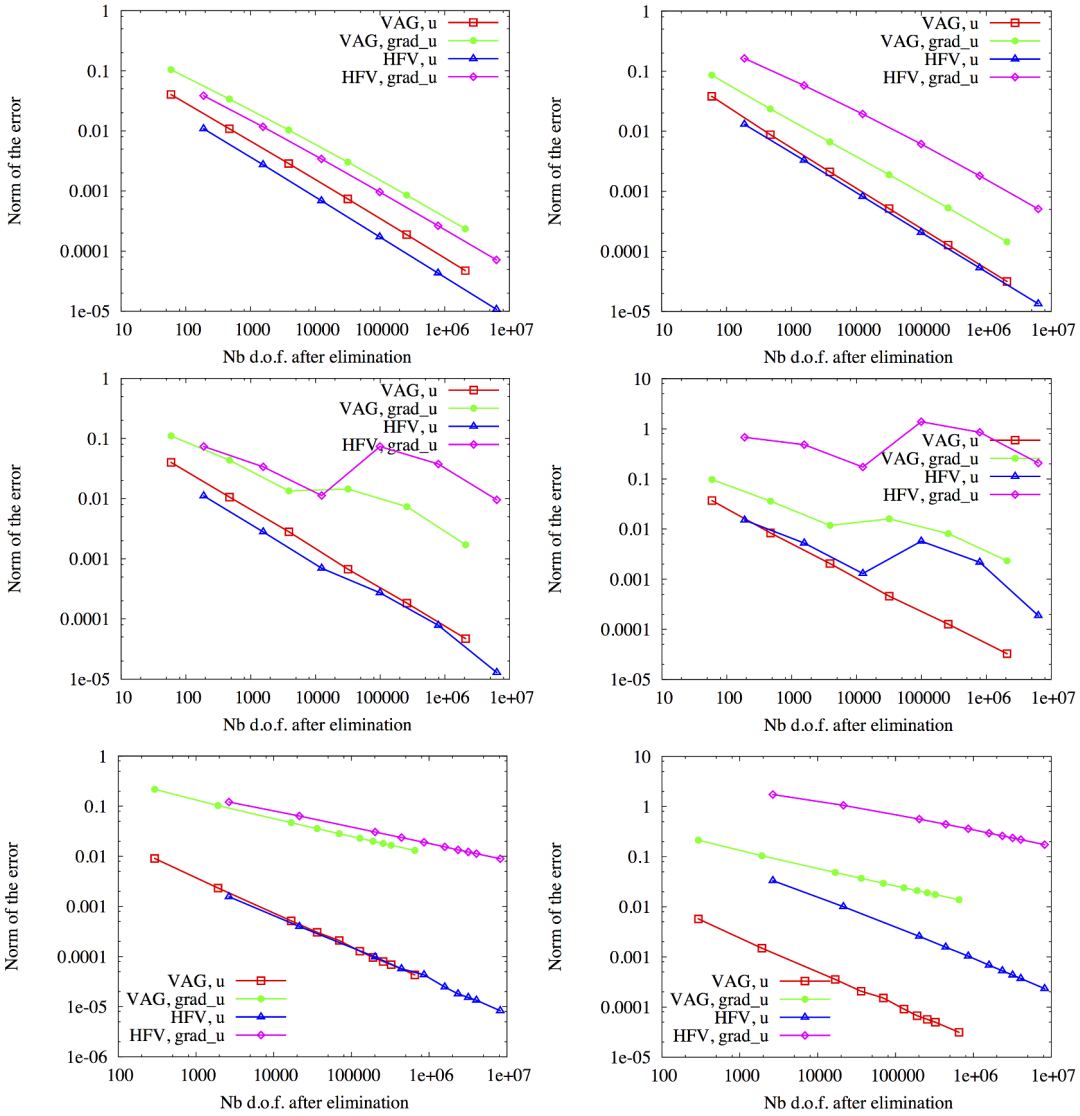

Figure 1.6: First test case. For the 3 families of meshes (top: Cartesian meshes, middle: randomly perturbated Cartesian meshes, and bottom: tetrahedral meshes), and for the isotropic (left) and anisotropic (right) subcases: sum of L^2 norm of the relative error in the matrix and in the fracture for the function and its gradients reconstruction both for VAG and HFV schemes as the function of the number of d.o.f. (after elimination of the cell and Dirichlet unknowns).

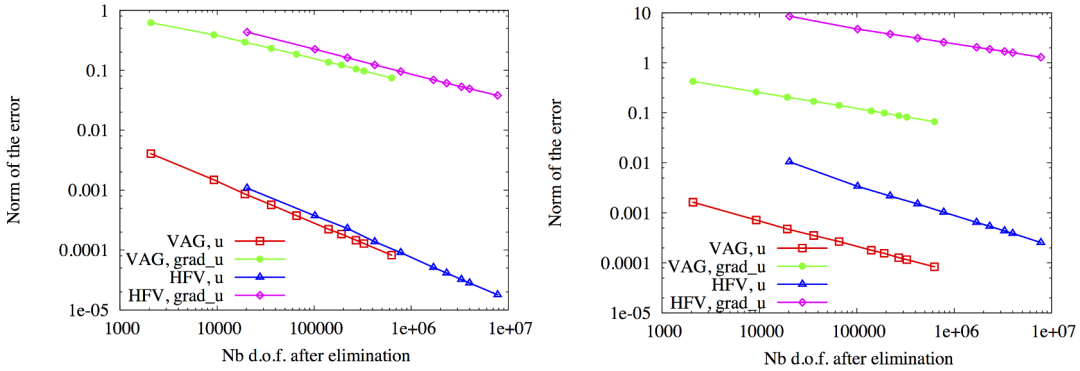

Figure 1.7: Second test case. For the 10 tetrahedral meshes and for the isotropic (left) and anisotropic (right) subcases: sum of L^2 norm of the relative error in the matrix and in the fracture for the function and its gradients reconstruction both for VAG and HFV schemes as the function of the number of d.o.f.(after elimination of the cell and Dirichlet unknowns).

	Isotropic case, Cartesian							***Anisotropic case, Cartesian***						
Vertex Approximate Gradient Discretization														
Nb	**It**	**F**	**Err**$_u$	**Err**$_g$	**CR**$_u$	**CR**$_g$	**CPU**	**It**	**F**	**Err**$_u$	**Err**$_g$	**CR**$_u$	**CR**$_g$	**CPU**
1	3	1.2	$4.03{\cdot}10^{-2}$	0.11	n/a	n/a	$9.6{\cdot}10^{-4}$	3	1.2	$3.8{\cdot}10^{-2}$	$8.5{\cdot}10^{-2}$	n/a	n/a	$7.7{\cdot}10^{-4}$
2	5	2.1	$1.08{\cdot}10^{-2}$	0.03	1.89	1.62	$6.9{\cdot}10^{-3}$	5	1.9	$8.7{\cdot}10^{-3}$	$2.3{\cdot}10^{-2}$	2.12	1.87	$6.1{\cdot}10^{-3}$
3	9	2.4	$2.9{\cdot}10^{-3}$	$1.04{\cdot}10^{-2}$	1.92	1.71	$9.9{\cdot}10^{-2}$	9	2.2	$2.1{\cdot}10^{-3}$	$6.6{\cdot}10^{-3}$	2.06	1.83	$8.1{\cdot}10^{-2}$
4	16	2.5	$7.4{\cdot}10^{-4}$	$3.03{\cdot}10^{-3}$	1.95	1.77	0.89	14	2.1	$5.1{\cdot}10^{-4}$	$1.9{\cdot}10^{-3}$	2.03	1.81	0.71
5	30	2.5	$1.9{\cdot}10^{-4}$	$8.5{\cdot}10^{-4}$	1.97	1.82	8.4	20	2.2	$1.3{\cdot}10^{-4}$	$5.3{\cdot}10^{-4}$	2.02	1.84	5.5
6	56	2.5	$4.8{\cdot}10^{-5}$	$2.3{\cdot}10^{-4}$	1.89	1.86	90	29	2.2	$3.2{\cdot}10^{-5}$	$1.4{\cdot}10^{-4}$	2.01	1.87	48
Hybrid Finite Volume Discretization														
Nb	**It**	**F**	**Err**$_u$	**Err**$_g$	**CR**$_u$	**CR**$_g$	**CPU**	**It**	**F**	**Err**$_u$	**Err**$_g$	**CR**$_u$	**CR**$_g$	**CPU**
1	6	3.3	$1.08{\cdot}10^{-2}$	$3.8{\cdot}10^{-2}$	n/a	n/a	$1.3{\cdot}10^{-3}$	4	2.5	$1.3{\cdot}10^{-2}$	0.16	n/a	n/a	$9.7{\cdot}10^{-4}$
2	10	3.6	$2.7{\cdot}10^{-3}$	$1.2{\cdot}10^{-2}$	1.98	1.64	$1.2{\cdot}10^{-2}$	6	3.1	$3.3{\cdot}10^{-3}$	$5.8{\cdot}10^{-2}$	1.97	1.23	$7.5{\cdot}10^{-3}$
3	17	3.6	$6.9{\cdot}10^{-4}$	$3.4{\cdot}10^{-3}$	1.99	1.71	0.14	10	3.6	$8.2{\cdot}10^{-4}$	$1.9{\cdot}10^{-2}$	1.99	1.49	$9.4{\cdot}10^{-2}$
4	29	3.6	$1.7{\cdot}10^{-4}$	$9.6{\cdot}10^{-4}$	1.99	1.77	1.4	18	3.7	$2.1{\cdot}10^{-4}$	$6.1{\cdot}10^{-3}$	2.01	1.58	1.4
5	59	3.6	$4.3{\cdot}10^{-5}$	$2.6{\cdot}10^{-4}$	2	1.82	17.7	30	3.8	$5.3{\cdot}10^{-5}$	$1.8{\cdot}10^{-3}$	1.99	1.68	18
6	122	3.6	$1.1{\cdot}10^{-5}$	$7.1{\cdot}10^{-5}$	2	1.86	313	65	3.8	$1.3{\cdot}10^{-5}$	$5.1{\cdot}10^{-4}$	1.99	1.78	303

	Isotropic case, Perturbated Cartesian							***Anisotropic case, Perturbated Cartesian***						
Vertex Approximate Gradient Discretization														
Nb	**It**	**F**	**Err**$_u$	**Err**$_g$	**CR**$_u$	**CR**$_g$	**CPU**	**It**	**F**	**Err**$_u$	**Err**$_g$	**CR**$_u$	**CR**$_g$	**CPU**
1	4	1.2	$4.03{\cdot}10^{-2}$	0.11	n/a	n/a	$7.8{\cdot}10^{-4}$	3	1.2	$3.8{\cdot}10^{-2}$	$8.6{\cdot}10^{-2}$	n/a	n/a	$7.8{\cdot}10^{-4}$
2	5	2.1	$1.08{\cdot}10^{-2}$	$3.4{\cdot}10^{-2}$	1.92	1.34	$6.3{\cdot}10^{-3}$	5	1.9	$8.7{\cdot}10^{-3}$	$2.3{\cdot}10^{-2}$	2.14	1.44	$5.8{\cdot}10^{-3}$
3	9	2.4	$2.8{\cdot}10^{-3}$	$1.03{\cdot}10^{-2}$	1.92	1.69	$9.8{\cdot}10^{-2}$	8	2.2	$2.1{\cdot}10^{-3}$	$6.6{\cdot}10^{-3}$	2.02	1.61	$7.6{\cdot}10^{-2}$
4	16	2.5	$7.4{\cdot}10^{-4}$	$3.02{\cdot}10^{-3}$	2.06	-0.11	0.908	14	2.1	$5.1{\cdot}10^{-4}$	$1.9{\cdot}10^{-3}$	2.16	-0.43	0.64
5	29	2.5	$1.9{\cdot}10^{-4}$	$8.5{\cdot}10^{-4}$	1.87	0.91	8.4	20	2.3	$1.3{\cdot}10^{-4}$	$5.2{\cdot}10^{-4}$	1.85	0.97	5.6
6	56	2.5	$4.7{\cdot}10^{-5}$	$2.3{\cdot}10^{-4}$	1.96	2.11	85	29	2.3	$3.2{\cdot}10^{-5}$	$1.4{\cdot}10^{-4}$	1.95	1.81	48
Hybrid Finite Volume Discretization														
Nb	**It**	**F**	**Err**$_u$	**Err**$_g$	**CR**$_u$	**CR**$_g$	**CPU**	**It**	**F**	**Err**$_u$	**Err**$_g$	**CR**$_u$	**CR**$_g$	**CPU**
1	5	3.3	$1.1{\cdot}10^{-2}$	$7.4{\cdot}10^{-2}$	n/a	n/a	$1.5{\cdot}10^{-3}$	5	2.9	$1.5{\cdot}10^{-2}$	0.67	n/a	n/a	$1.4{\cdot}10^{-3}$
2	9	3.6	$2.8{\cdot}10^{-3}$	$3.4{\cdot}10^{-2}$	1.99	1.12	$1.6{\cdot}10^{-2}$	8	3.4	$5.2{\cdot}10^{-3}$	0.48	1.52	0.48	$1.7{\cdot}10^{-2}$
3	16	3.6	$6.9{\cdot}10^{-4}$	$1.1{\cdot}10^{-2}$	2.01	1.58	0.15	11	3.7	$1.3{\cdot}10^{-3}$	0.17	2.01	1.47	0.17
4	27	3.6	$2.7{\cdot}10^{-4}$	$7.3{\cdot}10^{-2}$	1.35	-2.71	1.6	16	3.8	$5.7{\cdot}10^{-3}$	1.38	-2.14	-3.01	1.9
5	50	3.6	$7.8{\cdot}10^{-5}$	$3.8{\cdot}10^{-2}$	1.79	0.96	20	31	3.9	$2.2{\cdot}10^{-3}$	0.85	1.39	0.71	33
6	106	3.6	$1.3{\cdot}10^{-5}$	$9.5{\cdot}10^{-3}$	2.60	1.97	292	57	3.9	$1.9{\cdot}10^{-4}$	0.21	3.53	2.03	356

Table 1.4: First test case. For the isotropic (left) and anisotropic (right) subcases, the VAG and HFV schemes and the six Cartesian meshes (above) and the six perturbated Cartesian meshes (below): mesh number Nb, number IT of GMRES iterations preconditioned by ILUT, fill-in factor F, sum of the L^2 relative errors in the matrix and in the fractures for the function (Err_u) and for the gradient reconstruction (Err_g), convergence rates for the function (CR_u) and for the gradient (CR_g) reconstruction, CPU time in seconds.

	Isotropic case							***Anisotropic case***						
Vertex Approximate Gradient Discretization														
Nb	**It**	**F**	**ErrF**	**Err$_g$**	**CR$_u$**	**CR$_g$**	**CPU**	**It**	**F**	**ErrF**	**Err$_g$**	**CR$_u$**	**CR$_g$**	**CPU**
1	5	2.1	$9.1{\cdot}10^{-3}$	0.22	n/a	n/a	$3.6{\cdot}10^{-3}$	5	2.1	$5.7{\cdot}10^{-3}$	0.21	n/a	n/a	$3.8{\cdot}10^{-3}$
2	8	2.6	$2.3{\cdot}10^{-3}$	0.11	1.96	1.08	$4.9{\cdot}10^{-2}$	9	2.6	$1.5{\cdot}10^{-3}$	0.11	1.94	1.04	$4.5{\cdot}10^{-2}$
3	16	2.8	$5.1{\cdot}10^{-4}$	$4.6{\cdot}10^{-2}$	2.02	1.05	0.61	15	2.9	$3.5{\cdot}10^{-4}$	$4.8{\cdot}10^{-2}$	1.91	1.02	0.68
4	20	2.9	$3.1{\cdot}10^{-4}$	$3.6{\cdot}10^{-2}$	2.02	1.05	1.5	18	2.9	$2.1{\cdot}10^{-4}$	$3.7{\cdot}10^{-2}$	2.09	1.02	1.7
5	25	2.9	$2.1{\cdot}10^{-4}$	$2.8{\cdot}10^{-2}$	1.69	1.06	2.9	22	3	$1.5{\cdot}10^{-4}$	$2.9{\cdot}10^{-2}$	1.39	1.04	3.8
6	29	2.9	$1.3{\cdot}10^{-4}$	$2.3{\cdot}10^{-2}$	2.37	1.01	5.9	25	3	$9.1{\cdot}10^{-5}$	$2.4{\cdot}10^{-2}$	2.47	0.99	6.9
7	33	2.9	$9.6{\cdot}10^{-5}$	$2.1{\cdot}10^{-2}$	2.21	1.02	10	26	3	$6.7{\cdot}10^{-5}$	$2.1{\cdot}10^{-2}$	2.33	1.01	12
8	37	2.9	$7.9{\cdot}10^{-5}$	$1.8{\cdot}10^{-2}$	1.81	0.99	14	30	3	$5.7{\cdot}10^{-5}$	$1.9{\cdot}10^{-2}$	1.66	0.98	16
9	40	2.9	$6.9{\cdot}10^{-5}$	$1.7{\cdot}10^{-2}$	1.81	1.05	18	30	3	$4.9{\cdot}10^{-5}$	$1.7{\cdot}10^{-2}$	1.62	1.05	22
10	49	2.9	$4.3{\cdot}10^{-5}$	$1.3{\cdot}10^{-2}$	2.01	1.01	41	37	3	$3.1{\cdot}10^{-5}$	$1.4{\cdot}10^{-2}$	1.98	1.01	48
Hybrid Finite Volume Discretization														
Nb	**It**	**F**	**ErrF**	**Err$_g$**	**CR$_u$**	**CR$_g$**	**CPU**	**It**	**F**	**ErrF**	**Err$_g$**	**CR$_u$**	**CR$_g$**	**CPU**
1	10	4.4	$1.5{\cdot}10^{-3}$	0.12	n/a	n/a	$1.7{\cdot}10^{-2}$	15	4.6	$3.3{\cdot}10^{-2}$	1.7	n/a	n/a	$2.7{\cdot}10^{-2}$
2	17	4.7	$3.9{\cdot}10^{-4}$	$6.4{\cdot}10^{-2}$	1.97	0.92	0.23	25	5.1	$1.1{\cdot}10^{-2}$	1.1	1.72	0.72	0.49
3	33	4.8	$9.8{\cdot}10^{-5}$	$3.1{\cdot}10^{-2}$	1.87	0.98	3.3	39	5.2	$2.6{\cdot}10^{-3}$	0.56	1.83	0.85	7.2
4	42	4.9	$5.7{\cdot}10^{-5}$	$2.4{\cdot}10^{-2}$	2.08	0.99	8.9	48	5.2	$1.5{\cdot}10^{-3}$	0.44	1.90	0.92	18
5	52	4.9	$4.3{\cdot}10^{-5}$	$1.9{\cdot}10^{-2}$	1.25	0.97	22	62	5.2	$1.1{\cdot}10^{-3}$	0.36	1.86	0.92	40
6	69	4.9	$2.5{\cdot}10^{-5}$	$1.5{\cdot}10^{-2}$	2.73	1.03	47	82	5.2	$6.8{\cdot}10^{-4}$	0.29	2.03	0.98	87
7	78	4.9	$1.8{\cdot}10^{-5}$	$1.3{\cdot}10^{-2}$	2.42	1.05	74	94	5.2	$5.3{\cdot}10^{-4}$	0.25	1.96	0.97	141
8	86	4.9	$1.5{\cdot}10^{-5}$	$1.2{\cdot}10^{-2}$	1.62	0.92	106	112	5.2	$4.3{\cdot}10^{-4}$	0.23	1.94	0.94	203
9	94	4.9	$1.3{\cdot}10^{-5}$	$1.1{\cdot}10^{-2}$	1.60	0.98	154	125	5.2	$3.7{\cdot}10^{-4}$	0.21	1.95	0.97	285
10	122	4.9	$8.3{\cdot}10^{-6}$	$8.9{\cdot}10^{-3}$	2.03	0.99	346	192	5.2	$2.3{\cdot}10^{-4}$	0.17	1.97	0.98	725

Table 1.5: First test case. For the isotropic (left) and anisotropic (right) subcases, the VAG and HFV schemes and the ten tetrahedral meshes: mesh number Nb, number IT of GMRES iterations preconditioned by ILUT, fill-in factor F, sum of the L^2 relative errors in the matrix and in the fractures for the function (Err_u) and for the gradient reconstruction (Err_g), convergence rates for the function (CR_u) and for the gradient (CR_g) reconstruction, CPU time in seconds.

	Isotropic case							***Anisotropic case***						
Vertex Approximate Gradient Discretization														
Nb	**It**	**F**	**ErrF**	**Err$_g$**	**CR$_u$**	**CR$_g$**	**CPU**	**It**	**F**	**ErrF**	**Err$_g$**	**CR$_u$**	**CR$_g$**	**CPU**
1	11	2.5	$4.1{\cdot}10^{-3}$	0.61	n/a	n/a	$4.3{\cdot}10^{-2}$	13	2.5	$1.6{\cdot}10^{-3}$	0.42	n/a	n/a	$4.8{\cdot}10^{-2}$
2	32	2.7	$1.5{\cdot}10^{-3}$	0.38	1.96	0.91	0.34	20	2.8	$7.2{\cdot}10^{-4}$	0.26	1.52	0.91	0.31
3	51	2.8	$8.6{\cdot}10^{-4}$	0.29	2.28	1.06	0.77	52	2.8	$4.7{\cdot}10^{-4}$	0.21	1.60	0.92	0.83
4	51	2.8	$5.7{\cdot}10^{-4}$	0.23	1.94	1.05	1.5	51	2.9	$3.5{\cdot}10^{-4}$	0.17	1.38	0.89	1.7
5	51	2.9	$3.8{\cdot}10^{-4}$	0.18	2.07	1.04	3.1	51	2.9	$2.7{\cdot}10^{-4}$	0.14	1.35	0.89	3.4
6	51	2.9	$2.2{\cdot}10^{-4}$	0.13	2.08	1.06	7.9	51	2.9	$1.8{\cdot}10^{-4}$	0.11	1.53	0.98	7.9
7	51	2.9	$1.8{\cdot}10^{-4}$	0.12	1.88	0.97	9.8	51	2.9	$1.6{\cdot}10^{-4}$	$9.9{\cdot}10^{-2}$	1.37	0.88	11
8	52	2.9	$1.5{\cdot}10^{-4}$	0.11	2.12	1.12	14	53	2.9	$1.3{\cdot}10^{-4}$	$8.8{\cdot}10^{-2}$	1.73	1.08	18
9	60	2.9	$1.3{\cdot}10^{-4}$	$9.7{\cdot}10^{-2}$	1.95	1.03	19	56	2.9	$1.2{\cdot}10^{-4}$	$8.3{\cdot}10^{-2}$	1.41	0.95	22
10	78	2.9	$8.2{\cdot}10^{-5}$	$7.4{\cdot}10^{-2}$	2.04	1.03	40	72	3	$8.4{\cdot}10^{-5}$	$6.7{\cdot}10^{-2}$	1.48	0.97	48
Hybrid Finite Volume Discretization														
Nb	**It**	**F**	**ErrF**	**Err$_g$**	**CR$_u$**	**CR$_g$**	**CPU**	**It**	**F**	**ErrF**	**Err$_g$**	**CR$_u$**	**CR$_g$**	**CPU**
1	51	4.7	$1.08{\cdot}10^{-3}$	0.43	n/a	n/a	0.32	52	5.1	$1.1{\cdot}10^{-2}$	8.6	n/a	n/a	0.54
2	51	4.8	$3.7{\cdot}10^{-4}$	0.22	1.91	1.02	1.9	84	5.2	$3.4{\cdot}10^{-3}$	4.7	2.09	1.09	3.9
3	53	4.8	$2.3{\cdot}10^{-4}$	0.16	1.96	1.09	4.8	97	5.2	$2.2{\cdot}10^{-3}$	3.7	1.73	0.89	9.8
4	71	4.9	$1.4{\cdot}10^{-4}$	0.12	2.07	1.08	11	108	5.2	$1.5{\cdot}10^{-3}$	3.1	1.68	0.86	22
5	88	4.9	$9.1{\cdot}10^{-5}$	$9.5{\cdot}10^{-2}$	2.07	1.07	25	146	5.2	$1.1{\cdot}10^{-3}$	2.6	1.84	0.91	50
6	114	4.9	$5.1{\cdot}10^{-5}$	$6.9{\cdot}10^{-2}$	2.05	1.06	67	248	5.2	$6.5{\cdot}10^{-4}$	2.1	1.80	0.89	155
7	132	4.9	$4.1{\cdot}10^{-5}$	$6.1{\cdot}10^{-2}$	1.98	1.01	104	532	5.2	$5.4{\cdot}10^{-4}$	1.9	1.72	0.84	387
8	146	4.9	$3.2{\cdot}10^{-5}$	$5.3{\cdot}10^{-2}$	2.06	1.05	162	530	5.2	$4.4{\cdot}10^{-4}$	1.7	1.83	0.88	565
9	165	4.9	$2.8{\cdot}10^{-5}$	$4.9{\cdot}10^{-2}$	1.99	1.01	216	312	5.2	$3.9{\cdot}10^{-4}$	1.6	1.80	0.90	477
10	196	4.9	$1.8{\cdot}10^{-6}$	$3.8{\cdot}10^{-2}$	2.02	1.03	498	748	5.2	$2.6{\cdot}10^{-4}$	1.3	1.89	0.94	906

Table 1.6: Second test case. For the isotropic (left) and the anisotropic (right) subcases, the VAG and HFV schemes and the ten tetrahedral meshes: mesh number Nb, number IT of GMRES iterations preconditioned by ILUT, fill-in factor F, sum of the L_2 relative errors in the matrix and in the fractures for the function (Err_u) and for the gradient reconstruction (Err_g), convergence rates for the function (CR_u) and for the gradient (CR_g) reconstruction, CPU time in seconds.

1.6 Conclusion

In this Chapter, the gradient scheme framework [28] is extended to hybrid dimensional Darcy flow models in fractured porous media. Both the Vertex Approximate Gradient and the Hybrid Finite Volume schemes are shown to satisfy, whatever the choice of the control volumes, the coercivity, consistency, limit-conformity and compacity assumptions of the gradient scheme framework. These properties ensures in particular the convergence of the schemes to a weak solution of the model. One of the key ingredient to prove that both schemes satisfy this framework is the density of smooth function subspaces for both the solution and flux Hilbert spaces. This result is obtained for a general network of polygonal fractures including intersecting, immersed or non immersed fractures. The numerical experiments carried out on Cartesian, hexahedral and tetrahedral families of meshes exhibit the convergence of both schemes except as expected for the HFV scheme with non planar faces. The numerical results show that the VAG scheme is much cheaper in terms of CPU time than the HFV scheme on tetrahedral meshes for a given mesh, but on the other hand the HFV scheme is more accurate. It is also clear that the VAG scheme is more robust than the HFV scheme regarding anisotropy.

Chapter 2

Hybrid Dimensional Two-Phase Darcy Flows in Fractured Porous Media

Abstract: this Chapter extends the Vertex Approximate Gradient (VAG) and Hybrid Finite Volume (HFV) discretizations of Chapter 1 to two-phase Darcy flows in discrete fracture networks taking into account the mass exchange between the matrix and the fracture. As in Chapter 1, we consider the asymptotic model for which the fractures are represented as interfaces of codimension one immersed in the matrix domain, leading to the so called hybrid dimensional Darcy flow model. The pressures at the interfaces between the matrix and the fracture network are continuous corresponding to a ratio between the normal permeability of the fracture and the width of the fracture assumed to be large compared with the ratio between the permeability of the matrix and the size of the domain. To fix ideas, the convergence of the scheme to a weak solution is proved for the VAG scheme. The proof holds under the assumption that the relative permeabilities are bounded from below by a strictly positive constant. This assumption is needed in the convergence proof in order to take into account discontinuous capillary pressures in particular at the matrix fracture interfaces. The efficiency of our approach is assessed on numerical examples of fracture networks in 2D and 3D. We show in particular that, compared with Control Volume Finite Element (CVFE) approaches, the VAG scheme has the advantage to avoid the mixing of the fracture and matrix rocktypes at the interfaces between the matrix and the fractures, while keeping the low cost of a nodal discretization on unstructured meshes.

2.1 Introduction

The objective of this Chapter is to extend the hybrid dimensional model and its discretization presented in Chapter 1 for single phase Darcy flow to two-phase Darcy flows. As in Chapter 1, we focus on the particular case of permeable fractures for which the pressure can be assumed continuous at matrix fracture interfaces. This type of hybrid dimensional Darcy flow model has been introduced in [3] for single phase flows and in [54], [53], [43] for two-phase Darcy flows. In the framework of two-phase Darcy flows in fractured porous media, high contrasts of capillary pressures are expected in particular between the matrix and the fractures. Hence, it is crucial to take into account, in the model formulation, the saturation jumps at the matrix fracture interfaces. We refer to [29], [20], [21] for mathematical formulations taking into account discontinuous capillary pressures. In the present work, we employ the phase pressures formulation (see e.g. [35]) assuming that the capillary pressures are strictly monotone. Using the monotone graph extensions of the inverse of the capillary functions, both phase pressures can be assumed continuous at the matrix fracture interfaces. Hence, this is a good framework to capture the saturation jump condition at the matrix fracture interfaces without introducing any additional unknowns at these interfaces.

The discretization of the hybrid dimensional Darcy flow model with continuous pressures has been the object of several works. In [46] a cell-centred Finite Volume scheme using a Two Point Flux Approximation (TPFA) is proposed assuming the orthogonality

of the mesh and isotropic permeability fields. Cell-centred Finite Volume schemes can be extended to general meshes and anisotropic permeability fields using MultiPoint Flux Approximations (MPFA) following the ideas introduced in [60] for discontinuous pressure models. Nevertheless, MPFA schemes can lack robustness on distorted meshes and large anisotropies due to the non symmetry of the discretization. They are also very expensive compared with nodal discretizations on tetrahedral meshes. In [3], a Mixed Finite Element (MFE) method is proposed for single Darcy flows. It is extended to two-phase flows in [43] in an IMPES framework using a Mixed Hybrid Finite Element (MHFE) discretization for the pressure equation and a Discontinuous Galerkin discretization of the saturation equation. These approaches are adapted to general meshes and anisotropy but require as many degrees of freedom as faces. Control Volume Finite Element Methods (CVFE) [54], [53] have the advantage to use only nodal unknowns leading to much fewer degrees of freedom than MPFA and MHFE schemes on tetrahedral meshes. On the other hand, at the matrix fracture interfaces, the control volumes have the drawback to be shared between the matrix and the fractures. It results that a strong refinement of the mesh is needed at these interfaces in the case of large contrasts between the permeabilities of the matrix and of the fractures.

In this Chapter we extend to two-phase flows the VAG and HFV schemes introduced in Chapter 1 for single phase Darcy flows. For a single medium, the VAG scheme has been introduced for the discretization of multiphase Darcy flows in [36] for immiscible flows and in [32] for compositional models. The HFV scheme has been first introduced for two-phase Darcy flows in [5] using a phase pressures formulation for a Black Oil type model, and in [10] using a global pressure formulation for an immiscible flow. The VAG scheme basically uses nodal unknowns like the CVFE method but it also keeps the cell-centred unknowns, which are eliminated at the linear algebra level without any fill-in. Compared with CVFE methods, it has the advantage to provide a large flexibility in the choice of the control volumes in order to avoid mixing rocks with highly contrasted absolute permeabilities in a single control volume. In [35], using a phase pressures formulation, the interface unknowns of the VAG (or HFV) scheme are exploited in order to capture the saturation jumps at different rocktype interfaces. It is this latter approach that is used in this Chapter for both the VAG and HFV discretizations and extended to the case of the hybrid dimensional two-phase Darcy flows in fractured porous media.

The first convergence result for a finite volume discretization of single media two-phase Darcy flow models has been obtained for cell-centred TPFA schemes on admissible meshes in [51] and [33]. In [33] the convergence is obtained for the usual phase pressures and saturations formulation using a phase by phase upwinding of the mobilities. In [51] the convergence is obtained for the global pressure formulation introduced in [22] (see also [8]). This latter convergence result has been recently extended in [16] to the case of the VAG discretization. The convergence is shown to hold whatever the choice of the volumes at the nodal unknowns. In the case of two-phase Darcy flows with discontinuous capillary pressure, the convergence of a TPFA type discretization is obtained in [11]. The

extension to general meshes is done in [35] assuming the non degeneracy of the relative permeabilities in the framework of gradient scheme discretizations introduced in [31].

To our knowledge, there is not yet a proof of convergence for hybrid dimensional two-phase Darcy flows. In this Chapter, we propose to extend the results obtained in [35] in the particular case of the VAG scheme to the hybrid dimensional Darcy flow model. The convergence of the VAG scheme to a weak solution is obtained assuming that the relative permeabilities of both phases are bounded from below by a strictly positive constant, and assuming that the family of meshes is shape regular. This result could be easily extended to the gradient scheme framework of Chapter 1.

The outline of the Chapter is the following. In section 2.2, the two-phase Darcy flow hybrid dimensional model is introduced and its discretization using the VAG scheme is described in section 2.3. The convergence of the scheme is obtained in section 2.4 assuming the non degeneracy of the relative permeabilities and whatever the choice of the volumes at the nodal unknowns. Section 2.5 introduces the flux formulation of the VAG and HFV discretizations using a phase by phase upwinding of the mobilities and the notations of Subsection 1.4.3. 2D and 3D numerical tests are presented in section 2.6 using this flux formulation and both the VAG and HFV schemes.

2.2 Hybrid dimensional Two-Phase Darcy Flow Model in Fractured Porous Media

2.2.1 Two-Phase Darcy Flows in Phase Pressures Formulation

In the framework of two-phase Darcy flows in fractured porous media high contrasts of capillary pressures are expected in particular at the interfaces between the matrix and the fractures. Hence, it is crucial to take into account in the model formulation the saturation jumps at these interfaces (see for example [20], [21] for the mathematical formulations of two-phase Darcy flows with discontinuous capillary pressures). Our choice focuses on the phase pressures formulation (see e.g. [35]) which is extended to the case of hybrid dimensional two-phase Darcy flows in a variational formulation framework. The main advantage of this formulation is to choose as primary unknowns the phase pressures which can be assumed to be continuous at the interfaces between different rocktypes while the jump of the saturation is captured using the inverse of the capillary pressure monotone graph for each rocktype. An alternative choice using a global pressure approach is presented in [45].

Let u^2 (resp. u^1) denote the wetting (resp. non wetting) phase pressure, $p = u^1 - u^2$ the capillary pressure, and $p_{\rm ini} \in V$ the initial capillary pressure. For the sake of simplicity in the convergence analysis, homogeneous Dirichlet boundary conditions are assumed for u^1 and u^2 at the boundary $\partial\Omega$, as well as at Σ_0 for γu^1 and γu^2. The gravity is also not taken into account in the model to simplify the analysis. The extension of the convergence proof to the case with gravity and with non homogeneous Dirichlet boundary conditions

can be done easily following the same ideas as in [35].

Let us denote by $S_m^1(\mathbf{x},p)$ (resp. $S_f^1(\mathbf{x},p)$) the inverses of the monotone graph extension of the capillary pressure curves in the matrix domain Ω (resp. in the fracture network Γ), and let us set $S_m^2 = 1 - S_m^1$ (resp. $S_f^2 = 1 - S_f^1$).

In the matrix domain Ω (resp. in the fracture network Γ), let us denote by $k_m^\alpha(\mathbf{x}, S_m^\alpha)$ (resp. $k_f^\alpha(\mathbf{x}, S_f^\alpha)$), $\alpha = 1,2$, the phase mobilities, and by $\phi_m(\mathbf{x})$ (resp. $\phi_f(\mathbf{x})$) the porosity. As in Chapter 1, we denote by $\Lambda_m(\mathbf{x})$ (resp. $\Lambda_f(\mathbf{x})$) the permeability tensor, by $d_f(\mathbf{x}), \mathbf{x} \in \Gamma$ the width of the fractures, and by $d\tau_f(\mathbf{x})$ the weighted Lebesgue $d-1$ dimensional measure on Γ defined by $d\tau_f(\mathbf{x}) = d_f(\mathbf{x})d\tau(\mathbf{x})$.

Using the notations of Chapter 1, the strong formulation of our hybrid dimensional two phase Darcy flow model amounts to find u^α, $(\mathbf{q}_m^\alpha, \mathbf{q}_f^\alpha)$ such that one has for $\alpha = 1,2$:

$$\left\{\begin{array}{rll}
\phi_m \partial_t\Big(S_m^\alpha(\mathbf{x},p)\Big) + \mathrm{div}(\mathbf{q}_{m,\mathfrak{a}}^\alpha) = h_m^\alpha & \text{on } \Omega_\mathfrak{a},\, \mathfrak{a} \in \mathcal{A}, \\
\phi_f d_f \partial_t\Big(S_f^\alpha(\mathbf{x},\gamma_i p)\Big) + \mathrm{div}_{\tau_i}(\mathbf{q}_{f,i}^\alpha) - [\![\mathbf{q}_m^\alpha \cdot \mathbf{n}_i]\!] = d_f h_f^\alpha & \text{on } \Gamma_i,\, i \in I, \\
-k_m^\alpha(\mathbf{x}, S_m^\alpha(\mathbf{x},p))\Lambda_m \nabla u^\alpha = \mathbf{q}_{m,\mathfrak{a}}^\alpha & \text{on } \Omega_\mathfrak{a},\, \mathfrak{a} \in \mathcal{A}, \\
-d_f k_f^\alpha(\mathbf{x}, S_f^\alpha(\mathbf{x},\gamma_i p))\Lambda_f \nabla_{\tau_i}\gamma_i u^\alpha = \mathbf{q}_{f,i}^\alpha & \text{on } \Gamma_i,\, i \in I, \\
p|_{t=0} = p_{\mathrm{ini}}, & \text{on } \Omega,
\end{array}\right.$$

where the function h_m^α (resp. h_f^α), $\alpha = 1,2$ stands for the source terms in the matrix domain Ω (resp. in the fracture network Γ).

The corresponding weak formulation amounts to find $u^1, u^2 \in L^2(0,T;V^0)$ satisfying the following variational equalities for $\alpha = 1,2$, and for all $\varphi \in C_c^\infty([0,T)\times\Omega)$:

$$\left\{\begin{array}{l}
\displaystyle\int_0^T \int_\Omega \Big(-\phi_m(\mathbf{x}) S_m^\alpha(\mathbf{x},p)\partial_t\varphi(\mathbf{x},t) + k_m^\alpha(\mathbf{x}, S_m^\alpha(\mathbf{x},p))\Lambda_m(\mathbf{x})\nabla u^\alpha(\mathbf{x},t)\cdot\nabla\varphi(\mathbf{x},t)\Big) d\mathbf{x}dt \\
\displaystyle + \int_0^T \int_\Gamma -\phi_f(\mathbf{x}) S_f^\alpha(\mathbf{x},\gamma p)\partial_t\gamma\varphi(\mathbf{x},t) d\tau_f(\mathbf{x})dt \\
\displaystyle + \int_0^T \int_\Gamma k_f^\alpha(\mathbf{x}, S_f^\alpha(\mathbf{x},\gamma p))\Lambda_f(\mathbf{x})\nabla_\tau\gamma u^\alpha(\mathbf{x},t)\cdot\nabla_\tau\gamma\varphi(\mathbf{x},t) d\tau_f(\mathbf{x})dt \\
\displaystyle - \int_\Omega \phi_m(\mathbf{x}) S_m^\alpha(\mathbf{x},p_{\mathrm{ini}})\varphi(\mathbf{x},0)d\mathbf{x}dt - \int_\Gamma \phi_f(\mathbf{x}) S_f^\alpha(\mathbf{x},\gamma p_{\mathrm{ini}})\varphi(\mathbf{x},0) d\tau_f(\mathbf{x})dt \\
\displaystyle - \int_0^T \int_\Omega h_m^\alpha(\mathbf{x},t)\varphi(\mathbf{x},t)d\mathbf{x}dt - \int_0^T \int_\Gamma h_f^\alpha(\mathbf{x},t)\gamma\varphi(\mathbf{x},t) d\tau_f(\mathbf{x})dt = 0.
\end{array}\right. \tag{2.1}$$

As in [35], the following assumptions are made on the data:

(H1) ϕ_m is a measurable function from Ω to $\mathbb{R}$ with $\phi_m(\mathbf{x}) \in [\phi_{\min}, \phi_{\max}]$, $\phi_{\max} \geq \phi_{\min} > 0$. ϕ_f is a measurable function from Γ to $\mathbb{R}$ with $\phi_f(\mathbf{x}) \in [\phi_{\min}, \phi_{\max}]$. The fracture width d_f satisfies the same assumptions as in subsection 1.2.2.

(H2) The permeabilities Λ_m and Λ_f satisfy the same assumptions as in subsection 1.2.2.

(H3) $S_m^1(\mathbf{x},p) \in [0,1]$ for all $(\mathbf{x},p) \in \Omega \times \mathbb{R}$ with $S_m^1(\mathbf{x},p) = S_{m,j}^1(p)$ for a.e. $\mathbf{x} \in \Omega_j$ and all $p \in \mathbb{R}$, where $S_{m,j}^1$ is a non decreasing Lipschitz continuous function with constant L_S and $(\Omega_j)_{j\in J_m}$ is a finite family of disjoint connected polyhedral open sets such that $\bigcup_{j\in J_m} \overline{\Omega_j} = \overline{\Omega}$. $S_f^1(\mathbf{x},p) \in [0,1]$ for all $(\mathbf{x},p) \in \Gamma \times \mathbb{R}$ with $S_f^1(\mathbf{x},p) = S_{f,j}^1(p)$ for a.e. $\mathbf{x} \in \Upsilon_j$ and all $p \in \mathbb{R}$, where $S_{f,j}^1$ is a non decreasing Lipschitz continuous function with constant L_S and $(\Upsilon_j)_{j\in J_f}$ is a finite family of disjoint connected polygonal open sets such that $\bigcup_{j\in J_f} \overline{\Upsilon_j} = \overline{\Gamma}$.

(H4) $k_m^\alpha(\mathbf{x},s)$ (resp. $k_f^\alpha(\mathbf{x},s)$) $\in [k_{\min}, k_{\max}]$ for $(\mathbf{x},s) \in \Omega \times [0,1]$ (resp. $(\mathbf{x},s) \in \Gamma \times [0,1]$), $k_{\max} \geq k_{\min} > 0$ and $k_m^\alpha(\cdot,s)$ (resp. $k_f^\alpha(\cdot,s)$) measurable, $k_m^\alpha(\mathbf{x},\cdot)$ (resp. $k_f^\alpha(\mathbf{x},\cdot)$) continuous, $\alpha = 1,2$.

(H5) $p_{\rm ini} \in V$, $h_m^\alpha \in L^2(\Omega \times (0,T))$, $h_f^\alpha \in L^2(\Gamma \times (0,T))$, $\alpha = 1,2$.

Assumptions (H1-H5) are quite general, except for $k_{\min} > 0$ of hypothesis (H4). This assumption is needed in the mathematical part of this Chapter. Remark that it is not needed in the implementation of the numerical scheme and will be dropped in the numerical section. The influence of this parameter has already been studied numerically in [35]. The hypothesis (H3) that the functions $S_m^1(\mathbf{x},p)$ and $S_f^1(\mathbf{x},p)$ are defined by given functions in a partition of the domain is classical and the index j corresponds to the so called geological rocktypes.

2.3 Vertex Approximate Gradient Discretization

Let us consider the generalised polyhedral mesh of Definition 1.4.1 introduced in Subsection 1.4 as well as the VAG discretization of Subsection 1.4.1. Using the same notations, let us define the $\mathbb{P}_1$ conforming finite element approximation of the space V by

$$V_{\mathcal{T}} = \{\Pi_{\mathcal{T}} v, v \in X_{\mathcal{D}}\} \subset V$$

and its subspace with homogeneous Dirichlet boundary conditions on $\partial\Omega$ by

$$V_{\mathcal{T}}^0 = \{\Pi_{\mathcal{T}} v, v \in X_{\mathcal{D}}^0\} = V_{\mathcal{T}} \cap V^0.$$

The nodal basis of $V_{\mathcal{T}}$ will be denoted by η_K, $\eta_{\mathbf{s}}$, η_σ, for $K \in \mathcal{M}$, $\mathbf{s} \in \mathcal{V}$, $\sigma \in \mathcal{F}_\Gamma$.

The VAG discretization uses the finite element gradient operators $\nabla_{\mathcal{D}_m}$ in the matrix domain and $\nabla_{\mathcal{D}_f}$ in the fracture network introduced in (1.14) as well as the function reconstruction operators $\Pi_{\mathcal{D}_m}$ in the matrix domain (resp. $\Pi_{\mathcal{D}_f}$ in the fracture network) based on partitions of the cells (resp. the fracture faces) as defined in (1.15).

It is important to notice that in the particular case when the space discretization is conforming with respect to the sets $(\Omega_j)_{j\in J_m}$,$(\Gamma_j)_{j\in J_f}$ and when the source term h_m^α (resp. h_f^α) is a cellwise (resp. facewise) constant function, the implementation of the

VAG scheme does not require to build these partitions. In that case, it is sufficient to define the matrix volume fractions

$$\alpha_{K,\mathbf{s}} = \frac{\int_{\omega_{K,\mathbf{s}}} d\mathbf{x}}{\int_K d\mathbf{x}}, \mathbf{s} \in \mathcal{V}_K \cap \mathcal{V}_{int}, K \in \mathcal{M},\ \alpha_{K,\sigma} = \frac{\int_{\omega_{K,\sigma}} d\mathbf{x}}{\int_K d\mathbf{x}}, \sigma \in \mathcal{F}_K \cap \mathcal{F}_\Gamma, K \in \mathcal{M},$$

constrained to satisfy $\alpha_{K,\mathbf{s}} \geq 0$, $\alpha_{K,\sigma} \geq 0$, and $\sum_{\mathbf{s}\in\mathcal{V}_K\cap\mathcal{V}_{int}} \alpha_{K,\mathbf{s}} + \sum_{\sigma\in\mathcal{F}_K\cap\mathcal{F}_\Gamma} \alpha_{K,\sigma} \leq 1$, as well as the fracture volume fractions

$$\alpha_{\sigma,\mathbf{s}} = \frac{\int_{\Sigma_{\sigma,\mathbf{s}}} d\tau_f(\mathbf{x})}{\int_\sigma d\tau_f(\mathbf{x})}, \mathbf{s} \in \mathcal{V}_\sigma \cap \mathcal{V}_{int}, \sigma \in \mathcal{F}_\Gamma,$$

constrained to satisfy $\alpha_{\sigma,\mathbf{s}} \geq 0$, and $\sum_{\mathbf{s}\in\mathcal{V}_\sigma\cap\mathcal{V}_{int}} \alpha_{\sigma,\mathbf{s}} \leq 1$. The convergence of the VAG scheme will be shown to hold whatever the choice of these partitions or volume fractions. As will be detailed in the numerical section, this flexibility is a crucial asset, compared with usual CVFE approaches, in order to improve the accuracy of the scheme for highly heterogeneous test cases.

In addition to Lemma 1.4.1 and Proposition 1.4.1, we state without proof a Lemma that can be readily adapted from [16] noticing that the shape regularity of $\mathcal{T}$ implies the shape regularity of the triangular submesh of Γ defined by $\mathcal{T} \cap \Gamma$.

Lemma 2.3.1 *There exist $C_1, C_2 > 0$ depending only on $\theta_\mathcal{T}$ such that for all $u \in X_\mathcal{D}$*

$$\|\Pi_{\mathcal{D}_m} u\|_{\mathrm{L}^2(\Omega)} \leq C_1 \|\Pi_\mathcal{T} u\|_{\mathrm{L}^2(\Omega)} \quad \text{and} \quad \|\Pi_{\mathcal{D}_f} u\|_{\mathrm{L}^2(\Gamma)} \leq C_2 \|\gamma\Pi_\mathcal{T} u\|_{\mathrm{L}^2(\Gamma)}. \tag{2.2}$$

The VAG scheme has been introduced for the discretization of multiphase immiscible Darcy flows in [36] and in [32] for compositional models. Its convergence has been proved for two-phase flows using a global pressure formulation in [16]. In [35] it has been adapted to take into account discontinuous capillary pressures using a phase pressures formulation and the convergence proof is done in the general framework of gradient schemes. We extend here this approach to the case of hybrid dimensional two-phase Darcy flows.

For $N \in \mathbb{N}^*$, let us consider the time discretization $t^0 = 0 < t^1 < \cdots < t^{n-1} < t^n \cdots < t^N = T$ of the time interval $[0, T]$. We denote the time steps by $\Delta t^n = t^n - t^{n-1}$ for all $n = 1, \cdots, N$ while Δt stands for the whole sequence $(\Delta t^n)_{n=1,\ldots,N}$.

Let us denote by $u^{\alpha,n} \in X^0_\mathcal{D}$, $\alpha = 1, 2$ the discrete phase pressures, and by $p^n = u^{1,n} - u^{2,n}$ the discrete capillary pressure at time t^n for all $n = 1, \cdots, N$. Given an approximation $p^0 \in X_\mathcal{D}$ of the initial capillary pressure p_{ini}, the VAG discretization of the two-phase Darcy flow model in phase pressures formulation (2.1) looks for $u^\alpha = \left(u^{\alpha,n} \in X^0_\mathcal{D}\right)_{n=1,\cdots,N}$, $\alpha = 1, 2$, such that for $\alpha = 1, 2$, and for all $v \in X^0_\mathcal{D}$ one has

$$\int_\Omega \phi_m \frac{S^{\alpha,n}_{\mathcal{D}_m} - S^{\alpha,n-1}_{\mathcal{D}_m}}{\Delta t^n} \Pi_{\mathcal{D}_m} v \, d\mathbf{x} + \int_\Omega k^{\alpha,n}_{\mathcal{D}_m} \Lambda_m \nabla_{\mathcal{D}_m} u^{\alpha,n} \cdot \nabla_{\mathcal{D}_m} v \, d\mathbf{x}$$

$$+ \int_\Gamma \phi_f \frac{S^{\alpha,n}_{\mathcal{D}_f} - S^{\alpha,n-1}_{\mathcal{D}_f}}{\Delta t^n} \Pi_{\mathcal{D}_f} v \, d\tau_f(\mathbf{x}) + \int_\Gamma k^{\alpha,n}_{\mathcal{D}_f} \Lambda_f \nabla_{\mathcal{D}_f} u^{\alpha,n} \cdot \nabla_{\mathcal{D}_f} v \, d\tau_f(\mathbf{x}) \tag{2.3}$$

$$= \frac{1}{\Delta t^n} \int_{t^{n-1}}^{t^n} \Big(\int_\Omega h^\alpha_m \Pi_{\mathcal{D}_m} v \, d\mathbf{x} + \int_\Gamma h^\alpha_f \Pi_{\mathcal{D}_f} v \, d\tau_f(\mathbf{x}) \Big) dt,$$

where the saturations and relative permeabilities are discretized using the piecewise constant reconstruction operators

$$S^{\alpha,n}_{\mathcal{D}_m}(\mathbf{x}) = S^\alpha_m(\mathbf{x}, \Pi_{\mathcal{D}_m} p^n(\mathbf{x})), \;\; S^{\alpha,n}_{\mathcal{D}_f}(\mathbf{x}) = S^\alpha_f(\mathbf{x}, \Pi_{\mathcal{D}_f} p^n(\mathbf{x})),$$

and

$$k^{\alpha,n}_{\mathcal{D}_m}(\mathbf{x}) = k^\alpha_m(\mathbf{x}, S^{\alpha,n}_{\mathcal{D}_m}(\mathbf{x})), \;\; k^{\alpha,n}_{\mathcal{D}_f}(\mathbf{x}) = k^\alpha_f(\mathbf{x}, S^{\alpha,n}_{\mathcal{D}_f}(\mathbf{x})),$$

in order to capture the discontinuities at different rocktype interfaces.

2.4 Convergence Analysis

2.4.1 A priori estimates

Using the phase pressures as test functions in the discrete variational formulation (2.3), we deduce the following a priori estimate.

Lemma 2.4.1 *Assuming that hypotheses* (H1 − H5) *hold, let* u^α, $\alpha = 1, 2$, *be a solution to* (2.3), *then, there exists* $C_5 > 0$ *depending only on the data and on* $\theta_\mathcal{T}$ *such that*

$$\sum_{\alpha=1,2} \sum_{n=1}^{N} \Delta t^n \|\Pi_\mathcal{T} u^{\alpha,n}\|^2_V \leq C_5. \tag{2.4}$$

Let us introduce the following notations. For all $v \in X_\mathcal{D}$ we define the terms

$$A^{\alpha,n}_{\mathcal{D}_m}(v) = \int_\Omega \phi_m \frac{S^{\alpha,n}_{\mathcal{D}_m} - S^{\alpha,n-1}_{\mathcal{D}_m}}{\Delta t^n} \Pi_{\mathcal{D}_m} v \, d\mathbf{x}, \qquad A^{\alpha,n}_{\mathcal{D}_f}(v) = \int_\Gamma \phi_f \frac{S^{\alpha,n}_{\mathcal{D}_f} - S^{\alpha,n-1}_{\mathcal{D}_f}}{\Delta t^n} \Pi_{\mathcal{D}_f} v \, d\tau_f(\mathbf{x}) \tag{2.5}$$

$$B^{\alpha,n}_{\mathcal{D}_m}(v) = \int_\Omega k^{\alpha,n}_{\mathcal{D}_m} \Lambda_m \nabla_{\mathcal{D}_m} u^{\alpha,n} \cdot \nabla_{\mathcal{D}_m} v \, d\mathbf{x}, \qquad B^{\alpha,n}_{\mathcal{D}_f}(v) = \int_\Gamma k^{\alpha,n}_{\mathcal{D}_f} \Lambda_f \nabla_{\mathcal{D}_f} u^{\alpha,n} \cdot \nabla_{\mathcal{D}_f} v \, d\tau_f(\mathbf{x}) \tag{2.6}$$

$$C^{\alpha,n}_{\mathcal{D}_m}(v) = \frac{1}{\Delta t^n} \int_{t^{n-1}}^{t^n} \int_\Omega h^\alpha_m \Pi_{\mathcal{D}_m} v \, d\mathbf{x} dt, \qquad C^{\alpha,n}_{\mathcal{D}_f}(v) = \frac{1}{\Delta t^n} \int_{t^{n-1}}^{t^n} \int_\Gamma h^\alpha_f \Pi_{\mathcal{D}_f} v \, d\tau_f(\mathbf{x}) dt. \tag{2.7}$$

In order to prove Lemma 2.4.1, we first derive some estimates of the accumulation, gradient and right hand side terms of in the following propositions.

Firstly, the following estimate of the accumulation terms is a straightforward adaptation from Lemma 3.1 of [35].

Proposition 2.4.1 *Let u^α, $\alpha = 1, 2$, be a solution of (2.3), then*

$$\sum_{n=1}^{N} \sum_{\alpha=1,2} \sum_{j=m,f} \Delta t^n A_{\mathcal{D}_j}^{\alpha,n}(u^{\alpha,n}) \geq -\frac{\phi_{\max} L_S}{2} \Big(\|\Pi_{\mathcal{D}_m} p^0\|_{L^2(\Omega)}^2 + d_{\max} \|\Pi_{\mathcal{D}_f} p^0\|_{L^2(\Gamma)}^2 \Big).$$

Secondly, thanks to the assumptions (H2) and (H4) the following estimate readily holds for the gradient terms.

Proposition 2.4.2 *Let u^α, $\alpha = 1, 2$, be a solution of (2.3), then*

$$\sum_{n=1}^{N} \sum_{j=m,f} \Delta t^n B_{\mathcal{D}_j}^{\alpha,n}(u^{\alpha,n}) \geq k_{\min} \sum_{n=1}^{N} \Delta t^n \Big(\underline{\lambda}_m \|\nabla_{\mathcal{D}_m} u^{\alpha,n}\|_{L^2\Omega)^d}^2 + \underline{d}_f \underline{\lambda}_f \|\nabla_{\mathcal{D}_f} u^{\alpha,n}\|_{L^2(\Gamma)^{d-1}}^2 \Big),$$

for all $\alpha = 1, 2$.

Thirdly, we have the following straightforward estimate for the right hand side.

Proposition 2.4.3 *Let u^α, $\alpha = 1, 2$, be a solution of (2.3), then there exists $C > 0$ depending only on $d_{\max}$, C_P and $\theta_{\mathcal{T}}$ such that*

$$\sum_{n=1}^{N} \sum_{j=m,f} \Delta t^n C_{\mathcal{D}_j}^{\alpha,n}(u^{\alpha,n}) \leq C \Big(\|h_m^\alpha\|_{L^2(\Omega\times(0,T))}^2 + d_{\max} \|h_f^\alpha\|_{L^2(\Gamma\times(0,T))}^2 \Big)^{1/2} \Big(\sum_{n=1}^{N} \Delta t^n \|\Pi_{\mathcal{T}} u^{\alpha,n}\|_V^2 \Big)^{1/2}$$

for all $\alpha = 1, 2$.

Proof of Lemma 2.4.1: To complete the proof of Lemma 2.4.1, it follows from (2.3) that

$$\sum_{n=1}^{N} \sum_{\alpha=1,2} \sum_{j=m,f} \Delta t^n \Big(A_{\mathcal{D}_j}^{\alpha,n}(u^{\alpha,n}) + B_{\mathcal{D}_j}^{\alpha,n}(u^{\alpha,n}) - C_{\mathcal{D}_j}^{\alpha,n}(u^{\alpha,n}) \Big) = 0,$$

so that in view of Propositions 2.4.1, 2.4.2 and 2.4.3 there exists $C > 0$ depending only on the data and on $\theta_{\mathcal{T}}$ such that

$$\sum_{\alpha=1,2} \sum_{n=1}^{N} \Delta t^n \|\Pi_{\mathcal{T}} u^{\alpha,n}\|_V^2 \leq C \left(1 + \left(\sum_{\alpha=1,2} \sum_{n=1}^{N} \Delta t^n \|\Pi_{\mathcal{T}} u^{\alpha,n}\|_V^2 \right)^{1/2} \right).$$

The estimate (2.4) is then obtained using Young's inequality. □

Lemma 2.4.2 *Assuming that hypotheses* (H1−H5) *hold, there exists at least one solution to the problem* (2.3).

Proof: Let us consider the functions $S_m^{1,\theta} = \theta S_m^1 + (1-\theta)$ and $S_f^{1,\theta} = \theta S_f^1 + (1-\theta)$ instead of S_m^1 and S_f^1 as well as the functions $S_m^{2,\theta} = 1 - S_m^{1,\theta}$ and $S_f^{2,\theta} = 1 - S_f^{1,\theta}$ instead of S_m^2 and S_f^2. The problem corresponding to $\theta = 0$ reads : For each $\alpha = 1, 2$ and for each $n = 1, \ldots, N$ find $u^{\alpha,n} \in X_{\mathcal{D}}^0$ satisfying

$$\left\{ \begin{array}{l} \displaystyle\int_\Omega k_m^1(\mathbf{x},1)\Lambda_m \nabla_{\mathcal{D}_m} u^{1,n} \cdot \nabla_{\mathcal{D}_m} v \; d\mathbf{x} + \int_\Gamma k_f^1(\mathbf{x},1)\Lambda_f \nabla_{\mathcal{D}_f} u^{1,n} \cdot \nabla_{\mathcal{D}_f} v \; d\tau_f(\mathbf{x}) \\ \qquad \displaystyle = \frac{1}{\Delta t^n} \int_{t^{n-1}}^{t^n} \Big(\int_\Omega h_m^1 v \; d\mathbf{x} + \int_\Gamma h_f^1 \Pi_{\mathcal{D}_f} v \; d\tau_f(\mathbf{x}) \Big) dt \quad \forall v \in X_{\mathcal{D}}^0, \\ \displaystyle\int_\Omega k_m^2(\mathbf{x},0)\Lambda_m \nabla_{\mathcal{D}_m} u^{2,n} \cdot \nabla_{\mathcal{D}_m} v \; d\mathbf{x} + \int_\Gamma k_f^2(\mathbf{x},0)\Lambda_f \nabla_{\mathcal{D}_f} u^{2,n} \cdot \nabla_{\mathcal{D}_f} v \; d\tau_f(\mathbf{x}) \\ \qquad \displaystyle = \frac{1}{\Delta t^n} \int_{t^{n-1}}^{t^n} \Big(\int_\Omega h_m^2 v \; d\mathbf{x} + \int_\Gamma h_f^2 \Pi_{\mathcal{D}_f} v \; d\tau_f(\mathbf{x}) \Big) dt \quad \forall v \in X_{\mathcal{D}}^0. \end{array} \right. \tag{2.8}$$

In view of Lemma 2.3.1 and the assumptions on the data one deduces from Lax-Milgram theorem the existence and uniqueness of the solution to (2.8). We remark that the estimate (2.4) holds for all $\theta \in [0,1]$. Therefore the existence of a solution for all $\theta \in [0,1]$ can be deduced from a classical topological degree argument. □

2.4.2 Estimates on the time and space translates

Proposition 2.4.4 *Let $T > 0$, $N \in \mathbb{N}$ and $(t^n)_{n=0,\ldots,N} \in \mathbb{R}$ such that $0 = t^0 < t_1 < \ldots < t^N = T$. Let v be a piecewise constant mapping from $[0,T]$ to some space X (endowed with a semi-norm $\|\cdot\|_X$) such that $v(0) = v^0$ and $v(t) = v^n$ for all $t \in (t^{n-1}, t^n]$. Then,*

$$\int_0^{T-\tau} \|v(t+\tau) - v(t)\|_X \leq \tau \sum_{n=1}^N \|v^n - v^{n-1}\|_X \qquad \forall \tau \in [0,T].$$

Proof: For all $t \in [0,T]$ we set

$$n_{\Delta t}(t) = \left\{ \begin{array}{ll} 0 & \text{if} \quad t = 0, \\ n & \text{if} \quad t \in (t_{n-1}, t_n], \end{array} \right.$$

so that

$$\int_0^{T-\tau} \|v(t+\tau) - v(t)\|_X dt \leq \int_0^{T-\tau} \sum_{k=n_{\Delta t}(t)+1}^{n_{\Delta t}(t+\tau)} \|v^k - v^{k-1}\|_X dt.$$

We conclude the proof by applying Lemma 6.1 of [4]. □

Let us set $X_{\mathcal{D},\Delta t} = (X_{\mathcal{D}})^N$, and for all $v = (v^n)_{n=1,\cdots,N} \in X_{\mathcal{D},\Delta t}$ let us define

$$\Pi_{\mathcal{D}_m,\Delta t} v(\mathbf{x},t) = \Pi_{\mathcal{D}_m} v^n(\mathbf{x}) \text{ for all } (\mathbf{x},t) \in \Omega \times (t^{n-1},t^n],$$
$$\Pi_{\mathcal{D}_f,\Delta t} v(\mathbf{x},t) = \Pi_{\mathcal{D}_f} v^n(\mathbf{x}) \text{ for all } (\mathbf{x},t) \in \Gamma \times (t^{n-1},t^n],$$
$$\Pi_{\mathcal{T},\Delta t} v(\mathbf{x},t) = \Pi_{\mathcal{T}} v^n(\mathbf{x}) \text{ for all } (\mathbf{x},t) \in \Omega \times (t^{n-1},t^n].$$

We also define the functions

$$S^\alpha_{\mathcal{D}_m,\Delta t}(\mathbf{x},t) = S^\alpha(\mathbf{x}, \Pi_{\mathcal{D}_m,\Delta t} p(\mathbf{x},t)),$$
$$S^\alpha_{\mathcal{D}_f,\Delta t}(\mathbf{x},t) = S^\alpha(\mathbf{x}, \Pi_{\mathcal{D}_f,\Delta t} p(\mathbf{x},t)).$$

Lemma 2.4.3 *Assuming that hypotheses* (H1 − H5) *hold, let* u^α, $\alpha = 1,2$, *be a solution to* (2.3), *then there exists* $C > 0$ *only depending on the data and on* $\theta_{\mathcal{T}}$ *such that for all* $\tau > 0$ *one has*

$$\sum_{\alpha=1,2} \|S^\alpha_{\mathcal{D}_m,\Delta t}(\cdot,\cdot+\tau) - S^\alpha_{\mathcal{D}_m,\Delta t}\|^2_{L^2(\Omega\times(0,T))} + \|S^\alpha_{\mathcal{D}_f,\Delta t}(\cdot,\cdot+\tau) - S^\alpha_{\mathcal{D}_f,\Delta t}\|^2_{L^2(\Gamma\times(0,T))} \le C\sqrt{\tau},$$

where we have set $S^\alpha_{\mathcal{D}_m,\Delta t}(\mathbf{x},t) = S^\alpha_{\mathcal{D}_f,\Delta t}(\mathbf{x},t) = 0$ *for all* $t > T$.

Proof: Let us denote by U the space $L^2(\Omega) \times L^2(\Gamma)$ equipped with the scalar product $\langle u, v\rangle_U = \int_\Omega \phi_m u_m v_m d\mathbf{x} + \int_\Gamma \phi_f u_f v_f d\tau_f(\mathbf{x})$. For all $u = (u_m, u_f) \in U$ we also define the dual semi-norm $\|u\|_{-1,\mathcal{D}}$ by

$$\|u\|_{-1,\mathcal{D}} = \sup_{v\in X^0_{\mathcal{D}}, v\neq 0} \frac{\langle u, (\Pi_{\mathcal{D}_m} v, \Pi_{\mathcal{D}_f} v)\rangle_U}{\|\Pi_{\mathcal{T}} v\|_V}.$$

Setting $S^{\alpha,n}_{\mathcal{D}} = (S^{\alpha,n}_{\mathcal{D}_m}, S^{\alpha,n}_{\mathcal{D}_f}) \in U$, and using the assumptions (H_1), (H_2), (H_4), (H_5) on the data, we deduce from (2.3) that there exists $C > 0$ depending only on the data and on $\theta_{\mathcal{T}}$ such that

$$\left|\frac{1}{\Delta t^n}\langle S^{\alpha,n}_{\mathcal{D}} - S^{\alpha,n-1}_{\mathcal{D}}, (\Pi_{\mathcal{D}_m} v, \Pi_{\mathcal{D}_f} v)\rangle_U\right|$$
$$\le C\Big(\|\Pi_{\mathcal{T}} u^{\alpha,n}\|_V + \frac{1}{\Delta t^n}\int_{t^{n-1}}^{t^n} (\|h_m(.,t)\|_{L^2(\Omega)} + \|h_f(.,t)\|_{L^2(\Gamma)})dt\Big)\|\Pi_{\mathcal{T}} v\|_V$$

for all $v \in X^0_{\mathcal{D}}$. Therefore, one obtains the estimate

$$\frac{1}{\Delta t^n}\|S^{\alpha,n}_{\mathcal{D}} - S^{\alpha,n-1}_{\mathcal{D}}\|_{-1,\mathcal{D}} \le C\Big(\|\Pi_{\mathcal{T}} u^{\alpha,n}\|_V + \frac{1}{\Delta t^n}\int_{t^{n-1}}^{t^n} (\|h_m(.,t)\|_{L^2(\Omega)} + \|h_f(.,t)\|_{L^2(\Gamma)})dt\Big).$$

Multiplying by Δt^n, summing over $n = 1,\ldots,N$, and using Lemma 2.4.1, there exists $C > 0$ depending only on the data and on $\theta_{\mathcal{T}}$ such that

$$\sum_{n=1}^N \|S^{\alpha,n}_{\mathcal{D}} - S^{\alpha,n-1}_{\mathcal{D}}\|_{-1,\mathcal{D}} \le C. \tag{2.9}$$

Next setting $p = u^1 - u^2$ and $S^{\alpha,n}_{\mathcal{D},\Delta t} = (S^\alpha_{\mathcal{D}_m,\Delta t}, S^\alpha_{\mathcal{D}_f,\Delta t}) \in L^2(U \times (0,T))$ we have

$$\begin{aligned}
&\int_0^T \|S^\alpha_{\mathcal{D},\Delta t}(t+\tau) - S^\alpha_{\mathcal{D},\Delta t}(t)\|_U dt \\
&\leq \sqrt{L_S} \int_0^T \|S^\alpha_{\mathcal{D},\Delta t}(t+\tau) - S^\alpha_{\mathcal{D},\Delta t}(t)\|^{1/2}_{-1,\mathcal{D}} \, \|\Pi_{\mathcal{T},\Delta t} p(t+\tau) - \Pi_{\mathcal{T},\Delta t} p(t)\|^{1/2}_V dt \\
&\leq \frac{\sqrt{L_S}}{2\sqrt{\tau}} \int_0^T \|S^\alpha_{\mathcal{D},\Delta t}(t+\tau) - S^\alpha_{\mathcal{D},\Delta t}(t)\|_{-1,\mathcal{D}} dt + \frac{\sqrt{L_S}\sqrt{\tau}}{2} \int_0^T \|\Pi_{\mathcal{T},\Delta t} p(t+\tau) - \Pi_{\mathcal{T},\Delta t} p(t)\|_V dt.
\end{aligned}$$

In view of Proposition 2.4.4, the estimates (2.9), Lemma 2.4.1, and the assumption (H_3), there exists $C > 0$ depending only on the data and on $\theta_{\mathcal{T}}$ such that

$$\frac{\sqrt{L_S}}{2\sqrt{\tau}} \int_0^T \|S^\alpha_{\mathcal{D},\Delta t}(t+\tau) - S^\alpha_{\mathcal{D},\Delta t}(t)\|_{-1,\mathcal{D}} dt \leq C\sqrt{\tau},$$

and

$$\int_0^T \|\Pi_{\mathcal{T},\Delta t} p(t+\tau) - \Pi_{\mathcal{T},\Delta t} p(t)\|_V dt \leq C,$$

which implies that

$$\int_0^T \|S^\alpha_{\mathcal{D},\Delta t}(t+\tau) - S^\alpha_{\mathcal{D},\Delta t}(t)\|_U dt \leq C\sqrt{\tau}$$

with $C > 0$ depending only on the data and on $\theta_{\mathcal{T}}$. One concludes the proof using $0 \leq S^\alpha_m, S^\alpha_f \leq 1$. $\square$

Lemma 2.4.4 *It is assumed that hypotheses* $(\mathrm{H1} - \mathrm{H5})$ *hold. Let* $(\mathcal{D}^{(m)}, \Delta t^{(m)})_{m\in\mathbb{N}}$ *be a sequence of space-time discretizations such that there exists a positive constant* θ *satisfying* $\theta_{\mathcal{T}^{(m)}} \leq \theta$ *for all* $m \in \mathbb{N}$ *and such that* $h_{\mathcal{T}^{(m)}} \to 0$ *as* $m \to \infty$. *Let* $u^{\alpha,(m)}$, $S^\alpha_{\mathcal{D}_m^{(m)},\Delta t^{(m)}}$ *and* $S^\alpha_{\mathcal{D}_f^{(m)},\Delta t^{(m)}}$, $\alpha = 1, 2$, *be such that* (2.3) *holds for all* $m \in \mathbb{N}$.

1. *Let* $\xi \in \mathbb{R}^d$ *and*

$$T_m^{(m)}(\xi) = \sum_{\alpha=1,2} \|S^\alpha_{\mathcal{D}_m^{(m)},\Delta t^{(m)}}(\cdot + \xi, \cdot) - S^\alpha_{\mathcal{D}_m^{(m)},\Delta t^{(m)}}\|_{L^2(\mathbb{R}^d\times(0,T))},$$

   where $S^\alpha_{\mathcal{D}_m^{(m)},\Delta t^{(m)}}$ *is extended by 0 on* $\left(\mathbb{R}^d \backslash \overline{\Omega}\right) \times (0,T)$. *Then,* $\lim_{|\xi|\to 0} \sup_{m\in\mathbb{N}} T_m^{(m)}(\xi) = 0$.

2. *For all* $i \in I$ *let* $\tau(\mathcal{P}_i)$ *denote the vector subspace tangent to* $\mathcal{P}_i$, *let* $\xi \in \tau(\mathcal{P}_i)$, *and let us set*

$$T_f^{(m)}(\xi) = \sum_{\alpha=1,2} \|S^\alpha_{\mathcal{D}_{f,i}^{(m)},\Delta t^{(m)}}(\cdot + \xi, \cdot) - S^\alpha_{\mathcal{D}_{f,i}^{(m)},\Delta t^{(m)}}\|_{L^2(\mathcal{P}_i\times(0,T))},$$

   where $S^\alpha_{\mathcal{D}_{f,i}^{(m)},\Delta t^{(m)}}$ *denotes the restriction of* $S^\alpha_{\mathcal{D}_f^{(m)},\Delta t^{(m)}}$ *to* Γ_i, *extended by 0 on* $\left(\mathcal{P}_i \setminus \overline{\Gamma}_i\right) \times (0,T)$. *Then one has* $\lim_{|\xi|\to 0} \sup_{m\in\mathbb{N}} T_f^{(m)}(\xi) = 0$

Proof: For each $i \in I$ and for all $\xi \in \tau(\mathcal{P}_i)$ let us define the set $\Gamma_i^\xi = \{\mathbf{x} \in \Gamma_i, \mathbf{x}+\xi \in \Gamma_i\}$. Since $0 \leq S^\alpha_{\mathcal{D}_{f,i}} \leq 1$ there exists a positive C depending only on the geometry of Γ_i and on T such that

$$\|S^\alpha_{\mathcal{D}^{(m)}_{f,i},\Delta t^{(m)}}(\cdot+\xi,\cdot)-S^\alpha_{\mathcal{D}^{(m)}_{f,i},\Delta t^{(m)}}\|^2_{L^2(\Gamma_i\times(0,T))} \leq C|\xi|+\|S^\alpha_{\mathcal{D}^{(m)}_{f,i},\Delta t^{(m)}}(\cdot+\xi,\cdot)-S^\alpha_{\mathcal{D}^{(m)}_{f,i},\Delta t^{(m)}}\|^2_{L^2(\Gamma_i^\xi\times(0,T))}.$$

Denoting by $\Pi_{\mathcal{D}^{(m)}_{f,i},\Delta t^{(m)}}p^{(m)}$ the restriction of $\Pi_{\mathcal{D}^{(m)}_{f},\Delta t^{(m)}}p^{(m)}$ to Γ_i, one deduces from Lemma 1.4.1 and Lemma 2.4.1 that

$$\begin{aligned}
&\|S^\alpha_{\mathcal{D}^{(m)}_{f,i},\Delta t^{(m)}}(\cdot+\xi,\cdot) - S^\alpha_{\mathcal{D}^{(m)}_{f,i},\Delta t^{(m)}}\|_{L^2(\Gamma_i^\xi\times(0,T))} \\
&\qquad \leq L_S\|\Pi_{\mathcal{D}^{(m)}_{f,i},\Delta t^{(m)}}p^{(m)}(\cdot+\xi,\cdot) - \Pi_{\mathcal{D}^{(m)}_{f,i},\Delta t^{(m)}}p^{(m)}\|_{L^2(\Gamma_i^\xi\times(0,T))} \\
&\qquad \leq L_S\|\gamma_i\Pi_{\mathcal{T}^{(m)},\Delta t^{(m)}}p^{(m)}(\cdot+\xi,\cdot) - \gamma_i\Pi_{\mathcal{T}^{(m)},\Delta t^{(m)}}p^{(m)}\|_{L^2(\Gamma_i^\xi\times(0,T))} + 2L_SC_3\sqrt{C_5}h_{\mathcal{T}^{(m)}}.
\end{aligned}$$

Therefore, using Lemma 4.0.7 stated in the Appendix and Lemma B.2 of [34], we deduce that

$$\lim_{\xi\to 0}\sup_{m\in\mathbb{N}}\|S^\alpha_{\mathcal{D}^{(m)}_{f,i},\Delta t^{(m)}}(\cdot+\xi,\cdot) - S^\alpha_{\mathcal{D}^{(m)}_{f,i},\Delta t^{(m)}}\|_{L^2(\mathcal{P}_i\times(0,T))} = 0 \quad \forall i \in I.$$

One proves the first statement of the lemma using similar arguments. □

2.4.3 Convergence

In view of Lemma 2.4.3 and Lemma 2.4.4, the Kolmogorov-Fréchet theorem allows to establish the following relative compactness result for the saturation.

Lemma 2.4.5 *It is assumed that hypotheses* (H1 − H5) *hold. Let* $(\mathcal{D}^{(m)},\Delta t^{(m)})_{m\in\mathbb{N}}$ *be a sequence of space-time discretizations and* $u^{\alpha,(m)}$, $S^\alpha_{\mathcal{D}^{(m)}_m,\Delta t^{(m)}}$, $S^\alpha_{\mathcal{D}^{(m)}_f,\Delta t^{(m)}}$, $\alpha = 1,2$, *be s.t* (2.3) *holds for all* $m \in \mathbb{N}$. *Then, for each* $\alpha = 1,2$ *one has the following result.*

1. *The sequence* $(S^\alpha_{\mathcal{D}^{(m)}_m\Delta t^{(m)}})_{m\in\mathbb{N}}$ *is relatively compact in* $L^2(\Omega\times(0,T))$.
2. *For each* $i \in I$ *the sequence* $(S^\alpha_{\mathcal{D}^{(m)}_{f,i},\Delta t^{(m)}})_{m\in\mathbb{N}}$ *is relatively compact in* $L^2(\Gamma_i\times(0,T))$.

The limit of the saturation can be identified thanks to the following result.

Lemma 2.4.6 *It is assumed that hypotheses* (H1 − H5) *hold. Let* $(\mathcal{D}^{(m)},\Delta t^{(m)})_{m\in\mathbb{N}}$ *be a sequence of space-time discretizations such that there exist two positive constants* θ *and* γ *satisfying* $\theta_{\mathcal{T}^{(m)}} \leq \theta$, $\gamma_{\mathcal{M}^{(m)}} \leq \gamma$ *for all* $m \in \mathbb{N}$ *and such that* $h_{\mathcal{T}^{(m)}}, \max\Delta t^{(m)} \to 0$ *as* $m \to \infty$. *Let* $u^{\alpha,(m)}$, $S^\alpha_{\mathcal{D}^{(m)}_m,\Delta t^{(m)}}$ *and* $S^\alpha_{\mathcal{D}^{(m)}_f,\Delta t^{(m)}}$, $\alpha = 1,2$, *be s.t* (2.3) *holds for all* $m \in \mathbb{N}$. *Then, there exists a function pair* $(\overline{u}^\alpha)_{\alpha=1,2} \in \left(L^2(0,T;V^0)\right)^2$ *such that up to a subsequence*

$$\Pi_{\mathcal{T}^{(m)},\Delta t^{(m)}}u^{\alpha,(m)} \rightharpoonup \overline{u}^\alpha \text{ in } L^2(\Omega\times(0,T)) \quad \text{and} \quad \gamma\Pi_{\mathcal{T}^{(m)},\Delta t^{(m)}}u^{\alpha,(m)} \rightharpoonup \gamma\overline{u}^\alpha \text{ in } L^2(\Gamma\times(0,T))$$

as $m \to \infty$*; moreover setting* $\overline{p} = \overline{u}^1 - \overline{u}^2$*, one has*

$$S^{\alpha}_{\mathcal{D}_m^{(m)},\Delta t^{(m)}} \to S^{\alpha}_m(.,\overline{p}) \text{ in } L^2(\Omega\times(0,T)) \quad \text{and} \quad S^{\alpha}_{\mathcal{D}_f^{(m)},\Delta t^{(m)}} \to S^{\alpha}_f(.,\gamma\overline{p}) \text{ in } L^2(\Gamma\times(0,T))$$

as $m \to \infty$*.*

Proof: The existence of the weak limit $(\overline{u}^{\alpha})_{\alpha=1,2}$ follows from Lemma 2.4.1 and Lemma 4.0.6 stated in the Appendix. In order to prove the second statement we remark that it follows from Lemma 1.4.1 that $\Pi_{\mathcal{D}_m^{(m)},\Delta t^{(m)}} u^{\alpha}$ and $\Pi_{\mathcal{D}_f^{(m)},\Delta t^{(m)}} u^{\alpha}$ also converge weakly to $\overline{u}^{\alpha}$ in $L^2(\Omega\times(0,T))$ and to $\gamma\overline{u}^{\alpha}$ in $L^2(\Gamma\times(0,T)))$ respectively. From Lemma 2.4.5, there exist four functions $\overline{s}^{\alpha}_m \in L^2(\Omega\times(0,T))$ and $\overline{s}^{\alpha}_f \in L^2(\Gamma\times(0,T))$, $\alpha = 1,2$, with $\overline{s}^1_m + \overline{s}^2_m = 1$, $\overline{s}^1_f + \overline{s}^2_f = 1$, such that, up to a subsequence, $S^{\alpha}_{\mathcal{D}_m^{(m)}\Delta t^{(m)}}$ converges strongly to $\overline{s}^{\alpha}_m$ in $L^2(\Omega\times(0,T))$, and $S^{\alpha}_{\mathcal{D}_f^{(m)}\Delta t^{(m)}}$ converges strongly to $\overline{s}^{\alpha}_f$ in $L^2(\Gamma\times(0,T))$. Then, one can conclude the proof using the Minty trick stated in Lemma 3.6 of [35] to show that $\overline{s}^{\alpha}_m = S^{\alpha}_m(.,\overline{u}^1 - \overline{u}^2)$ and $\overline{s}^{\alpha}_f = S^{\alpha}_f(.,\gamma(\overline{u}^1 - \overline{u}^2))$. □

Theorem 2.4.1 *It is assumed that hypotheses* (H1 − H5) *hold. Let* $(\mathcal{D}^{(m)},\Delta t^{(m)})_{m\in\mathbb{N}}$ *be a sequence of space-time discretizations such that there exist two positive constants* θ *and* γ *satisfying* $\theta_{\mathcal{T}^{(m)}} \le \theta$, $\gamma_{\mathcal{M}^{(m)}} \le \gamma$ *for all* $m \in \mathbb{N}$ *and such that* $h_{\mathcal{T}^{(m)}}, \max_n \Delta t^{(m),n} \to 0$ *as* $m \to \infty$*. Let* $u^{\alpha,(m)}$, $S^{\alpha}_{\mathcal{D}_m^{(m)},\Delta t^{(m)}}$ *and* $S^{\alpha}_{\mathcal{D}_f^{(m)},\Delta t^{(m)}}$, $\alpha = 1,2$*, be s.t* (2.3) *holds for all* $m \in \mathbb{N}$*. It is also assumed that* $\Pi_{\mathcal{D}_m^{(m)}} p^{0,(m)}$ *converges strongly to* p^{ini} *in* $L^2(\Omega)$*, and that* $\Pi_{\mathcal{D}_f^{(m)}} p^{0,(m)}$ *converges strongly to* γp^{ini} *in* $L^2(\Gamma)$*. Then there exists a weak solution* $(\overline{u}^1,\overline{u}^2)$ *to the problem* (2.1) *such that for each phase* $\alpha = 1,2$

$$\Pi_{\mathcal{T}^{(m)},\Delta t^{(m)}} u^{\alpha,(m)} \rightharpoonup \overline{u}^{\alpha} \text{ in } L^2(\Omega\times(0,T)) \quad \text{and} \quad \gamma\Pi_{\mathcal{T}^{(m)},\Delta t^{(m)}} u^{\alpha,(m)} \rightharpoonup \gamma\overline{u}^{\alpha} \text{ in } L^2(\Gamma\times(0,T))$$

up to a subsequence.

Proof: For all $\alpha = 1,2$ we denote by $\overline{u}^{\alpha}$ a weak limit of $\Pi_{\mathcal{T}^{(m)},\Delta t^{(m)}} u^{\alpha,(m)}$, whose existence is stated by Lemma 2.4.6. We show below that $(\overline{u}^1,\overline{u}^2)$ satisfies the variational formulation (2.1). In order to simplify the notation we drop the index (m).

Let $\overline{\psi}$ be an arbitrary function from $C^{\infty}_c(\Omega\times[0,T))$ and $\psi(t)$ the projection of $\overline{\psi}(.,t)$ to $X^0_{\mathcal{D}}$ defined by $\psi_{\nu}(t) = \psi(\mathbf{x}_{\nu},t)$ for all $\nu \in \mathcal{M}\cup\mathcal{V}\cup\mathcal{F}_{\Gamma}$. Taking $v = \psi(t^{n-1})$ in (2.3) for all $n = 1,\dots,N$ and summing over $n = 1,\dots,N$ we obtain that

$$\sum_{n=1}^{N}\sum_{j=m,f}\Delta t^n\Big(A^{\alpha,n}_{\mathcal{D}_j}(\psi(t^{n-1})) + B^{\alpha,n}_{\mathcal{D}_j}(\psi(t^{n-1}))\Big) = \sum_{n=1}^{N}\sum_{j=m,f}\Delta t^n C^{\alpha,n}_{\mathcal{D}_j}(\psi(t^{n-1})).$$

for each phase $\alpha = 1,2$.

Accumulation terms. Let us consider the term $\sum_{n=1}^{N}\Delta t^n A^{\alpha,n}_{\mathcal{D}_m}(\psi(t^{n-1}))$. Applying the chain rule we obtain that

$$\sum_{n=1}^{N}\Delta t^n A^{\alpha,n}_{\mathcal{D}_m}(\psi(t^{n-1})) = -\sum_{n=1}^{N}\int_{t^{n-1}}^{t^n}\int_{\Omega}\phi_m\ S^{\alpha,n}_{\mathcal{D}_m}\partial_t\Pi_{\mathcal{D}_m}\psi(t)\ d\mathbf{x}dt - \int_{\Omega}\phi_m\ S^{\alpha,0}_{\mathcal{D}_m}\Pi_{\mathcal{D}_m}\psi(t^0)\ d\mathbf{x}.$$

Thanks to the strong convergence of the function $S^{\alpha}_{\mathcal{D}_m,\Delta t}$ given by Lemma 2.4.6, to the regularity of $\overline{\psi}$, and to the convergence of $\Pi_{\mathcal{D}_m} p^0$, one deduces that

$$\sum_{n=1}^{N} \Delta t^n A^{\alpha,n}_{\mathcal{D}_m}(\psi(t^{n-1})) \to -\int_0^T \int_\Omega \phi_m S^{\alpha}_m(.,\overline{p}) \partial_t \overline{\psi}\ d\mathbf{x}dt - \int_\Omega \phi_m S^{\alpha}_m(.,p_{ini}) \overline{\psi}(\mathbf{x},0)\ d\mathbf{x}dt.$$

Similarly we obtain that

$$\sum_{n=1}^{N} \Delta t^n A^{\alpha,n}_{\mathcal{D}_f}(\psi(t^{n-1})) \to -\int_0^T \int_\Gamma \phi_f S^{\alpha}_f(.,\gamma\overline{p}) \partial_t \gamma\overline{\psi}\ d\tau_f(\mathbf{x})dt - \int_\Gamma \phi_f S^{\alpha}_f(.,\gamma p_{ini}) \gamma\overline{\psi}(\mathbf{x},0)\ d\tau_f(\mathbf{x})dt.$$

Diffusion terms. From Lemma 4.0.6 stated in the Appendix, Proposition 1.4.1, Lemma 2.4.6 and hypothesis (H_4), we deduce that

$$\sum_{n=1}^{N} \Delta t^n B^{\alpha,n}_{\mathcal{D}_m}(\psi(t^{n-1})) \to \int_0^T \int_\Omega k^{\alpha}_m(\mathbf{x}, S^{\alpha}_m(.,\overline{p})) \Lambda_m \nabla \overline{u} \cdot \nabla \overline{\psi}\ d\mathbf{x}$$

and

$$\sum_{n=1}^{N} \Delta t^n B^{\alpha,n}_{\mathcal{D}_f}(\psi(t^{n-1})) \to \int_0^T \int_\Gamma k^{\alpha}_f(\mathbf{x}, S^{\alpha}_f(.,\overline{p})) \Lambda_f \nabla_\tau \gamma\overline{u} \cdot \nabla_\tau \gamma\overline{\psi}\ d\tau_f(\mathbf{x}).$$

Source terms. From Lemma 1.4.1 and Proposition 1.4.1, we deduce that

$$\sum_{n=1}^{N} \Delta t^n C^{\alpha,n}_{\mathcal{D}_m}(\psi(t^{n-1})) = \sum_{n=1}^{N} \int_{t^{n-1}}^{t^n} \int_\Omega h^{\alpha}_m \Pi_{\mathcal{D}_m} \psi(t^{n-1})\ d\mathbf{x}dt \to \int_0^T \int_\Omega h^{\alpha}_m \overline{\psi}\ d\mathbf{x}dt$$

and

$$\sum_{n=1}^{N} \Delta t^n C^{\alpha,n}_{\mathcal{D}_f}(\psi(t^{n-1})) = \sum_{n=1}^{N} \int_{t^{n-1}}^{t^n} \int_\Gamma h^{\alpha}_f \Pi_{\mathcal{D}_f} \psi(t^{n-1})\ d\tau_f(\mathbf{x})dt \to \int_0^T \int_\Gamma h^{\alpha}_f \gamma\overline{\psi}\ d\tau_f(\mathbf{x})dt.$$

□

2.5 Upwind flux formulation

Let us consider the previous two-phase flow model extended to take into account the gravity and with vanishing source terms $h_m = 0$ and $h_f = 0$. We denote by $\mathbf{g}$ the gravity vector, by g its norm and we set on each fracture Γ_i, $i \in I$

$$\mathbf{g}_{\tau_i} = \mathbf{g} - (\mathbf{g} \cdot \mathbf{n}_i^+)\mathbf{n}_i^+.$$

The mass densities of the phases are denoted by ρ^α for $\alpha = 1, 2$. The two-phase flow model with gravity amounts to find formally $u^\alpha \in L^2(0,T;V^0)$, $\alpha = 1,2$, and $(\mathbf{q}^\alpha_m, \mathbf{q}^\alpha_f) \in$

$L^2(0,T;H_\Sigma(\Omega,\Gamma))$ such that one has for $\alpha=1,2$:

$$\left\{\begin{array}{rll}
\phi_m\partial_t\Big(S_m^\alpha(\mathbf{x},p)\Big)+\mathrm{div}(\mathbf{q}_{m,\mathfrak{a}}^\alpha)=0 & \text{on } \Omega_\mathfrak{a},\,\mathfrak{a}\in\mathcal{A}, \\
\phi_f d_f\partial_t\Big(S_f^\alpha(\mathbf{x},\gamma_i p)\Big)+\mathrm{div}_{\tau_i}(\mathbf{q}_{f,i}^\alpha)-[\![\mathbf{q}_m^\alpha\cdot\mathbf{n}_i]\!]=0 & \text{on } \Gamma_i,\,i\in I, \\
-k_m^\alpha(\mathbf{x},S_m^\alpha(\mathbf{x},p))\Lambda_m(\nabla u^\alpha-\rho^\alpha\mathbf{g})=\mathbf{q}_{m,\mathfrak{a}}^\alpha & \text{on } \Omega_\mathfrak{a},\,\mathfrak{a}\in\mathcal{A}, \\
-d_f k_f^\alpha(\mathbf{x},S_f^\alpha(\mathbf{x},\gamma_i p))\Lambda_f(\nabla_{\tau_i}\gamma_i u^\alpha-\rho^\alpha\mathbf{g}_{\tau_i})=\mathbf{q}_{f,i}^\alpha & \text{on } \Gamma_i,\,i\in I, \\
p|_{t=0}=p_{\mathrm{ini}}, & \text{on } \Omega,
\end{array}\right.$$

with $p=u^1-u^2$. In order to improve the stability of the scheme on coarse meshes for convective dominant regimes, the implementation of the VAG or HFV schemes is based on the flux formulation with upwinding of the mobilities rather than on the discrete variational formulation (2.3). We follow the notations introduced for the matrix and fractures fluxes in Subsection 1.4.3 which account both for the VAG and HFV schemes.

The space discretization is assumed to be compatible with the rocktype partitions $(\Omega_j)_{j\in J_m}$ for the matrix domain and $(\Upsilon_j)_{j\in J_f}$ for the fracture networks (see the notations of Assumption (H3)), that is to say, for all $K\in\mathcal{M}$ there exists $j_K\in J_m$ such that $K\subset\Omega_{j_K}$ and for all $\sigma\in\mathcal{F}_\Gamma$ there exists $j_\sigma\in J_f$ such that $\sigma\subset\Upsilon_{j_\sigma}$. In other words, j_K is the unique rocktype of cell K and j_σ is the unique rocktype of the fracture face σ.

The matrix and fracture relative permeabilities are piecewise constant w.r.t. $\mathbf{x}$ on the same partitions of the matrix and fracture network domains as the capillary pressure curves. In the following, we will denote the mobilities (ratio of the phase relative permeability to the phase viscosity) by $k_{m,j}^\alpha(s)$ in the matrix for each rocktype $j\in J_m$ and by $k_{f,j}^\alpha(s)$ in the fracture network for each rocktype $j\in J_f$.

As exhibited in Figure 2.1 for the VAG scheme, the definition of the saturations at the matrix fracture interfaces takes into account the jump of the saturations induced by the different rocktypes. More precisely, for $p^n=u^{1,n}-u^{2,n}\in X_\mathcal{D}^0$, we set for $\alpha=1,2$

$$\left\{\begin{array}{l}
S_K^{\alpha,n}=S_{m,j_K}^\alpha(p_K^n),\ K\in\mathcal{M}, \\
S_{K,\nu}^\alpha=S_{m,j_K}^\alpha(p_\nu^n),\ \nu\in dof_{\partial K},K\in\mathcal{M},
\end{array}\right. \tag{2.10}$$

and

$$\left\{\begin{array}{l}
S_\sigma^{\alpha,n}=S_{f,j_\sigma}^\alpha(p_\sigma^n),\ \sigma\in\mathcal{F}_\Gamma, \\
S_{\sigma,\nu}^{\alpha,n}=S_{f,j_\sigma}^\alpha(p_\nu^n),\ \nu\in dof_{\partial\sigma},\sigma\in\mathcal{F}_\Gamma.
\end{array}\right. \tag{2.11}$$

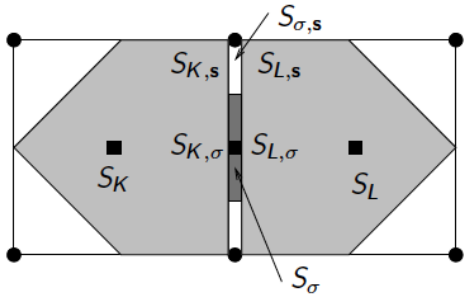

Figure 2.1: For the VAG scheme, saturations inside the cells K and L, the fracture face σ and at the matrix fracture interfaces taking into account the saturation jumps induced by the different rocktypes.

Let us also set

$$\phi_K = (1 - \sum_{\nu \in dof_{\partial K} \setminus dof_{Dir}} \alpha_{K,\nu}) \int_K \phi_m(\mathbf{x}) d\mathbf{x}$$

and

$$\phi_\sigma = (1 - \sum_{\nu \in dof_{\partial \sigma} \setminus dof_{Dir}} \alpha_{\sigma,\nu}) \int_\sigma \phi_f(\mathbf{x}) d\tau_f(\mathbf{x}),$$

as well as

$$\phi_{K,\nu} = \alpha_{K,\nu} \int_K \phi_m(\mathbf{x}) d\mathbf{x}, \ \nu \in dof_{\partial K} \setminus dof_{Dir},$$

and

$$\phi_{\sigma,\nu} = \alpha_{\sigma,\nu} \int_\sigma \phi_f(\mathbf{x}) d\tau_f(\mathbf{x}), \ \nu \in dof_{\partial \sigma} \setminus dof_{Dir}.$$

which correspond to the porous volume distributed to the degrees of freedom or control volumes.

Given $p^0 \in X^0_{\mathcal{D}}$, the VAG or HFV upwind scheme looks for $u^{1,n} \in X^0_{\mathcal{D}}$, $u^{2,n} \in X^0_{\mathcal{D}}$, $n = 1, \cdots, N$, such that for all $\alpha = 1, 2$ and for all $v \in X^0_{\mathcal{D}}$ one has:

$$\left\{ \begin{array}{l} \sum_{K \in \mathcal{M}} \Big(\frac{\phi_K}{\Delta t^n} (S_K^{\alpha,n} - S_K^{\alpha,n-1}) + \sum_{\nu \in dof_{\partial K}} k^\alpha_{m,j_K}(S^{\alpha,n}_{K,\nu,up}) F^\alpha_{K,\nu}(u^{\alpha,n}) \Big) v_K \\ + \sum_{K \in \mathcal{M}} \sum_{\nu \in dof_{\partial K} \setminus dof_{Dir}} \Big(\frac{\phi_{K,\nu}}{\Delta t^n} (S_{K,\nu}^{\alpha,n} - S_{K,\nu}^{\alpha,n-1}) - k^\alpha_{m,j_K}(S^{\alpha,n}_{K,\nu,up}) F^\alpha_{K,\nu}(u^{\alpha,n}) \Big) \ v_\nu \\ + \sum_{\sigma \in \mathcal{F}_\Gamma} \Big(\frac{\phi_\sigma}{\Delta t^n} (S_\sigma^{\alpha,n} - S_\sigma^{\alpha,n-1}) + \sum_{\nu \in dof_{\partial \sigma}} k^\alpha_{f,j_\sigma}(S^{\alpha,n}_{\sigma,\mathbf{s},up}) F^\alpha_{\sigma,\mathbf{s}}(u^{\alpha,n}) \Big) v_\sigma \\ + \sum_{\sigma \in \mathcal{F}_\Gamma} \sum_{\nu \in dof_{\partial \sigma} \setminus dof_{Dir}} \Big(\frac{\phi_{\sigma,\nu}}{\Delta t^n} (S_{\sigma,\nu}^{\alpha,n} - S_{\sigma,\nu}^{\alpha,n-1}) - k^\alpha_{f,j_\sigma}(S^{\alpha,n}_{\sigma,\nu,up}) F^\alpha_{\sigma,\nu}(u^{\alpha,n}) \Big) v_\nu = 0, \end{array} \right. \quad (2.12)$$

with the phase fluxes definition

$$\begin{cases} F^{\alpha}_{K,\nu}(u^{\alpha}) = F_{K,\nu}(u^{\alpha}) + \rho^{\alpha} g F_{K,\nu}(Z),\ \nu \in dof_{\partial K},\ K \in \mathcal{M}, \\ F^{\alpha}_{\sigma,\nu}(u^{\alpha}) = F_{\sigma,\nu}(u^{\alpha}) + \rho^{\alpha} g F_{\sigma,\nu}(Z),\ \nu \in dof_{\partial \sigma},\ \sigma \in \mathcal{F}_{\Gamma}, \end{cases}$$

setting $Z = \Big(z_{\nu}\Big)_{\nu \in dof_{\mathcal{D}}}$, and the upwinding of the mobilities

$$\begin{cases} S^{\alpha,n}_{K,\nu,up} = S^{\alpha,n}_{K} \text{ if } F^{\alpha}_{K,\nu}(u^{\alpha,n}) \geq 0, \\ S^{\alpha,n}_{K,\nu,up} = S^{\alpha,n}_{K,\nu} \text{ if } F^{\alpha}_{K,\nu}(u^{\alpha,n}) < 0, \end{cases} \qquad \begin{cases} S^{\alpha,n}_{\sigma,\nu,up} = S^{\alpha,n}_{\sigma} \text{ if } F^{\alpha}_{\sigma,\nu}(u^{\alpha,n}) \geq 0, \\ S^{\alpha,n}_{\sigma,\nu,up} = S^{\alpha,n}_{\sigma,\nu} \text{ if } F^{\alpha}_{\sigma,\nu}(u^{\alpha,n}) < 0. \end{cases} \tag{2.13}$$

In the following numerical experiments, the volume fractions $\alpha_{K,\nu}$, $\alpha_{\sigma,\nu}$ are chosen to avoid the mixing of the fracture and matrix rocktypes. They are such that $\alpha_{K,\nu} = 0$ if $\nu \in dof_{\partial K}$ belongs to the fracture network Γ, $\alpha_{K,\nu} = \omega_m$ otherwise, and such that $\alpha_{\sigma,\nu} = \omega_f$ for $\nu \in dof_{\partial \sigma}$.

To illustrate the importance of non mixing rocktypes with large permeability contrasts, this choice denoted by VAG-1 (for the VAG scheme) will be compared with a second choice denoted by VAG-2 for which we simply set $\alpha_{K,\nu} = \omega_m$ and $\alpha_{\sigma,\nu'} = \omega_f$ for all $\nu \in dof_{\partial K}, \nu' \in dof_{\partial \sigma}$. In order to roughly balance the volumes, the parameters ω_m and ω_f are set in the following tests to $\omega_m = 0.15$ in 2D and 0.05 in 3D, and to $\omega_f = 0.25$ in 2D and 0.1 in 3D. Figure 2.2 exhibits an example of the control volumes at cells, fracture face and nodes for both the VAG-1 and VAG-2 choices.

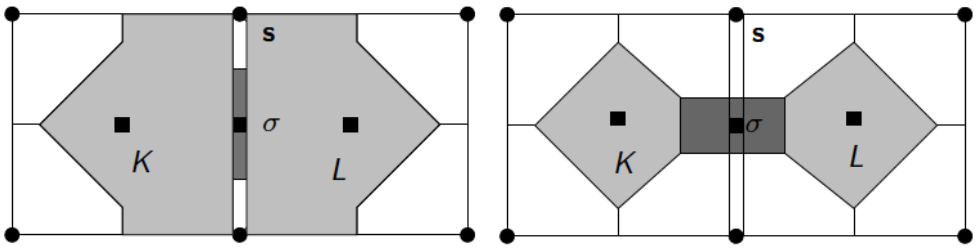

Figure 2.2: For VAG-1 (left) and VAG-2 (right), example of the choices of the control volumes at cells, fracture face, and nodes, in the case of two cells K and L splitted by one fracture face σ (the width of the fracture has been enlarged in this figure).

2.6 Numerical experiments

The nonlinear systems obtained at each time step are solved by a Newton Raphson algorithm. The time stepping is defined by an initial time step, a maximum time step and the following rule: if the Newton solver does not converge after 20 iterations, the time step is chopped by a factor 2 and recomputed. The time step is increased by a factor 1.2 after each successful time step until it reaches the maximum time step. The stopping criteria on the relative residuals are fixed to 10^{-7} for the GMRes solver and to 10^{-6} for the Newton solver. A CPR-AMG right preconditioner [48], [58] is used in the GMRes iterative

solver. Let us also stress that, using the two equations in each cell, the cell unknowns are eliminated from the discrete linearized system at each Newton iteration without any fill-in, reducing the Jacobian system to nodal and fracture face unknowns only.

In the following test cases, the inverse of the capillary pressure monotone graph will be defined by the Corey law

$$S_j^1(p) = \begin{cases} 0 & \text{if } p < p_{ent,j}, \\ (1 - s_{r,j}^2)(1 - e^{\frac{p_{ent,j}-p}{b_j}}) & \text{if } p \geq p_{ent,j}, \end{cases} \tag{2.14}$$

and the mobilities of the two phases are given by the Corey laws

$$k_j^\alpha(\mathbf{x}, s^\alpha) = \begin{cases} 0 & \text{if } \bar{s}^\alpha < 0, \\ \frac{1}{\mu^\alpha} & \text{if } \bar{s}^\alpha > 1, \\ \frac{(\bar{s}^\alpha)^2}{\mu^\alpha} & \text{else,} \end{cases} \tag{2.15}$$

for phase $\alpha = 1$ (oil), and phase $\alpha = 2$ (water) where $\bar{s}^1 = \frac{s^1 - s_{r,j}^1}{1 - s_{r,j}^1 - s_{r,j}^2}$, and $\bar{s}^2 = \frac{s^2 - s_{r,j}^2}{1 - s_{r,j}^2 - s_{r,j}^1}$ are the reduced saturations, $s_{r,j}^1$, $s_{r,j}^2$ are the residual saturations for both phases, $p_{ent,j}$ is the entry pressure, and μ^1, μ^2 are the viscosities of the phases.

2.6.1 Oil migration in a 2D basin with one barrier and a fault

We consider the simulation of the oil migration process, within the 2D cross section $\Omega = (0, L) \times (0, H)$ of a basin with $H = L = 100$ m (see Figure 2.3). Let us denote by (x, y) the Cartesian coordinates of $\mathbf{x}$ and let us define the two points $\mathbf{x}_1 = (50, 50)$ and $\mathbf{x}_2 = (50, 69.177)$. The basin includes an immersed fault $\Gamma = (\mathbf{x}_1, \mathbf{x}_2)$, a barrier $\Omega_2 = \{(x, y) \in \Omega \,|\, 25 + \frac{x}{2} < y < 35 + \frac{x}{2}, x \in (0, 1)\} \setminus \overline{\Gamma}$, and a drain $\Omega_1 = \Omega \setminus (\overline{\Omega}_2 \cup \overline{\Gamma})$. The permeability $\Lambda_m(\mathbf{x})$ is defined by the tensor

$$\Lambda_m(\mathbf{x}) = \lambda_1 \begin{pmatrix} 0.82 & -0.36 \\ -0.36 & 0.28 \end{pmatrix}.$$

for $\mathbf{x} \in \Omega_1$, and by $\Lambda_m(\mathbf{x}) = \frac{\lambda_1}{100}\mathrm{Id}$ for $\mathbf{x} \in \Omega_2$, with $\lambda_1 = 10^{-12}$ m^2. Note that the eigenvalues of $\Lambda_m(\mathbf{x})$ for $\mathbf{x} \in \Omega_1$ are $0.1\lambda_1$ and λ_1 and the corresponding eigenvectors are $(\frac{1}{\sqrt{5}}, \frac{2}{\sqrt{5}})$, $(\frac{2}{\sqrt{5}}, -\frac{1}{\sqrt{5}})$.

The permeability of the fault Γ is defined by $\Lambda_f = 100\lambda_1\mathrm{Id}$ and its width is equal to $d_f = 0.1$ m. The porosity is constant and equal to $\phi_m = \phi_f = 0.1$.

The inverse of the capillary pressure monotone graph in each subdomain $\Omega_j, j = 1, 2$ is exhibited in figure 2.3 and defined by (2.14) with the parameters $p_{ent,1} = 10^5$ Pa, $p_{ent,2} = 2\ 10^5$ Pa, $b_1 = 10^2$ Pa, and $b_2 = 10^4$ Pa, $s_{r,1}^2 = s_{r,2}^2 = 0$. In the matrix $S_m^1(\mathbf{x}, p)$ is equal to $S_1^1(p)$ for $\mathbf{x} \in \Omega_1$, and to $S_2^1(p)$ for $\mathbf{x} \in \Omega_2$. In the fault, the inverse of the capillary pressure is defined by $S_f^1(\mathbf{x}, p) = S_1^1(p)$ for $\mathbf{x} \in \Gamma$. The mobilities of the two phases are given by (2.15) with $\mu^1 = 0.005$ Pa.s and $\mu^2 = 0.001$ Pa.s and $s_r^1 = s_r^2 = 0$ both in the matrix and in the fracture.

The migration occurs by gravity due to the lower density of the oil phase $\rho^1 = 850$ Kg/m^3 compared with the water phase $\rho^2 = 1000$ Kg/m^3. Phase 1 is injected at the bottom boundary $(0, 10) \times \{0\}$ with imposed pressures $u^2 = 8\ 10^6 + \rho^2 g H$ Pa, $u^1 = u^2 + (S_1^1)^{-1}(0.8)$ corresponding to an input phase 1 saturation $s^1 = 0.8$. At the top boundary the phase pressures are fixed to $u^2(\mathbf{x}) = 8\ 10^6$, and $u^1(\mathbf{x}) = u^2(\mathbf{x}) + p_{ent,1}$. The remaining boundaries are assumed to be impervious as well as the boundaries of the fault. At initial time the porous media is saturated with phase 2 with a hydrostatic pressure $u^2_{ini}(\mathbf{x}) = 8\ 10^6 + \rho_2 g(H - y)$, and a phase 1 pressure defined by $u^1_{ini}(\mathbf{x}) = u^2_{ini}(\mathbf{x}) + p_{ent,j}$ for $\mathbf{x} \in \Omega_j$, $j = 1, 2$, and $u^1_{ini}(\mathbf{x}) = u^2_{ini}(\mathbf{x}) + p_{ent,1}$ for $\mathbf{x} \in \Gamma$.

The mesh is a $n_x \times n_x$ topologically Cartesian quadrangular grid which is refined below the barrier as exhibited in figure 2.3. The simulation is done over 1800 days with an initial time step equal to the maximum time step and fixed to 5 days. The VAG-1 choice of the control volumes is fixed for all simulations of this test case.

Figure 2.4 exhibits the oil (phase 1) saturation at final time. We clearly see that the oil phase rises by gravity along the direction of the highest permeability and accumulates below the barrier. Due to the saturation jump condition at the barrier drain interface given by the capillary pressure functions, oil can only cross the barrier through the fault. Figure 2.4 exhibits the convergence of the oil saturation s^1 at final time for the family of meshes obtained with $n_x = 50, 100, 200, 400$. Figure 2.5 plots the volume of oil below the barrier, above the barrier, and in the fault function of time for this family of meshes. In both cases, we observe the numerical convergence of the solution when the mesh is refined.

Table 2.1 exhibits the numerical behavior of the simulation for the family of quadrangular meshes with a rather good scalability both in terms of linear and nonlinear solvers.

Mesh	$N_{\Delta t}$	N_{Chop}	N_{Newton}	N_{GMRes}	CPU (s)
50×50	360	0	2.11	9.35	22.20
100×100	364	2	2.34	11.75	106
200×200	369	5	3.37	14.45	637
400×400	392	17	4.41	17.84	3933

Table 2.1: For each mesh: number $N_{\Delta t}$ of successful time steps, number N_{Chop} of time step chops, number N_{Newton} of Newton iterations per successful time step, number N_{GMRes} of GMRes iterations by Newton iteration, CPU time in seconds.

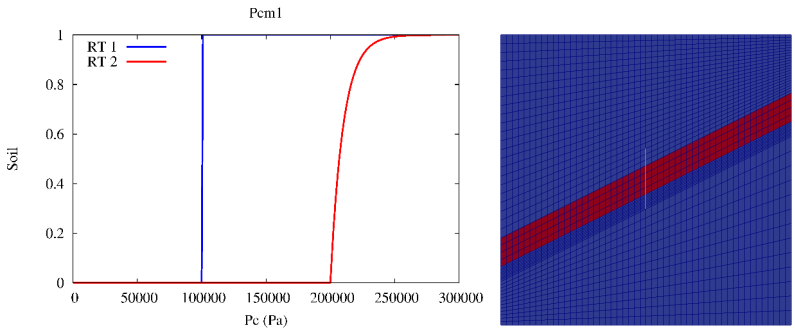

Figure 2.3: Inverses of the extended monotone graphs of the capillary pressures S_1^1 (in blue in subdomain Ω_1 and in the fault Γ_f) and S_2^1 (in red in subdomain Ω_2). Mesh of the basin with the barrier in red, the drain in blue, and the fault in cyan.

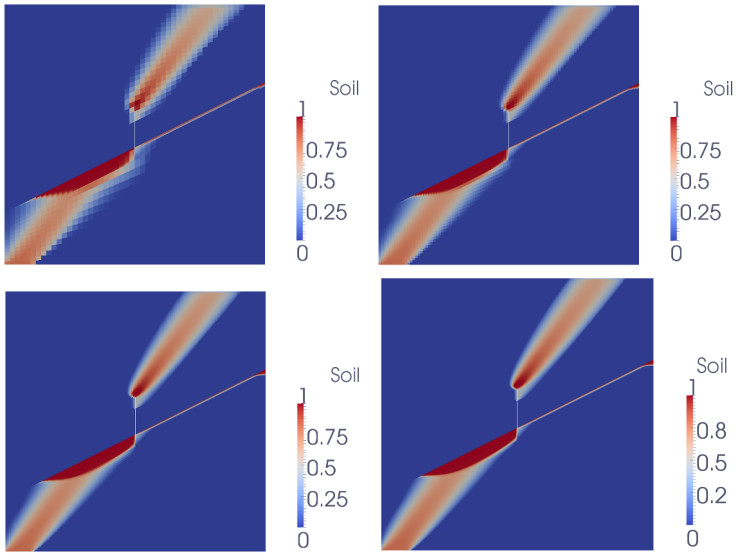

Figure 2.4: Discrete oil saturations at final time obtained for $n_x = 50, 100, 200, 400$.

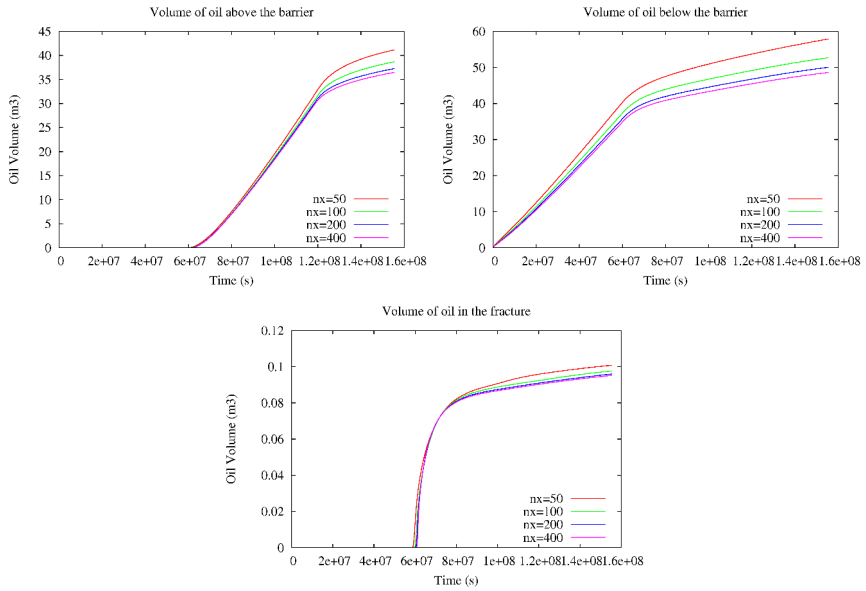

Figure 2.5: Volume of oil above the barrier, below the barrier and in the fault function of time for $n_x = 50, 100, 200, 400$.

2.6.2 Oil migration in a basin with a random network of fractures

We consider the migration of oil in the 2D cross section $\Omega = (0, L) \times (0, H)$ of a basin with $H = L = 100$ m. The basin comprises a random network of 927 fractures exhibited in Figure 2.6. The permeability of the matrix $\Lambda_m = \lambda_m \mathrm{Id}$ and the permeability of the fractures $\Lambda_f = \lambda_f \mathrm{Id}$ are highly contrasted with $\lambda_m = 10^{-15}$ m^2, $\lambda_f = 10^{-10}$ m^2. The width of the fractures is fixed to $d_f = 0.01$ m and their porosity to $\phi_f = 0.3$. The porosity of the matrix is set to $\phi_m = 0.1$.

The inverses of the capillary pressure monotone graph in the matrix ($j = m$) and in the fractures ($j = f$) are exhibited in Figure 2.6 and defined by the Corey law (2.14) with the rocktype $b_m = 5\ 10^3$ Pa, $s^2_{r,m} = 0.2$, $s^1_{r,m} = 0$ in the matrix and the rocktype $b_f = 10^2$ Pa, $s^2_{r,f} = s^1_{r,f} = 0$ in the fractures. The mobilities are defined for $j = m$ and $j = f$ by the Corey law (2.15) with $\mu^1 = 0.005$ Pa.s and $\mu^2 = 0.001$ Pa.s.

The densities of phases are fixed to $\rho^1 = 700$ Kg/m^3 for the oil phase and $\rho^2 = 1000$ Kg/m^3 for the water phase.

Phase 1 is injected at the bottom boundary $(25, 75) \times \{0\}$ with imposed pressures $u^2(\mathbf{x}) = 8.1\ 10^6 + \rho^2 g H$ Pa, $u^1(\mathbf{x}) = u^2(\mathbf{x}) + (S^1_f)^{-1}(0.999999)$ corresponding to an input phase 1 saturation $s^1 = 0.999999$ in the fractures. At the top boundary, the phase pressures are fixed to $u^2(\mathbf{x}) = 8\ 10^6$ and $u^1(\mathbf{x}) = u^2(\mathbf{x})$. The remaining boundaries of the basin are assumed to be impervious. The boundaries of the fracture network not located at the top boundary of the basin nor at the bottom boundary $(25, 75) \times \{0\}$ are also assumed impervious.

At initial time the porous media is saturated with phase 2 with a hydrostatic pressure $u^2_{ini}(\mathbf{x}) = 8\ 10^6 + \rho_2 g(H - y)$, and a phase 1 pressure defined by $u^1_{ini}(\mathbf{x}) = u^2_{ini}(\mathbf{x})$.

The mesh is a $n_x \times n_x$ topologically Cartesian quadrangular grid obtained by a uniform refinement of a given randomly distorted 30×30 Cartesian grid (see figure 2.6). The simulation is fixed to 75 days with an initial time step of 0.01 day and a maximum time step of 0.1 day. All the runs for this test case are performed on a laptop equipped with a dual core 3GHz.

Figure 2.7 exhibits the discrete oil saturation at final time obtained with a topologically Cartesian mesh of size $n_x = 480$, and a non uniform refinement of the mesh with cell widths away from the fracture equal to roughly $2.6, 4.1, 6.45, 10.1, 16.0, 25.2, 39.6, 62.4$ cm (to be compared with the width of say 21 cm obtained with the uniform mesh for $n_x = 480$). The choice of the volume fractions $\alpha_{K,\nu}$, $\alpha_{\sigma,\mathbf{s}}$ is set to VAG-1. The numerical convergence of this solution has been checked and it will be our reference solution for the comparison of the VAG-1 and VAG-2 choices. The Figures 2.8, 2.9 compare the convergence of the oil saturation on the family of uniformly refined meshes with $n_x = 60, 120, 240, 480$, for the two choices of the volume fractions. It is clear that the choice VAG-1 which avoids to mix matrix and fracture volumes provides a much better convergence. It is explained in Figure 2.10 exhibiting that the choice VAG-2 of the volume distribution yields a too large volume of oil in the matrix and a too small volume of oil in the fractures due to the enlarged volumes at the matrix fracture interfaces. This is a clear advantage of the VAG scheme compared with usual CVFE approaches which cannot avoid the mixing of fracture and matrix volumes due to the use of a dual mesh and the absence of cell unknowns.

The numerical behavior of the simulations for both choices of the distribution of the volumes and for the family of meshes is exhibited in Table 2.2 showing the number of successful time steps, the number of time step chops, the number of Newton iterations by successful time steps, the number of GMRes iterations by Newton iteration, the CPU time in seconds, and the maximum CFL number. This maximum CFL number is the one obtained for the oil saturation Buckley Leverett equation (without the capillary diffusion) discretized by an upwind monotone scheme and an Euler explicit time integration, and using the total Darcy velocity and the buoyancy forces of the simulation.

In both cases a rather good scalability is obtained both in terms of nonlinear and linear solvers although very large CFL numbers are observed in the fracture network. The results are slightly better for VAG-2 due to the larger control volumes at the matrix fracture interfaces as can be checked on the comparison of the maximum CFL numbers in table 2.2.

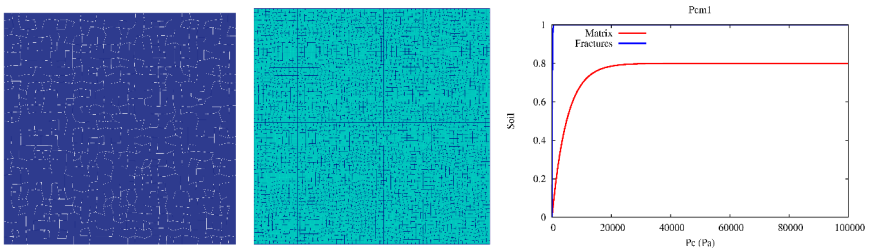

Figure 2.6: Network of 927 fractures and mesh obtained for $n_x = 60$. Inverses of the extended monotone graphs of the capillary pressures S_m^1 in the matrix, and S_f^1 in the fractures.

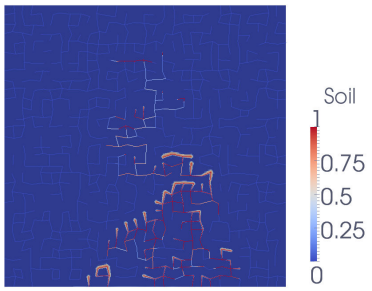

Figure 2.7: Discrete oil saturation at final time obtained for $n_x = 480$ with refinement at the matrix fracture interfaces and the choice VAG-1 of the volumes.

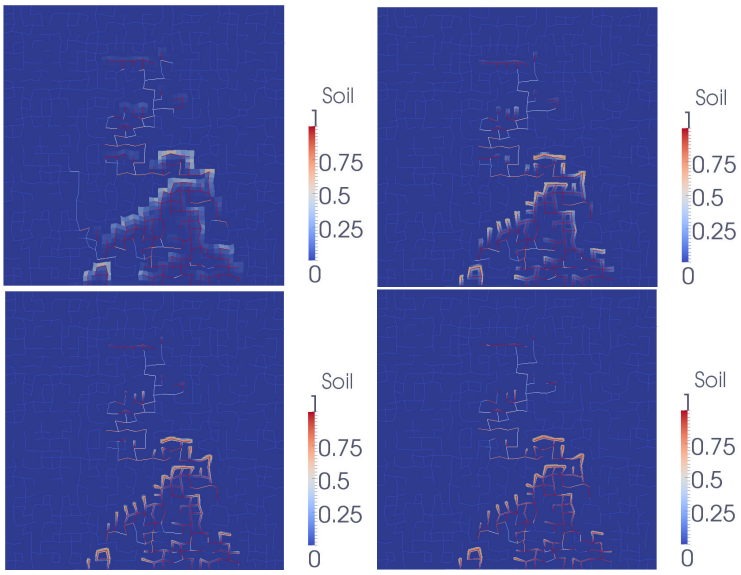

Figure 2.8: Discrete oil saturation at final time obtained for the family of uniformly refined meshes $n_x = 60, 120, 240, 480$, and the choice VAG-1 of the volumes.

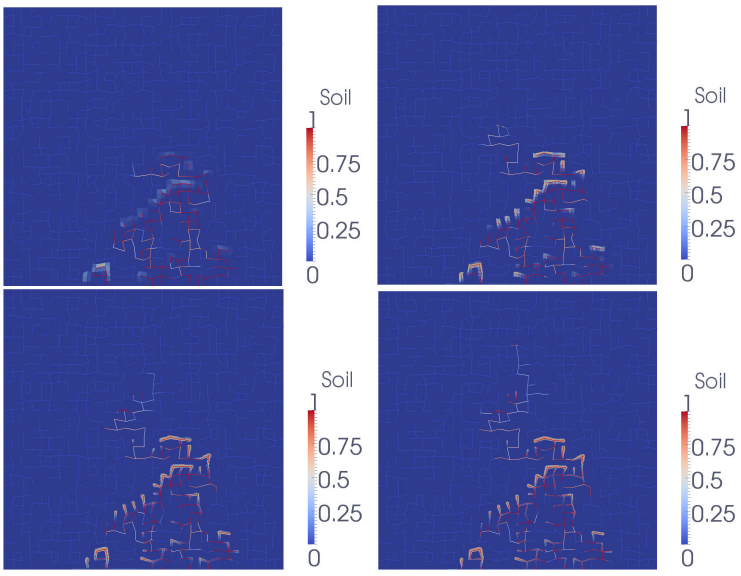

Figure 2.9: Discrete oil saturation at final time obtained for the family of uniformly refined meshes $n_x = 60, 120, 240, 480$, and the choice VAG-2 of the volumes.

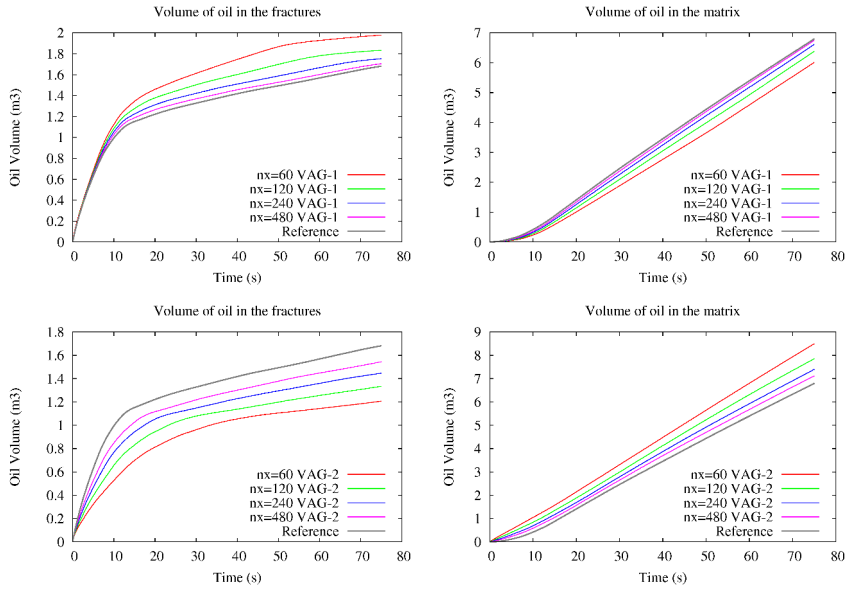

Figure 2.10: Volume of oil in the fracture and in the matrix function of time for $n_x = 60, 120, 240, 480$, and for the two choices VAG-1 and VAG-2 of the distribution of the volumes.

Volumes	n_x	$N_{\Delta t}$	N_{Chop}	N_{Newton}	N_{GMRes}	CPU (s)	CFL
VAG-1	60	759	0	2.62	8.08	164	210
VAG-1	120	759	0	2.90	8.84	535	420
VAG-1	240	777	14	3.94	9.44	2480	840
VAG-1	480	889	69	5.79	9.85	15062	1675
VAG-2	60	759	0	2.08	6.26	126	6.4
VAG-2	120	759	0	2.48	6.81	441	27
VAG-2	240	759	0	3.16	7.83	1868	106
VAG-2	480	788	21	4.98	8.53	11074	384

Table 2.2: For each choice VAG-1 and VAG-2 of the volume distribution and each mesh size $n_x = 60, 120, 240, 480$: number $N_{\Delta t}$ of successful time steps, number N_{Chop} of time step chops, number N_{Newton} of Newton iterations per successful time step, number N_{GMRes} of GMRes iterations by Newton iteration, CPU time in seconds, maximum CFL number.

2.6.3 3D network of fractures

This test case considers the migration of oil in a 3D basin $\Omega = (0, L) \times (0, L) \times (0, H)$ with $H = L = 100$ m. Figure 2.11 exhibits the test case geometry where the fractures in the cube are represented by parallelograms and are intersected with the top and the

bottom of the basin. The family of tetrahedral meshes is generated using TetGen [59] in order to be refined at the neighbourhood of the fracture network. Figure 2.11 shows the coarsest mesh $i_{mesh} = 1$, and Table 2.3 defines for each mesh the number Nb_{cells} of cells, the number Nb_{nodes} of nodes, the number Nb_{FracF} of fracture faces, the number of d.o.f. $\mathrm{Card}(\mathcal{V} \cup \mathcal{M} \cup \mathcal{F}_\Gamma)$ of the scheme (with two unknowns per d.o.f.), and the number of d.o.f. $\mathrm{Card}(\mathcal{V} \diagup \mathcal{V}_D \cup \mathcal{F}_\Gamma)$ of the linear system (with two unknowns per d.o.f.) after elimination without fill-in of the cells and Dirichlet nodes, where $\mathcal{V}_D$ is the set of Dirichlet nodes at the boundary of Ω. It also specifies for each mesh the cubic root of the mean volume of all cells at the matrix fracture interface, denoted by ρ_i, and defined by

$$\varrho_i = \Big(\frac{1}{\mathrm{Card}\{K \in \mathcal{M} | K \cap \Gamma \neq \emptyset\}} \sum_{K \in \mathcal{M} \,|\, K \cap \Gamma \neq \emptyset} |K| \Big)^{1/3}. \tag{2.16}$$

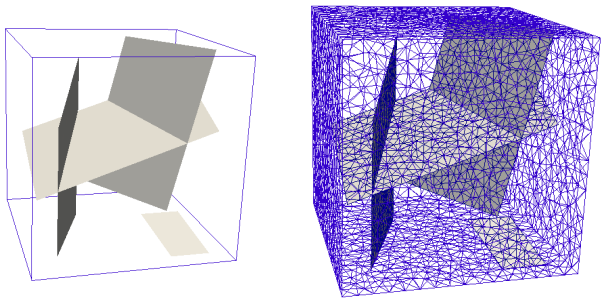

Figure 2.11: Geometry of the basin, fracture network, and coarsest three-dimensional Delaunay mesh $i_{mesh} = 1$.

i_{mesh}	Nb_{cells}	Nb_{nodes}	Nb_{FracF}	ϱ_i	scheme d.o.f.	linear system d.o.f.	$\theta_\mathcal{T}$
1	47 670	8 348	1 678	2.42	57 696	9 278	209
2	253 945	41 043	6 655	1.23	301 643	46 283	86
3	837 487	132 778	16 497	0.78	986 762	147 148	142
4	3 076 262	483 786	42 966	0.48	3 603 014	523 453	200

Table 2.3: For each mesh: number Nb_{cells} of mesh cells, number Nb_{nodes} of nodes, number Nb_{FracF} of fracture faces, scheme and linear system number of d.o.f. (with 2 unknowns per d.o.f), cubic root of the average cell volume at the matrix fracture interface ϱ_i, and shape regularity $\theta_\mathcal{T}$.

We suppose again a high contrast between the permeability of the matrix $\Lambda_m = \lambda_m \mathrm{Id}$ and the permeability of the fractures $\Lambda_f = \lambda_f \mathrm{Id}$ with $\lambda_m = 10^{-17}$ m^2, $\lambda_f = 10^{-11}$ m^2. The porosities, the phase densities, the mobilities and the capillary pressures are the same than in the previous test case. The initial and boundary conditions are also the same except that the oil phase is injected at the full bottom side of the domain. The simulation

is run over a period of 10 years with an initial time step of 0.2 days, and a maximum time step fixed to 5 days, except on mesh 4 for which a smaller maximum time step of 2.5 days is used. All the numerical tests have been performed on the Cicada Cluster located at the University Nice Sophia-Antipolis and which includes 1152 nodes equipped with two eight-core Intel(R) E5-2670 processors. Figure 2.12 exhibits the oil saturation obtained on the coarsest mesh $i_{mesh} = 1$ at final simulation time. We observe that the oil phase injected at the bottom side in the domain initially saturated with water, quickly rises by gravity along the faults and slowly penetrate in the matrix.

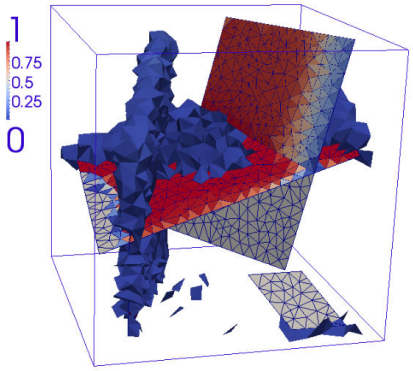

Figure 2.12: Discrete solution obtained by the VAG-1 scheme with the first mesh $i_{mesh} = 1$ at final simulation time: oil saturation in the fracture network and in the matrix using the lower threshold in the matrix equal to 0.001.

Figure 2.13 compares the convergence of the oil saturation on the family of refined meshes for the two choices of the volume fractions VAG-1 and VAG-2. It is clear, as in the 2D test case, for such high ratio of the fracture and matrix permeabilities, that VAG-1 provides a much better convergence than VAG-2 since it does not mix porous volumes from the matrix and the fracture network. It illustrates again the advantage of the VAG scheme compared with CVFE discretizations which cannot avoid such mixing of porous volumes. Table 2.4 presents the numerical behavior of the simulations for both choices of the distribution of the volumes and for the family of meshes. The results obtained demonstrate the good robustness and scalability of the proposed numerical scheme both in terms of Newton convergence, linear solver convergence and CPU time. As for the 2D network test case, the robustness of the nonlinear solver is slightly better for VAG-2 due to the larger control volumes at the matrix fracture interfaces for VAG-2 than for VAG-1.

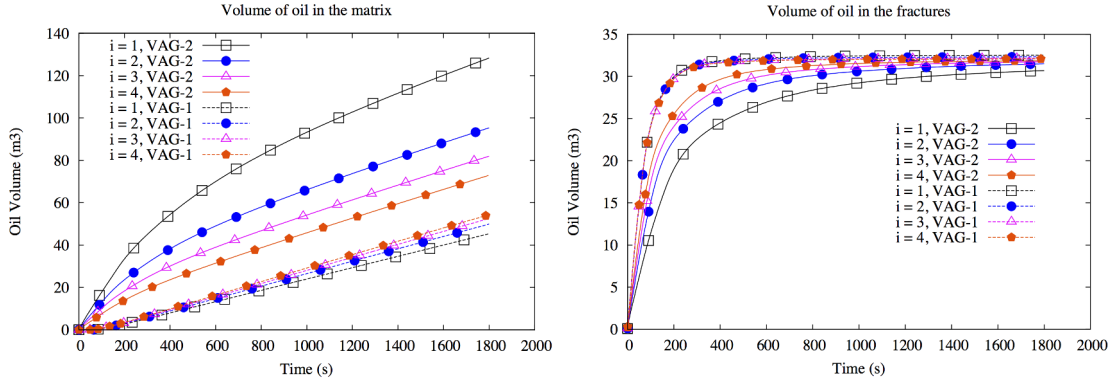

Figure 2.13: Volumes of oil in the fracture and in the matrix function of time for the family of meshes $i_{mesh} = 1, .., 4$, and for both choices VAG-1 and VAG-2 of the volume distribution.

Volumes	i_{mesh}	$N_{\Delta t}$	N_{Chop}	N_{Newton}	N_{GMRes}	CPU (s)
VAG-1	1	384	6	2.20	10.05	588
VAG-1	2	390	10	3.08	15.11	5 898
VAG-1	3	415	21	4.02	15.93	31 806
VAG-1	4	784	30	3.37	16.75	209 485
VAG-2	1	373	0	1.87	6.94	482
VAG-2	2	373	0	2.42	13.05	4 452
VAG-2	3	375	1	3.02	14.56	21 645
VAG-2	4	747	13	2.92	16.55	172 946

Table 2.4: For each choice VAG-1 and VAG-2 of the volume distribution and for each mesh $i_{mesh} = 1, .., 4$: number $N_{\Delta t}$ of successful time steps, number N_{Chop} of time step chops, number N_{Newton} of Newton iterations per successful time step, number N_{GMRes} of GMRes iterations by Newton iteration, CPU time in seconds.

2.6.4 Comparisons between the VAG and HFV discretizations

Tracer test case

In order to compare the accuracy of the VAG and HFV schemes, we first consider a simple tracer problem with a single fracture for which we can derive an analytical solution. This model can be obtained from the two-phase flow model assuming that $k_m^\alpha(\mathbf{x}, s) = k_f^\alpha(\mathbf{x}, s) = s$ and vanishing capillary pressures. In that case, the pressure is solution of the hybrid dimensional single phase flow problem described in Chapter 1 and the saturation s^1 denoted by c is solution of an hyperbolic equation (see [62] for details).

Let us set $\Omega = (0,1)^2$, and denote by (x,y) the Cartesian coordinates of $\mathbf{x}$. We then define $\mathbf{x}_1 = (0, \frac{1}{4})$, $\theta \in (0, \arctan(\frac{3}{4}))$, $\mathbf{x}_2 = (1, \frac{1}{4} + \tan(\theta))$. Let $\Omega_1 = \{(x,y) \in \Omega \,|\, y > \frac{1}{4} + x\tan(\theta)\}$, and $\Omega_2 = \Omega \setminus \overline{\Omega}_1$. We consider a single fracture defined by $\Gamma = (\mathbf{x}_1, \mathbf{x}_2) = \partial\Omega_1 \cap \partial\Omega_2$ with tangential permeability $\Lambda_f > 0$, and width $d_f > 0$. The matrix permeability is isotropic and set to $\Lambda_m = 1$, the matrix and fracture porosities are set to $\phi_m = \phi_f = 1$, and the fluid viscosity is set to $\mu = 1$. The pressure solution is fixed to $u(x,y) = 1 - x$. In this case, the tracer model reduces to the following equations which specifies our choice of the boundary and initial conditions:

$$\left\{\begin{array}{rll}
\partial_t c_{m,\mathfrak{a}}(x,y,t) + \partial_x c_{m,\mathfrak{a}}(x,y,t) = 0 & \text{on } \Omega_{\mathfrak{a}} \times (0,T),\ \mathfrak{a} = 1,2, \\
c_{m,\mathfrak{a}}(x,y,0) = 0 & \text{on } \Omega_{\mathfrak{a}},\ \mathfrak{a} = 1,2, \\
c_{m,1}(0,y,t) = 1 & \text{on } (\frac{1}{4},1) \times (0,T), \\
c_{m,2}(0,y,t) = 1 & \text{on } (0,\frac{1}{4}) \times (0,T), \\
c_{m,2}(x, \frac{1}{4} + x\tan(\theta), t) = c_f(x,t) & \text{on } (0,1) \times (0,T), \\
\mathcal{L}c_f(x,t) = \beta c_{m,1}(x, \frac{1}{4} + x\tan(\theta), t) & \text{on } (0,1) \times (0,T), \\
c_f(0,t) = 1 & \text{on } (0,T), \\
c_f(x,0) = 0 & \text{on } (0,1),
\end{array}\right. \tag{2.17}$$

where $\mathcal{L} = \partial_t + k\partial_x + \beta$ with $\beta = \frac{\sin(\theta)}{d_f}$ and $k = \Lambda_f \cos^2(\theta)$. It is assumed that $k > 1$. This system can be integrated along the characteristics of the matrix and fracture velocity fields leading to the following analytical solution:

$$c_{m,1}(x,y,t) = \left\{\begin{array}{ll} 0 \text{ if } & t < x, \\ 1 \text{ if } & t > x, \end{array}\right.$$

$$c_f(x,t) = \left\{\begin{array}{lll} 0 & \text{if} & t < \frac{x}{k}, \\ e^{-\frac{\beta}{k-1}(x-t)} & \text{if} & \frac{x}{k} < t < x, \\ 1 & \text{if} & t > x, \end{array}\right.$$

$$c_{m,2}(x,y,t) = \left\{\begin{array}{l} \text{if } y \in (0,\frac{1}{4}) \left\{\begin{array}{ll} 0 \text{ if } & t < x, \\ 1 \text{ if } & t > x, \end{array}\right. \\ \text{if } y \in (\frac{1}{4}, \frac{1}{4} + \tan(\theta)) \left\{\begin{array}{lll} 0 & \text{if} & t < x - \frac{4y-1}{4\tan(\theta)}, \\ c_f(\frac{4y-1}{4\tan(\theta)}, t + \frac{4y-1}{4\tan(\theta)} - x) & \text{if} & t > x - \frac{4y-1}{4\tan(\theta)}. \end{array}\right. \end{array}\right.$$

In the following numerical experiments the parameters are set to $\tan(\theta) = \frac{1}{2}$, $\Lambda_f = 20$ and $d_f = 0.01$. The mesh is a topologically Cartesian $n_x \times n_x$ grid. Figure 2.14 shows an example of the mesh with $n_x = 20$ as well as the analytical solution in the matrix obtained at time $t_f = 0.5$ chosen as the final time of the simulation.

The VAG and HFV finite volume discretizations of this model use the fluxes defined in Subsection 1.4.3. Since the pressure is linear, the discrete pressure and fluxes are exact for both the HFV and VAG schemes. The discretization in space of the tracer model uses a first order upwind approximation of the concentration in the spirit of the two-phase flow model discretization of Section 2.5. It is combined with an explicit time integration using the time step defined by the maximum time step allowed by the CFL condition.

Figure 2.15 compares the convergence of the L1 error for the discrete solutions at final time $t_f = 0.5$ obtained in the matrix domain and in the fracture for both the VAG and HFV schemes. The numerical order of convergence is the same for both scheme but the VAG scheme is slightly more accurate for this test case. This is confirmed by the comparison of the discrete solutions in the fracture at final time $t_f = 0.5$ exhibited in Figure 2.16 for the VAG scheme and in Figure 2.17 for the HFV scheme.

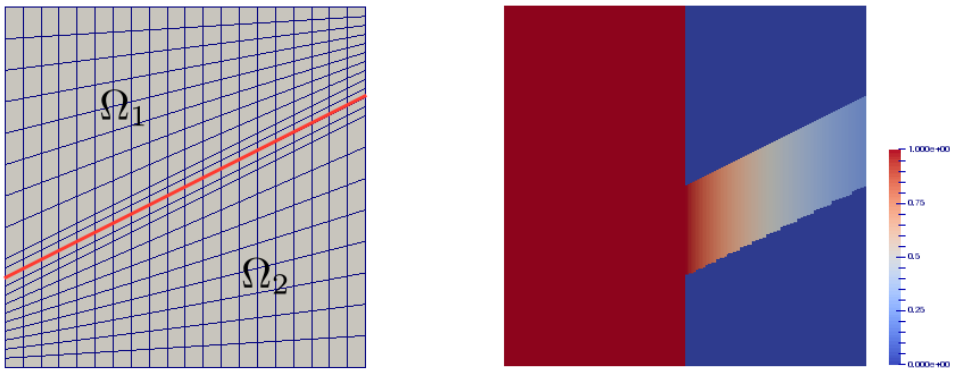

Figure 2.14: Left: example of mesh with $n_x = 20$ where the red line is the fracture. Right: analytical solution of (2.17) at time $t_f = 0.5$.

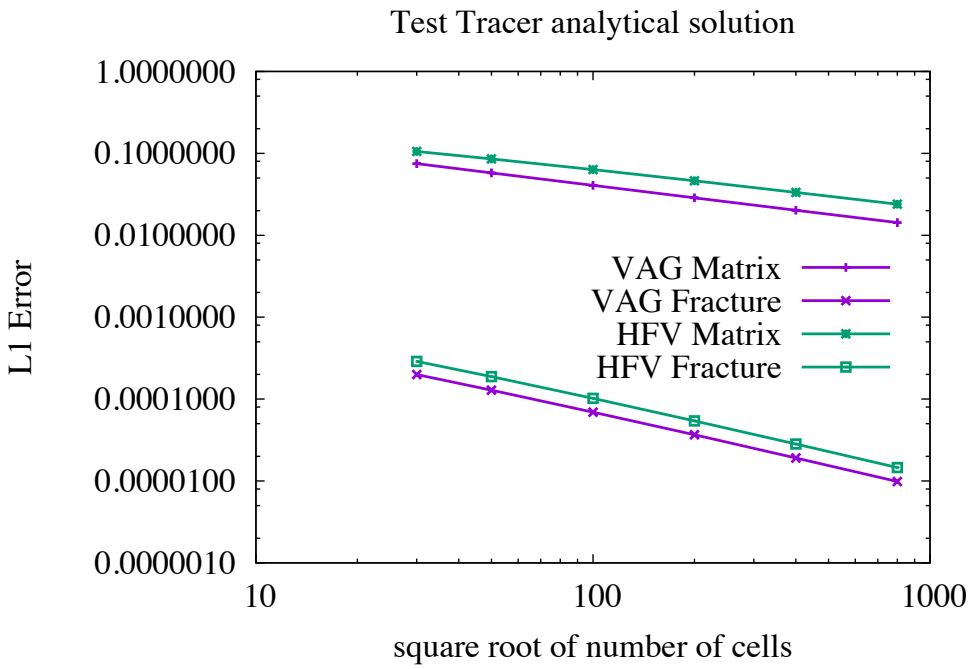

Figure 2.15: Discrete L^1 error for the solutions of the VAG and HFV schemes at time $t_f = 0.5$ in the matrix and in the fracture as a function of $n_x = 30, 50, 100, 200, 400, 800$.

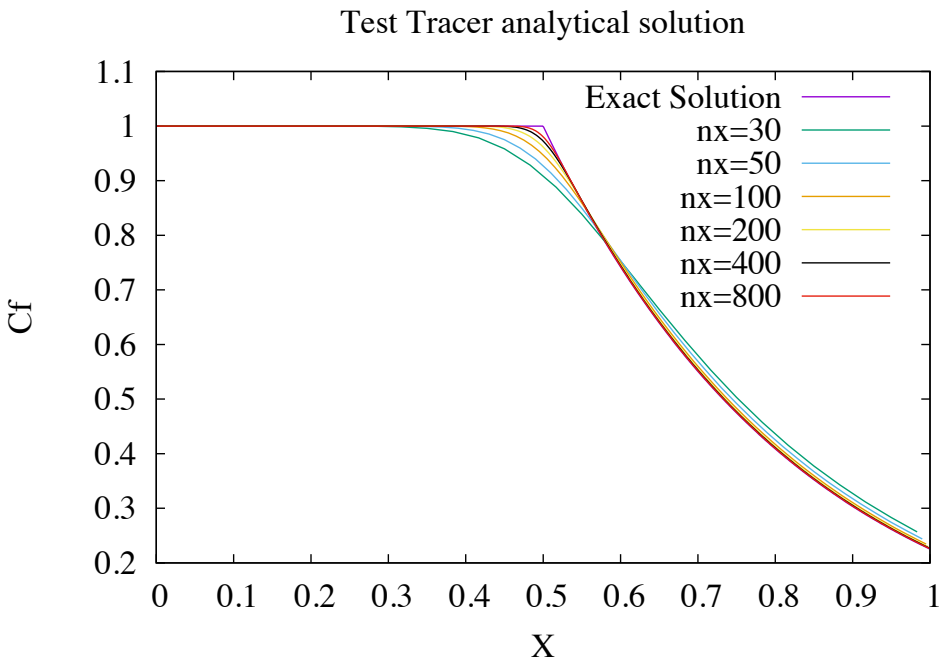

Figure 2.16: Exact and discrete solutions in the fracture at time $t_f = 0.5$ obtained with the VAG scheme for $n_x = 30, 50, 100, 200, 400, 800$.

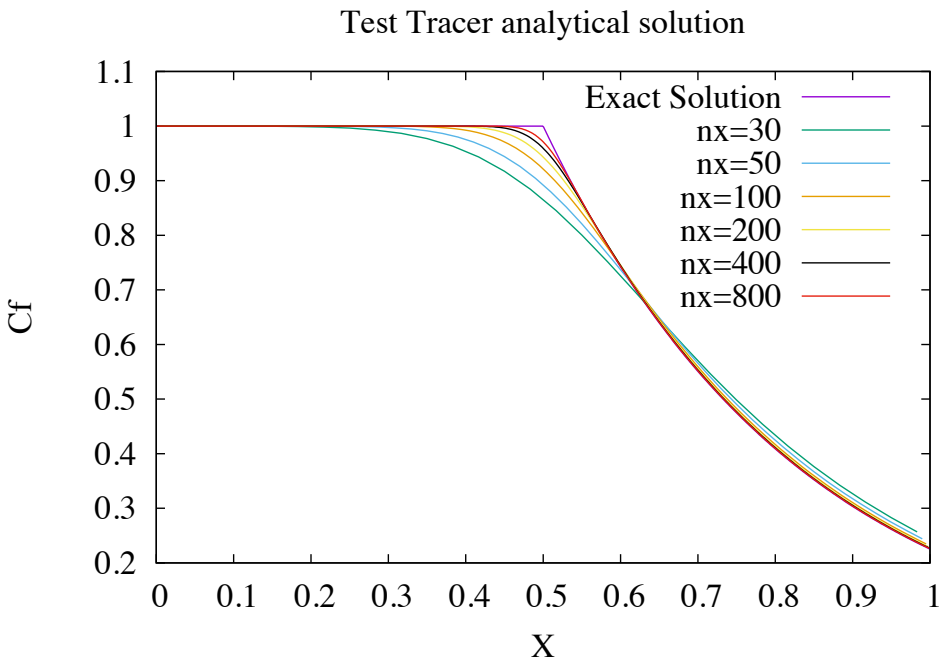

Figure 2.17: Exact and discrete solutions in the fracture at time $t_f = 0.5$ obtained with the HFV scheme for $n_x = 30, 50, 100, 200, 400, 800$.

Two phase flow test case

We consider the test case of Subsection 2.6.3 and compare the discrete solutions obtained by the VAG and HFV schemes as well as the numerical behavior of both schemes. The comparison is done on three tetrahedral meshes with number of cells $Nb_{cells} = 47600$ ($47k$), 124000 ($124k$) and 253945 ($253k$). For the larger mesh $i_{mesh} = 3$, the simulation with the HFV scheme was too long (more than one week). Figure 2.18 compare the volume of oil in the fracture and in the matrix obtained with the VAG and HFV schemes with the 3 meshes. The reference solution is provided by the solution obtained with the VAG scheme on the largest mesh $i_{mesh} = 4$ ($3000k$). It appears that the solutions obtained with the VAG scheme is closer to this reference solution than the ones obtained with the HFV scheme. The comparison in Table 2.5 of the CPU times obtained with both schemes shows huge difference of CPU times, roughly speaking of a factor 10 to 20 for a given mesh. Since the HFV scheme does not seem to be more accurate than the VAG scheme due to the first order upwind approximation of the transport terms, it is clear that the VAG scheme is much better than the HFV scheme on tetrahedral meshes for such fully implicit discretization combined with a first order upwind approximation of the mobility

terms.

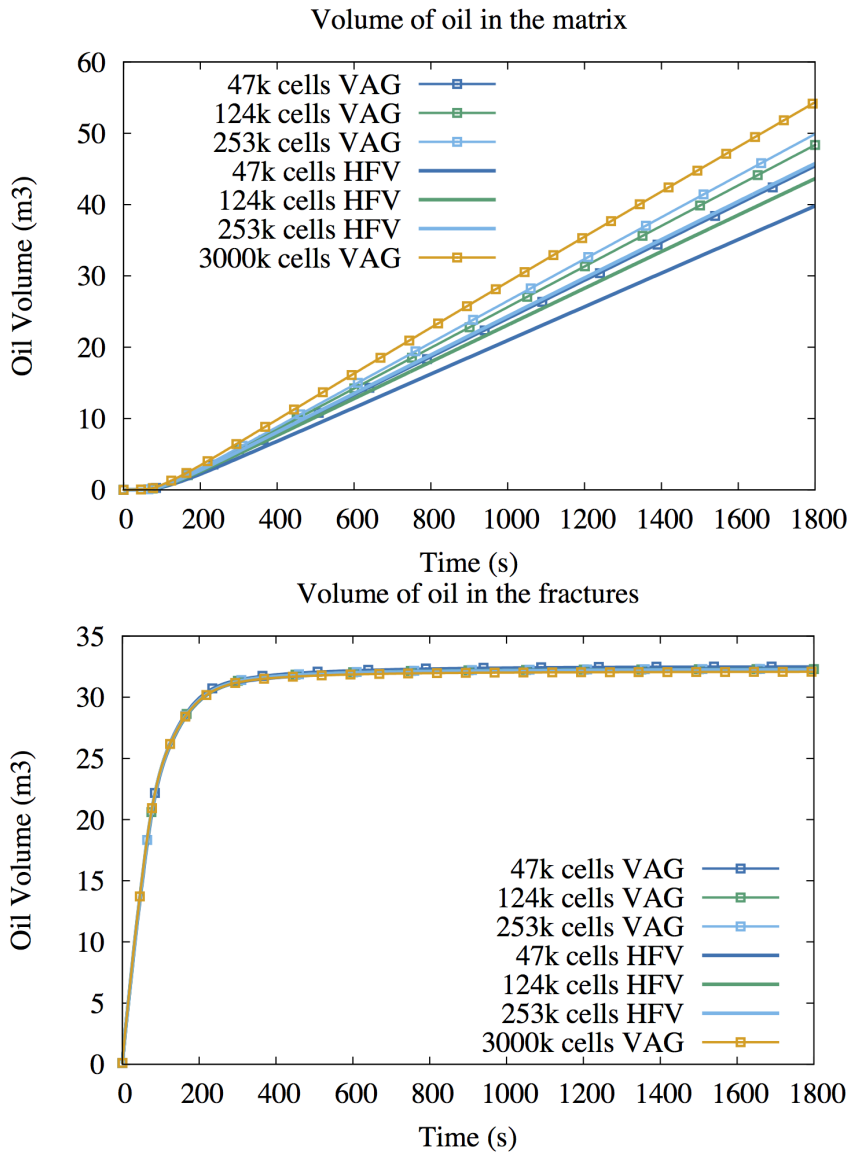

Figure 2.18: Volumes of oil in the fracture and in the matrix function of time for the tetrahedral meshes with $N_{Cells} = 47k, 124k, 253k$ cells for the VAG and HFV schemes, and for the tetrahedral mesh with $N_{Cells} = 3000k$ for the VAG scheme. The distribution of the volume is done following the VAG-1 type choice.

Scheme	N_{Cells}	dof	N_{zeros}	$N_{\Delta t}$	N_{Chop}	N_{Newton}	N_{GMRes}	CPU (s)
VAG	47k	9k	130k	384	6	2.2	10	590
VAG	124k	23k	338k	391	8	2.5	11	2000
VAG	253k	46k	686k	390	10	3.1	15	5900
HFV	47k	98k	682k	385	10	2.9	20	4900
HFV	124k	254k	1777k	413	20	3.9	34	25000
HFV	253k	517k	3628k	449	33	4.9	47	95000

Table 2.5: For the schemes VAG and HFV and for different tetrahedral meshes: number N_{Cells} of cells, number dof of degrees of freedom after elimination of the cell unknowns, number of nonzero connections in the Jacobian after elimination of the cell unknowns (with a 2×2 matrix per connection), number $N_{\Delta t}$ of successful time steps, number N_{Chop} of time step chops, number N_{Newton} of Newton iterations per successful time step, number N_{GMRes} of GMRes iterations by Newton iteration, CPU time in seconds.

2.7 Conclusion

This Chapter has introduced the VAG and HFV discretizations of hybrid dimensional two-phase Darcy flows modelling discrete fracture networks with mass exchange between the matrix and the fractures. Our discretization takes into account general polyhedral meshes, general discrete fracture networks, the anisotropy of the matrix and of the fracture permeability fields, and discontinuous rocktypes.

Compared with CVFE approaches, the numerical tests clearly exhibit that the VAG scheme has the advantage to avoid the mixing of the fracture and matrix rocktypes at the interfaces between the matrix and the fractures, while keeping the low cost of a nodal discretization on unstructured meshes.

The numerical experiments also show that the HFV scheme is much more expensive than the VAG scheme on tetrahedral meshes and do not provide a better accuracy due to the first order upwind approximation of the mobility terms.

The convergence of the VAG scheme to a weak solution of the model has been proved for arbitrary choices of the volumes at the nodal unknowns assuming the non degeneracy of the relative permeabilities and a network of planar fractures. To our knowledge, this is the first convergence result for this type of hybrid dimensional two-phase Darcy flow model, and it also provides an existence result for such models. This proof can be readily extended to cover any scheme which fit into the gradient scheme framework introduced in Chapter 1.

Chapter 3

Two-phase Darcy flow model accounting for vanishing and discontinuous capillary pressures

Abstract: fully implicit time-space discretizations applied to the two-phase Darcy flow problem lead to the systems of nonlinear equations, which are traditionally solved by some variant of Newton's method. The efficiency of the resulting algorithms heavily depends on the choice of the primary unknowns since Newton's method is not invariant with respect to a nonlinear change of variable. In this regard the role of capillary pressure/saturation relation is paramount because the choice of primary unknowns is restricted by its shape. We propose an elegant mathematical framework for two-phase flows in heterogeneous porous media resulting in a family of formulations, which apply to general monotone capillary pressure/saturation relations and handle the saturation jumps at rocktype interfaces. The presented approach is applied to the hybrid dimensional two-phase Darcy flow model introduced in Chapter 2 using the phase pressure formulation. The new formulation allows to extend this model in order to take into account more general capillary pressure curves and also to provide a more robust nonlinear solver. The two-phase flow model is discretized using the VAG scheme described in Chapter 2 in the case of the phase pressure formulation. The discrete model requires as previously only two unknowns by degree of freedom.

3.1 Introduction

In the framework of two-phase Darcy flows in fractured porous media, highly contrasted capillary pressure curves are expected in particular between the matrix and the fractures. Hence, it is crucial to take into account in the model formulation the saturation jumps at the matrix fracture interfaces. In order to do so, as it has been stressed out in [21], the capillary pressure curves have to be extended into the monotone graphs (see e.g. Figures 3.1).

In Chapter 2, the VAG discretization, employing phase pressures formulation, was applied to model two-phase Darcy flows in heterogeneous porous media. In the context of vertex-centered schemes the phase pressures formulation allows to capture the saturation jump condition at the interface between different rocktypes without introducing any additional unknowns at these interfaces. It is, however, limited to strictly increasing capillary pressure curves and lacks robustness compared to pressure saturation formulations. In this Chapter we extend the scheme introduced in Chapter 2 to the case of general increasing capillary pressure curves. The same notations as in Chapter 2 are used and some of them are recalled for conveniency.

In the matrix domain Ω (resp. in the fracture network Γ), we denote by $\phi_m(\mathbf{x})$ (resp. $\phi_f(\mathbf{x})$) the porosity and by $\Lambda_m(\mathbf{x})$ (resp. $\Lambda_f(\mathbf{x})$) the permeability (resp. tangential permeability) tensor. The thickness of the fractures is denoted by $d_f(\mathbf{x})$ for $\mathbf{x} \in \Gamma$. For each phase $\alpha = 1, 2$ (where $\alpha = 1$ stands for the non wetting phase and $\alpha = 2$ stands for the wetting phase) we denote by $k^\alpha_{r,m}(\mathbf{x}, s)$ (resp. $k^\alpha_{r,f}(\mathbf{x}, s)$), the phase relative permeabilities and by $S^1_m(\mathbf{x}, p)$ (resp. $S^1_f(\mathbf{x}, p)$) the possibly set-valued inverses of the monotone graph extension of the capillary pressure curves. For $\alpha = 1, 2$, we will also denote by ρ^α the phase densities and by μ^α the phase viscosities which for the sake of clarity are assumed

constant.

We denote by u^α the pressure of phase $\alpha = 1, 2$ and by s_m^α (resp. s_f^α) the saturation of phase $\alpha = 1, 2$ in the matrix (resp. the fracture network) domain. We define the water saturations by

$$s_m^1 = 1 - s_m^2 \text{ and } s_f^1 = 1 - s_f^2.$$

The Darcy flux of phase $\alpha = 1, 2$ in the matrix domain is defined by

$$\mathbf{q}_m^\alpha = -\frac{k_{r,m}^\alpha(\mathbf{x}, s_m^\alpha)}{\mu^\alpha}\Lambda_m(\nabla u^\alpha - \rho^\alpha \mathbf{g}),$$

where $\mathbf{g} = g\nabla z$ stands for the gravity vector. The flow in matrix domain is described by the mass balance equation

$$\phi_m \partial_t s_m^\alpha + \operatorname{div}(\mathbf{q}_m^\alpha) = 0, \tag{3.1}$$

and the macroscopic capillary pressure law

$$s_m^1 \in S_m^1(\mathbf{x}, u^1 - u^2). \tag{3.2}$$

The Darcy flux of phase $\alpha = 1, 2$ in the fracture Γ_i, $i \in I$ integrated other the width of the fracture is defined by

$$\mathbf{q}_{f,i}^\alpha = -d_f \frac{k_{r,f}^\alpha(\mathbf{x}, s_f^\alpha)}{\mu^\alpha}\Lambda_f(\nabla_{\tau_i}\gamma_i u^\alpha - \rho^\alpha \mathbf{g}_{\tau_i}),$$

with $\mathbf{g}_{\tau_i} = \mathbf{g} - (\mathbf{g}\cdot\mathbf{n}_i^+)\mathbf{n}_i^+$. The flow in each fracture Γ_i is described by

$$d_f\phi_f\partial_t s_f^\alpha + \operatorname{div}_{\tau_i}(\mathbf{q}_{f,i}^\alpha) - [\![\mathbf{q}_m^\alpha \cdot \mathbf{n}_i]\!] = 0. \tag{3.3}$$

and

$$s_f^1 \in S_f^1(\mathbf{x}, \gamma_i u^1 - \gamma_i u^2). \tag{3.4}$$

The hybrid dimensional two-phase flow model looks for s_m^1, s_f^1, and $(u^\alpha)_{\alpha=g,w}$ satisfying (3.1)-(3.4). In addition to (3.1)-(3.4) we prescribe a no-flux boundary conditions at the tips of the immersed fractures, that is to say on $\partial\Gamma \setminus \partial\Omega$, and the mass conservation and pressure continuity conditions at the fracture intersections. We refer to [13] for more details on those conditions. Finally, one should provide some appropriate initial and boundary data (see Chapter 2 for a more detailed description).

Remark that for a fixed $\mathbf{x} \in \Omega$ (resp. $\mathbf{x} \in \Gamma$) the functions S_m^1 and S_f^1 are, generally speaking, set-valued, this is the case e.g. when the capillary pressure is neglected. Indeed, in such situation the non wetting phase saturation takes any value in $[0, 1]$ as long as $u^1 - u^2 = 0$. In addition, S_m^1 and S_f^1 depend on the space variable $\mathbf{x}$ and we will assume that $S_m^1(\mathbf{x}, \cdot)$ is piecewise constant and is defined with respect to a set of so-called rocktypes. The following assumptions hold on S_m^1 and S_f^1:

(A_1) Assumption (H3) of Chapter 2 is reproduced in this Chapter, i.e. Ω can be decomposed into a set of disjoint connected open polyhedral sets $(\Omega_j)_{j\in J_m}$ with $\bigcup_{j\in J_m}\overline{\Omega_j} =$

$\overline{\Omega}$, such that $S^1_m(\mathbf{x}, p) = S^1_{m,j}(\mathbf{x}, p)$ for a.e. $\mathbf{x} \in \Omega_j$ and all $p \in \mathbb{R}$. Similarly, we suppose that there exists a family of disjoint connected polygonal open sets $(\Upsilon_j)_{j\in J_f}$ such that $\bigcup_{j\in J_f} \overline{\Upsilon_j} = \overline{\Gamma}$ and such that $S^1_f(\mathbf{x}, p) = S^1_{f,j}(p)$ for a.e. $\mathbf{x} \in \Upsilon_j$ and all $p \in \mathbb{R}$.

(A_2) $\left(S^1_{m,j}\right)_{j\in J_m}$ and $\left(S^1_{f,j}\right)_{j\in J_f}$ are maximal monotone graphs with domain $\mathbb{R}$ satisfying $S^1_{l,j}(p) \subset [0, 1]$ for all $p \in \mathbb{R}$ and $l = m, f$, $j \in J_l$.

The matrix and fracture relative permeabilities are piecewise constant w.r.t. $\mathbf{x}$ on the same partitions of the matrix and fracture network domains as the capillary pressure curves. In the following, we will denote the mobilities (ratio of the phase relative permeability to the phase viscosity) by $k^\alpha_{m,j}(s)$ in the matrix for each rocktype $j \in J_m$ and by $k^\alpha_{f,j}(s)$ in the fracture network for each rocktype $j \in J_f$.

In order to illustrate the difficulty of dealing with both heterogeneous and multi-valued saturation curves S^1_m and S^1_f, let us admit for the moment that S^1_m are S^1_f do not depend on $\mathbf{x}$ and that $S^1_m(p)$, $S^1_f(p)$ are single-valued continuous increasing functions satisfying for $l = m, f$

$$S^1_l(p \le p_{ent,l}) = 0 \text{ and } \lim_{p\to+\infty} S^1_l(p) = 1$$

with $p_{ent,l} \in \mathbb{R}$, $l = m, f$ been an entry pressure. The figure 3.1a exhibits a typical form of multi-valued capillary pressure curves corresponding to $S^1_m(p)$ are $S^1_f(p)$.

When the system (3.1) - (3.4) is solved numerically it is desirable to reduce the number of unknowns by eliminating the algebraic equations (3.2) and (3.4), in particular one may expect to have as much as two unknowns by degree of freedom. Note that as long as the functions S^1_l, $l = m, f$, are single valued (which is the case when the capillary pressure graphs do not have "horizontal" parts) it is possible to express s^1_m and s^1_f in terms of u^1 and u^2. In other words (u^2, u^1) is an admissible couple of primary unknowns. The other admissible couple is (u^2, s^1_f) since u^1 and s^1_m can be expressed as

$$u^1 = u^2 + (S^1_f)^{-1}(s^1_f) \text{ and } s^1_m = S^1_m \circ (S^1_f)^{-1}(s^1_f).$$

In contrast, unless $p_{ent,m}$ is less or equal to $p_{ent,f}$, it is not possible to describe any possible values of u^1 and s^1_f at the matrix/fracture interface using the pair (u^1, s^1_m). However this formulation still can be applied "away" from Γ.

Let us remark that both (u^2, u^1) and (u^2, s^1_f) formulations lead, after a space-time discretization of (3.1) and (3.3), to the equivalent systems of nonlinear algebraic equations. Nevertheless, in practice, the performance of numerical algorithm would heavily depend on the choice of primary variables. In particular it is well known that the use of the formulation based on u^1 and u^2 has to be avoided when modeling imbibition in very dry soil. This is explained by the the fact that applying Newton-Raphson method (or some other linearization scheme) for solving nonlinear problems resulting from both formulation breakes the equivalence.

Next, let's assume that the capillary pressure is neglected in the fracture network domain (see Figure 3.1b). In that case both S^1_f and its inverse are set-valued, which

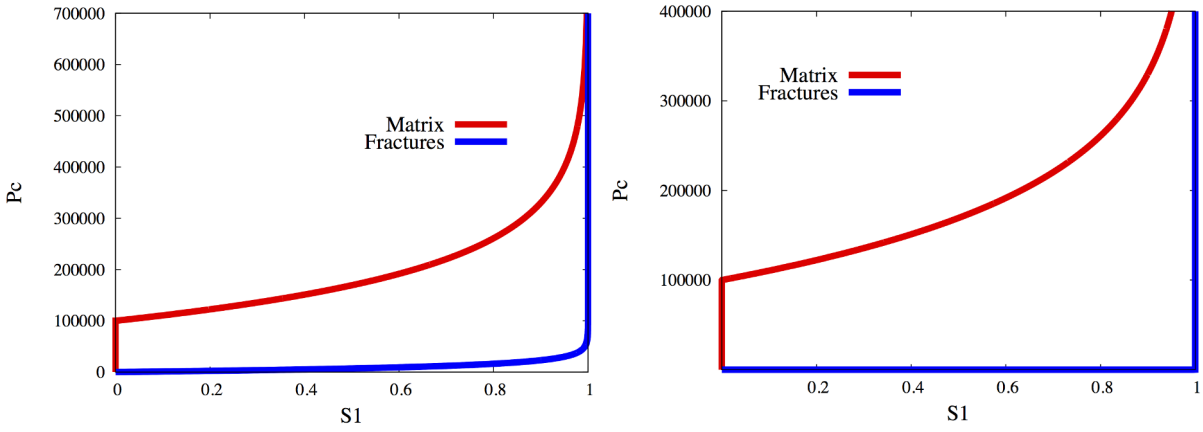

(a) S_m^1 and S_f^1 are single-valued (b) S_m^1 is single-valued, S_f^1 is set-valued

Figure 3.1: Typical form of capillary pressure curves in matrix and fracture domains.

in particular implies that neither (u^2, s_f^1) nor (u^2, u^1) can be used as a pair of primary variables for the whole range of values of saturation and capillary pressure. Instead one may switch, as capillary pressure grows, from (u^2, s_f^1) to (u^2, u^1), and even possibly from (u^2, u^1) to (u^2, s_m^1) for $u^1 - u^2 \geq p_{ent,m}$. Note that if the capillary pressure in the fracture domain is very small, but not strictly zero one cannot expect the numerical scheme based on (u^2, s_f^1) formulation to be computationally efficient.

Finally, let us remark that there is no reason to restrict the choice of primary variables to the set of natural variables, that is to say, to u^2, u^1, s_m^1 and s_f^1. Consider the functions

$$\mathcal{P} \text{ and } (\mathcal{S}_l^1)_{l=m,f} \tag{3.5}$$

defined on an open convex set $\mathcal{I} \subset \mathbb{R}$ such that $\mathcal{P}(\mathcal{I}) = \mathbb{R}^+$ and such that for $\tau \in \mathcal{I}$

$$\mathcal{S}_l^1(\tau) \in S_l^1(\mathcal{P}(\tau)) \text{ for all } l = m, f \tag{3.6}$$

Then the couple (u^2, τ) is an admissible couple of primary unknowns with

$$u^1 = u^2 + \mathcal{P}(\tau) \text{ and } s_l^1 = \mathcal{S}_l^1(\tau),\ l = m, f.$$

The map $\tau \mapsto (\mathcal{P}(\tau), \mathcal{S}_l^1(\tau))$, $l = m, f$, can be seen as the parametrization of the curve S_l^1. The parametrization (3.5) is not uniquely defined by (3.6) even under some additional regularity assumptions (see Proposition 3.2.1) and hence one can try to choose the functions $\mathcal{P}(\tau)$ and $\mathcal{S}_l^1(\tau)$, $l = m, f$, in order to improve the convergence of the nonlinear solver.

The remaining of this Chapter is organized as follows. In the next section we detail the parametrization approach presented above and provide the extension of the VAG discretization accounting for general monotone capillary pressure graphs related to multiple rocktypes, and finally we present numerical experiments, which aims to compare the classical pressure-saturation formulations with more advanced parametrizations following the above ideas.

3.2 Parametrization of Saturation Curves at the Rocktype Interfaces

Assuming that $S_m^1(\mathbf{x},\cdot)$ and $S_f^1(\mathbf{x},\cdot)$ are single valued, the discretization of the two-phase flow hybrid dimensional model using (u^1,u^2) as primary variables is presented in Subsection 2.5.

In this section, the upwind VAG or HFV finite volume discretization (2.12)-(2.10)-(2.11)-(2.13) is extended to the case of the inverse capillary pressure graphs satisfying (A_2).

Let $J = J_m \cup J_f$, for all $K \in \mathcal{M}$ we set

$$\chi_K = \{j_K\}.$$

For all $\sigma \in \mathcal{F}_\Gamma$ we set

$$\chi_\sigma = \{j_\sigma\} \cup \left(\bigcup_{\{K \,|\, \sigma \in \mathcal{F}_K\}} \{j_K\} \right).$$

For all $\nu \in dof \setminus (\mathcal{M} \cup \mathcal{F}_\Gamma)$ we set

$$\chi_\nu = \left(\bigcup_{\{K \,|\, \nu \in dof_{\partial K}\}} \{j_K\} \right) \cup \left(\bigcup_{\{\sigma \,|\, \nu \in dof_{\partial\sigma}\}} \{j_\sigma\} \right).$$

Roughly speaking, for each $\nu \in dof$ the set $\chi_\nu \in 2^J$ denote the collection of rocktypes intersecting at the degree of freedom ν. We finally define

$$\chi_{\mathcal{D}} = \{\chi_\nu, \nu \in dof\},$$

where $\chi_{\mathcal{D}}$ is seen as a subset of 2^J.

The following proposition justifies the fact that a pair of unknowns is sufficient at any degrees of freedom located on the rocktype intersection.

Proposition 3.2.1 *Let $\chi \in \chi_{\mathcal{D}}$ and $\left(S_j^1\right)_{j\in\chi}$ be a finite family of maximal monotone graphs with domain $\mathbb{R}$ and such that $S_j^1(p) \subset [0,1]$ for all $p \in \mathbb{R}$ and $j \in \chi$. Then there exists a family of continuous piecewise differentiable functions $\mathcal{P}_\chi$ and $\left(\mathcal{S}_{\chi,j}^1\right)_{j\in\chi}$ defined on an open convex set $\mathcal{I} \subset \mathbb{R}$ such that $\mathcal{P}_\chi(\mathcal{I}) = \mathbb{R}$ and such that for $\tau \in \mathcal{I}$ and $j \in \chi$*

$$\mathcal{S}_{\chi,j}^1(\tau) \in S_j^1(\mathcal{P}_\chi(\tau)); \tag{3.7}$$

moreover they can be chosen such that the following non-degeneracy condition

$$\sum_{j\in\chi} \frac{\mathrm{d}}{\mathrm{d}\tau} \left(\mathcal{S}_{\chi,j}^1(\tau), \mathcal{P}_\chi(\tau)\right) \neq (0,0) \tag{3.8}$$

is satisfied for a.e. $\tau \in \mathcal{I}$. In addition, without loss of generality on can assume that $\mathcal{S}_{\chi,j}^1{}'(\tau), \mathcal{P}_\chi'(\tau) \geq 0$ for a.e. $\tau \in \mathcal{I}$.

For all $\chi \in \chi_{\mathcal{D}}$ let $\mathcal{P}_\chi$ and $\left(\mathcal{S}^1_{\chi,j}\right)_{j\in\chi}$ be some family of non decreasing functions associated with the family of graphs $\left(S^1_j\right)_{j\in\chi}$ and satisfying (3.7) and (3.8).

The saturations are defined by

$$\left\{\begin{array}{ll} S^{1,n}_K = \mathcal{S}^1_{\chi_K,j_K}(\tau^n_K), \quad S^{2,n}_K = 1 - S^{1,n}_K & \text{for all } K \in \mathcal{M}, \\ S^{1,n}_\sigma = \mathcal{S}^1_{\chi_\sigma,j_\sigma}(\tau^n_\sigma), \quad S^{2,n}_\sigma = 1 - S^{1,n}_\sigma & \text{for all } \sigma \in \mathcal{F}_\Gamma, \\ S^{1,n}_{K,\nu} = \mathcal{S}^1_{\chi_\nu,j_K}(\tau^n_\nu), \quad S^{2,n}_{K,\nu} = 1 - S^{1,n}_{K,\nu} & \text{for all } K \in \mathcal{M}, \nu \in dof_{\partial K}, \\ S^{1,n}_{\sigma,\nu} = \mathcal{S}^1_{\chi_\nu,j_\sigma}(\tau^n_\nu), \quad S^{2,n}_{\sigma,\nu} = 1 - S^{1,n}_{\sigma,\nu} & \text{for all } \sigma \in \mathcal{F}_\Gamma, \nu \in dof_{\partial\sigma}, \end{array}\right. \tag{3.9}$$

and the water pressures by

$$\left\{\begin{array}{ll} u^{2,n}_K = u^{1,n}_K + \mathcal{P}_{\chi_K}(\tau^n_K) & \text{for all } K \in \mathcal{M}, \\ u^{2,n}_\sigma = u^{1,n}_\sigma + \mathcal{P}_{\chi_\sigma}(\tau^n_\sigma) & \text{for all } \sigma \in \mathcal{F}_\Gamma, \\ u^{2,n}_\nu = u^{1,n}_\nu + \mathcal{P}_{\chi_\nu}(\tau^n_\nu) & \text{for all } \nu \in dof \setminus (\mathcal{M} \cup \mathcal{F}_\Gamma). \end{array}\right. \tag{3.10}$$

The new scheme consist in finding $u^{1,n}, \tau^{2,n} \in X^0_{\mathcal{D}}$, $n = 1, \cdots, N$, satisfying (2.12), (2.13) along with (3.9)-(3.10).

3.3 Implementation and Numerical Experiments

In this section we present numerical experiments which aims to compare the robustness and efficiency of the classical pressure-saturation formulation with more advanced choices of primary unknowns which are implemented using the graph parametrization approach presented above. The pressure-pressure formulation is excluded from the comparison since is has a very poor efficiency when dealing with dry (s^1 close to 1) media. In practice, the pressure-pressure formulation has also been tested and it failed to converge for matrix fracture capillarity ratio $\frac{b_m}{b_f}$ larger than 10 (see below for the definition of this ratio).

We consider only two rocktypes, the matrix rocktype denoted by $j = m$ and the fracture (or fault) rocktype denoted by $j = f$. The phase mobilities are defined for both rocktypes $j = m, f$ and for $\alpha = 1, 2$ by the following Corey law

$$k^\alpha_j(s^\alpha, \mathbf{x}) = \frac{k^\alpha_{j,max}(\bar{s}^\alpha)^{n^\alpha_j}}{\mu^\alpha}, \tag{3.11}$$

where $\bar{s}^2 = \frac{s^2 - s^2_{r,j}}{1 - s^2_{r,j} - s^1_{r,j}}$, and $\bar{s}^1 = \frac{s^1 - s^1_{r,j}}{1 - s^1_{r,j} - s^2_{r,j}}$ are the reduced saturations and μ^α is the phase viscosity.

The capillary pressure/saturation relation are also given for the matrix ($j = m$) and fracture ($j = f$) rocktypes by the following Corey law

$$S^1_j(p) = \left\{\begin{array}{ll} 0 & \text{if } \; p - p_{ent,j} < 0, \\ 1 - e^{-\frac{p - p_{ent,j}}{b_j}} & \text{if } \; p - p_{ent,j} \geq 0, \end{array}\right. \tag{3.12}$$

where the parameter $p_{ent,j} > 0$ stands for the entry pressure. Both b_j and $p_{ent,j}$ depend on the rocktype $j = m, f$. Figure 3.2 exhibits, the typical shape of the matrix and fracture

capillary pressure graphs P_{cm} and P_{cf}, which are the multi-valued inverses of S_m^1 and S_f^1 respectively. Remark that, when b_j tends to 0, the graph of S_j^1 tends to the graph of the multi-valued Heaviside function centered at $p = p_{ent,j}$. The following numerical experiments will assess the efficiency of the different choices of primary unknowns for different values of the parameters b_j and $p_{ent,j}$, $j = m, f$.

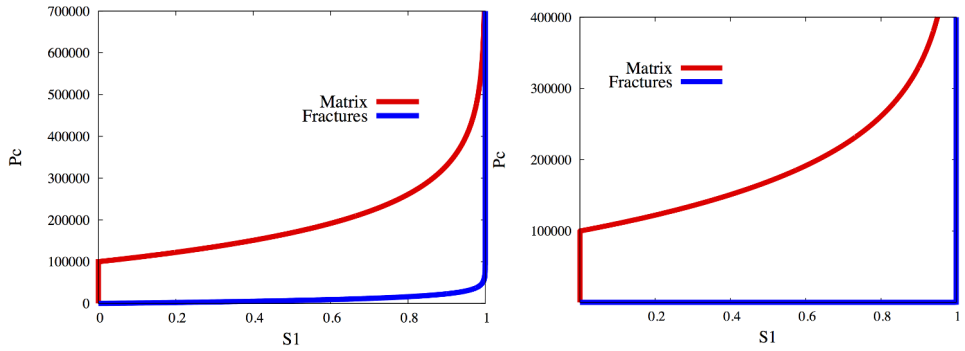

Figure 3.2: The graphs of the capillary pressures P_{cm} in the matrix, and P_{cf} in the fractures for $b_m = 10^5$ Pa, $b_f = 10^4$ Pa, $p_{ent,m} = 10^5$ Pa, $p_{ent,f} = 0$ (left) and $b_m = 10^5$ Pa, $b_f = 0$, $p_{ent,m} = 10^5$ Pa, $p_{ent,f} = 0$ (right).

The following numerical experiments compare the pressure saturation formulation using non wetting phase pressure and the non wetting phase saturation as the primary unknowns with some more advanced parametrizations inspired by variable switch techniques. Since only one fracture and one matrix rocktypes are considered, the set $\chi_{\mathcal{D}}$ is equal to

$$\chi_{\mathcal{D}} = \{\{m\}, \{m, f\}\},$$

where $\chi = \{m\}$ corresponds to degrees of freedom located in the matrix only and $\chi = \{m, f\}$ corresponds to degrees of freedom located at the matrix fracture interfaces. In the following numerical experiments, the primary unknowns for $\chi = \{m\}$ are fixed for both formulations to (u^1, s_m^1) since this is an efficient and simple choice for a single rocktype. The choices of parametrization at the matrix fracture interfaces i.e. for $\chi = \{m, f\}$ will result in functions $\mathcal{S}_m^1(\tau)$, $\mathcal{S}_f^1(\tau)$, $\mathcal{P}(\tau)$, which we define below for several types of capillary pressures curves given by Corey law. We will distinguish the following five cases ordered with increasing complexity:

(C1) $b_m > 0$, $0 < b_f < b_m$, $p_{ent,m} = p_{ent,f} = 0$;

(C2) $b_m > 0$, $b_f = 0$, $p_{ent,m} = p_{ent,f} = 0$;

(C3) $b_m > 0$, $0 < b_f < b_m$, $p_{ent,m} > 0$, $p_{ent,f} = 0$;

(C4) $b_m > 0$, $b_f = 0$, $p_{ent,m} > 0$, $p_{ent,f} = 0$;

(C5) $b_m = 0$, $b_f = 0$, $p_{ent,m} > 0$, $p_{ent,f} = 0$.

The choices of the primary unknowns will be compared in terms numerical behavior of the simulations based on the number of linear and nonlinear iterations and on the CPU time.

3.3.1 Parametrizations for the pressure-saturation and variable-switch formulations

C1 and C2 cases

In this case, the entry pressures are both set to zero i.e. $p_{ent,j} = 0$, $j = m, f$ leading to the following Corey laws

$$S_j^1(p) = \begin{cases} 0 & \text{if } p < 0, \\ 1 - e^{-\frac{p}{b_j}} & \text{if } p \geq 0, \end{cases} \tag{3.13}$$

and we assume that $\frac{b_m}{b_f} > 1$. Figure 3.3 exhibits the capillary pressure graphs P_{cm} and P_{cf} for $b_m = 10^5$ Pa and the ratio $\frac{b_m}{b_f} = 10$.

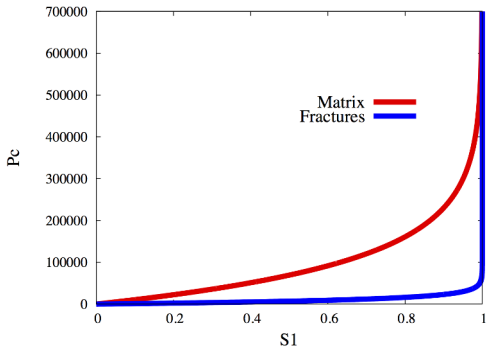

Figure 3.3: P_{cm} in the matrix, and P_{cf} in the fractures for $b_m = 10^5$ Pa, $b_f = 10^4$ Pa, $p_{ent,m} = p_{ent,f} = 0$.

Pressure-saturation formulation: The formulation is defined by the following set of functions

$$\begin{cases} \mathcal{S}_m^1(\tau) = \tau \\ \mathcal{S}_f^1(\tau) = P_{cf}^{-1}(P_{cm}(\tau)) = 1 - (1-\tau)^{\frac{b_m}{b_f}} \\ \mathcal{P}(\tau) = P_{cm}(\tau) = -b_m \ln(1-\tau) \end{cases} \tag{3.14}$$

with $\tau \in [0, 1)$.

When $\frac{b_m}{b_f}$ goes to infinity (i.e. when the capillary pressure in the fracture network goes to zero), the function $\mathcal{S}_f^1(\tau)$ tends to the graph, which is multi-valued at $\tau = 0$. Numerically, this would lead to the lost of robustness for large values $\frac{b_m}{b_f}$.

The pressure-saturation formulation is compared to the variable switch $(u^1, s_f^1)/(u^1, s_m^1)$ formulation picking the "steepest" saturation unknown, that is to say the one which has a largest derivative with respect to the capillary pressure.

Variable-switch formulation: this formulation is obtained using the conditions (3.7) in the framework of Proposition 3.2.1 to which we add the following conditions

$$\max\left(\frac{\mathrm{d}\mathcal{S}_m^1}{\mathrm{d}\tau}, \frac{\mathrm{d}\mathcal{S}_f^1}{\mathrm{d}\tau}\right) = 1$$

and

$$\mathcal{S}_m^1(0) = \mathcal{S}_f^1(0) = 0.$$

The computations give (see Figure 3.4):

$$\mathcal{S}_f^1(\tau) = \begin{cases} \tau, & \tau \in [0, \tau_1), \\ P_{cf}^{-1}(P_{cm}(\tau - \tau_1 + P_{cm}^{-1}(P_{cf}(\tau_1)))) = 1 - (\tau_1 + (1-\tau_1)^{\frac{b_f}{b_m}} - \tau)^{\frac{b_m}{b_f}}, & \tau \in [\tau_1, \tau_2), \end{cases} \tag{3.15}$$

$$\mathcal{S}_m^1(\tau) = \begin{cases} P_{cm}^{-1}(P_{cf}(\tau)) = 1 - (1-\tau)^{\frac{b_f}{b_m}}, & \tau \in [0, \tau_1), \\ \tau - \tau_1 + P_{cm}^{-1}(P_{cf}(\tau_1)) = \tau - \tau_1 + 1 - (1-\tau_1)^{\frac{b_f}{b_m}}, & \tau \in [\tau_1, \tau_2), \end{cases} \tag{3.16}$$

$$\mathcal{P}(\tau) = \begin{cases} P_{cf}(\mathcal{S}_f^1(\tau)) = -b_f \ln(1-\tau), & \tau \in [0, \tau_1), \\ P_{cm}(\mathcal{S}_m^1(\tau)) = -b_m \ln(\tau_1 + (1-\tau_1)^{\frac{b_f}{b_m}} - \tau), & \tau \in [\tau_1, \tau_2), \end{cases} \tag{3.17}$$

where $\tau_1 = 1 - (\frac{b_f}{b_m})^{\frac{b_m}{b_m - b_f}}$ and $\tau_2 = \tau_1 + (1-\tau_1)^{\frac{b_f}{b_m}}$. It is worth noticing that, by construction, the derivatives of the functions $\mathcal{S}_f^1(\tau)$, $\mathcal{S}_m^1(\tau)$ and $\mathcal{P}(\tau)$ are continuous at $\tau = \tau_1$.

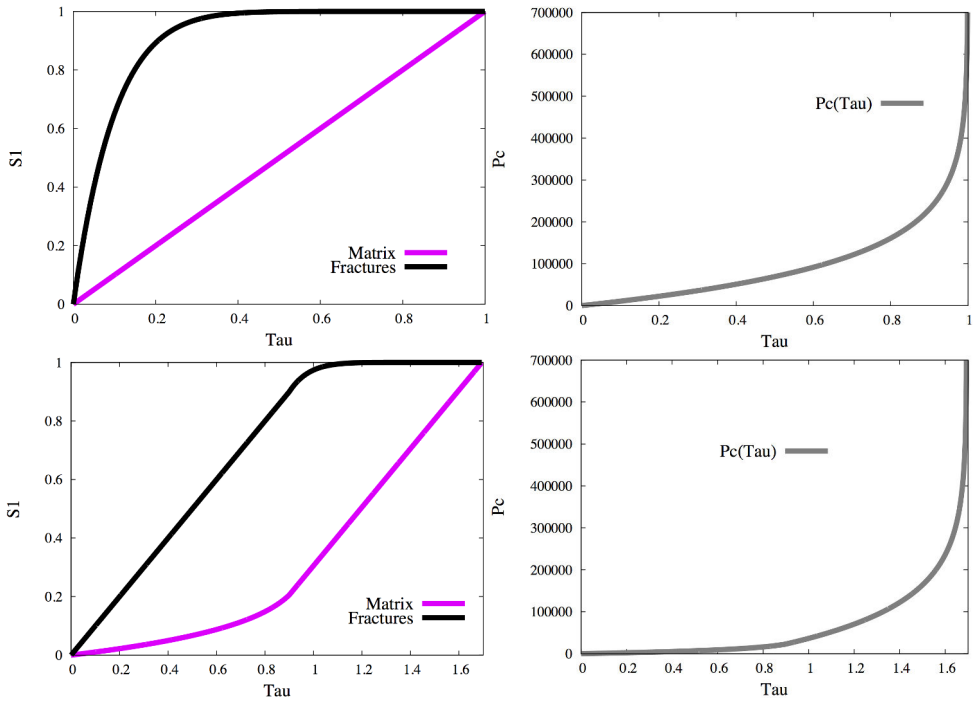

Figure 3.4: $\mathcal{S}_m^1(\tau)$, $\mathcal{S}_f^1(\tau)$, and $\mathcal{P}(\tau)$ curves for the pressure-saturation formulation (on the top) and for variable switch formulation (at the bottom), obtained for $b_m = 10^5$ Pa, $b_f = 10^4$ Pa, and $p_{ent,m} = p_{ent,f} = 0$.

When, for a fixed b_m, the ratio $\frac{b_m}{b_f}$ goes to infinity, the variable switch parametrization tends to the following formulation (see Figure 3.5):

$$\mathcal{S}_f^1(\tau) = \begin{cases} \tau, & \tau \in [0, \tau_1), \\ 1, & \tau \in [\tau_1, \tau_2), \end{cases} \tag{3.18}$$

$$\mathcal{S}_m^1(\tau) = \begin{cases} 0, & \tau \in [0, \tau_1), \\ \tau - \tau_1, & \tau \in [\tau_1, \tau_2), \end{cases} \tag{3.19}$$

$$\mathcal{P}(\tau) = \begin{cases} 0, & \tau \in [0, \tau_1), \\ (P_{cm}(\mathcal{S}_m^1(\tau)) = -b_m \ln(1 - (\tau - \tau_1)), & \tau \in [\tau_1, \tau_2), \end{cases} \tag{3.20}$$

with $\tau_1 = 1$, $\tau_2 = 2$. Note that this limit case of a vanishing capillary pressure in the fractures cannot be accounted for by the pressure-saturation formulation.

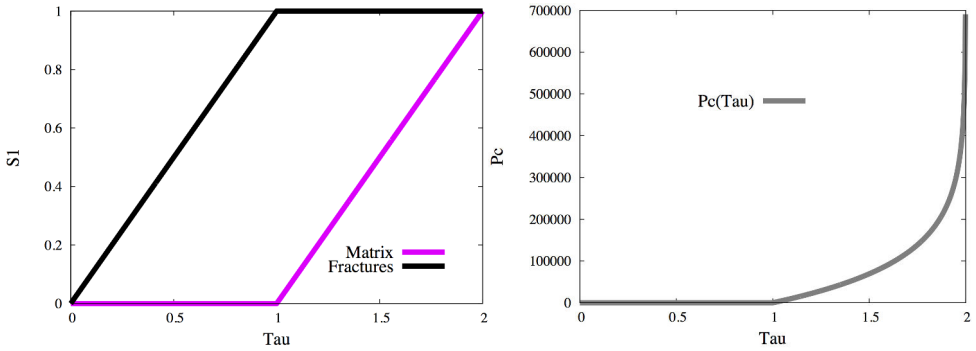

Figure 3.5: $\mathcal{S}_m^1(\tau)$, $\mathcal{S}_f^1(\tau)$, and $\mathcal{P}(\tau)$ curves for the variable switch formulation obtained for $b_m = 10^5$ Pa, $b_f = 0$, and $p_{ent,m} = p_{ent,f} = 0$.

C3 and C4 cases

Next we consider the test cases with non zero entry pressure in the matrix $p_{ent,m} > 0$ and with zero entry pressure in the fractures $p_{ent,f} = 0$. The graphs of P_{cj}, $j = m, f$ are represented in Figure 3.2 for $p_{ent,m} = 10^5$ Pa, $b_m = 10^5$ Pa, and $b_f = 10^4$ Pa.

Pressure-saturation formulation: At the matrix fracture interfaces the capillary pressure (see Figure 3.2) can not be expressed as a function of s_m^1 for $p < p_{ent,m}$, but it is however a function of s_f^1. Hence we choose s_f^1 as primary unknown at the matrix fracture interfaces, which leads to

$$\mathcal{S}_f^1(\tau) = \tau, \qquad \mathcal{P}_m(\tau) = (S_f^1)^{-1}(\tau) = -b_f \ln(1-\tau),$$

and

$$\mathcal{S}_m^1(\tau) = \begin{cases} 0, & \tau < S_f^1(p_{ent,m}) = 1 - e^{\frac{-p_{ent,m}}{b_f}}, \\ P_{cm}^{-1}(P_{cf}(\tau)) = 1 - e^{\frac{p_{ent,m}}{b_m}}(1-\tau)^{\frac{b_f}{b_m}}, & \tau \geq 1 - e^{\frac{-p_{ent,m}}{b_f}}. \end{cases}$$

Remark that when $\frac{b_m}{b_f}$ goes to infinity the function $P_{cm}^{-1}(P_{cf}(\tau))$ becomes multi-valued at $\tau = 1$ which results in severe numerical instabilities. As a result, we were unable to obtain the convergence of the nonlinear solver for $\frac{b_m}{b_f} > 10$.

Variable-switch formulation: When $b_f = 0$ it is clear that the capillary pressure is no longer a function of the saturation for its values in the interval $(0, p_{ent,m})$. Actually, for those values of capillary pressure the relevant pair of unknowns is (u^2, u^1). This leads to the following formulation, which roughly speaking switches between the three unknowns s_f^1, P_c, and s_m^1

$$\mathcal{S}_f^1(\tau) = \begin{cases} \tau, & \tau \in [0, \tau_1), \\ P_{cf}^{-1}(p_{ent,m}(\tau - \tau_1) + P_{cf}(\tau_1)) = 1 - (1-\tau_1)e^{-\frac{p_{ent,m}}{b_f}(\tau-\tau_1)}, & \tau \in [\tau_1, \tau_2), \\ P_{cf}^{-1}(P_{cm}(\tau - \tau_2)) = 1 - (1-(\tau-\tau_2))^{\frac{b_m}{b_f}} e^{\frac{-p_{ent,m}}{b_f}}, & \tau \in [\tau_2, \tau_3], \end{cases} \quad (3.21)$$

$$\mathcal{S}_m^1(\tau) = \begin{cases} 0, & \tau \in [0, \tau_2), \\ \tau - \tau_2, & \tau \in [\tau_2, \tau_3], \end{cases} \tag{3.22}$$

$$\mathcal{P}(\tau) = \begin{cases} P_{cf}(\tau) = -b_f \ln(1-\tau), & \tau \in [0, \tau_1), \\ p_{ent,m}(\tau - \tau_1) + P_{cf}(\tau_1) = p_{ent,m}(\tau - \tau_1) - b_f \ln(1-\tau_1), & \tau \in [\tau_1, \tau_2), \\ P_{cm}(\tau - \tau_2) = p_{ent,m} - b_m \ln(1-(\tau-\tau_2)), & \tau \in [\tau_2, \tau_3]. \end{cases} \tag{3.23}$$

One can see that $P_{cf}(\tau_1) < p_{ent,m}$ and the derivatives of the functions $\mathcal{S}_f^1(\tau)$, $\mathcal{S}_m^1(\tau)$, $\mathcal{P}(\tau)$ are continuous at $\tau = \tau_1$, where $\tau_1 = 1 - \frac{b_f}{p_{ent,m}}$. Also we define $\tau_2 = \tau_1 + 1 - \frac{P_{cf}(\tau_1)}{p_{ent,m}}$ and $\tau_3 = \tau_2 + 1$ such that $\mathcal{P}(\tau_2) = p_{ent,m}$ and $\mathcal{S}_m^1(\tau_3) = 1$. When the ratio $\frac{b_m}{b_f}$ goes to infinity (see Figure 3.7) the following formulas are recovered

$$\mathcal{S}_f^1(\tau) = \begin{cases} \tau, & \tau \in [0, \tau_1), \\ 1, & \tau \in [\tau_1, \tau_3), \end{cases} \tag{3.24}$$

$$\mathcal{S}_m^1(\tau) = \begin{cases} 0, & \tau \in [0, \tau_2), \\ \tau - \tau_2, & \tau \in [\tau_2, \tau_3), \end{cases} \tag{3.25}$$

$$\mathcal{P}(\tau) = \begin{cases} 0, & \tau \in [0, \tau_1), \\ p_{ent,m}(\tau - \tau_1), & \tau \in [\tau_1, \tau_2), \\ P_{cm}(\mathcal{S}_m^1(\tau) = -b_m \ln(1-(\tau-\tau_2)) + p_{ent,m}, & \tau \in [\tau_2, \tau_3), \end{cases} \tag{3.26}$$

where $\tau_1 = 1$, $\tau_2 = 2$, and $\tau_3 = 3$.

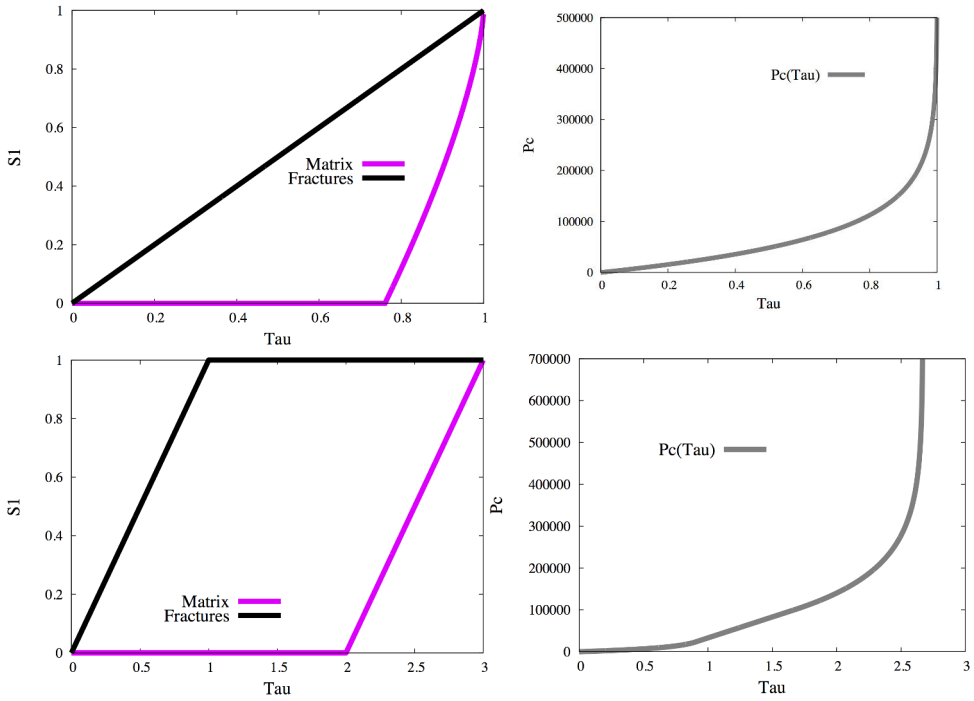

Figure 3.6: $\mathcal{S}_m^1(\tau)$, $\mathcal{S}_f^1(\tau)$, and $\mathcal{P}(\tau)$ curves for the pressure-saturation formulation (on the top) and variable switch formulation (at the bottom) for $b_m = 10^5$ Pa, $b_f = 10^4$ Pa, $p_{ent,m} = 10^5$ Pa, $p_{ent,f} = 0$.

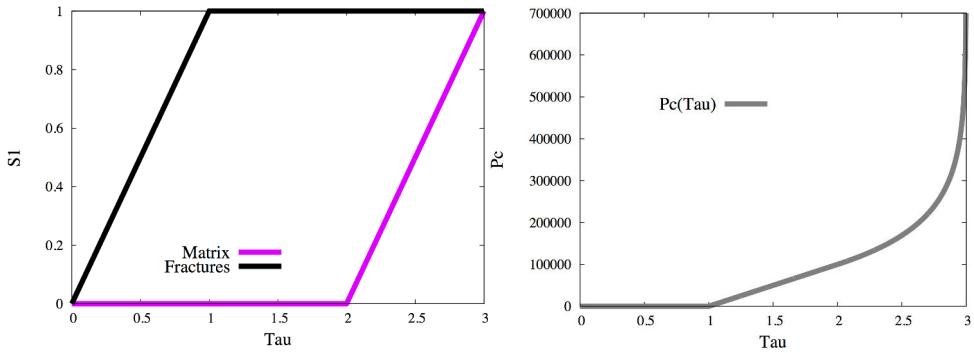

Figure 3.7: $\mathcal{S}_m^1(\tau)$, $\mathcal{S}_f^1(\tau)$, and $\mathcal{P}(\tau)$ curves for variable switch formulation for $b_m = 10^5$ Pa, $b_f = 0$, $p_{ent,m} = 10^5$ Pa, $p_{ent,f} = 0$.

C5 case

We consider the case $b_m = b_f = 0$, and $p_{ent,m} > 0$, and $p_{ent,f} = 0$ (see Figure 3.8). This test case can only be treated using the formulation involving multiple primary variable switches.

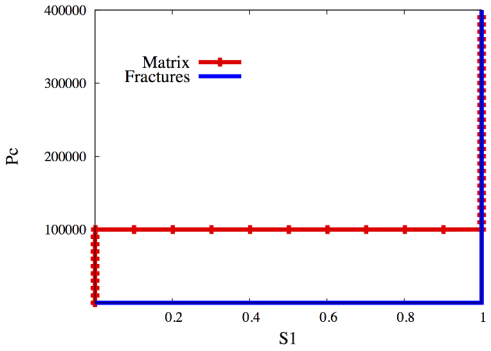

Figure 3.8: The capillary pressure curves P_{cm} in the matrix and P_{cf} in the fractures for $b_m = b_f = 0$, $p_{ent,m} = 10^5$ Pa, and $p_{ent,f} = 0$.

In the spirit of the previous case we define the following parametrization:

$$\mathcal{S}_f^1(\tau) = \begin{cases} \tau, & \tau \in [0, \tau_1), \\ 1, & \tau \in [\tau_1, \tau_3), \end{cases} \tag{3.27}$$

$$\mathcal{S}_m^1(\tau) = \begin{cases} 0, & \tau \in [0, \tau_2), \\ \tau - \tau_2, & \tau \in [\tau_2, \tau_3], \end{cases} \tag{3.28}$$

$$\mathcal{P}(\tau) = \begin{cases} 0, & \tau \in [0, \tau_1), \\ p_{ent,m}(\tau - \tau_1), & \tau \in [\tau_1, \tau_2), \\ p_{ent,m}, & \tau \in [\tau_2, \tau_3], \end{cases} \tag{3.29}$$

with $\tau_1 = 1$, $\tau_2 = 2$, and $\tau_3 = 3$.

The curves $\mathcal{S}_m^1$, $\mathcal{S}_f^1$ and $\mathcal{P}$ are exhibited in Figure 3.9.

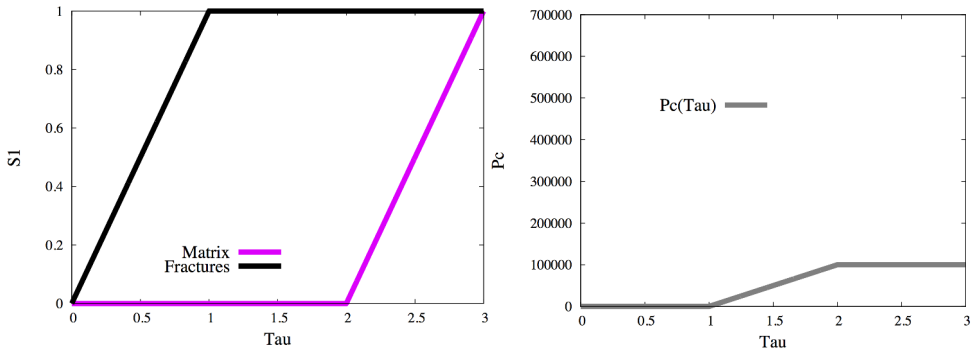

Figure 3.9: $\mathcal{S}_m^1(\tau)$, $\mathcal{S}_f^1(\tau)$, and $\mathcal{P}(\tau)$ curves for variable switch formulation for $b_m = b_f = 0$, $p_{ent,m} = 10^5$ Pa, and $p_{ent,f} = 0$.

3.3.2 Tight gas test case

The family of test cases presented here simulates the liquid gas two phase Darcy flow in a tight gas reservoir. The liquid phase denoted by w corresponds to the wetting phase 2 and the gas phase denoted by g corresponds to the non wetting phase 1. The data set is similar to Example 2 of [25] except for the choice of the capillary pressure curves. The reservoir is defined by the domain $\Omega = (-500, 500) \times (-250, 250) \times (-100, 100)$ (in meters). Three transverse fractures $\Gamma_i, i = 1, 2, 3$ of width $d_f = 0.02$ m are initiated by hydraulic fracturing from a horizontal well. They are defined by the squares $\{x_i\} \times (-50, 50) \times (-50 \times 50)$ with $x_1 = -250$, $x_2 = 0$, $x_3 = +250$. An horizontal well of radius $r_w = 0.1$ m is located along $y = z = 0$ and perforates each fracture $\Gamma_i, i = 1, 2, 3$ in a triangular equilateral face of center $x_i, y = z = 0$ and of edge size 1 m. During the water injection phase, the water penetrates only a few tens of centimeters in the matrix due to the low permeability of the reservoir. Therefore in order to obtain an accurate water saturation in the neighbourhood of the fractures with a reasonnable number of cells, a strong anisotropic refinement is needed in the normal direction in the neihbourhood of each fracture. As exhibited in Figures 3.10 and 3.11 this anisotropic refinement is obtained using prismatic meshes with triangular base. In order to match the boundaries of these refined boxes with the surrounding tetrahedral mesh of the reservoir, a layer of pyramids is added around each fracture box as exhibited in Figure 3.10. The tetrahedral mesh matching the triangulation of the fracture box boundaries has been obtained using TetGen [59]. Table 3.1 summarizes the characteristics of the resulting hybrid mesh that will be used in the following numerical test cases. This mesh includes ten layers of prisms of thickness 0.1 m on both sides of each fracture.

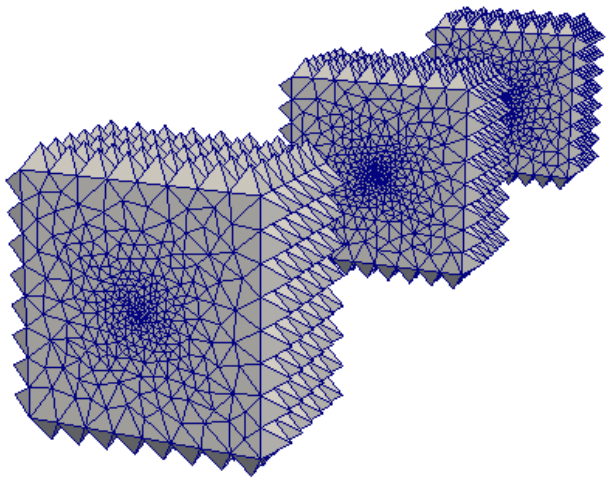

Figure 3.10: The prismatic meshes with their layer of pyramids for each refined box around each fracture located at the center of each box (the thickness of the prisms and pyramids has been enlarged for the sake of clarity).

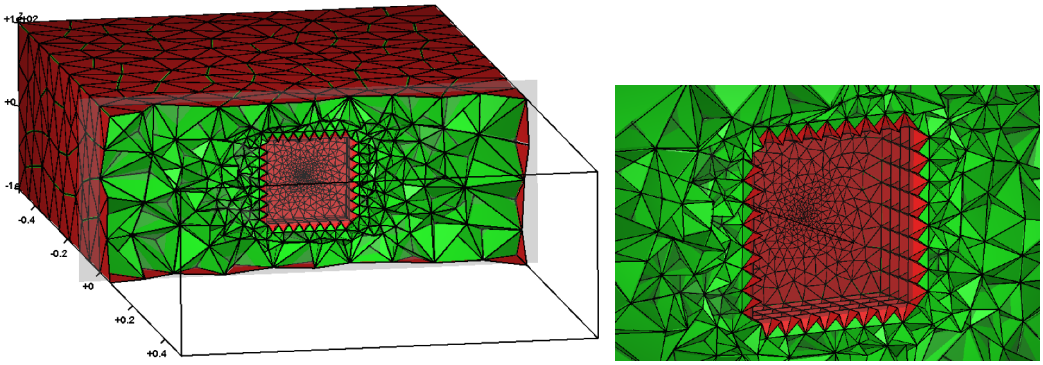

Figure 3.11: Connection of the prismatic mesh around one fracture with the surrounding tetrahedral mesh using a layer of pyramids (the thickness of the prisms and pyramids has been enlarged for the sake of clarity).

$\mathbf{N_{cells}}$	$\mathbf{N_{nodes}}$	$\mathbf{N_{FracF}}$	Linear system d.o.f.
232 920	45 193	1 634	46 827

Table 3.1: Number N_{cells} of cells, number N_{nodes} of nodes, number N_{FracF} of fracture faces and number of d.o.f. in the linear system after elimination of the cell d.o.f. (2 physical unknowns per d.o.f.).

In this test case the mobilities are defined by $s^w_{r,m} = 0.2$, $s^g_{r,m} = 0$, $k^w_{m,max} = 0.3$, $k^g_{m,max} = 0.6$, $n^w_m = 1.5$, $n^g_m = 3$ in the matrix, and by $s^w_{r,f} = s^g_{r,f} = 0$, $k^w_{f,max} = k^g_{f,max} = 1$, $n^w_f = n^g_f = 1$ in the fractures. The parameters of the Corey capillary pressures are fixed to $b_m = 10^5$ Pa for cases C1, C2, C3 and C4, and to $p_{ent,m} = 10^5$ Pa for cases C3, C4, and C5. For cases C1 and C3 we will investigate the set of values $b_f = 1, 10, 10^2, 10^3, 10^4$ Pa in the fractures.

The viscosities of the two phases are set to $\mu^w = 10^{-3}$ $\mu^g = 2.35\ 10^{-5}$ Pa.s, and their densities are fixed to the constant value $\rho^w = 1000$ kg/m^3 for the water phase, and to the perfect gas density $\rho^g(u^g) = \frac{M}{RT}u^g$ kg/m^3 for the gas phase with $M = 0.016$ Kg corresponding to methane and $R = 8.32$ J·mol^{-1} ·K^{-1}.The reservoir is initially at the liquid pressure $u^w = 400\ 10^5$ Pa, at the residual water saturation in the matrix and at water saturation close to 0 in the fractures obtained by the continuity of the capillary pressure at the matrix fracture interfaces. The permeability of the matrix is isotropic and set to $\Lambda_m = \lambda_m \mathrm{Id}$ with $\lambda_m = 2\ 10^{-17}$ m^2, very low compared with the permeability of the fractures $\Lambda_f = \lambda_f \mathrm{Id}$ with $\lambda_f = 2\ 10^{-12}$ m^2. The porosity is equal to $\phi_m = 0.1$ in the matrix and to $\phi_f = 0.3$ in the fractures.

The liquid is first injected at high hydraulic fracturing pressure $1000\ 10^5$ Pa fixed at each perforation during 1 day. This high pressure water injection phase mimics indeed the invasion of the matrix by fracturing fluid during hydraulic fracturing operations. After

injection, the well is closed during the next three days. The well is then put in production at a constant bottom pressure of 300 10^5 Pa during the next 296 days. Only a part of the invaded water will be back-produced in this early phase of production. The simulation runs over a period of 300 days and the nonlinear systems obtained at each time step are solved by a Newton-Raphson method. The time stepping is defined by an initial time step of 0.001 hour and a maximum time step of 0.05 days during the water injection period, of 0.1 days during the well closure, and of 5 days during the production period. If the Newton method does not converge after 35 iterations, the time step is chopped by a factor 2 and recomputed. The time step is increased by a factor 1.2 after each successful time step until it reaches the maximum time step. The stopping criteria on the relative residuals are fixed to 10^{-6} for the GMRes solver preconditioned by ILU0 and to 10^{-5} for the Newton method.

The numerical behavior of the simulations for both the variable switch and pressure-saturation formulations for cases C1 and C3, and for the variable switch formulation only for cases C2,C4 and C5, is exhibited in Tables 3.2, 3.3 and 3.4. These tables exhibit the number of successful time steps, the number of time step chops, the number of Newton iterations by successful time steps, the number of GMRes iterations by Newton iteration, and the CPU time.

The variable switch formulation turns out to be more efficient and more robust w.r.t. the value of $\frac{b_m}{b_f}$ both in terms of number of Newton iterations and the number of time step chops. Note that, as it can be expected, for $\frac{b_m}{b_f} = \infty$ the variable switch formulation performs similarly as for the case $\frac{b_m}{b_f} = 10^5$. As shown in Table 3.3, in the case of the entry pressure $p_{ent,m} = 10^5$ Pa, the pressure-saturation formulation fails to converge except for very small ratios while the variable switch formulation is still robust w.r.t. the ratio $\frac{b_m}{b_f}$. Table 3.4 shows that the good performance of the proposed formulation is maintained for the degenerate case C5 which confirms the efficiency of the proposed method. Note that, for this test case, we have adapted the Newton solver such that if the Newton iterate for the τ variable tries to jump from above to below the value $\tau_i = \tau_1, \tau_2$ (or from below to above), it is projected onto $\tau = \tau_i + \epsilon$ ($\tau = \tau_i - \epsilon$ correspondingly).

	pressure-saturation					variable switch				
$\frac{b_m}{b_f}$	$\mathbf{N_{\Delta t}}$	$\mathbf{N_{Chop}}$	$\mathbf{N_{Newton}}$	$\mathbf{N_{GMRes}}$	**CPU(s)**	$\mathbf{N_{\Delta t}}$	$\mathbf{N_{Chop}}$	$\mathbf{N_{Newton}}$	$\mathbf{N_{GMRes}}$	**CPU(s)**
10	226	2	4.2	25.9	4 638	226	2	4.3	26.2	5 523
10^2	294	21	10.7	20.1	14 557	246	8	7.5	22.2	9 016
10^3	297	22	11.7	19.7	16 183	225	1	5.5	24.2	6 245
10^4	304	24	12.9	19.8	17 742	225	1	4.8	25.1	5 492
10^5	313	26	12.8	19.6	18 346	235	4	5.4	23.9	6 260
∞	n/a	n/a	n/a	n/a	n/a	235	4	5.3	23.9	6 448

Table 3.2: Numerical results for the pressure-saturation and variable switch formulations for $b_m = 10^5$ Pa, $p_{ent,m} = p_{ent,f} = 0$, and different values of the ratio $\frac{b_m}{b_f}$: number $N_{\Delta t}$ of successful time steps, number N_{Chop} of time step chops, number N_{Newton} of Newton iterations per successful time step, number N_{GMRes} of GMRes iterations by Newton iteration, and CPU time in seconds.

	pressure-saturation					variable switch				
$\frac{b_m}{b_f}$	$\mathbf{N_{\Delta t}}$	$\mathbf{N_{Chop}}$	$\mathbf{N_{Newton}}$	$\mathbf{N_{GMRes}}$	**CPU(s)**	$\mathbf{N_{\Delta t}}$	$\mathbf{N_{Chop}}$	$\mathbf{N_{Newton}}$	$\mathbf{N_{GMRes}}$	**CPU(s)**
2	221	0	3	29.2	3 937	221	0	3.1	28.9	4 479
10	398	52	9.9	20.2	23 400	262	13	6.8	22.7	10 378
10^2	n/c	n/c	n/c	n/c	n/c	269	14	9.9	20.8	14 185
10^3	n/c	n/c	n/c	n/c	n/c	285	18	8.9	20.1	13 740
10^4	n/c	n/c	n/c	n/c	n/c	242	6	6.9	22.8	9 067
10^5	n/c	n/c	n/c	n/c	n/c	276	16	7.5	21.3	11 516
∞	n/a	n/a	n/a	n/a	n/a	299	22	8.1	19.1	10 770

Table 3.3: Numerical results for the pressure-saturation and variable switch formulations for $b_m = 10^5$ Pa, $p_{ent,m} = 10^5$ Pa, $p_{ent,f} = 0$ and different values of the ratio $\frac{b_m}{b_f}$: number $N_{\Delta t}$ of successful time steps, number N_{Chop} of time step chops, number N_{Newton} of Newton iterations per successful time step, number N_{GMRes} of GMRes iterations by Newton iteration, and CPU time in seconds.

variable switch				
$\mathbf{N_{\Delta t}}$	$\mathbf{N_{Chop}}$	$\mathbf{N_{Newton}}$	$\mathbf{N_{GMRes}}$	**CPU(s)**
221	0	5.8	26.3	5 948

Table 3.4: Numerical results for the pressure-saturation and variable switch formulations for $b_m = b_f = 0$, $p_{ent,m} = 10^5$ Pa, and $p_{ent,f} = 0$: number $N_{\Delta t}$ of successful time steps, number N_{Chop} of time step chops, number N_{Newton} of Newton iterations per successful time step, number N_{GMRes} of GMRes iterations by Newton iteration, and CPU time in seconds.

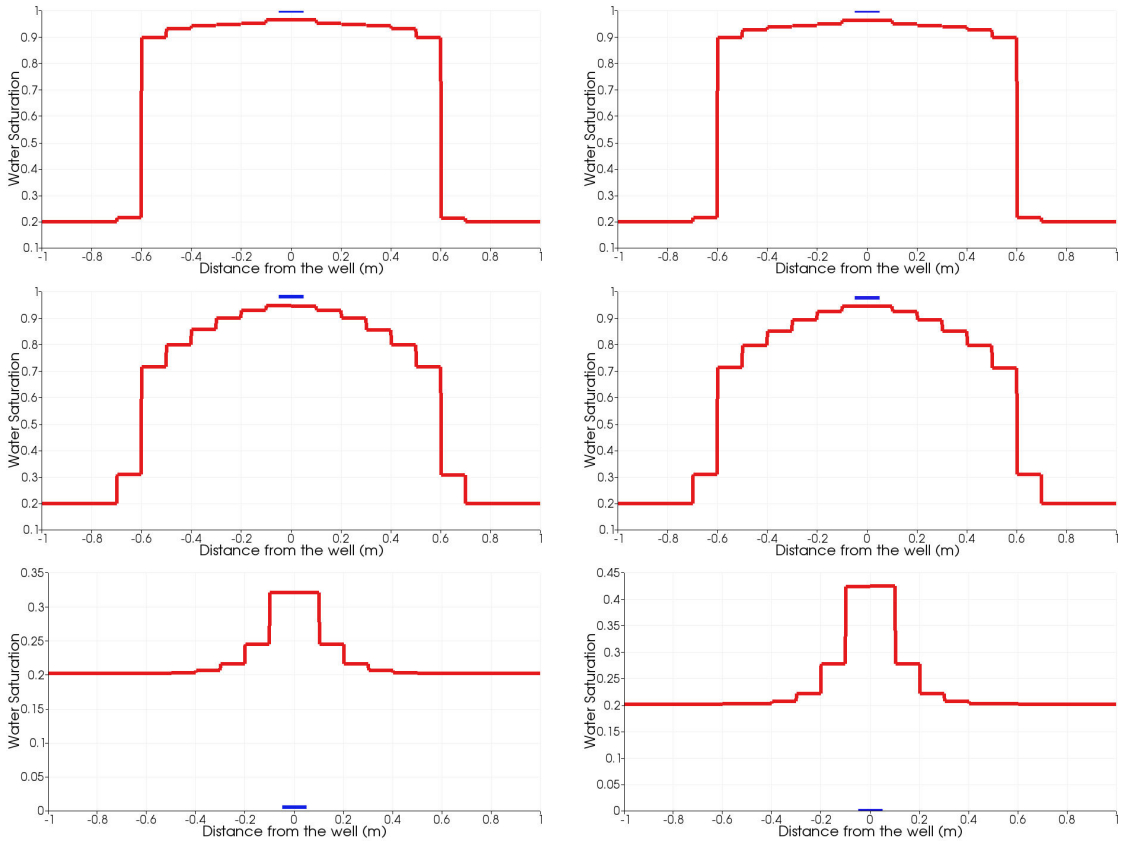

Figure 3.12: Water saturation in the perforated face in the fracture at $\mathbf{x} = 0$ (blue) and cut of the water saturation in the matrix (red) along the line $y = z = 0$ as a function of the distance to the fracture at the end of each simulation period $t = 1$ day (top), $t = 4$ days (middle) and $t = 300$ days (bottom). The left plots (a) correspond to $b_m = 10^5$ Pa, $b_f = 10^4$ Pa, $p_{ent,m} = p_{ent,f} = 0$, and the right plots (b) to $b_m = 10^5$ Pa, $b_f = 0$, $p_{ent,m} = p_{ent,f} = 0$

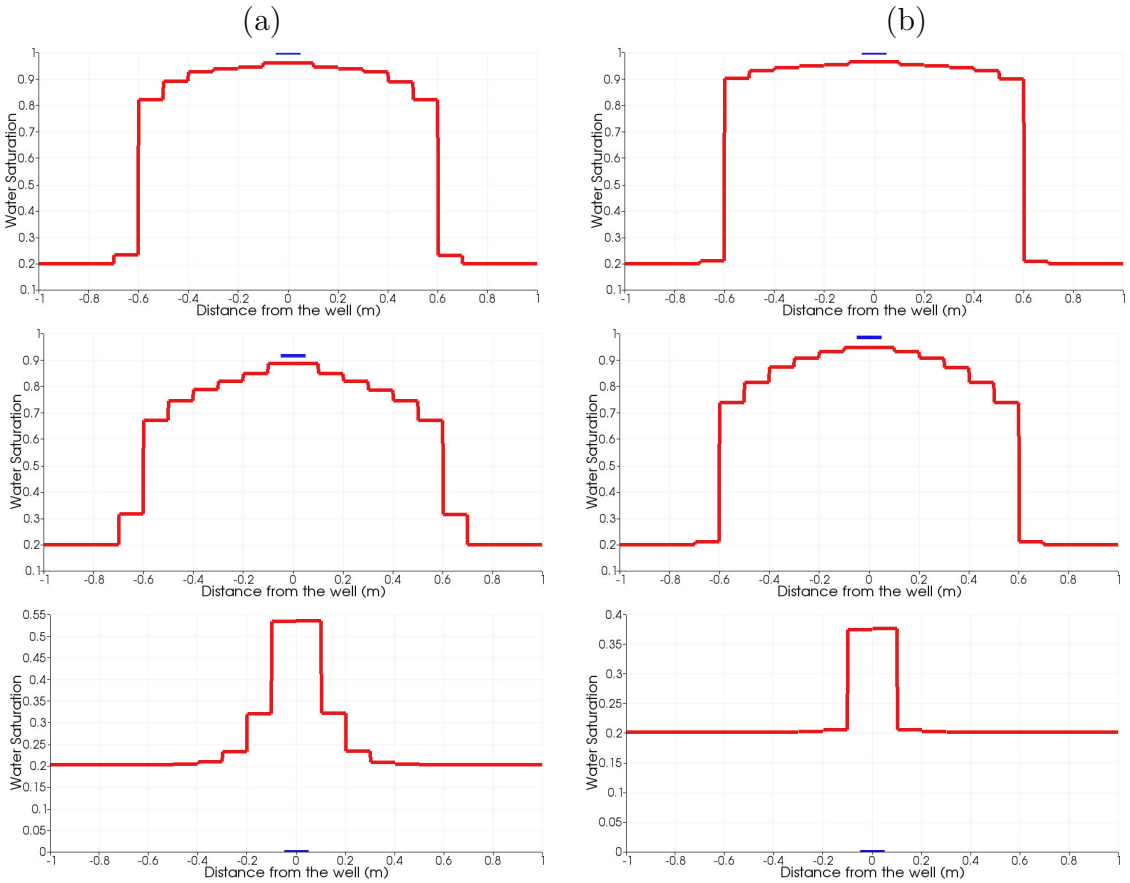

Figure 3.13: Water saturation in the perforated face in the fracture at $\mathbf{x} = 0$ (blue) and cut of the water saturation in the matrix (red) along the line $y = z = 0$ as a function of the distance to the fracture at the end of each simulation period $t = 1$ day (top), $t = 4$ days (middle) and $t = 300$ days (bottom). The left plots (a) correspond to $b_m = 10^5$ Pa, $b_f = 0$, $p_{ent,m} = 10^5$ Pa, $p_{ent,f} = 0$, and the right plots (b) to $b_m = b_f = 0$, $p_{ent,m} = 10^5$ Pa, $p_{ent,f} = 0$.

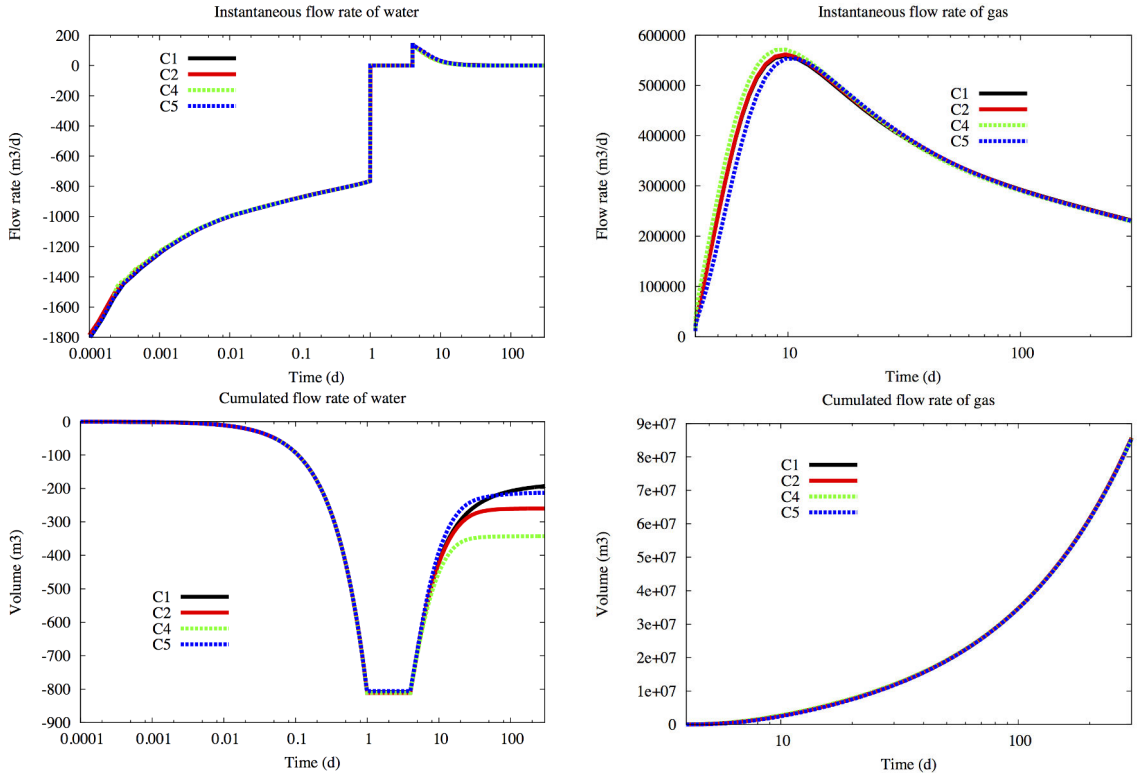

Figure 3.14: On the top: instantaneous flow rates of water (left) and of gas (right) in m^3/day at the bottom: cumulated flow rates of water (left) and gas (right) in m^3 as a function of time, for the following four test cases. C1: $b_m = 10^5$ Pa, $b_f = 10^4$ Pa, $p_{ent,m} = p_{ent,f} = 0$, C2: $b_m = 10^5$ Pa, $b_f = 0$, $p_{ent,m} = p_{ent,f} = 0$, C4: $b_m = 10^5$ Pa, $b_f = 0$, $p_{ent,m} = 10^5$ Pa, $p_{ent,f} = 0$, C5: $b_m = b_f = 0$, $p_{ent,m} = 10^5$ Pa, $p_{ent,f} = 0$.

Figures 3.12 and 3.13 exhibit, at the end of each simulation period at $t = 1$ day, $t = 4$ days and $t = 300$ days, the water saturation in the perforated face in the fracture and the cut of the water saturation in the matrix along the line $y = z = 0$ as a function of the distance to the fracture. One clearly sees that the water phase fills the fractures during the water injection period and penetrates the matrix less than one meter from the fractures. At the end of the well closure period, water has been sucked by imbibition from the fractures to the matrix. At the end of the simulation, the fractures are again fully filled with the gas phase and the water phase above the residual saturation is only partially removed during the production period due to the water retention by capillary effect. Figure 3.14 exhibits the instantaneous and cumulated flow rates of water and gas at the well with a positive value for production and a negative value for injection. It can be checked in Figures 3.12, 3.13 and 3.14 that the larger the difference between the capillary pressure in the matrix and in the fractures, the more water is retained by the capillary effect into the matrix and at the same time the less water and the more gas are produced.

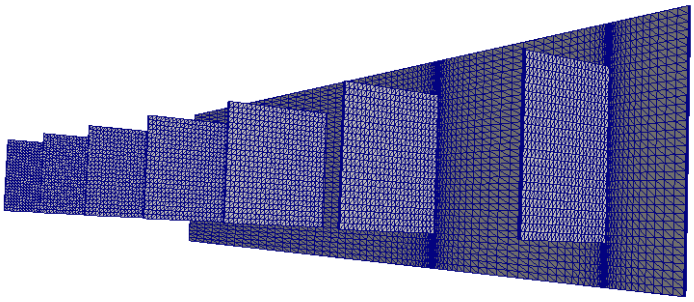

Figure 3.15: View of the topologically Cartesian refined mesh in the neighbourhood of the 8 fractures. The mesh is refined along the normal directions of the fractures. The quadrangular faces at the boundary of this refined mesh are cut into two triangles in order to match this refined mesh with the tetrahedral mesh of the surrounding reservoir domain.

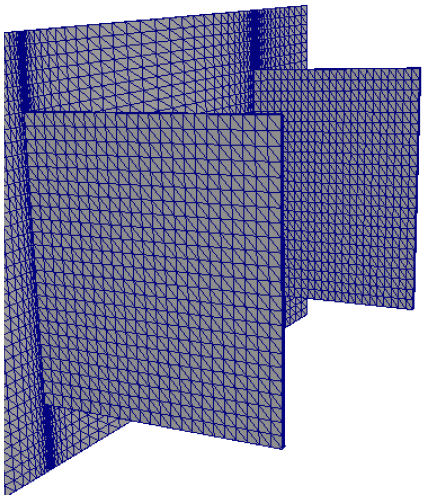

Figure 3.16: Zoom of the refined mesh in the neighbourhood of the intersections between the 2 hydraulic fractures and the natural fracture.

The next test case investigates the interaction between 7 hydraulic fractures and one natural fracture (see Figures 3.15, 3.16) intersecting 2 among the 7 hydraulic fractures. The reservoir is defined by the domain $\Omega = (-300, 850) \times (-250, 250) \times (-200, 200)$ (m). In this case seven transverse fractures $\Gamma_i, i = 1, 7$ are initiated by hydraulic fracturing from a horizontal well. The geometry of $\Gamma_i, i = 1, 7$ is defined as $\{x_i\} \times (-50, 50) \times (-50 \times 50)$ with $x_1 = 0$, $x_2 = -150$, $x_3 = +150$, $x_4 = +300$, $x_5 = +450$, $x_6 = +600$, $x_7 = +750$. An horizontal well is located along $y = z = 0$ and perforates each fracture $\Gamma_i, i = 1, 7$. The

natural fracture $\Gamma_i, i = 8$ intersects the two hydraulic fractures $\Gamma_i, i = 1, 2$.
All the physical characteristics as well as the simulation parameters are the same as in the previous test case.

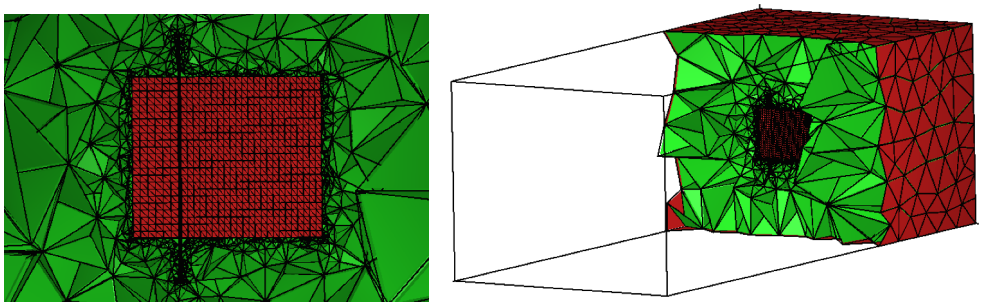

Figure 3.17: Cut of the mesh at $x = -149$ showing the matching between the topologically Cartesian refined mesh and the surrounding tetrahedral mesh.

To ease the construction of the refined mesh in the normal directions of the intersecting fractures, a topologically Cartesian mesh is used in the neighbourhood of the 8 fractures (see Figures 3.15, 3.16). The matching between this topologically Cartesian mesh and the surrounding tetrahedral mesh is done by cutting the quadrangular faces at the boundary of the refined mesh in two triangles, taking advantage of the ability of the VAG scheme to deal with polyhedral cells (see Figures 3.17, 3.16). The construction is based on a non uniform Cartesian discretization of each fracture, then 7 layers of uniform width $h_l = 0.14$ m are extruded in the normal directions of the fractures at both sides of the fractures. In a second step, each quadrangular face at the boundary of this refined zone is cut into two triangles in order to connect this grid to the tetrahedral mesh generated during the third step of the construction by TetGen [59]. As exhibited in Figure 3.16, the natural Fracture $\Gamma_i, i = 8$ is refined in the neighbourhood of the intersections with the fractures $\Gamma_i, i = 1, 2$. The main characteristics of this hybrid mesh are summarized in Table 3.5.

Nb_{cells}	Nb_{nodes}	Nb_{FracF}	linear system d.o.f.
240 889	109 078	6 688	115 766

Table 3.5: Number Nb_{cells} of cells, number Nb_{nodes} of nodes, number Nb_{FracF} of fracture faces and reduced linear system number of d.o.f. (with 2 unknowns per d.o.f).

The numerical behavior of the simulation for both the variable switch and pressure-saturation formulations for case C1 is exhibited in Table 3.6. The variable switch formulation turns out to be more efficient for the value of $\frac{b_m}{b_f} = 10$ both in terms of number of Newton iterations and number of time step chops which confirms the efficiency of the proposed method. As it could be expected as a result of the very small volumes generated by the combination of the intersections and of the refinement, the number of time step

chops and of Newton iterations is larger than for the ones obtained with the previous test case without intersections.

	pressure-saturation					variable switch				
$\frac{b_m}{b_f}$	$\mathbf{N_{dt}}$	$\mathbf{N_{Chop}}$	$\mathbf{N_{Newton}}$	$\mathbf{N_{GMRes}}$	**CPU(s)**	$\mathbf{N_{dt}}$	$\mathbf{N_{Chop}}$	$\mathbf{N_{Newton}}$	$\mathbf{N_{GMRes}}$	**CPU(s)**
10	292	27	9.23	39.81	25 859	268	19	8.35	43.54	22 482

Table 3.6: Zero entry pressures both in the matrix and in the faults - C1 case. Numerical results for the pressure-saturation, and variable switch formulations for $b_m = 10^5$ Pa, $p_{ent,m} = p_{ent,f} = 0$, and ratio $\frac{b_m}{b_f} = 10$: number $N_{\Delta t}$ of successful time steps, number N_{Chop} of time step chops, number N_{Newton} of Newton iterations per successful time step, number N_{GMRes} of GMRes iterations by Newton iteration, and CPU time in seconds.

3.3.3 Oil migration in a 2D basin

In this section we consider the oil migration in a faulted 2D basin exhibited in Figure 3.18 initially saturated with water. Note that, according to our previous notations, the oil phase denoted by o stands for the non wetting phase $\alpha = 1$ and the water phase corresponds to the wetting phase 2 denoted here by w. The domain Ω is of extension $(0, 400)m \times (0, 800)m$ and the fault width is assumed to be constantly $d_f = 4m$. The 2D triangular mesh of the domain Ω exhibited in Figure 3.18 is extended to 3D by one layer of prism since our code deals with 3D meshes. The characteristics of the resulting mesh used in the following numerical test cases is exhibited in Table 3.7.

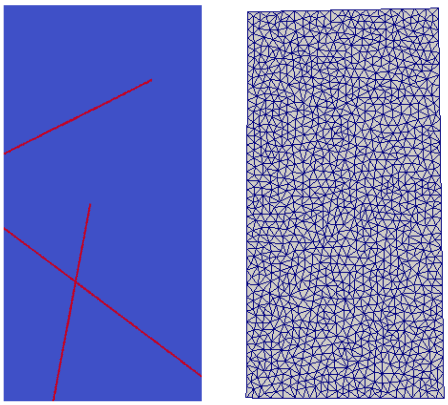

Figure 3.18: On the left: geometry of the basin $\Omega = (0, 400)m \times (0, 800)m$ with the fault network in red and the matrix domain in blue. On the right: coarse triangular mesh (with 2441 cells) of the 2D basin conforming to the fault network.

Nb_{cells}	Nb_{nodes}	Nb_{FracF}	linear system d.o.f.
16 889	17 226	176	17 284

Table 3.7: Prismatic mesh: number Nb_{cells} of cells (equal to the number of triangles of the 2D mesh), number Nb_{nodes} of nodes, number Nb_{FracF} of fracture faces and reduced linear system number of d.o.f. (with 2 unknowns per d.o.f).

Initially, the reservoir is saturated with the water phase (of constant density 1000 kg/m^3 and viscosity 10^{-3} Pa.s), and the oil phase (of constant density 700 kg/m^3 and viscosity 5 10^{-3} Pa.s) is injected at the bottom boundary of the bottom fault, which is managed by imposing non-homogeneous Neumann conditions at the injection location. The oil then rises by gravity, thanks to it's lower density compared to water and by the overpressure induced by the imposed injection rate. Also, Dirichlet boundary conditions are imposed at the upper boundary of the domain. Elsewhere, we have homogeneous Neumann conditions.

We consider isotropic permeabilities in the matrix and in the faults set to $\Lambda_m = \lambda_m \mathrm{Id}$ with $\lambda_m = 10^{-13}$ m^2 and $\Lambda_f = \lambda_f \mathrm{Id}$ with $\lambda_f = 10^{-10}$ m^2. The parameters of the Corey capillary pressures are fixed to $b_m = 10^6$ Pa for cases C1, C2, C3 and C4, and to $p_{ent,m} = 10^6$ Pa for cases C3, C4, and C5. For cases C1 and C3 we will investigate the set of values $b_f = 1, 10, 10^4, 10^5$ Pa in the faults. The porosity is equal to $\phi_m = 0.2$ in the matrix and to $\phi_f = 0.4$ in the faults. The mobilities are given for both the matrix and fault rocktypes $j = m, f$ by the Corey laws (3.12) with $s^w_{r,m} = s^g_{r,m} = 0$, $k^w_{m,max} = k^g_{m,max} = 1$, $n^w_m = n^g_m = 2$ in the matrix, and by $s^w_{r,f} = s^g_{r,f} = 0$, $k^w_{f,max} = k^g_{f,max} = 1$, $n^w_f = n^g_f = 1$ in the faults. The simulation is run over a period of 5400 days with an initial time step of 1 day and a maximum time step fixed to 180 days.

The numerical behavior of the simulations for both the variable switch and pressure-saturation formulations for cases C1 and C3, and for the variable switch formulation only for cases C2,C4 and C5, is exhibited in Tables 3.8, 3.9 and 3.10. These tables exhibit the number of successful time steps, the number of time step chops, the number of Newton iterations by successful time steps, the number of GMRes iterations by Newton iteration, and the CPU time. According to Table 3.8, the variable switch formulation turns out to be more robust than the pressure-saturation formulation w.r.t. the value of the ratio $\frac{bm}{bf}$ both in terms of number of Newton iterations and number of time step chops. The difference of behavior between both formulations exhibited in Table 3.9 is much more striking in the case of the nonzero entry pressure $p_{ent,m} = 10^6$ Pa. As previously, in that case, the pressure-saturation formulation fails except for very small ratios $\frac{bm}{bf}$ while the variable switch formulation is robust w.r.t. the ratio $\frac{bm}{bf}$. Table 3.10 shows the good performance of the variable switch formulation even for the degenerate case C5 both in terms of time step chops and Newton iterations.

	pressure-saturation					variable switch				
$\frac{b_m}{b_f}$	$\mathbf{N_{\Delta t}}$	$\mathbf{N_{Chop}}$	$\mathbf{N_{Newton}}$	$\mathbf{N_{GMRes}}$	**CPU(s)**	$\mathbf{N_{\Delta t}}$	$\mathbf{N_{Chop}}$	$\mathbf{N_{Newton}}$	$\mathbf{N_{GMRes}}$	**CPU(s)**
10	95	0	4.99	38.96	554	95	0	5.23	37.12	602
100	95	0	5.78	23.15	524	95	0	7.29	22.89	693
10^5	364	72	15.72	14.52	3791	110	4	13.47	29.26	1565
10^6	304	57	15.52	13.47	3311	110	4	13.41	19.23	1397
∞	n/a	n/a	n/a	n/a	n/a	102	2	12.74	20.79	1188

Table 3.8: Zero entry pressures both in the matrix and in the faults - C1 and C2 cases. Numerical results for the pressure-saturation, and variable switch formulations for $b_m = 10^6$ Pa, $p_{ent,m} = p_{ent,f} = 0$, and different values of the ratio $\frac{b_m}{b_f}$: number $N_{\Delta t}$ of successful time steps, number N_{Chop} of time step chops, number N_{Newton} of Newton iterations per successful time step, number N_{GMRes} of GMRes iterations by Newton iteration, and CPU time in seconds.

	pressure-saturation					variable switch				
$\frac{b_m}{b_f}$	$\mathbf{N_{\Delta t}}$	$\mathbf{N_{Chop}}$	$\mathbf{N_{Newton}}$	$\mathbf{N_{GMRes}}$	**CPU(s)**	$\mathbf{N_{\Delta t}}$	$\mathbf{N_{Chop}}$	$\mathbf{N_{Newton}}$	$\mathbf{N_{GMRes}}$	**CPU(s)**
10	102	2	6.07	30.67	707	95	0	5.62	28.49	572
100	n/c	n/c	n/c	n/c	n/c	95	0	7.38	26.37	727
10^5	n/c	n/c	n/c	n/c	n/c	121	7	12.76	23.89	1633
10^6	n/c	n/c	n/c	n/c	n/c	106	3	11.81	26.31	1277
∞	n/a	n/a	n/a	n/a	n/a	114	5	12.46	22.65	1321

Table 3.9: Nonzero entry pressure in the matrix - C3 and C4 cases. Numerical results for the pressure-saturation and variable switch formulations for $b_m = 10^6$ Pa, $p_{ent,m} = 10^6$ Pa, $p_{ent,f} = 0$ and different values of the ratio $\frac{b_m}{b_f}$: number $N_{\Delta t}$ of successful time steps, number N_{Chop} of time step chops, number N_{Newton} of Newton iterations per successful time step, number N_{GMRes} of GMRes iterations by Newton iteration, and CPU time in seconds.

variable switch				
$\mathbf{N_{\Delta t}}$	$\mathbf{N_{Chop}}$	$\mathbf{N_{Newton}}$	$\mathbf{N_{GMRes}}$	**CPU(s)**
185	17	14.28	25.92	2147

Table 3.10: Nonzero entry pressure in the matrix and in the faults - C5 case. Numerical results for the pressure-saturation and variable switch formulations for $b_m = b_f = 0$, $p_{ent,m} = 10^6$ Pa, and $p_{ent,f} = 0$: number $N_{\Delta t}$ of successful time steps, number N_{Chop} of time step chops, number N_{Newton} of Newton iterations per successful time step, number N_{GMRes} of GMRes iterations by Newton iteration, and CPU time in seconds.

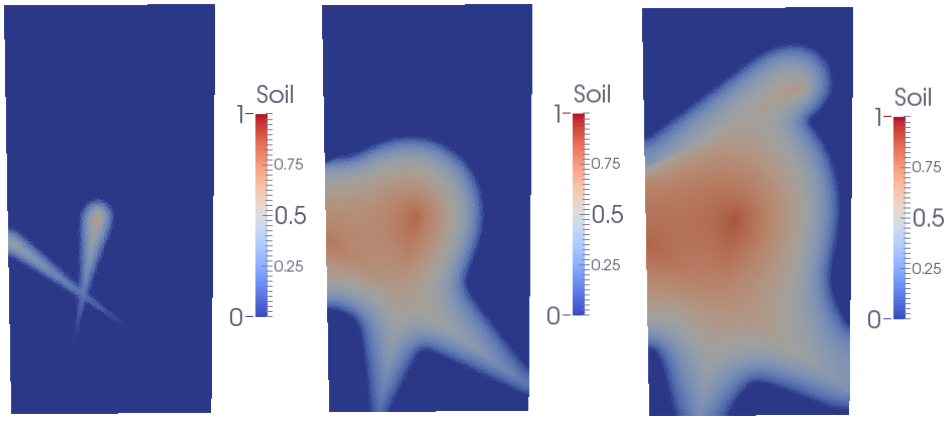

Figure 3.19: Oil saturation at $t = 360$ days (left), $t = 2880$ days (middle) and $t = 5400$ at the end (right) of simulation obtained for the C1 case with $\frac{bm}{bf} = 10$ and the variable switch formulation.

Figure 3.20 exhibits the volume of oil in the faults as a function of time for C1, C2, C4 and C5 test case solutions obtained with the variable switch formulation. As expected, larger constrasts of capillary pressures between the matrix and the faults result in a larger amount of oil in the fault up to the total pore volume and a quicker infill. Figure 3.19 shows the propagation of the oil saturation in the basin at times $t = 360, 2880, 5400$ days for the C1 case with $\frac{bm}{bf} = 10$ obtained with the variable switch formulation.

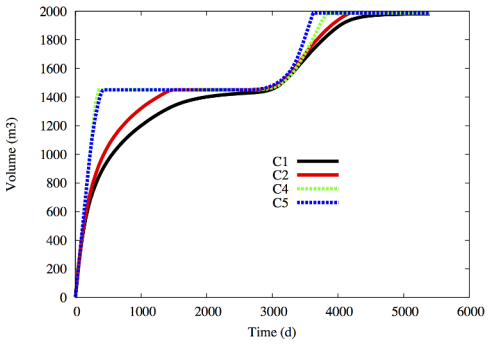

Figure 3.20: Amount of oil in the faults in m^3 as a function of time for the following four test cases. C1: $b_m = 10^6$ Pa, $b_f = 10^5$ Pa, $p_{ent,m} = p_{ent,f} = 0$, C2: $b_m = 10^6$ Pa, $b_f = 0$, $p_{ent,m} = p_{ent,f} = 0$, C4: $b_m = 10^6$ Pa, $b_f = 0$, $p_{ent,m} = 10^6$ Pa, $p_{ent,f} = 0$, C5: $b_m = b_f = 0$, $p_{ent,m} = 10^6$ Pa, $p_{ent,f} = 0$.

3.4 Conclusions

This Chapter has introduced a general framework for the formulation of two phase Darcy flows with discontinuous capillary pressure curves at rocktype interfaces. This framework is based on the parametrization of the capillary pressure monotone graphs and it allows to (1) capture the jumps of the saturations at the different rocktype interfaces, (2) maintain the minimal number of primary unknowns per degree of freedom, (3) deal with arbitrary capillary pressures including multi-valued saturation curves. This framework has been tested on two families of test cases and compared with the classical pressure-saturation formulation using the Vertex Approximate Gradient scheme for two-phase hybrid dimensional Darcy flows in fractured porous media. The numerical results show clearly the robustness and efficiency of our approach for a wide range of capillary pressures with highly constrasted matrix and fracture rocktypes.

Conclusions et perspectives

Bilan des résultats obtenus

Au Chapitre 1 on a présenté le modèle dimensionnel hybride couplant l'écoulement dans la matrice et celui dans le réseau de fractures représentées comme des surfaces de codimension 1. On a montré que VAG et HFV sont des schémas de type gradient satisfaisant les hypothèses de coercivité, de consistence, de conformité à la limite et de compacité. Les résultats de densité établis en Annexe de sous espaces de fonctions lisses dans les espaces de pression et de flux sont essentiels afin d'établir la convergence des schémas numériques étudiés. Ces résultats sont obtenus pour le cas de réseaux de fractures s'intersectant, débouchantes ou non débouchantes. Une etude comparative des deux schémas VAG et HFV sur des solutions analytiques 3D en milieu homogène ou hétérogène, isotrope ou anisotrope a été menée pour différentes familles de maillages cartésiens, hexaèdriques ou tétraèdriques. Ce travail a donné lieu à la publication [12].

Le Chapitre 2 étudie un modèle d'écoulement diphasique immiscible dans les milieux poreux prenant en compte les réseaux de fractures discrètes et les échanges entre le milieux poreux environnant, la matrice, et le réseau de fractures. On a utilisé une formulation implicite en pressions des phases qui est adaptée aux pressions capillaires discontinues au sens où elle capte le saut des saturations aux interfaces entre différents types de roche, en particulier à l'interface matrice fracture. Les résultats numériques confirment que le schéma VAG a l'avantage, par rapport aux schémas Control Volume Finte Element (CVFE) d'éviter le mélange des milieux matrice et fracture dans les volumes de contrôle, tout en conservant un coût du même ordre que les méthodes nodales sur des maillages non structurés à dominante tétraèdrique. La comparaison des schémas VAG et HFV sur un cas test traceur et un cas test diphasique 3D montre que le schéma VAG est moins coûteux à précision donnée que le schéma HFV pour le type de discrétisation en temps fully implicite considéré dans ce chapitre.
On a démontré la convergence du schéma VAG sous l'hypothèse que les perméabilités relatives sont minorées par une constante strictement positive. Ce résultat prend en compte les pressions capillaires discontinues ce qui est particulièrement important aux interfaces matrice fracture. Il s'agit à notre connaissance de la première preuve de convergence pour ce type de modèle. Ce travail a donné lieu à la publication [13].

Au Chapitre 3 on a présenté une formulation des écoulements diphasiques prenant en compte des pressions capillaires non strictement croissantes tout en permettant de capturer le saut des saturations aux interfaces entre différents types de roches et d'utiliser un nombre minimal d'inconnues par degré de liberté à savoir deux inconnues dans le cas de notre modèle diphasique immiscible. La méthodologie proposée repose sur une paramétrisation des graphes monotones des pressions capillaires pour les rocktypes présents à l'interface. Différents cas tests incluant la simulation de la récupération de gaz dans des réservoirs peu perméables par fracturation hydraulique sont présentés. Notre nouvelle formulation, de type variable switch est comparée numériquement à une formulation en variables pression et saturation sur plusieurs cas tests incluant la simulation de la

récupération de gaz dans des réservoirs peu perméables par fracturation hydraulique. Les résultats présentés montrent la robustesse et l'efficacité de cette nouvelle approche sur des cas avec fort contraste de perméabilités entre la matrice et les fractures. Ce travail a donné lieu à une publication dans les actes de la conférence internationale ECMOR XV [17].

Perspectives

Comparaisons du modèle réduit au modèle volumique en diphasique. Les modèles réduits ou dimensionnels hybrides ont été comparés aux modèles équi-dimensionnels représentant les fractures comme des volumes pour des modèles monophasiques ou encore dans le cas de traceurs (voir [2]). Dans le cas diphasique, cette comparaison reste à faire afin de mieux comprendre les conditions de validité de la réduction de modèle.

Ordre 2 sur le transport dans la matrice. Les schémas étudiés dans cette thèse pour les écoulements diphasiques reposent sur une discrétisation en temps implicite couplé et une discrétisation par décentrage amont du premier ordre des termes de transport. Cette approche a l'avantage d'être robuste et d'autoriser des grands nombres CFL ce qui est important dans le contexte des milieux fracturés pour maintenir des pas de temps raisonnables malgré les petits volumes générés par les fractures. En revanche, le schéma amont d'ordre 1 sur le transport est très diffusif. Une alternative à étudier serait d'utiliser pour le transport une schéma d'ordre 2 explicite dans la matrice tout en conservant un schéma d'ordre 1 implicite dans les fractures dans le but de monter en précision tout en maintenant un pas de temps suffisamment grand.

Réseaux 3D de grande taille. Une autre perspective est de pouvoir travailler avec les géométries et géologies plus complexes. Dans le cadre de cette thèse on s'intèresse à la simulation de la récupération assistée de gaz dans des réservoirs de très faible perméabilité par des méthodes de fracturation hydraulique. Il est alors nécessaire de raffiner fortement le maillage à l'interface matrice fracture pour éviter d'élargir artificiellement les drains que constituent les fractures. Les ressources mémoire et le temps de calcul sont limités et les défis à relever pour traiter les gros réseaux de fractures concernent le maillage (amélioration de la qualitè du maillage, raffinement anisotrope), la conception de schémas de discrétisation robustes par rapport à la qualité du maillage, et de solveurs linéaires et non linéaires robustes et parallèles.

Modèles à pressions discontinues pour traiter à la fois les drains et les barrières. Dans cette thèse on étudie le cadre avec pression continue à l'interface modélisant uniquement les drains. L'une des principales perspectives de recherche concerne le cas dit à pressions discontinues avec sauts de pression aux interfaces matrice fracture modélisant à la fois les barrières et les drains. Ce type de modèle prenant en compte les fractures pouvant agir soit comme des drains soit comme des barrières a été introduit dans [49] et

[15] pour le cas d'écoulement monophasiques.

Chapter 4

Appendices

Density results for the pressure and flux spaces

This section proves the density results stated in Propositions 1.2.2 and 1.2.3.

Smooth function subspace density result for the pressure space

We prove in this subsection Proposition 1.2.2 stating that the space $C^\infty(\overline{\Omega})$ is a dense subspace of V. The density of $C_c^\infty(\overline{\Omega})$ in V^0 can be proved in the same way. We begin with technical lemmas concerning the fractional Sobolev spaces.

Let s be a non-negative real number, for an non-empty open set $\Omega \subseteq \mathbb{R}^d$ we denote by $H^s(\Omega)$ the standard Sobolev space $W^{s,p}(\Omega)$ with exponent $p = 2$. Note that for $0 \leq s_1 \leq s_2$ one has $H^{s_2}(\Omega) \subset H^{s_1}(\Omega)$, where $H^0(\Omega)$ stands for $L^2(\Omega)$. We also define the spaces $H_0^s(\Omega) = \overline{C_c^\infty(\Omega)}^{H^s(\Omega)}$ and $\widetilde{H}^s(\Omega) = \overline{C_c^\infty(\Omega)}^{H^s(\mathbb{R}^d)}$.

If Ω is a Lipschitz domain, then the trace operator $\gamma_{\partial\Omega} : C^\infty(\overline{\Omega}) \to C^\infty(\partial\Omega)$ can be continuously extended to $\gamma_{\partial\Omega} : H^s(\Omega) \to H^{s-1/2}(\partial\Omega)$ for all $\frac{1}{2} < s < \frac{3}{2}$; moreover the trace operator is surjective and has a continuous right inverse [23, Lemma 3.6]. For $s > \frac{1}{2}$ we define

$$H^s_{\partial\Omega}(\Omega) = \{u \in H^s(\Omega) \text{ such that } \gamma_{\partial\Omega} u = 0\}.$$

The following lemma summarizes some relations between the spaces $H^s(\Omega)$, $H_0^s(\Omega)$, $\widetilde{H}^s(\Omega)$ and $H^s_{\partial\Omega}(\Omega)$ for Lipschitz domains.

Lemma 4.0.1 *If Ω is a Lipschitz domain, then*

(i) If $s \geq 0$, then $\widetilde{H}^s(\Omega) \subset H_0^s(\Omega)$; moreover if $s - \frac{1}{2} \notin \mathbb{Z}$, then $\widetilde{H}^s(\Omega) = H_0^s(\Omega)$.

(ii) If $0 \leq s \leq \dfrac{1}{2}$, then $H_0^s(\Omega) = H^s(\Omega)$.

(iii) If $\dfrac{1}{2} < s < \dfrac{3}{2}$, then $H_0^s(\Omega) = H^s_{\partial\Omega}(\Omega)$.

Proof: See [41, Theorems 1.4.4.5 and 1.4.2.4] for the proof of (i) and (ii). The proof of (iii) for $\dfrac{1}{2} < s \leq 1$ is also given in [50, Theorem 3.40], for $1 < s < \frac{3}{2}$ see [52]. □

Lemma 4.0.1 implies in particular that for $\frac{1}{2} < s < \frac{3}{2}$ one has $H_0^s(\Omega) = \widetilde{H}^s(\Omega) = H^s_{\partial\Omega}(\Omega)$ and that for any $u \in H_0^s(\Omega)$ its extension by zero belongs to $H^s(\mathbb{R}^n)$.

Let Ω be a Lipschitz domain, let $l \in \mathbb{N}$ and let $\Big(\Omega_i \subset \Omega\Big)_{i\in\{1,\dots,l\}}$ be a family of Lipschitz domains satisfying $\bigcup_{i\in\{1,\dots,l\}} \overline{\Omega_i} = \overline{\Omega}$ and $\Omega_i \cap \Omega_j = \emptyset$ for all $i, j \in \{1, \dots, l\}$ with $i \neq j$. Let $\Big(u_i \in H^1(\Omega_i)\Big)_{i\in\{1,\dots,l\}}$ be a set of functions such that for all $i, j \in \{1, \dots, l\}$ satisfying $\partial\Omega_i \cap \partial\Omega_j \neq \emptyset$, then $\Big(\gamma_{\partial\Omega_i} u_i\Big)|_{\partial\Omega_i\cap\partial\Omega_j} = \Big(\gamma_{\partial\Omega_j} u_j\Big)|_{\partial\Omega_i\cap\partial\Omega_j}$. For all $i \in \{1, \dots, l\}$ we denote by χ_{Ω_i} the indicator function of the domain Ω_i, it is classical that the function

$u = \sum_{i\in\{1,\dots,l\}} u_i \chi_{\Omega_i}$ belongs to $H^1(\Omega)$. The following lemma gives a similar result for functions in $H^s(\Omega)$, with $\frac{1}{2} < s < 1$ and Ω being the boundary of a polyhedral domain.

Lemma 4.0.2 *Let K be a bounded polyhedral domain in $\mathbb{R}^3$, let $\mathcal{F}_K$ be the set of its polygonal faces and $\mathcal{E}_K$ the set of its edges. For all $\sigma \in \mathcal{F}_K$ we denote by $\mathcal{E}_\sigma$ the set of edges of σ and for all $e \in \mathcal{E}_K$ by $\mathcal{F}_{K,e} \subset \mathcal{F}_K$ the two faces containing e. Let $\frac{1}{2} < s < 1$, for all $\sigma \in \mathcal{F}_K$ and $e \in \mathcal{E}_\sigma$ we denote by $\gamma_{\sigma,e}$ the trace operator from $H^s(\sigma)$ to $H^{s-\frac{1}{2}}(e)$.*

Let $u \in L^2(\partial K)$ such that $u|_\sigma \in H^s(\sigma)$ for all $\sigma \in \mathcal{F}_K$ and such that for all $e \in \mathcal{E}_K$ with $\mathcal{F}_{K,e} = \{\sigma, \sigma'\}$ one has $\gamma_{\sigma,e}(u|_\sigma) = \gamma_{\sigma',e}(u|_{\sigma'})$. Then, $u \in H^s(\partial K)$.

Proof: Let $e \in \mathcal{E}_K$ and $\mathcal{F}_{K,e} = \{\sigma, \sigma'\}$, we associate with e a couple of Lipschitz domains $(D_e^\sigma)_{\sigma\in\mathcal{F}_{K,e}}$ such that $D_e^\sigma \subset \sigma$ and $\partial D_e^\sigma \cap \partial\sigma = e$ for all $\sigma \in \mathcal{F}_{K,e}$, and such that $D_e^{\sigma'}$ is obtained by a rotation of D_e^σ around e. We denote $\overline{D}_e = \overline{D}_e^\sigma \cup \overline{D}_e^{\sigma'}$ and $D_e = \overline{D}_e \setminus \partial\overline{D}_e$. The function $\gamma_{\sigma,e} u_e^\sigma$ is in $H^{s-\frac{1}{2}}(e)$, implying in view of statements (i) and (ii) of Lemma 4.0.1 that its extension by zero on ∂D_e^σ belongs to $H^{s-\frac{1}{2}}(\partial D_e^\sigma)$. The trace operator $\gamma_{\partial D_e^\sigma} : H^s(D_e^\sigma) \to H^{s-\frac{1}{2}}(\partial D_e^\sigma)$ is surjective, therefore there exists $u_e^\sigma \in H^s(D_e^\sigma)$ such that

$$\gamma_{\partial D_e^\sigma} u_e^\sigma = \begin{cases} \gamma_{\sigma,e} u_\sigma & \text{on } e, \\ 0 & \text{on } \partial D_e^\sigma \setminus e. \end{cases}$$

We denote by u_e the extension by symmetry of u_e^σ to D_e. One can show that $u_e \in H_0^s(D_e)$, implying that its extension by zero to the whole ∂K, denoted by $\overline{u}_e$, belongs to $H^s(\partial K)$. Let us consider the function

$$v_\sigma = u|_\sigma - \sum_{e\in\mathcal{E}_\sigma} \overline{u}_e|_\sigma.$$

Since $v_\sigma \in H_0^s(\sigma)$ it can be extended by zero to the whole ∂K; we denote this extension by $\overline{v}_\sigma$. To complete the proof we remark that

$$u = \sum_{\sigma\in\mathcal{F}_K} \overline{v}_\sigma + \sum_{e\in\mathcal{E}_K} \overline{u}_e \in H^s(\partial K).$$

□

Lemma 4.0.3 *The trace operator γ is onto from V to $H^1(\Gamma)$.*

Proof: Given $u \in H^1(\Gamma)$ we prove that there exists $U \in V$ such that $\gamma U = u$. We focus on the case $d = 3$, the adaptation to the bidimensional setting is straightforward. The proof relies on the definition of a polyhedral mesh which is slightly different from Definition 1.4.1. More precisely in addition to Definition 1.4.1 it is assumed that all the mesh faces $\sigma \in \mathcal{F}$ are planar. On the other hand the existence of cell (and face) "centers" is not required. Such polyhedral partitioning of $\Omega \setminus \overline{\Gamma}$ always exists. For example we can define the set of cells $\mathcal{M}$ as the set of connected components of $\Omega \setminus \bigcup_{i\in I} \mathcal{P}_i$. In addition to the previous notations, we will denote by $\mathcal{F}_e$ the set of faces sharing a given edge $e \in \mathcal{E}$.

For all $e \in \mathcal{E}_\Gamma$ we denote by γ_e the trace operator acting from $H^1(\Gamma)$ to $H^{\frac{1}{2}}(e)$, and for all $e \in \mathcal{E}$ we define

$$u_e = \begin{cases} \gamma_e u & \text{if} \quad e \in \mathcal{E}_\Gamma, \\ 0 & \text{else.} \end{cases}$$

Let $\sigma \in \mathcal{F} \setminus \mathcal{F}_\Gamma$ and let us denote by χ_e, $e \in \mathcal{E}_\sigma$ the indicator function of e defined on $\partial\sigma$. In view of statements (i) and (ii) of Lemma 4.0.1 the function $u_{\partial\sigma} = \sum_{e\in\mathcal{E}_\sigma} \chi_e u_e$ belongs to $H^s(\partial\sigma)$ for any $0 < s < \dfrac{1}{2}$.

For all $\sigma \in \mathcal{F} \setminus \mathcal{F}_\Gamma$ there exists a function $u_\sigma \in H^{s+\frac{1}{2}}(\sigma)$ having the trace on $\partial\sigma$ equal to $u_{\partial\sigma}$. For $\sigma \in \mathcal{F}_\Gamma$ we denote by $u_\sigma \in H^1(\sigma)$ the restriction of u on σ. Let χ_σ be the indicator function of σ defined on $\bigcup_{\sigma\in\mathcal{F}} \sigma$, we set $u^* = \sum_{\sigma\in\mathcal{F}} \chi_\sigma u_\sigma$. Lemma 4.0.2 implies that for all $K \in \mathcal{M}$ the restriction of u^* on ∂K belongs $H^{s+\frac{1}{2}}(\partial K)$

Finally, for all $K \in \mathcal{M}$ we denote by U_K some lifting of $u^*|_{\partial K}$ in $H^{s+1}(K)$ and we define $U = \displaystyle\sum_{K\in\mathcal{M}} \chi_K U_K$, where χ_K is the indicator function of a cell K. Then, it follows that $U \in H^1(\Omega)$ and that $\gamma U = u$. $\square$

Let us recall (see e.g. [18] Proposition 1.9) that the density of a linear subspace M of V is equivalent to the fact that any linear form of V' vanishing on M is vanishing on V.

The caracterization of V' can be obtained from the Riesz theorem, implying that any continuous linear form ζ on V writes $\zeta = \xi + \gamma^t\tau$ where $\xi \in (H^1(\Omega))'$ and $\tau \in (H^1(\Gamma))'$. Then, assuming that $\langle\zeta, \varphi\rangle = 0$ for all $\varphi \in C^\infty(\overline{\Omega})$ it results from Lemma 4.0.4 stated and proved below that $\zeta = 0$. Therefore the space $C^\infty(\overline{\Omega})$ is dense in V.

Lemma 4.0.4 *Let $\zeta = \xi + \gamma^t\tau$ where $\xi \in (H^1(\Omega))'$ and $\tau \in (H^1(\Gamma))'$ be such that $\langle\zeta, \varphi\rangle = 0$ for all $\varphi \in C^\infty(\overline{\Omega})$, then $\zeta = 0$.*

Proof: It is known that $C_c^\infty(\overline{\Omega} \setminus \overline{\Gamma})$, defined as the space of $C^\infty(\overline{\Omega})$ functions vanishing in a neighbourhood of Γ, is a dense subspace of $H^1_\Gamma(\Omega \setminus \overline{\Gamma})$ defined as the space of $H^1(\Omega \setminus \overline{\Gamma})$ functions vanishing on Γ. From the surjectivity and continuity of the trace operator γ from V to $H^1(\Gamma)$, there exists a continuous lifting operator denoted by r_Γ from $H^1(\Gamma)$ to V. Using $< \xi, \varphi >= 0$ for all $\varphi \in C_c^\infty(\overline{\Omega} \setminus \overline{\Gamma})$, and the density of $C_c^\infty(\overline{\Omega} \setminus \overline{\Gamma})$ in $H^1_\Gamma(\Omega \setminus \overline{\Gamma})$, we deduce that $< \xi, v >=< \xi, r_\Gamma(\gamma(v)) >$ for all $v \in V$. It results that $\tilde{\tau} = r_\Gamma^t \xi \in (H^1(\Gamma))'$ is such that $\xi = \gamma^t\tilde{\tau}$. Hence, we can assume in the remaining of the proof that $\xi = 0$.

Let us set $E = \bigcup_{i\in I} \partial\Gamma_i$. We have $E = \bigcup_{e\in\mathcal{E}_\Gamma} \bar{e}$ where $\mathcal{E}_\Gamma$ is the set of edges of Γ in the mesh defined above. Let γ_E the trace operator from $H^1(\Gamma)$ to $L^2(E)$ and let us define the space $H^{\frac{1}{2}}(E)$ as $\gamma_E(H^1(\Gamma))$. We also define the space $H^{\frac{1}{2}}(\partial\Gamma_i)$ as the set of traces on $\partial\Gamma_i$ of functions in $H^1(\Gamma_i)$. Then, it is easy to show that a function $v \in L^2(E)$ belongs to $H^{\frac{1}{2}}(E)$ iff for all $i \in I$, the restriction v_i of v to $\partial\Gamma_i$ belongs to $H^{\frac{1}{2}}(\partial\Gamma_i)$. The function space $H^{\frac{1}{2}}(E)$ is endowed with the Hilbertian norm

$$\|v\|_{H^{\frac{1}{2}}(E)} = \sum_{i\in I} \Big(\|v_i\|^2_{H^{\frac{1}{2}}(\partial\Gamma_i)} \Big)^{\frac{1}{2}}.$$

From the continuity and surjectivity of the trace operator γ_E from $H^1(\Gamma)$ to $H^{\frac{1}{2}}(E)$, we deduce that there exists a continuous lifting operator denoted by r_E from $H^{\frac{1}{2}}(E)$ to $H^1(\Gamma)$. Let us denote by $H^1_E(\Gamma \setminus E)$ the subspace of functions in $H^1(\Gamma)$ with a vanishing trace on E. From the known density of $C^\infty_c(\Gamma \setminus E)$ in $H^1(\Gamma \setminus E)$, we deduce as above that $l = r^t_E \tau \in (H^{\frac{1}{2}}(E))'$ is such that $\tau = \gamma^t_E l$

Let us denote by $\mathcal{V}_E$ the set of the vertices of E. For all $\phi \in C^\infty_c(E \setminus \mathcal{V}_E)$, there exists $\varphi \in C^\infty(\overline{\Omega})$ such that $\phi = \varphi|_E$. Hence, $l \in (H^{\frac{1}{2}}(E))'$ is such that $< l, \phi >= 0$ for all $\phi \in C^\infty_c(E \setminus \mathcal{V}_E)$. Since $C^\infty_c(e)$ is dense in $H^{\frac{1}{2}}(e)$ for any edge e ([41] Theorem 1.4.2.4), we can deduce that $C^\infty_c(E \setminus \mathcal{V}_E)$ is dense in $H^{\frac{1}{2}}(E)$ and hence that $l = 0$, and then that $\zeta = 0$. $\square$.

Smooth function subspace density result for the flux space

We prove in this subsection Proposition 1.2.3 stating that the space $\mathcal{C}^\infty_{H_\Sigma}(\Omega, \Gamma)$ is a dense subspace of $H_\Sigma(\Omega, \Gamma)$.

Let us start by the following technical lemma.

Lemma 4.0.5 *Let $v_m \in L^2(\Omega)$, $\mathbf{g}_m \in L^2(\Omega)^d$, and $v_f \in L^2(\Gamma)$, $\mathbf{g}_f \in L^2(\Gamma)^{d-1}$ be such that*

$$a_\Sigma\Big((\mathbf{q}_m, \mathbf{q}_f), (v_m, v_f, \mathbf{g}_m, \mathbf{g}_f)\Big) = 0 \text{ for all } (\mathbf{q}_m, \mathbf{q}_f) \in \mathcal{C}^\infty_{H_\Sigma}(\Omega, \Gamma), \tag{4.1}$$

then $v_m \in V^0$, $v_f = \gamma v_m$, $\mathbf{g}_m = \nabla v_m$ and $\mathbf{g}_f = \nabla_\tau \gamma v_m$.

Proof: It follows from (4.1) that $\sum_{\mathfrak{a} \in \mathcal{A}} \int_{\Omega_\mathfrak{a}} (v_m \mathrm{div}(\mathbf{q}_{m,\mathfrak{a}}) + \mathbf{q}_{m,\mathfrak{a}} \cdot \mathbf{g}_m) d\mathbf{x} = 0$, for all $\mathbf{q}_m \in C^\infty_c(\Omega \setminus \overline{\Gamma})^d$, we classically deduce that $v_m \in H^1(\Omega \setminus \overline{\Gamma})$ and that $\mathbf{g}_m = \nabla v_m$. Next, let us denote by $\gamma^\pm_i : H^1(\Omega \setminus \overline{\Gamma}) \to L^2(\Gamma_i)$ the trace operators on Γ_i from the sides $\pm$ of $\Omega \setminus \overline{\Gamma}$. For any given $i \in I$, let us denote by ω_{Γ_i} any open ball of Γ_i. For any $\varphi_i \in C^\infty_c(\omega_{\Gamma_i})$, one can build a function $\mathbf{q}_{m,\mathfrak{a}^+_i} \in C^\infty_b(\Omega_{\mathfrak{a}^+_i})$ such that $\mathbf{q}_{m,\mathfrak{a}^+_i} \cdot \mathbf{n}^+_i = \varphi_i$ on ω_{Γ_i} and $\mathbf{q}_{m,\mathfrak{a}^-_i} \cdot \mathbf{n}^-_i = 0$ on ω_{Γ_i} if $\mathfrak{a}^+_i = \mathfrak{a}^-_i$, $\mathbf{q}_{m,\mathfrak{a}^+_i} \cdot \mathbf{n} = 0$ on $\partial\Omega_{\mathfrak{a}^+_i} \cap \partial\Omega$, and $\mathbf{q}_{m,\mathfrak{a}^\pm_j} \cdot \mathbf{n}^\pm_j = 0$ on the sides $\pm$ of the fractures $i \neq j \in I$ such that $\mathfrak{a}^\pm_j = \mathfrak{a}^+_i$. It follows from (4.1) that

$$\int_{\omega_{\Gamma_i}} (\gamma^+_i v_m - v_f) \varphi_i d\tau(\mathbf{x}) = 0.$$

which implies that $\gamma^+_i v_m = v_f|_{\Gamma_i}$ in $L^2(\Gamma_i)$ for all $i \in I$. Similarly, we can show that $\gamma^-_i v_m = v_f|_{\Gamma_i}$ in $L^2(\Gamma_i)$ for all $i \in I$, and $v_m = 0$ on $\partial\Omega$. Hence we deduce that $v_m \in H^1_0(\Omega)$ with $v_f = \gamma v_m$. Next, for all $i \in I$ and for all $\mathbf{q}_{f,i} \in C^\infty_c(\Gamma_i)^{d-1}$, one has

$$\int_{\Gamma_i} (v_f \mathrm{div}_{\tau_i}(\mathbf{q}_{f,i}) + \mathbf{g}_f \cdot \mathbf{q}_{f,i}) d\tau(\mathbf{x}) = 0,$$

which implies that $v_f|_{\Gamma_i} \in H^1(\Gamma_i)$ with $\mathbf{g}_f|_{\Gamma_i} = \nabla_{\tau_i} v_f|_{\Gamma_i}$. Next, for all $(i,j) \in I \times I$, $i \neq j$, such that $\Sigma_{i,j} \setminus \Sigma_0$ is of codimension 2 non zero measure, let us consider any open segment

$L_{i,j} \subset \Sigma_{i,j} \setminus \Sigma_0$, $r_{i,j} \in C_c^\infty(L_{i,j})$ and its extension r_i (resp. r_j) by zero outside of $L_{i,j}$ on Σ_i (resp. Σ_j). Then, one can build $(0, \mathbf{q}_f) \in \mathcal{C}^\infty_{H_\Sigma}(\Omega, \Gamma)$ such that $\mathbf{q}_{f,i} \cdot \mathbf{n}_{\Sigma_i} = r_i$, and $\mathbf{q}_{f,j} \cdot \mathbf{n}_{\Sigma_j} = -r_j$ and $\mathbf{q}_{f,l} = 0$ for all $l \in I \setminus \{i, j\}$. It follows from (4.1) that

$$\int_{L_{i,j}} \Big((\mathbf{q}_{f,i} \cdot \mathbf{n}_{\Sigma_i}) \gamma_{\Sigma_i} v_f|_{\Gamma_i} + (\mathbf{q}_{f,j} \cdot \mathbf{n}_{\Sigma_j}) \gamma_{\Sigma_j} v_f|_{\Gamma_j} \Big) dl(\mathbf{x}) \\ = \int_{L_{i,j}} r_{i,j} (\gamma_{\Sigma_i} v_f|_{\Gamma_i} - \gamma_{\Sigma_j} v_f|_{\Gamma_j}) dl(\mathbf{x}) = 0,$$

and hence that $\gamma_{\Sigma_i} v_f|_{\Gamma_i} = \gamma_{\Sigma_j} v_f|_{\Gamma_j}$ on $L_{i,j}$. Also, for all $i \in I$ such that $\Sigma_{i,0}$ has a non vanishing codimension 2 measure, let us consider any open segment $L_{i,0} \subset \Sigma_{i,0}$, $r_{i,0} \in C_c^\infty(L_{i,0})$ and its extension r_i by zero outside of $L_{i,0}$ on Σ_i. Then, one can build $(0, \mathbf{q}_f) \in \mathcal{C}^\infty_{H_\Sigma}(\Omega, \Gamma)$ such that $\mathbf{q}_{f,i} \cdot \mathbf{n}_{\Sigma_i} = r_i$ and $\mathbf{q}_{f,l} = 0$ for all $l \in I \setminus \{i\}$. It results from (4.1) that

$$\int_{L_{i,0}} (\mathbf{q}_{f,i} \cdot \mathbf{n}_{\Sigma_i}) \gamma_{\Sigma_i} v_f|_{\Gamma_i} \, dl(\mathbf{x}) = \int_{L_{i,0}} (\gamma_{\Sigma_i} v_f|_{\Gamma_i}) r_{i,0} \, dl(\mathbf{x}) = 0,$$

and hence that $\gamma_{\Sigma_i} v_f|_{\Gamma_i} = 0$ on $L_{i,0}$ which implies together with the previous properties that $v_f \in H^1_{\Sigma_0}(\Gamma)$ and concludes the proof. □

Let us now prove the density of $\mathcal{C}^\infty_{H_\Sigma}(\Omega, \Gamma)$ in $H_\Sigma(\Omega, \Gamma)$. Similarly as in the previous subsection, it is equivalent to prove that any linear form in $H_\Sigma(\Omega, \Gamma)'$ which vanishes on the subspace $\mathcal{C}^\infty_{H_\Sigma}(\Omega, \Gamma)$, vanishes on the whole space $H_\Sigma(\Omega, \Gamma)$.

Since $H_\Sigma(\Omega, \Gamma)$ is a closed Hilbert subspace of $H(\Omega, \Gamma)$, any continuous linear form on $H_\Sigma(\Omega, \Gamma)$ can be continuously extended to $H(\Omega, \Gamma)$. From the Riez representation theorem, a continuous linear form ξ on $H(\Omega, \Gamma)$ writes for all $(\mathbf{q}_m, \mathbf{q}_f) \in H(\Omega, \Gamma)$

$$\langle \xi, (\mathbf{q}_m, \mathbf{q}_f) \rangle = a_\Sigma \Big((\mathbf{q}_m, \mathbf{q}_f), (v_m, v_f, \mathbf{g}_m, \mathbf{g}_f) \Big)$$

with $v_m \in L^2(\Omega)$, $\mathbf{g}_m \in L^2(\Omega)^d$, and $v_f \in L^2(\Gamma)$, $\mathbf{g}_f \in L^2(\Gamma)^{d-1}$. It is assumed that ξ vanishes on $\mathcal{C}^\infty_{H_\Sigma}(\Omega, \Gamma)$. Then, it results from Lemma 4.0.5 that $v_m \in V^0$, $v_f = \gamma v_m$, $\mathbf{g}_m = \nabla v_m$ and $\mathbf{g}_f = \nabla_\tau \gamma v_m$. From the definition (1.2) of $H_\Sigma(\Omega, \Gamma)$, we conclude that ξ vanishes on $H_\Sigma(\Omega, \Gamma)$ which proves the density of $\mathcal{C}^\infty_{H_\Sigma}(\Omega, \Gamma)$ in $H_\Sigma(\Omega, \Gamma)$.

Compactness lemmas

The following lemma states the weak compactness of bounded sequences in $L^2(0, T; V^0)$.

Lemma 4.0.6 *Let $(v^{(m)})_{m \in \mathbb{N}}$ be a sequence of functions in $L^2(0, T; V^0)$ such that $\|v^{(m)}\|_{L^2(0,T;V)} \leq C$ for some positive C. Then, there exists $v \in L^2(0, T; V^0)$ such that up to the same subsequence*

$$v^{(m)} \rightharpoonup v \quad in \quad L^2(\Omega \times (0, T)) \quad and \quad \gamma v^{(m)} \rightharpoonup \gamma v \quad in \quad L^2(\Gamma \times (0, T));$$

moreover

$$\nabla v^{(m)} \rightharpoonup \nabla v \quad in \quad L^2(\Omega \times (0, T))^d \quad and \quad \nabla \gamma v^{(m)} \rightharpoonup \nabla \gamma v \quad in \quad L^2(\Gamma \times (0, T))^{d-1}.$$

Proof: First, let us recall that the normal trace operator $\gamma_{\mathbf{n}} : H_{\rm div}(\Omega) \to H^{-1/2}(\partial\Omega)$ is surjective. Indeed, for any $l \in H^{-1/2}(\partial\Omega)$ we consider the unique weak solution $u \in H^1(\Omega)$ of $-\Delta u + u = 0$ on Ω with $\nabla u \cdot \mathbf{n} = l$ on $\partial\Omega$ defined by $\langle u, v\rangle_{H_1(\Omega)} = \langle l, \gamma_{\partial\Omega} v\rangle_{H^{-1/2}(\partial\Omega), H^{1/2}(\partial\Omega)}$ for all $v \in H^1(\Omega)$, where $\gamma_{\partial\Omega}$ is the trace operator from $H^1(\Omega)$ to $H^{1/2}(\partial\Omega)$. Hence the function $\mathrm{G} := \nabla u$ is in $H_{\rm div}(\Omega)$ and satisfies $\gamma_{\mathbf{n}}\mathrm{G} = l$.

Next, from the Poincaré inequality and the continuity of the trace operators γ_i, the sequence $v^{(m)}$ is bounded in $L^2(0,T;H^1(\Omega))$ and the sequences $v_i^{(m)} = \gamma_i v^{(m)}$ are bounded in $L^2(0,T;H^1(\Gamma_i))$ for all $i \in I$. Hence, it is classical to show that there exist $v \in L^2(0,T;H^1_0(\Omega))$ and $v_i \in L^2(0,T;H^1_{\Sigma_{i,0}}(\Gamma_i))$ such that up to the same subsequence:

$$\left\{\begin{array}{ll} v^{(m)} \rightharpoonup v & \text{in } L^2(\Omega\times(0,T)),\\ \nabla v^{(m)} \rightharpoonup \nabla v & \text{in } L^2(\Omega\times(0,T))^d,\\ v_i^{(m)} \rightharpoonup v_i & \text{in } L^2(\Gamma_i\times(0,T)),\\ \nabla v_i^{(m)} \rightharpoonup \nabla v_i & \text{in } L^2(\Gamma_i\times(0,T))^{d-1}, \end{array}\right.$$

for all $i \in I$, where $H^1_{\Sigma_{i,0}}(\Gamma_i)$ is the subspace of $H^1(\Gamma_i$ with vanishing trace on $\Sigma_{i,0}$. It remains to show that $v \in L^2(0,T;V^0)$ with $(\gamma v)_i = v_i$. Let us first show that $\gamma_i v = v_i$. We extend the fracture Γ_i in the direction of the plane $\mathcal{P}_i$ in order to reach $\partial\Omega$ and to decompose the domain Ω into two subdomains, say Ω_i and $\Omega_{i'}$. Now let us introduce $r_i \in L^2(\Gamma_i)$ and a function $l \in L^2(\partial\Omega_i)$ which is defined by

$$l = \left\{\begin{array}{ll} r_i & \text{on } \Gamma_i,\\ 0 & \text{otherwise.}\end{array}\right.$$

Thus, since $l \in L^2(\partial\Omega_i) \subset H^{-1/2}(\partial\Omega_i)$ and, thanks to the surjectivity of the normal trace operator recalled above, there exists $\mathbf{q}_i \in H_{\rm div}(\Omega_i)$ such that $\mathbf{q}_i \cdot \mathbf{n}_i = l$. Then, passing to the limit in the equality

$$\int_0^T \int_{\Omega_i} \Big(\mathbf{q}_i(\mathbf{x})\cdot\nabla v^{(m)}(\mathbf{x},t) + v^{(m)}(\mathbf{x},t)\mathrm{div}\mathbf{q}_i(\mathbf{x})\Big)\varphi(t)d\mathbf{x}dt = \int_0^T \int_{\Gamma_i} \varphi(t) r_i(\mathbf{x}) v_i^{(m)}(\mathbf{x},t) d\tau(\mathbf{x})dt,$$

yields

$$\int_0^T \int_{\Gamma_i} \varphi(t) r_i(\mathbf{x})(v_i(\mathbf{x},t) - \gamma_i v(\mathbf{x},t)) d\tau(\mathbf{x})dt = 0,$$

for all $r_i \in L^2(\Gamma_i)$ and $\varphi \in L^2(0,T)$, hence $v_i = \gamma_i v$. Next, let us introduce the following trace operators

$$\gamma_{i,j} : H^1(\Gamma_i) \to L^2(\Sigma_{i,j}),$$

for each $(i,j) \in I^2_\Sigma$ where I^2_Σ is the subset of $I \times I$ such that $\Sigma_{i,j}$ has a non zero $d-2$ dimensional Lebesgue measure. We will prove that $\gamma_{i,j} v_i = \gamma_{j,i} v_j$ for all $(i,j) \in I^2_\Sigma$. Let us introduce $r_{i,j} = -r_{j,i} \in L^2(\Sigma_{i,j})$ and the function l_i and l_j defined by

$$l_i = \left\{\begin{array}{ll} r_{i,j} & \text{on } \Sigma_{i,j},\\ 0 & \text{on } \partial\Gamma_i \setminus \Sigma_{i,j},\end{array}\right.$$

and

$$l_j = \begin{cases} r_{j,i} & \text{on } \Sigma_{i,j}, \\ 0 & \text{on } \partial\Gamma_j \setminus \Sigma_{i,j}. \end{cases}$$

Thus, thanks again to the surjectivity of the normal trace operator, there exist $\mathbf{q}_i \in H_{\rm div}(\Gamma_i)$ and $\mathbf{q}_j \in H_{\rm div}(\Gamma_j)$ such that $\mathbf{q}_i \cdot \mathbf{n}_i = l_i$ and $\mathbf{q}_j \cdot \mathbf{n}_j = l_j$. Then, passing to the limit in the equality

$$\int_0^T \varphi(t) \int_{\Gamma_i} \nabla v_i^{(m)} \cdot \mathbf{q}_i + v_i^{(m)} \, \mathrm{div}(\mathbf{q}_i) \, d\tau(\mathbf{x}) dt + \int_0^T \varphi(t) \int_{\Gamma_j} \nabla v_j^{(m)} \cdot \mathbf{q}_j + v_j^{(m)} \, \mathrm{div}(\mathbf{q}_j) \, d\tau(\mathbf{x}) dt = 0,$$

we obtain that

$$\int_0^T \int_{\Sigma_{i,j}} \varphi(t) r_{i,j}(\mathbf{x}) \Big(\gamma_{i,j} v_i(\mathbf{x},t) - \gamma_{j,i} v_j(\mathbf{x},t) \Big) dl(\mathbf{x}) dt = 0,$$

for all $r_{i,j} \in L^2(\Sigma_{i,j})$, $\varphi \in L^2(0,T)$ which implies that $\gamma_{i,j} v_i = \gamma_{j,i} v_j$, and hence that $v \in L^2(0,T;V^0)$. $\square$

The following Lemma states an estimate on the space translates for bounded sequences in $L^2(0,T;H_0^1(\Omega))$ or in $L^2(0,T;H_0^1(\Gamma_i))$.

Lemma 4.0.7 *Let $d \in \mathbb{N}^*$, $t > 0$ and let Υ be an open polyhedral ($d = 3$) or polygonal ($d = 2$) domain in $\mathbb{R}^d$. Let $(u^{(m)})_{m\in\mathbb{N}}$ be a sequence of functions from $L^2(0,T;H_0^1(\Upsilon))$ such that $\|u^{(m)}\|_{L^2(0,T;H^1(\Upsilon))} < C$ for some positive C. Then, extending the functions $u^{(m)}$ by 0 on $(\mathbb{R}^d \setminus \Upsilon) \times (0,T)$, one has*

$$\sup_{m\in\mathbb{N}} \|u^{(m)}(\cdot, \cdot + \xi) - u^{(m)}\|^2_{L^2(\mathbb{R}^d \times (0,T))} \to 0 \quad as \quad |\xi| \to 0.$$

Proof : It is sufficient to notice that for all $\varphi \in C_\infty^c(\mathbb{R}^d \times (0,T))$ one has

$$\|\varphi(\cdot + \xi) - \varphi\|_{L^2(\mathbb{R}^d \times (0,T))} = |\xi| \|\nabla \varphi\|_{(L^2(\mathbb{R}^d \times (0,T)))^d}.$$

Therefore the result is deduced form the density of the set $C_\infty^c(\mathbb{R}^d \times (0,T))$ in $L^2(0,T;H^1(\mathbb{R}^d))$ and from the fact that $u^{(m)} \in L^2(0,T;H^1(\mathbb{R}^d))$. $\square$

Bibliography

[1] Adams, R.A.: Sobolev Spaces, Pure and Applied Mathematics. Academic Press, Vol. 140, New York, 1978.

[2] Ahmed, R., Edwards, M.G., Lamine, S., Huisman, B.A.H.: Control-volume distributed multi-point flux approximation coupled with a lower-dimensional fracture model. J. Comp. Physics, 462-489, Vol. 284, 2015.

[3] Alboin, C., Jaffré, J., Roberts, J., Serres, C.: Modeling fractures as interfaces for flow and transport in porous media. Fluid flow and transport in porous media 295, 13-24, 2002.

[4] Angelini, O., Brenner, K., Hilhorst, D.: A finite volume method on general meshes for a degenerate parabolic convection-reaction-diffusion equation. Numer. Math., vol. 123, issue 2, pp. 219-257, 2013.

[5] Angelini, O., Chavant, C., Chénier, E., Eymard, R, Granet, S.: Finite volume approximation of a diffusion-dissolution model and application to nuclear waste storage. Mathematics and Computers in Simulations, 81,10, pp. 2001-1017, 2011.

[6] Angot, P., Boyer, F., Hubert, F.: Asymptotic and numerical modelling of flows in fractured porous media. ESAIM Mathematical Modelling and Numerical Analysis 23, 239-275, 2009.

[7] Antonietti, P.F., Formaggia, L., Scotti, A., Verani, M., Verzotti, N.: Mimetic Finite Difference Approximation of flows in Fractured Porous Media. MOX Report No 20/2015, 2015.

[8] Antontsev, S. N., Kazhikhov, A. V., Monakhov, V. N.: Boundary value problems in mechanics of nonhomogeneous fluids, volume 22 of Studies in Mathematics and its Applications. North-Holland Publishing Co., Amsterdam, 1990. Translated from Russian.

[9] Baliga, B.R., Patankar, S.V.: A control volume finite-element method for two dimensional fluid flow and heat transfer. Numerical Heat Transfer, vol. 6, pp. 245-261, 1983.

[10] Brenner, K.: Méthodes de volumes finis sur maillages quelconques pour des systèmes d'évolution non linéaires. Thèse de Doctorat de l'Université d'Orsay, 2011.

[11] Brenner, K., Cancès, C., Hilhorst, D.: Finite volume approximation for an immiscible two-phase flow in porous media with discontinuous capillary pressure, Computational Geosciences, 2013.

[12] Brenner, K., Groza, M., Guichard, C., Lebeau, G., Masson, R.: Gradient discretization of Hybrid Dimensional Darcy Flows in Fractured Porous Media. Numerische Mathematik, pp. 1-41, 2015.

[13] Brenner, K., Groza, M., Guichard, C., Masson, R.: Vertex Approximate Gradient Scheme for Hybrid Dimensional Two-Phase Darcy Flows in Fractured Porous Media. ESAIM Mathematical Modelling and Numerical Analysis, 49, 303-330, 2015.

[14] Brenner, K., Hennicker, J., Masson, R., Samier, P.: Hybrid Dimensional Modelling and Discretization of Two Phase Darcy Flow through DFN in Porous Media. ECMOR XV- 15th European Conference on the Mathematics of Oil Recovery, 29 august-1 september 2016, Amsterdam, Netherlands, 2016.

[15] Brenner, K., Hennicker, J., Masson, R., Samier, P.: Gradient Discretization of Hybrid Dimensional Darcy Flows in Fractured Porous Media with Discontinuous Pressure at Matrix Fracture Interfaces. IMA Journal of Numerical Analysis, 2016.

[16] Brenner, K., Masson, R.: Convergence of a Vertex centered Discretization of Two-Phase Darcy flows on General Meshes. Int. Journal of Finite Volume Methods, 2013.

[17] Brenner, K., Groza, M., Jeannin, L., Masson, R., Pellerin, J., Immiscible two-phase Darcy flow model accounting for vanishing and discontinuous capillary pressures: application to the flow in fractured porous media, Proceedings of the Ecmor XV Conference, Amsterdam, august 2016.

[18] Brezis, H.: Functional Analysis, Sobolev Spaces and Partial Differential Equations. Springer, Universitext, 2011.

[19] Brezzi, F., Lipnikov K., Simoncini V.: A family of mimetic finite difference methods on polygonal and polyhedral meshes. Mathematical Models and Methods in Applied Sciences, vol. 15, 10, 2005, 1533-1552.

[20] Cancès, C.: Finite volume scheme for two-phase flows in heterogeneous porous media involving capillary pressure discontinuities. M2AN, Mathematical Modelling and Numerical Analysis, 43,5, pp. 973-1001, 2009.

[21] Cancès, C., Pierre, M.: An existence result for multidimensional immiscible two-phase flows with discontinuous capillary pressure field. SIAM J. Math. Anal., 44,2, pp. 966-992, 2012.

[22] Chavent, G., Jaffré, J.: Mathematical Models and Finite Elements for Reservoir Simulation. volume 17. North-Holland, Amsterdam, stud. math. appl. edition, 1986.

[23] Costabel, M.: Boundary integral operators on Lipschitz domains: elementary results. SIAM J. Math. Anal., 19, 613-626, 1988.

[24] D'Angelo, C., Scotti, A.: A mixed finite element method for Darcy flow in fractured porous media with non-matching grids. ESAIM Mathematical Modelling and Numerical Analysis 46,2, 465-489, 2012.

[25] Ding, D.Y., Langouet, H., Jeannin, L.: Simulation of Fracturing Induced Formation Damage and Gas Production from Fractured Wells in Tight Gas Reservoirs. SPE, 2012.

[26] Droniou, J., Eymard, R., Gallouët, T., Guichard, C., Herbin, R.: Gradient schemes for elliptic and parabolic problems, in preparation, 2015.

[27] Droniou, J., Eymard, R., Gallouët, T., Herbin, R.: A Unified Approach to Mimetic Finite Difference, Hybrid Finite Volume and Mixed Finite Volume Methods. Math. Models and Methods in Appl. Sci. 20,2, 265-295, 2010.

[28] Droniou, J., Eymard, R., Gallouët, T., Herbin, R.: Gradient schemes: a generic framework for the discretisation of linear, nonlinear and nonlocal elliptic and parabolic equations. Math. Models Methods Appl. Sci. 23, 13, 2395-2432, 2013.

[29] Duijn, C. J., Molenaar, J., Neef, M. J.: The effect of capillary forces on immiscible two-phase flows in heterogeneous porous media. Transp. Porous Media, 21, pp. 71-93, 1995.

[30] Eymard, R., Gallouët, T., Herbin, R.: Discretisation of heterogeneous and anisotropic diffusion problems on general nonconforming meshes SUSHI: a scheme using stabilisation and hybrid interfaces. IMA J. Numer. Anal. 30, 4, 1009-1043, 2010.

[31] Eymard, R., Guichard, C., Herbin, R.: Small-stencil 3D schemes for diffusive flows in porous media. Mathematical Modelling and Numerical Analysis 46, 265-290, 2012.

[32] Eymard, R., Herbin, R., Guichard, C., Masson, R.: Vertex Centered discretization of compositional Multiphase Darcy flows on general meshes. Comp. Geosciences 16, 4, 987-1005 (2012).

[33] Eymard, R., Herbin, R., Michel, A.: Mathematical study of a petroleum-engineering scheme. M2AN Math. Model. Numer. Anal., 37(6) pp. 937-972, 2003.

[34] Eymard, R., Féron, P., Gallouët, T., Herbin, R., Guichard, C.: Gradient schemes for the Stefan problem. IJFV - International Journal on Finite Volumes, june 2013.

[35] Eymard, R., Guichard, C., Herbin, R., Masson, R.: Gradient schemes for two-phase flow in heterogeneous porous media and Richards equation. article first published online, ZAMM - Journal of Applied Mathematics and Mechanics, 2013. doi: 10.1002/zamm.201200206

[36] Eymard, R., Guichard, C., Herbin, R., Masson, R.: Vertex centred Discretization of Two-Phase Darcy flows on General Meshes. ESAIM Proceedings, volume 35, pp. 59-78, 2012.

[37] Eymard, R., Guichard, C., Herbin, R., Masson, R: TP or not TP, that is the question. Computational Geosciences, 18, pp. 285-296, 2014.

[38] Faille, I., Fumagalli, A., Jaffré, J., Robert, J.: Reduced models for flow in porous media containing faults with discretization using hybrid finite volume schemes. https://hal-ifp.archives-ouvertes.fr/hal-01162048, 2015.

[39] Flauraud, E., Nataf, F., Faille, I., Masson, R.: Domain Decomposition for an asymptotic geological fault modeling, Comptes Rendus à l'académie des Sciences de Mécanique 331, 849-855, 2003.

[40] Formaggia, L., Fumagalli, A., Scotti, A., Ruffo, P.: A reduced model for Darcy's problem in networks of fractures. ESAIM Mathematical Modelling and Numerical Analysis 48,4, 1089-1116, 2014.

[41] Grisvard, P.: Elliptic Problems on non smooth domains. Pitman Publishing Inc., Marshfield, Massachusetts, 1985.

[42] Haegland, H., Aavatsmark, I., Guichard, C., Masson, R., Kaufmann, R.: Comparison of a Finite Element Method and a Finite Volume Method for Flow on General Grids in 3D. In the proceedings of ECMOR XIII, Biarritz, 2012.

[43] Hoteit, J., Firoozabadi, A.: An efficient numerical model for incompressible two-phase flow in fracture media. Advances in Water Resources, 31, pp. 891-905, 2008.

[44] Huber, R., Helmig, R.: Node-centred finite volume discretizations for the numerical simulation of multi-phase flow in heterogeneous porous media. Computational Geosciences, 4, pp. 141-164, 2000.

[45] Jaffré, J., Mnejja, M., Roberts, J.E.: A discrete fracture model for two-phase flow with matrix-fracture interaction. Procedia Computer Science 4, pp. 967-973, 2011.

[46] Karimi-Fard, M., Durlofsky, L.J., Aziz, K.: An efficient discrete-fracture model applicable for general-purpose reservoir simulators. SPE journal, 2004.

[47] Kazemi, H.: Pressure transient analysis of naturally fractured reservoirs with uniform fracture distribution. Trans. Soc. Pet. Engng AIME 246, 451-462, 1969.

[48] Lacroix, S., Vassilevski, Y. V., Wheeler, M. F.: Decoupling preconditioners in the Implicit Parallel Accurate Reservoir Simulator (IPARS). Numerical Linear Algebra with Applications, 8, pp. 537-549, 2001.

[49] Martin, V., Jaffré, J., Roberts, J.E.: Modeling fractures and barriers as interfaces for flow in porous media. SIAM J. Sci. Comput. 26,5, 1667-1691, 2005.

[50] McLean, W.: Strongly Elliptic Systems and Boundary Integral Equations. Cambridge University Press, Cambridge, UK, 2000.

[51] Michel, A.: A finite volume scheme for two-phase immiscible flow in porous media. SIAM J. Numer. Anal., 41(4), pp. 1301-1317, 2003.

[52] Mikhailov, S. E.: Traces, extensions and co-normal derivatives for elliptic systems on Lipschitz domains. J. Math. Anal. Appl. 378, 1, 324-342, 2011.

[53] Monteagudu, J., Firoozabadi, A.: Control-volume model for simulation of water injection in fractured media: incorporating matrix heterogeneity and reservoir wettability effects. SPE Journal 12, 355-366, 2007.

[54] Reichenberger, V., Jakobs, H., Bastian, P., Helmig, R.: A mixed-dimensional finite volume method for multiphase flow in fractured porous media. Adv. Water Resources 29, 7, 1020-1036, 2006.

[55] Saad, Y.: Iterative Methods for Sparse Linear Systems. 2nd edition, SIAM, Philadelphia, PA, 2003.

[56] Saad, Y.: http://www-users.cs.umn.edu/ saad/software/

[57] Sandve, T.H., Berre, I., Nordbotten, J.M.: An efficient Multi-Point Flux Approximation Method for discrete Fracture-Matrix Simulations. J. Comp. Phys. 231, 3784-3800, 2012.

[58] Scheichl, R., Masson, R., Wendebourg, J.: Decoupling and block preconditioning for sedimentary basin simulations. Computational Geosciences, 7, pp. 295-318, 2003.

[59] Si, H.: http://tetgen.org

[60] Tunc, X., Faille, I., Gallouët, T., Cacas, M.C., Havé, P.: A model for conductive faults with non matching grids. Comp. Geosciences 16, 277-296, 2012.

[61] Warren, J.E., Root, P.J.: The Behavior of Naturally Fractured Reservoirs. SPEJ, pp. 245-55, 1963.

[62] Xing, F., Masson, R., Lopez, S.: Parallel Vertex Approximate Gradient discretization of hybrid dimensional Darcy flow and transport in discrete fracture networks. preprint https://hal.archives-ouvertes.fr/hal-01272498, 2016.